Current Commutation and Control of Brushless Direct Current Drives Using Back Electromotive Force Samples

Stroomcommutatie en sturing van borstelloze gelijkstroomaandrijvingen op basis van de bemonsterde elektromotorische kracht van beweging

Araz Darba

Promotoren: prof. dr. ir. J. Melkebeek, dr. ir. F. De Belie
Proefschrift ingediend tot het behalen van de graad van
Doctor in de Ingenieurswetenschappen: Werktuigkunde-Elektrotechniek

Vakgroep Elektrische Energie, Systemen en Automatisering
Voorzitter: prof. dr. ir. J. Melkebeek
Faculteit Ingenieurswetenschappen en Architectuur
Academiejaar 2015 - 2016

UNIVERSITEIT
GENT

ISBN 978-90-8578-835-5
NUR 959, 961
Wettelijk depot: D/2015/10.500/79

Promoters:

Prof. dr. ir. Jan Melkebeek
Dr. ir. Frederik De Belie

Members of the examining board

Prof. dr. ir. Rik Van de Walle, Dean FirW, ELIS - UGent, Chairman
Prof. dr. ir. Pieter Rombauts, ELIS - UGent, Secretary
Prof. dr. ir. Pablo García Fernández, University of Oviedo
Prof. dr. ir. Rene Boel, EESA - UGent
Prof. dr. ir. Mia Loccufier, EESA - UGent
Prof. dr. ir. Dirk Stroobandt, ELIS - UGent

Ghent University

Faculty of Engineering and Architecture

Department of Electrical Energy, Systems and Automation (EESA)

Electrical Energy Laboratory (EELAB)

Technologiepark 913,

B-9052 Zwijnaarde (Gent), Belgium

Acknowledgement

I would like to express my sincere gratitude to my promoters Prof. dr. ir. Jan Melkebeek and Dr. ir. Frederik De Belie. I specially would like to thank them for offering me the opportunity to perform this research at Electrical Energy Laboratory (EELAB) and their great guidance and supervision. As well as providing such an nice atmosphere at EELAB to give the freedom for me to choose my preferred approach towards obtaining the PhD.

My deepest gratitude to Prof. Jan Melkebeek for his incredible support during the hard times that I had. I learned a lot from him and together with all experiences that I gained during working at EELAB will remain always with me.

I would like to thank Dr. ir. Ferderik De Belie for his willingness to share his ideas and giving his invaluable suggestions for incoming challenges during my research. His support greatly improved the quality of this research. Special thanks to Mrs. Marilyn Van Den Bossche not for all the administrative works (educational and non educational) that she has done for me but for being my best friend.

I am very grateful of all my colleagues which I was sitting next to them and sharing the office with them. Dr. ir. Frederik De Belie, Dr. ir. Jeroen De Mayer, Dr. ir. Steven Thielemans, Ir. Aboubakr Salem, Dr. ir. Ronny Bockstaele, Ir. Bart Wymeersch and Ir. Joachim Druant for the nice working atmosphere, help and support. I wish to thank Ir. Francisco Ramirez Perez and Ir. Dimitar Bozalakov for their interest in my work and for the pleasant moments that we spend together at the laboratory. Another thank to Dr. ir. Thomas Vyncke for sharing his experiences on FPGAs. I also appreciate all the detailed information which were provided by Prof. dr. Alex Van Den Bossche during my PhD. I wish to thank Tony Boone and Stefaan Dhondt for their technical assistance for my projects and Nic Vermeulen for his solutions regarding computer and IT problems.

Een speciaal dank aan Ingrid Dubois voor de vele hulp, het verzorgen van de vergadering, het zetten van koffie en het afwassen. We allemaal te danken u een grote dank.

I am very grateful of my parents for all good things that they have done for me at the first place. Secondly, for their unconditional support and unlimited love that I received from them. Last but not least I would like to thank Shabnam for her support and love which was a great motivation during this period.

Thank you all!

Gent, 31 maart 2015
Araz Darba

Samenvatting

Borstelloze gelijkstroommachines (BLDC machines) zetten elektrische energie om in mechanische bewegingsenergie en worden vaak aangewend in huishoudelijke toestellen, in automobiel toepassingen alsook in actuatoren voor ruimtevaart wegens hun eenvoud in constructie en sturing. Bovendien vertonen deze machines interessante eigenschappen zoals een hogere energiedensiteit vergeleken met inductiemachines en gelijkstroomcommutatormachines en dit vaak aan een lagere kost. Tijdens de aansturing van de BLDC machine worden de verschillende ingangsklemmen van energie voorzien en dit afhankelijk van de stand van het rotationele onderdeel ten opzichte van de stator, het stilstaande onderdeel. In deze aansturing is dus kennis omtrent de rotorpositie of beter gezegd de positie van de permanente magneten onontbeerlijk. Vaak gebruikt men daartoe Hall-effect sensoren. In modernere aandrijvingen worden deze sensoren vervangen door algoritmes waarin de positie geschat wordt aan de hand van het meten van stromen en spanningen aan de klemmen van de machine. De redenen daartoe zijn vaak gerelateerd aan meetruis en onbetrouwbaarheid van de sensoren. Bovendien geeft het voordelen op het vlak van volume, installatiekost en onderhoud. Ondanks de aanwezige metingen omtrent spanning en stroom wordt het bepalen van de rotorpositie aan de hand van schattingen vaak aangeduid met een sensorloze aandrijving, verwijzend naar de afwezigheid van een sensor voor de rotorpositie.

Momenteel bestaan verschillende sensorloze technieken voor BLDC machines. In dit doctoraatswerk worden een tweetal methodes bestudeerd waarbij gebruik wordt gemaakt van de bemonsterde snelheidsgeïnduceerde spanning, namelijk de e.m.k. van beweging. De aansturing van de BLDC machine laat toe deze spanning direct op te meten daar steeds één van de ingangsklemmen stroomloos is. Met behulp van wiskundige analyse, simulatiemodellen en experimentele opstellingen worden de aangebrachte verbeteringen geverifieerd en vergeleken met reeds bestaande sensorloze technieken. Om tot deze verbeteringen te komen, wordt rekening gehouden met de storing in het aandrijven als gevolg van de belasting. Deze belasting kan resulteren in een variatie van de mechanische inertie alsook wrijving. In bestaande sensorloze methodes wordt zelden rekening gehouden met

deze variaties waardoor de stabiliteit en de dynamische performantie niet steeds gehaald wordt. Directe metingen van de belasting dienen vermeden te worden daar de nodige sensoren vaak te duur zijn, onnodig plaats innemen of dienen geplaatst te worden in gevaarlijke, stofrijke omgevingen. Ook hier biedt een schatter oplossing. Het geschatte lastkoppel wordt vervolgens aangewend in de sensorloze BLDC aandrijving om de gevoeligheid ten opzichte van mechanische storingen te verlagen.

BLDC machines zijn vaak kleine machines, met een kleine mechanische inertie. Vaak betekent dit dat de mechanische en elektrische tijdsconstanten vergelijkbare waarden hebben waardoor de vaak gebruikte cascaderegeling voor snelheid en stroom moet herbekeken worden. In plaats van te werken met een snelle regellus voor de stroom en een trage regellus daarrond voor de snelheid, wordt een modelgebaseerde voorspellende regelaar bestudeerd aan de hand van simulatie modellen en experimenten. Aandacht wordt geschonken aan het gedrag van de regelaar bij variaties in het lastkoppel.

In de eerste hoofdstukken wordt de huidige stand van zaken en de problematiek in het sensorloos aandrijven van BLDC machines beschreven. Na het opsommen van de doelstellingen en de methodiek in Hoofdstuk 1 worden de fundamentele principes in het aansturen van BLDC machines neergeschreven in Hoofdstuk 2. Om tot de sensorloze sturing van de BLDC machine te komen is het nodig de BLDC aandrijving te modelleren, Hoofdstuk 3. Zowel het model in continue tijd als een discreettijdsmodel komen aan bod. Onder meer zal het laatst vermelde model aangewend worden in de modelgebaseerde voorspellende regelaar uitgevoerd op een Field Programmable Gate Arrays testplatform.

Een eerste belangrijke bijdrage van dit doctoraatswerk is terug te vinden in Hoofdstuk 4 waarin het sensorloze algoritme beschreven wordt. Het vernieuwende aan deze methode is het gebruik van het bemonsterde e.m.k.-signaal om de rotorpositie en rotorsnelheid te schatten. Naast simulatieresultaten worden tevens metingen besproken om deze techniek te bespreken. Nadruk wordt gelegd op het accuraat schatten van de commutatiemomenten voor de stroom.

Hoofdstuk 5 bevat de tweede bijdrage van het doctoraatswerk en beschrijft het algoritme om het lastkoppel te schatten om vervolgens het dynamisch gedrag van de sensorloze aandrijving te verbeteren. Het gebruik van geschatte waarden van het lastkoppel in de regellus verlaagt de gevoeligheid van de aandrijving ten opzichte van storingen de mechanische belasting. Aangezien hierbij een model wordt gebruikt met onder meer de mechanische inertie en spanningsconstante van de machine wordt de gevoeligheid van deze techniek voor variaties in de machineparameters bekeken.

Een laatste belangrijke bijdrage wordt beschreven in Hoofdstuk 6, met name de toepassing van en modelgebasseerde voorspellende regelaar ter vervanging van de vaak gebruikte cascaderegeling met proportionele en integrerende acties. Hiertoe zal vooreerst een algemene beschrijving van deze regelaars gegeven worden waarna de toepassing volgt op de BLDC aandrijving. Wegens de vereiste rekenkracht bij dit algoritme, worden enkele vernieuwingen ingevoerd in het FPGA platform waardoor de vereiste middelen in de FPGA gereduceerd worden. Een belangrijk aandachtspunt is het limiteren van de stroom waarbij nog steeds een snelle reactie verkregen wordt in de snelheidsregellus. Hiertoe zal een aangepaste kostenfunctie gedefinieerd worden. Ten slotte zal de combinatie van deze techniek met de sensorloze methode uit Hoofdstuk 4 bestudeerd worden.

In een laatste deel, Hoofdstuk 7, worden de voornaamste besluiten opgesomd waarbij aandacht wordt geschonken aan de eigen bijdragen in het gebied van sensorloze aandrijvingen. Tevens wordt aangegeven in welke wijze dit onderzoek kan worden verdergezet.

Summary

Brushless DC machines (BLDC) are widely used in home, automotive, aerospace and military applications. The reason of this interest in different industries in this type of machine is due to their significant advantages. Brushless DC machines have a high power density, simple construction and higher efficiency compared to conventional AC and DC machines and lower cost comparing to permanent magnet AC synchronous machines. The phase currents of a BLDC machine have to commutate properly which is realised by using power semiconductors. For a proper commutation the rotor position is often obtained by an auxiliary instrument, mostly an arrangement of three Hall-effect sensors with 120 spatial displacement. In modern and cost-effective BLDC drives the focus is on replacing the noise sensitive and less reliable mechanical sensors by numerical algorithms, often referred to as sensorless or self-sensing methods. The advantage of these methods is the use of current or voltage measurements which are usually available as these are required for the control of the drive or the protection of the semiconductor switches. Avoiding the mechanical position sensor yields remarkable savings in production, installation and maintenance costs. It also implies a higher power to volume ratio and improves the reliability of the drive system. Different self-sensing techniques have been developed for BLDC machines. Two algorithms are proposed in this thesis for self-sensing commutation of BLDC machines using the back-EMF samples of the BLDC machine. Simulations and experimental tests as well as mathematical analysis verify the improved performance of the proposed techniques compared to the conventional back-EMF based self-sensing commutation techniques.

For a robust BLDC drive control algorithm with a wide variety of applications, load torque is as a disturbance within the control-loop. Coupling the load to the motor shaft may cause variations of the inertia and viscous friction coefficient besides the load variation. Even for a drive with known load torque characteristics there are always some unmodelled components that can affect the performance of the drive system. In self-sensing controlled drives, these disturbances are more critical due to the limitations of the self-sensing algorithms compared to drives equipped with position sensors. To compensate or reject torque disturbances, control algorithms need the information of those disturbances. Direct measurement of the load torque

on the machine shaft would require another expensive and sensitive mechanical sensor to the drive system as well as introducing all of the sensor related problems to the drive. An estimation algorithm can be a good alternative. The estimated load torque information is introduced to the self-sensing BLDC drive control loop to increase the disturbance rejection properties of the speed controller. This technique is verified by running different experimental tests within different operation conditions.

The electromagnetic torque in an electrical machine is determined by the stator current. When considering the dynamical behaviour, the response time of this torque on a stator voltage variation depends on the electric time constant, while the time response of the mechanical system depends on the mechanical time constant. In most cases, the time delays in the electric subsystem are negligible compared to the response time of the mechanical subsystem. For such a system a cascaded PI speed and current control loop is sufficient to have a high performance control. However, for a low inertia machine when the electrical and mechanical time constants are close to each other the cascaded control strategies fail to provide a high performance in the dynamic behavior. When two cascade controllers are used changes in the speed set-point should be applied slowly in order to avoid stability problems. To solve this, a model based predictive control algorithm is proposed in this thesis which is able to control the speed of a low inertia brushless DC machine with a high bandwidth and good disturbance rejection properties. The performance of the proposed algorithm is evaluated by simulation and verified by experimental results as well. Additionally, the improvement on the disturbance rejection properties of the proposed algorithm during the load torque variations is studied.

In chapters 1 and 2 the basic operation principles of the BLDC machine drives will be introduced. A short introduction is also given about the state of the art in control of BLDC drives and self-sensing control techniques.

In chapter 3, a model for BLDC machines is derived, which allows to test control algorithms and estimators using simulations. A further use of the model is in Model Based Predictive Control (MBPC) of BLDC machines where a discretised model of the BLDC machine is implemented on a computation platform such as Field Programmable Gate Arrays (FPGA) in order to predict the future states of the machine.

Chapter 4 covers the theory behind the proposed self-sensing commutation methods where new methodologies to estimate the rotor speed and position from back-EMF measurements are explained. The results of the simulation and experimental tests verifies the performance of the proposed position and speed estimators. It will also be proved that using the proposed techniques improve the detection accuracy of the commutation instants.

In chapter 5, the focus is on the estimation of load torque, in order to use it to improve the dynamic performance of the self-sensing BLDC machine drives. The load torque information is used within the control loop to improve the disturbance rejection properties of the speed control for the disturbances resulting from the applied load torque of the machine. Some of the machine parameters are used within speed and load torque estimators such as back-EMF constant K_e and rotor inertia J. The accuracy with which machine parameters are known is limited. Some of the machine parameters can change during operation. Therefore, the influence of parameter errors on the position, speed and load torque is examined in chapter 5.

In Chapter 6 the fundamentals of Model based Predictive Control for a BLDC drive is explained, which are then applied to a BLDC drive to control the rotor speed. As the MPC algorithm is computationally demanding, some enhancements on the FPGA program is also introduced in order to reduce the required resources within the FPGA implementation. To keep the current bounded and a high speed response a specific cost function is designed to meet the requirements. later on, the proposed MPC method is combined with the proposed self-sensing algorithm and the advantages of the combined algorithms is also investigated. The effects of the MPC parameters on the speed and current control performance is also examined by simulations and experiments.

Finally, in chapter 7 the main results of the research is summarized . In addition, the original contributions that is give by this work in the area of self-sensing control is highlighted. It is also shown how the presented work could be continued and expanded.

Contents

List of notations, symbols and abbreviations

List of principal symbols No distinct notation is used for absolute or per-unit values

general	
x	real or complex number
$\overline{x}$	phasor
$\boldsymbol{x}$	vector or matrix with elements x_i or x_{ii}
$\boldsymbol{x}^T$	transpose conjugate of $\boldsymbol{x}$
$\dot{x}$	time derivative of x
$\hat{x}$	estimated value of x
x^*	reference value of x
x_{pred}	predicted value of x
x_{meas}	measured value of x
x_{error}	$x^* - x_{\text{meas}}$

symbols

$e, (e_{xy}, e_x)$	back EMF, (coupled between x and y phases, phase x), [V]
F	speed normalized back-EMF, [Vs/rad]
$i, (i_x, i_{DC})$	current, (phase x, DC-bus), [A]
J	inertia, [kgm^2]
k	discrete sample
K_e	voltage constant, [rad/Vs]
K_t	torque constant, [Nm/A]
K_v	voltage constant, [rad/Vs]
$L, (L_x)$	inductance, (x axis inductance) [H]
M	mutual inductance, [H]
m_L	slope of the linear part in the back-EMF signal, [V/s]
N_p	number of poles pairs
$\omega, \omega_e, \omega_m$	angular frequency, (electrical, mechanical), [rad/s]
R	resistance, [Ω]
$T, (T_e, T_l)$	torque, (electromagnetic, load), [Nm]
$\tau, (\tau_m, \tau_e)$	time constant (mechanical, electrical), [s]
$\theta, (\theta_e, \theta_m)$	angular position, (electrical, mechanical), [rad]
T_s	sampling time, [s]
$v, (v_{xy}, v_x, v_n, v_{n'}, v_{DC}, v_{\text{br}})$	voltage, (coupled between x and y phases, neutral point, virtual neutral point, phase x, DC-bus, brush voltage drop), [V]

Abbreviations

AC	Alternating Current
BLAC	BrushLess AC Machine
BLDC	BrushLess DC Machine
CORDIC	COordinate Rotation DIgital Computer
CSI	Current-Source Inverter
DC	Direct Current
DSP	Digital Signal Processor
DTC	Direct Torque Control
EFOSMO	Encoderless Full-Order Sliding Mode Observer
EKF	Extended Kalman Filter
EPSAC	Extended Prediction Self-Adaptive Control
EMC	Electro-Magnetic Compatibility
EMI	Electro-Magnetic Interference
EMF	ElectroMotive Force
FI	Field Intensified
FOC	Field Oriented Control
FCS	Finite Control Set
FPGA	Field-Programmable Gate Array
GPS	Global Positioning System
HFSI	High Frequency Signal Injection
HIL	Hardware In the Loop
HVAC	Heating, Ventilation and Air Conditioning
IGBT	Insulated-Gate Bipolar Transistor
IPM	Interior Permanent-Magnet
IPMSM	Interior Permanent-Magnet Synchronous Machine
MBPC	Model Based Predictive Control
MIMO	Multiple Input Multiple Output
MMUAV	Multirotor Miniature Unmanned Air Vehicles
MOSFET	Metal-Oxide-Semiconductor Field-Effect Transistor
MPDTC	Model Predictive Direct Torque Control
MPC	Model Predictive Control
MRAS	Model Reference Adaptive System
MTPA	Maximum Torque Per Ampere
PCC	Predictive Current Control
PI	Proportional-Integral
PID	Proportional-Integral-Derivative
PLL	Phase Locked Loop
PM	Permanent Magnet
PMSM	Permanent-Magnet Synchronous Machine

Abbreviations

PTC	Predictive Torque Control
PWM	Pulse-Width Modulation
RMS	Root-Mean-Square
SISO	Single Input Single Output
SPMSM	Surface Permanent-Magnet Synchronous Machine
VSI	Voltage-Source Inverter
ZCV	Zero Sequence Voltage

Chapter 1

Introduction

Brushless DC machines (BLDC) are rotating electrical devices and used in numerous branches of industry: automation, robotics, automotive, household appliances and industrial applications. These machines are used in electric and hybrid vehicles, Heating Ventilating and Air Conditioning (HVAC) and refrigeration applications, as well as for motion and position control of actuation systems. Or in Multirotor Miniature Unmanned Air Vehicles (MMUAV) technology intended to utilize Global Positioning System (GPS) to autonomously fly individual packages to customer's doorsteps within a short time after ordering or to fly with a pilot on the ground for more complicated tasks. This revolutionary concept covers a wide variety of applications such as search and rescue, fire fighting, police surveillance and fast food industry, letter or package delivery services. The main propelling component of all these drones are BLDC machines due to the specific features that will be discussed later.

1.1 General Aspects of BLDC Machines

BLDC machines belong to the family of Permanent Magnet Synchronous Machines (PMSM). The two most fundamental permanent magnet synchronous machines are discussed in Section 1.1.2. The fundamental ideas behind the basic control of Brushless Direct Current (BLDC) machines are explained in Chapter 2. More advanced control techniques based on self-sensing commutation will be introduced in Chapters 5 and 6.

1.1.1 DC Versus BLDC Machines

The speed ω_e and electromagnetic torque T_{em} of a regular DC machine are controlled without much computational effort. The relative speed between the magnetic rotor field and the armature winding results in an induced voltage e in the armature winding that is called Back Electromotive Force (Back-EMF), which is proportional to the rotor speed:

$$e = K_e \phi \omega_e \tag{1.1}$$

where ϕ is the rotor flux, ω is the angular velocity and K_e is the voltage constant. The terms back-EMF constant K_e, generic electrical constant K_b and speed constant K_ω are also used with the similar meaning. K_e is the ratio of the motor no-load speed to the peak back-EMF voltage. For example, a no-load motor of $K_e = 2.63 \times 10^{-3}$ V/rpm, supplied with 18 V, will run at a nominal speed of 6840 rpm. It also means that if the same machine is rotated externally with a speed of 6840 rpm will generate 18 V over its terminals. The interaction between the magnetic field and the armature windings gives rise to an electromagnetic torque T_e, which is proportional to the armature current.

$$T_e = K_t \phi i \tag{1.2}$$

where K_t is the machine torque constant and i is the current flowing through the stator winding. By controlling the current in the armature winding, the produced electromagnetic torque is controlled.

A major drawback of regular DC machines is the need for mechanical commutators to drive these machines. Indeed, the flux ϕ is the flux coupled with the stator winding and generated on the rotor. For this a winding on the rotor is placed supplied by a current which requires brushes and commutator. These commutators are liable to wear: they are always under severe mechanical (friction, vibration, heat) and electrical (electrical arcs) stresses and because of a nonideal electrical contact between brushes and commutator a voltage drop across the brushes v_{br} is always present. As a result, DC machines require periodic maintenance and their lifetime is as low as one third of modern BLDC machines, where the current is commutated using advanced power electronic components such as semiconductor switches.

1.1.2 Classification of Permanent Magnet Synchronous Machines

Different types of Permanent Magnet Synchronous Machines (PMSM) exist. Generally, they can be classified and characterized based on the following criteria:

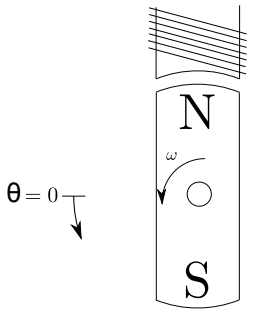

Figure 1.1. Definition of the angle θ and ω, the rotor position is shown for $t = 0$.

- The waveform of the back-EMF of the machine. This waveform can be trapezoidal, sinusoidal or in between.
- The mounting of the magnets (surface mounted or magnets buried in rotor).
- The flux direction (radial or axial).
- Structural configuration: radial (internal or external rotor), axial (single or multiple rotor and stators, with or without magnetic core).

In this section, the waveforms of two types of PMSM are discussed. The waveforms are described in terms of the angle θ, that determines the position of the rotor in the air gap, and the dimensionless time ωt. The definition of θ and ω is shown in Fig. 1.1. The shown rotor position corresponds with $t = 0$.

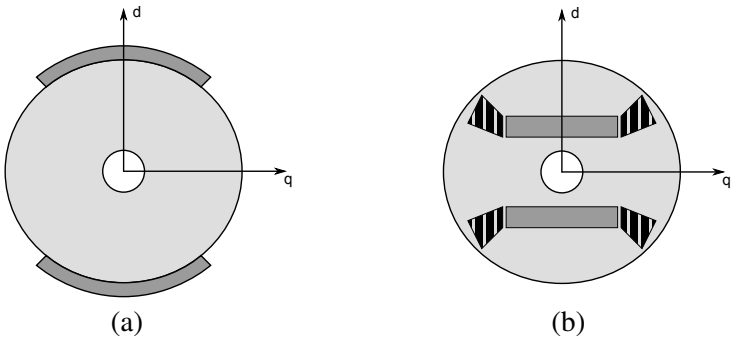

Figure 1.2. Position of permanent magnets in rotor of (a): SPMSM, (b): IPMSM,

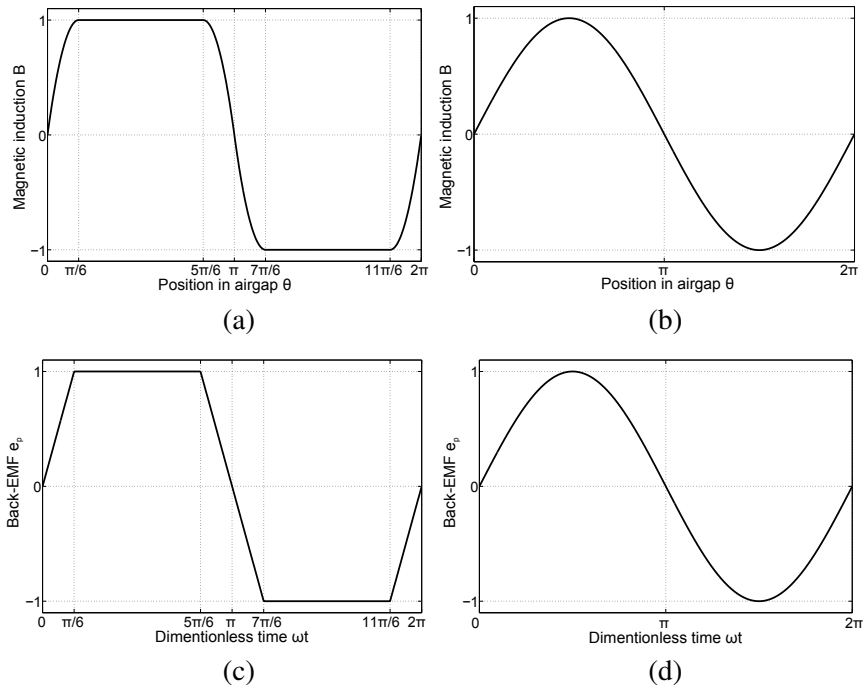

Figure 1.3. Comparison between the waveforms of the magnetic induction and the back-EMF of SPMSM (left) and IPMSM (right)

Two types of PMSM are commonly used in practice. In the first type, the magnets are mounted on the surface of the rotor, as illustrated in Fig. 1.2(a), producing an approximately rectangular magnetic induction field in the air gap as shown in Fig. 1.3(a). In the second type, the magnets are positioned in the interior of the rotor, as shown in Fig. 1.2(b), the resulting magnetic induction can be rectangular or sinusoidal, Fig. 1.3(b). The magnetic inductance B in Fig. 1.3(a) and (b) is normalized to an amplitude of 1. The positioning of the magnets in the second type results in a smaller risk of dismounting magnets due to centrifugal forces at high operating speeds. A cup motor (external rotor) can be used in order to improve the structural integrity of the machine by placing the Permanent Magnets (PM) on the inner surface of the rotor. In this way, by increasing the speed, permanent magnets are actually pushed against the rotor iron by centrifugal forces. Besides the permanent magnets (dark grey coloured parts in Fig. 1.2), non-magnetic material (hatched parts in Fig. 1.2) is used to prevent magnetic short circuit. The difference in the positioning of the permanent magnets leads to a different ratio of direct (aligned with the direction of the rotor field) and quadrature axis (perpendicular to the rotor field) inductances, L_d and L_q respectively. Indeed, the magnetic reluctance of the permanent magnets is comparable to that of air. For

the SPMSM (Surface mounted Permanent-Magnet Synchronous Machine), the permanent magnets lie partially or completely in the air gap between stator and rotor. As a result, there is only a small difference between L_d and L_q for SPMSM. In this case, the reluctance torque can be neglected. Conversely, a difference between L_d and L_q exists for IPMSM (Interior Permanent-Magnet Synchronous Machine) as more magnetic reluctance is seen in the d-axis resulting in $L_d < L_q$. For these machines, L_d is smaller than L_q.

To obtain a good electromagnetic energy conversion, the spatial distribution of the stator winding along the airgap is chosen in such a way that it generates a magnetic field similar to the permanent magnet rotor field. For an SPMSM, this implies a concentrated stator winding. For an IPMSM, a distributed stator winding is chosen.

Due to the choice of the winding distribution in the stator, the induced voltage in the stator winding (the counter electromotive force or the back-EMF) is trapezoidal Fig. 1.3(c) when the induction field is rectangular. In case the induction field is sinusoidal the back-EMF is sinusoidal as well, see Fig. 1.3(d). The trapezoidal waveform of the back-EMF of an SPMSM is often assumed constant over 120° electrical. Hence, the back-EMF varies linearly over 60° electrical in between the intervals where the back-EMF is constant. When the back-EMF is trapezoidal, the machine is called a Brushless DC Machine (BLDC), due to the resemblance of the magnetic field in the air gap to that of a DC machine. Due to the sinusoidal field, a synchronous machine with interior permanent magnets (sinusoidal back-EMF) is also called a Brushless AC Machine (BLAC). Note that the amplitude of the back-EMF waveforms in Fig. 1.3(c) and Fig. 1.3(d) is normalized to 1.

To achieve a constant power output, the machine is fed by a switching power converter that guarantees the synchronism between the armature current waveform and the back-EMF waveform. In the case of a BLDC machine, the inverter often delivers a square current waveform of 120° electrical. This current then matches the back-EMF waveform in the 120° interval where it is constant (trapezoidal waveform). Between positive and negative current blocks, the armature current is set to zero for 60° electrical, Fig. 1.4(a). This implies that the converter should be of the current-source type (CSI) in which the supply current is constant. Another possibility to obtain such a current and which is used more often, is to use the voltage-source inverter type (VSI), where the amplitude of the output is voltage using a pulse-width modulation (PWM) to control the output current. Considering the sinusoidal field of an IPMSM it needs to be fed by a sinusoidal steered current Fig. 1.4(b).

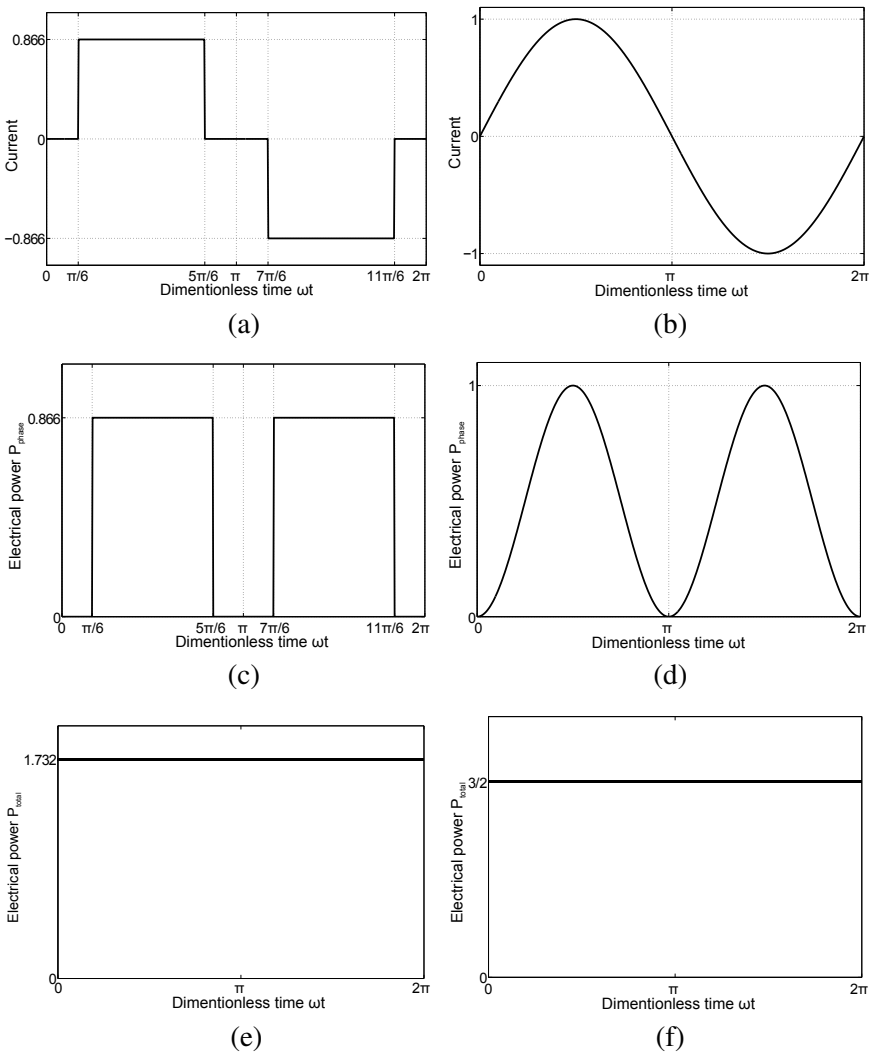

Figure 1.4. Comparison between the waveforms of the curent, the power per phase and the total power of (left): SPMSM and (right): IPMSM

To produce the maximum obtainable power, the current should be in phase with the back-EMF. As the instantaneous back-EMF is dependent on the rotor position and induced by the permanent magnets this implies that the rotor position information is required in order to have a high performance operation.

One advantage of a BLDC machine over a BLAC machine, is that for the same peak current and peak back-EMF, the BLDC machine delivers a power that is a factor $2\frac{\sqrt{3}}{3}$ greater than that of the BLAC machine as it is shown in Fig. 1.4.

The electromagnetic field in a BLDC machine is generated using permanent magnets that are mounted on the rotor. This implies that copper losses related to the generation of the electromagnetic field are absent. This aspect entails that the efficiency of the BLDC machine is higher than that of a DC machine. In addition, the armature winding of the BLDC machine, which caries the load current, is placed in the stator. This results in a better heat conduction to the surroundings of the machine (assuming an internal rotor). As thermal aspects contribute in sizing the machine, a BLDC machine can thus be produced more compactly than a regular DC machine.

When comparing BLDC machines to AC machines, it can be noted that BLDC machines are more compact than induction machines for the same output power, due to the presence of stator and rotor windings in an induction machine. A BLDC machine is also able to produce its maximum torque at lower speed. Due to winding distribution in the stator and the positioning of the permanent magnets in the rotor, a BLDC machine is able to produce more torque for the same machine volume than other PM machines.

With energy bills getting higher, all these effects drive the advance of BLDC machines in industry. Regardless of the aforementioned advantages, driving a BLDC machine requires the rotor position information. Acquiring rotor position information from sensors will increase the cost, volume, maintenance effort and decrease the reliability of the drive system.

1.2 Self-Sensing Control of Permanent Magnet Machines

As mentioned in the previous section, to drive a PM machine rotor position information is required in order to steer the applied voltages and currents to the stator windings. For a PMSM with a sinusoidal field a high resolution position sensor is required to drive the machine properly with respect to that field. On the other hand for a BLDC machine with a trapezoidal field a low resolution sensor can be used as current commutates several times (six or sometimes twelve) only each revolution. However, it has to be aligned accurately with the back-EMF of the rotor. A slight misalignment of the sensors result in a reduction in generated maximum electromagnetic torque per ampere (MTPA). This reduces the power

conversion rate, increases the losses, torque ripple, noise, vibration and could even affect stability of the drive.

Different sensors can be used for detecting the rotor position of PM machines. For an IPMSM that requires high resolution an encoder or resolver is more suitable. However, for a BLDC machine 3 Hall-effect sensors with 120° spatial displacement around the stator is sufficient. If the sensors are well aligned to the rotor, the current and back-EMF will be aligned as well. The accurate mounting of the sensors could be an issue for some applications as reported in [JianchengFang2014].

Position sensors are sensitive optical or electromagnetic components. All these sensors require an independent power supply and data transmission lines. The data flowing through these wires are always prone to Electro Magnetic Interferences (EMI) originated from the switching of power electronic devices that carry the phase currents of the machine. The Electromagnetic Compatibility (EMC) of the sensors has to be verified before using them in a drive. Moreover, mounting extra components to the PM machines increases the weight and volume and hence reduces the power-to-mass/volume ratio of the machine. Another consequence of using sensors is the increased production complexity and cost. These latter issues are more prominent in small machines where PM machines are often preferred. Furthermore, as such sensors are fragile, it excludes the application of PM machines in harsh environments. Harsh environments come in many forms and are more common than might be expected. They are the norm in many sectors such as aerospace, automotive, defence, heavy industrial, utility, oil and gas. There is no hard and fast rule as to what constitutes a “harsh environment” but, for the intended application of the sensors, a harsh environment may defined as one containing one or more of the following factors: low or high temperatures, thermal cycling, vacuum, high pressure, vibration, shock, EMI/EMC, radiation, water, dirt, aggressive chemicals, long term immersion, explosive dusts & gases.

It can be concluded that elimination of the position sensors will result in the following benefits:

- Extended application range of the PM machines.
- Increased reliability of the drive system.
- Reduced cost, assembly time and the maintenance.
- Increased power-to-mass/volume ratio.

The self-sensing algorithms can be classified to three main groups as: rotor

position estimation at standstill, low speed operation and rated speed operation.

1.2.1 Initial Rotor Position Estimation at Standstill

For some applications such as electric fans or propellers the rotor can first be aligned to one of the stator magnetic axes from any initial position then the controller can start from a predetermined position with a torque in the correct direction. However, in other applications the initial rotor position cannot be arbitrary chosen for which it is necessary to determine the rotor position before start-up. In [Champa2009] an initial rotor position estimation is proposed based on the detection and comparison of phase voltage and current responses and the dependence of these responses to the stator inductance variation with the position of the rotor magnet. This method is in particular suitable for salient machines as inductance can vary largely with the rotor position. In [Wook-JinLee2006] the initial rotor position is estimated for a PMSM by the difference in the current response as a result of a different magnetic state of the machine. A larger response is measured when the permanent magnet field is more weakened by the stator current. For a surface mounted PMSM rotor magnetic saliency is not sufficient to be used in a self-sensing algorithm. In [Scaglione2012] successive voltage pulses are applied to two of the machine phases. Due to the B-H hysteresis characteristics of the stator iron. The difference in the response on both pulses is also dependent on the rotor position. This phenomenon is used to detect the initial rotor position of a non-salient machine without the need of saturating the stator teeth.

1.2.2 Low Speed Operation

For electrical machines rotating at low speed, accurate rotor position estimations can be obtained by measuring the phase current responses to high-frequency voltage test signals [Jung-IkHa1999, Consoli2001, Ji-HoonJang2003]. A sufficient magnetic saliency or magnetic reluctance along the airgap is required for these methods [Jansen1995] to obtain a rotor position usable in control loops. Based on the switching power converter, machine topology and working conditions the effectiveness of the high frequency signal injection methods can change significantly. In [Bianchi2007a, Bianchi2007b, Bianchi2008, Bianchi2009, Reigosa2010, Sergeant2012] the influence of different machine design aspects are studied and key rules are given to design a PM motor suitable for rotor position detection during low speed operation region based on High Frequency Signal Injection (HFSI) techniques.

In general, HFSI techniques exert undesired signals to the machines windings that may result in torque ripples, increased losses and acoustic noises. Different enhancements have been proposed to eliminate the disadvantages of HFSI methods. By injecting high-frequency voltages, the average-current samples used for current control can be distorted by the high-frequency current responses. To reduce these distortions in [DeBelie2010, DeBelie2012] the test voltages are made adaptive to the steady-state voltage, where the restriction imposed by the DC supply voltage is taken into account. When saturation of the main flux path is taken into account, some parameters have to be modified and additional terms introduced; stator (and rotor) self inductances in orthogonal axes are no longer equal. These are the consequence of cross-saturation. To account for magnetic cross-saturation an adaptive full-order observer with signal injection is implemented in [Tuovinen2014]. The audible noise can be reduced by extracting the rotor position information using a voltage signal injection at the same frequency as the PWM, in [SungminKim2012]. In [Chen-YenYu2013] an improvement in the estimation accuracy and system robustness is obtained using different HFSI designs for a Flux Intensified IPMSM (FI-IPMSM). The flux-intensified interior permanent magnet (FI-IPM) not only reduces the flux-weakening current and hence losses but also achieves better characteristics for the self-sensing position estimation because of its low inductive coupling between d (direct) and q (quadrature) axes [ShanshanWu2009].

1.2.3 Rated Speed Operation

In permanent magnet machines, movement of the magnets relative to the armature windings causes a speed induced EMF. Since in BLDC machines the instantaneous magnitude of the back-EMF is a function of the rotor position back-EMF samples can be used to estimate this position. At normal speed operation (from 5-10% nominal speed up to the rated speed) the back-EMF signal can be sampled with high accuracy and samples can be used for rotor position estimation and machine control. Different methods have been proposed to commutate the current in BLDC machines based on the measured back-EMF signal as will be evaluated in Chapter 4. However, the common way in using the back-EMF in order to implement a self-sensing algorithm, is using the zero-crossing instants of the back-EMF in each phase, because these occur in the unexcited phase making it possible to detect it without need of current measurements or a model. However, the back-EMF zero crossings do not occur at instants at which current commutations between phases should take place. A time delay counting from these zero crossing events has to be added in order to detect the current commutations correctly.

The simple back-EMF sensing scheme described above has number of limitations that prevents its general application:

In general with all back-EMF schemes, estimation is difficult at low speeds. There are two restrictions on low-speed operation. First is the absence of back-EMF at zero speed, which can be addressed by different solutions as discussed in 1.2.1. A second factor is the requirement to add a time delay starting from the zero-crossing event. The proposed solutions in literature often limit the dynamic performance of the position-sensing scheme.

It is assumed that the voltage appearing across the terminals of the unexcited phase is equal to the back-EMF. This assumption may not be true at speeds approaching the base speed, or in the field-weakening region. Therefore, there is an upper limit on the useful speed range obtainable with this form of back-EMF sensing.

The back-EMF is measured across the terminals of the machine phases. For a star-connected machine, it is necessary to have an additional connection to the machine's star point, and therefore there are four, rather than the conventional three, machine connections.

In this study the main focus is on the rated speed operation of the self-sensing BLDC drives where the back-EMF signal is used to detect more accurate commutation instants. The work here will be extended to improve the speed control dynamic performance of the self-sensing BLDC drives, and will provide some solutions to the aforementioned problems.

1.3 Objectives and Methodology

The main objectives of this thesis, can be classified as firstly, to implement an enhanced reliable self-sensing current commutation algorithm addressing aforementioned restrictions and limitations of the conventional back-EMF methods. This will extend the application range of self-sensing BLDC drives. Secondly, to improve the control performance of self-sensing BLDC drives in order to be able to present the self-sensing BLDC drives as a solution in the fields of high end variable speed applications. The objectives of the control performance improvement are also classified in two categories. Firstly, to improve the torque disturbance rejection properties of the conventional PI speed controllers by introducing the load torque information to the control loop. Secondly, to increase the bandwidth of the speed control loop for the machines with low inertia using model based predictive control method.

1.3.1 Self-Sensing Commutation Algorithm

A. Back EMF Measurement

To achieve the first objective some pre-requisitions are necessary. As the main focus of this thesis is on normal speed operation (above 10% of the nominal speed) a self-sensing commutation algorithm based on the machine back-EMF is a good choice. Therefore, a good back-EMF measurement and sampling technique can improve the results and must have two main characteristics:

Accuracy The measured back-EMF values have to be as accurate as possible while having a minimum measurement delay. A more accurate back-EMF measurement will result in a more accurate control of the machine.

Reliability It is necessary to have the lowest possible sensitivity to noise while keeping the simplicity of the measurement circuit to be able to relay on the entire control system of the drive on those measured values.

Integration The measurement technique should be applicable to any BLDC drive. A seamless integration would be the most desirable choice. The measurement hardware must use the signals and terminals which are available in most drives.

B. Performance of the Self-Sensing technique

One of the main objectives of this study is improvement of the control performance of the self-sensing BLDC drive. The overall performance of the drive will not be optimal unless maximizing the performance of the self-sensing commutation. A self-sensing commutation algorithm that has an inherent high accuracy will improve the overall performance of the speed control.

1.3.2 Improvement of the Control Performance

After achieving a reliable and high accuracy self-sensing commutation algorithm the next objective is to use this technique to improve the performance of the control loops. Modern high performance electrical drives use different states of the drive system in order to improve the dynamic behaviour. In this study rotor speed,

position and load torque estimations are used to improve the dynamic performance conventional cascaded PI speed and current control loops. In addition, a more advanced Model Based Predictive Control (MBPC) or shorter Model Predictive Control (MPC) is implemented to overcome the issues of conventional cascaded controllers.

1.4 Required Tools to Understand This Book

In order to follow and understand the contents of this thesis a sufficient knowledge of generalized theory on electrical machines is required. Readers are also required to have an advanced knowledge on classical control theory as well as on some topics of modern control theory such as state-space modelling of SISO and MIMO systems, predictive control, digital control techniques, continuous time and discrete time systems. To understand the topics related to the implementation of the proposed algorithms basic knowledge of the concurrent programming and FPGA will be very useful. Moreover, a basic knowledge of electronics is required for the implementation procedure of the used electronic circuits and printed circuit boards. Understanding the analytical models of the machines and other components of the drive system require a good knowledge of mathematics. Finally, all models and algorithms are simulated in a Matlab/Simulink environment so an advanced knowledge of the programming in Matlab and Simulink could be required.

1.5 Conclusions

BLDC machines are used more and more in industrial applications due to their energy-efficiency and their favourable power-to-volume ratio. Conventional BLDC machines are equipped with position sensors, which are required to drive the machine in an optimal way. However, these additional sensors lead to a bigger, a more costly and a less reliable drive. Therefore, self-sensing control of BLDC machines is an important branch of the research of BLDC machines.
The goal of this PhD dissertation is the development of new self-sensing control methods for BLDC machines, which have a better performance during rotor speed transients. The self-sensing control methods proposed in this thesis are based on back-EMF samples. The performance of the proposed self-sensing algorithms are proven by simulations in Matlab/Simulink and by practical results from an FPGA implementation.

In the other part of the thesis, it is shown that combining the self-sensing control algorithm with a load torque estimator improves the dynamic behaviour of the drive considerably. The influence of load torque disturbances on the rotor speed is decreased significantly.

In the last part, a model based predictive control (MBPC) algorithm for speed control of BLDC machines is proposed. It is shown that using load torque information in a MBPC strategy for BLDC machines has a positive effect on the dynamics of the drive as well.

Chapter 2

BLDC Machine Drive Principles

In the first section of this chapter the basic operation principles of a simple BLDC machine and the torque production mechanism will be explained. Later on, basic power electronic devices that are required to drive these machines will be studied. The most often used commutation technique for BLDC machines will be explained at the end of first section.

Second section covers the state of the art on the speed, torque and current control of BLDC machines. Reading these two section will be useful for the people who are willing to start using BLDC machines.

2.1 Basic Principles

2.1.1 Basic Torque Production in BLDC Machines

In conventional permanent magnet brushed DC machines the permanent magnets are installed on the stator and the rotor is made of wounded poles. A mechanical commutator is used to commutate the current between rotor windings. Compared to PM brushed DC machines the topology of Brushless DC machines is quite different in the sense that the coils are on the stator and the permanent magnets are on the rotor. Commutation of current is done using switching power converters. For instance, by energizing the stator coils in such a way that it creates a north pole at the top stator piece and a south pole at the bottom stator piece as it is illustrated in Fig. 2.1(a). Now, by rotating the rotor over 360° mechanical in the indicated direction the generated torque is plotted in Fig. 2.1(b) by the solid black line.

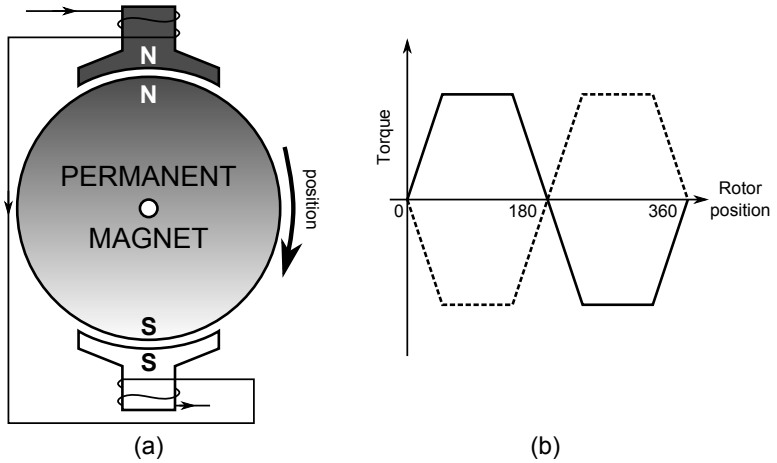

Figure 2.1. Single phase permanent magnet machine

For the initial position in Fig 2.1(a), In the beginning it can be seen that the north pole (south pole) of the rotor and stator are opposite each other and the forces are applied directed to the centre of the rotor. Such radial force result in zero torque. Any displacement will swing the rotor over 180° due to the attraction between the stator current field and rotor magnetic field. At this point the rotor will resist any rotation, either clockwise or counter clockwise. In order to force the motor to rotate another 180° it is necessary to change the direction of the current flow in the stator coils. By doing so the torque as a function of rotor position is as illustrated by the dashed line in Fig. 2.1(b). Whether the rotor is going via a clockwise or counter clockwise direction depends on the direction of the initial displacement. Such a behaviour of a single phase machine is not desirable. To define the direction of the rotation unambiguously more phases are added to the stator as it is illustrated in Fig. 2.2(a).

By energizing phase A the rotor will be aligned in the indicated position in Fig. 2.2(a). In order to get the motor to spin in a clockwise direction the current should become zero in phase A and commutated to phase C in the opposite direction. In this way, C' becomes a north pole (and C a south pole) so that rotor aligns with the phase C. The sequence of current commutation is given by the phase current waveforms in Fig. 2.2(b). By continuing the commutation process the rotor spins around and follows the rotating magnetic field of the stator. However, the mentioned process is not an efficient process as two out of three phase are not conducting at any given time during the process. A more efficient way

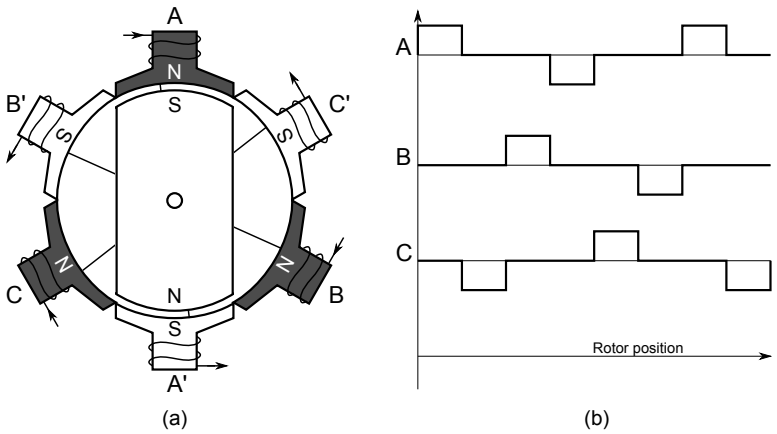

Figure 2.2. Three phase permanent magnet brushless DC motor

is to energize two coils in order to generate more torque. In order to do that lets consider there is a positive current flowing through each phase as was done for the single phase motor in Fig. 2.1(a). In this case the phases of the motor will produce a torque waveform as illustrated in Fig. 2.3. The waveforms are displaced in time due to a 120° spatial displacement of the phases. The idea to produce a positive torque with two phases in any given time is as follows:

- Consider a particular commutation interval

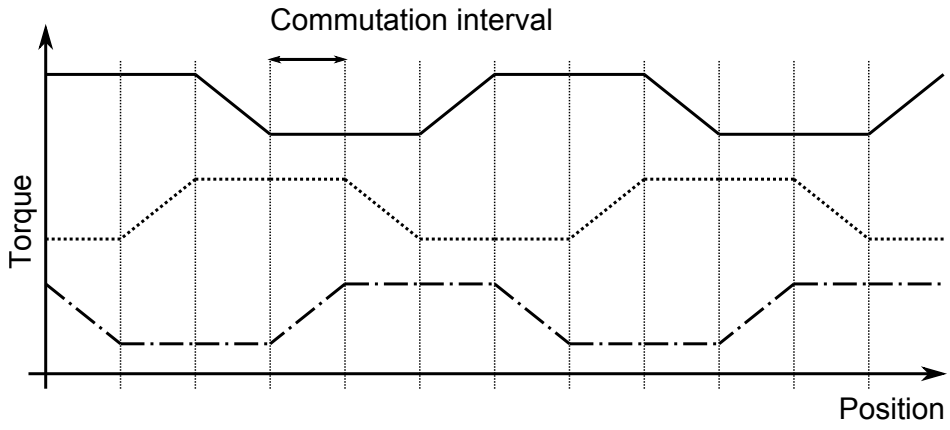

Figure 2.3. Produced torque per phase

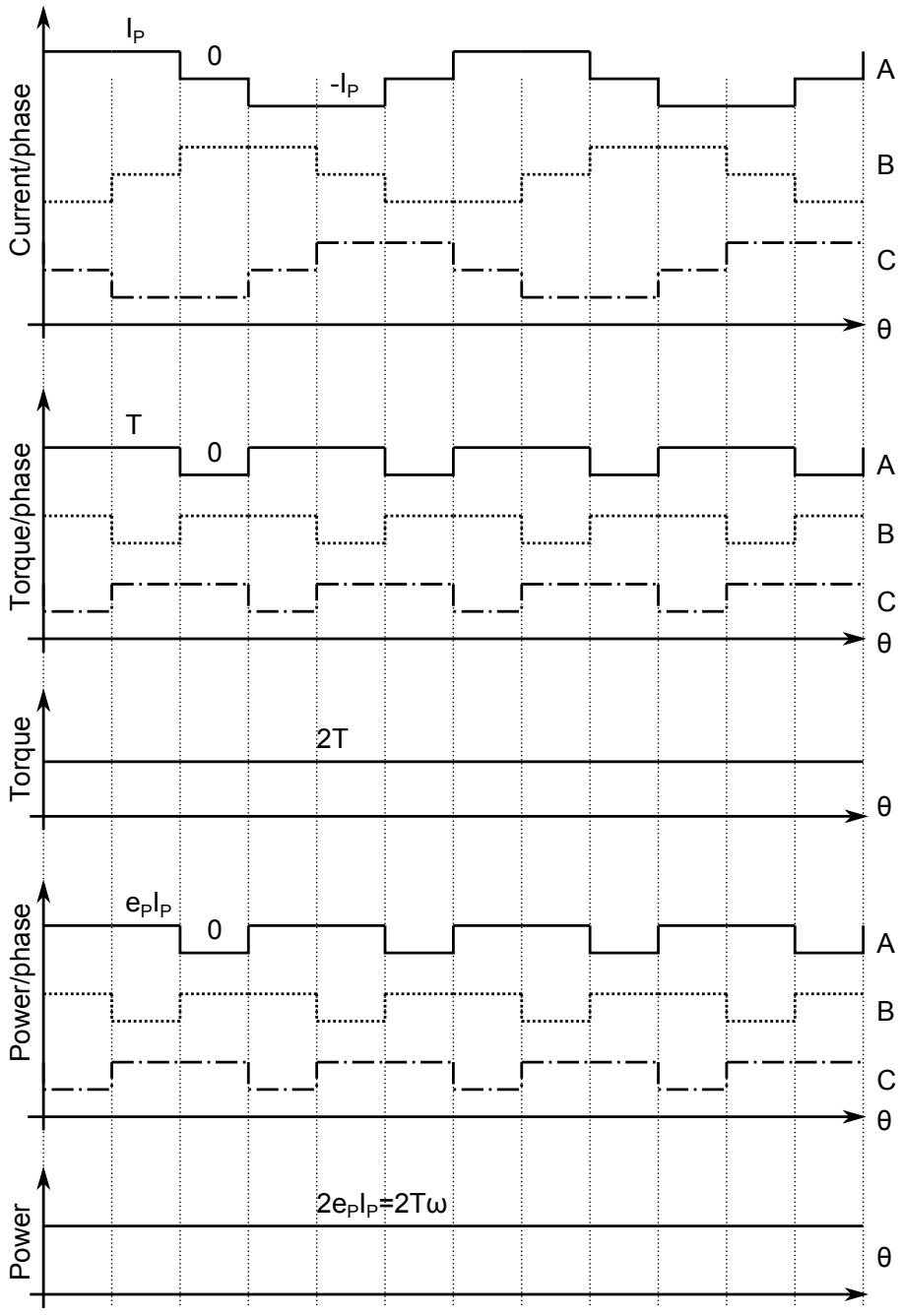

Figure 2.4. Torque, current, power waveforms for a three phase BLDC machine

- If the torque varies from low to high value or the other way around the current will be set to zero
- If the torque is positive, the current flow direction is correct else the current flow direction should be changed.

When applying the aforementioned algorithm the torque, current and the power of the BLDC machine is illustrated in Fig. 2.4. Despite the torque varies in each phase the total torque is a constant. The power is given as:

$$P = 2T\omega_m \tag{2.1}$$

where ω_m is the mechanical speed. Due to the power balance, P also equals to $2e_pI_p$.

Another interesting characteristic of applying this algorithm is that in every commutation interval the current of one phase is zero, hence current flowing through one phase should flow in the opposite direction through the second phase. The current can be used in multiple phases and one end of each phase windings can be connected together to make the star point of the machine as it is illustrated in Fig. 2.5.

If phase A is connected to the positive side of the DC-bus voltage and phase B is connected to the negative side of the DC-bus voltage or ground the current path will be as follows:

For a particular current commutation state the current can flow through phase A to phase A' and then to the neutral point. It will continue to phase B' and finally through phase B coil to the negative DC-bus. It can be seen that a positive current in one phase result in a negative current in another phase.

For the next current commutation state the current flows through another set of phases. For instance from phase A to A' and neutral point and then to the phase C' and C. This procedure can be implemented in any controller (logic gates, micro controllers, micro processors, ...) and with use of six transistors the current can be commutated between machine phases.

In order to know which transistors should be turned on or off it is necessary to know where the rotor position is. This information can be acquired from Hall-effect sensor arrangements. It can be seen in Fig. 2.6 where a disc of four magnetic pole

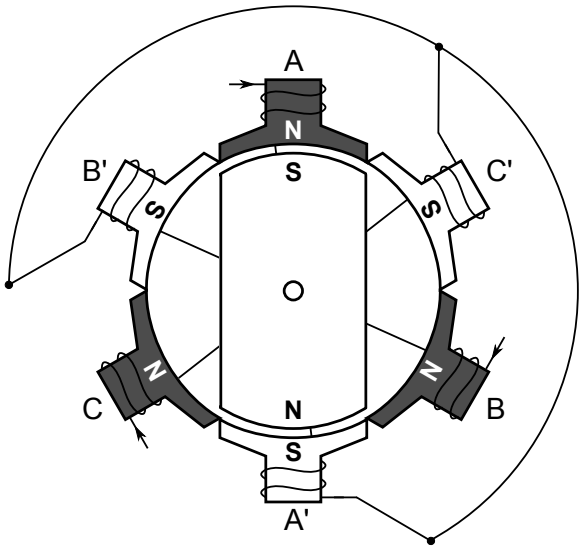

Figure 2.5. Realisation of the stator star (neutral) point

pieces on it surrounded by three Hall-effect sensors displaced by 120°. These Hall-effect sensors are actually digital sensors and do not detect the absolute value of the field strength of the magnetic disc but detect the transition from north pole to south pole and vice versa only. From these three sensors, each providing binary data, eight possible conditions can be detected. By having four magnetic poles on the disc each pole covering 90° and three sensors with 120° spatial phase displacement the output of the sensors will never be 000 or 111. In the end there will be six possible combination coming from the sensing array, receiving 000 and 111 means there is a fault in the system.

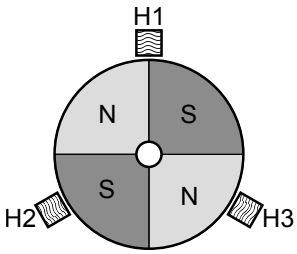

Figure 2.6. Three Hall-effect sensors plus magnetic disc array

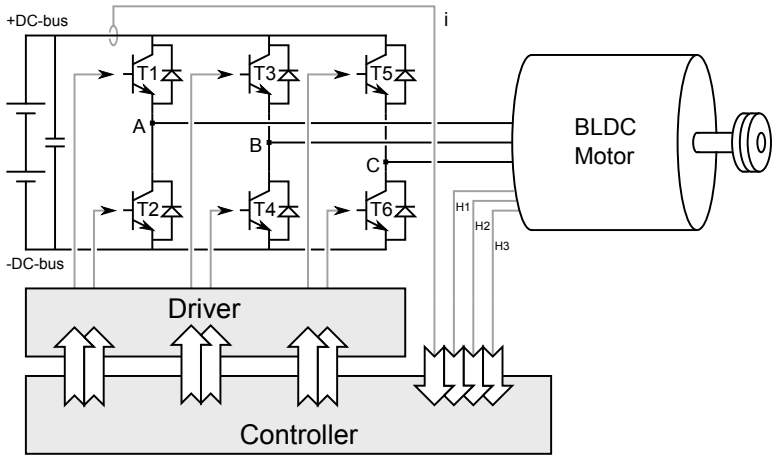

Figure 2.7. Three phase inverter, controller and BLDC machine in a typical BLDC drive

2.1.2 Topology of Power Electronics Commonly Used in BLDC Drives

In Section 2.1.1 it is mentioned that to rotate BLDC machines efficiently, the current flowing through the phases should become repeatedly negative and positive. This can be realised using a conventional three phase two level inverter. Such a typical inverter topology also used in BLDC drives is illustrated in Fig. 2.7.

Each inverter switch includes a fully controlled power semiconductor device such as a Metal-Oxide-Semiconductor Field-Effect Transistor (MOSFET) or an Insulated-Gate Bipolar Transistor (IGBT) with an anti-parallel diode. Equipping each switch with an anti-parallel diode is necessary for the application with an inductive load. The anti-parallel diode is normally integrated inside the package. In the presence of an anti-parallel diode, when the switch turns off the current flows automatically through the anti-parallel diodes.

2.1.3 Six-Step Current Commutation Technique

From the current waveforms in Fig. 2.4, it follows that the inverter connects the terminals of two phases to the DC supply at every given time. One terminal is connected to the positive side of the supply, one is connected to the negative side of the supply. In steady state, the current in the first phase is opposite to the current in the second phase and the terminal of the third phase is not connected hence referred to as unexcited phase.

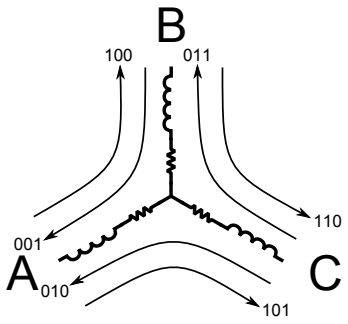

Figure 2.8. Current commutation states in the stator of a BLDC machine

Commutation state	Active switches
001	T_3, T_2: ON
010	T_5, T_2: ON
011	T_5, T_4: ON
100	T_1, T_4: ON
101	T_1, T_6: ON
110	T_3, T_6: ON

Table 2.1. Commutation states table regarding to the rotation direction and outputs of Hall effect sensors

Due to the symmetry of the machine, it follows that each of commutation states is active during 60° electrical. Six different states can be obtained from an arrangement of three Hall-effect sensors and based on the desired rotation direction inverter switches can be turned on and off. For example with respect to the current direction in the phases as shown in Fig. 2.8 and related Hall-effect sensors outputs a table can be used to determine the sequence of commutation as indicated in Table 2.1.

Using this strategy, there are six possibilities for the inverter to conduct the current in the phases of the machine. Hence referring to this method as a Six-Step Current Commutation Technique. The control algorithm chooses the stator voltage which is fixed with respect to the back-EMF position. The conduction path in steady-state when phase A is connected to the positive side of the DC supply and phase B to the negative side, is shown in Fig. 2.9. Transient currents can exist in the diodes.

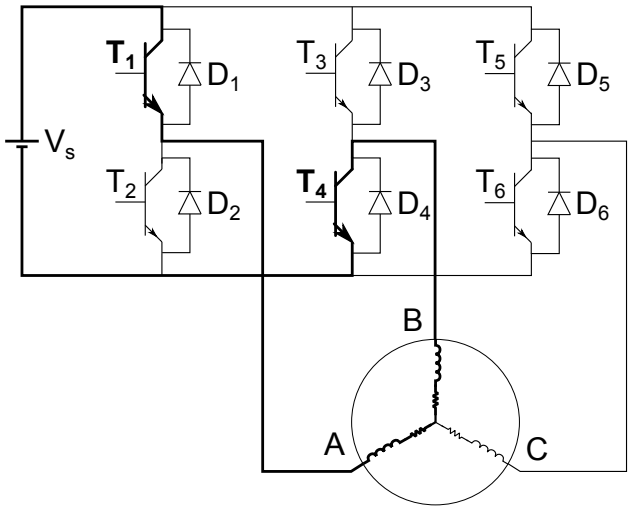

Figure 2.9. Conduction path of current when switch T_1 and T_4 are conducting

2.2 State of the Art in BLDC Drives Control

2.2.1 Torque, Current and Speed Control

In general PI (proportional-integral) controllers are used in order to control the current, torque, speed or position of electrical machines. These controllers can be used for BLDC machines as well.

The magnitude of the DC-bus current is equal to the current that is flowing through one of the phases of the BLDC machine operated by the six-step commutation method. Other two phases have zero and negative DC-bus current value. This is shown in Fig 2.10. Therefore, to control the current in a BLDC drive operated by the six-step commutation, a single current sensor within the DC-bus is sufficient. The DC-bus current can be measured by either a shunt resistor in the DC-bus or by a Hall-effect sensor. Using a shunt resistor reduces the cost but it limits the operation range of the drive.

A single PI control loop as shown in Fig. 2.11(a) or an hysteresis control as shown in Fig. 2.11(b) is sufficient to control the current amplitude. By commutating the current between machine phases in synchronism with the back-EMF vector direction, the demanded torque can be obtained as well.

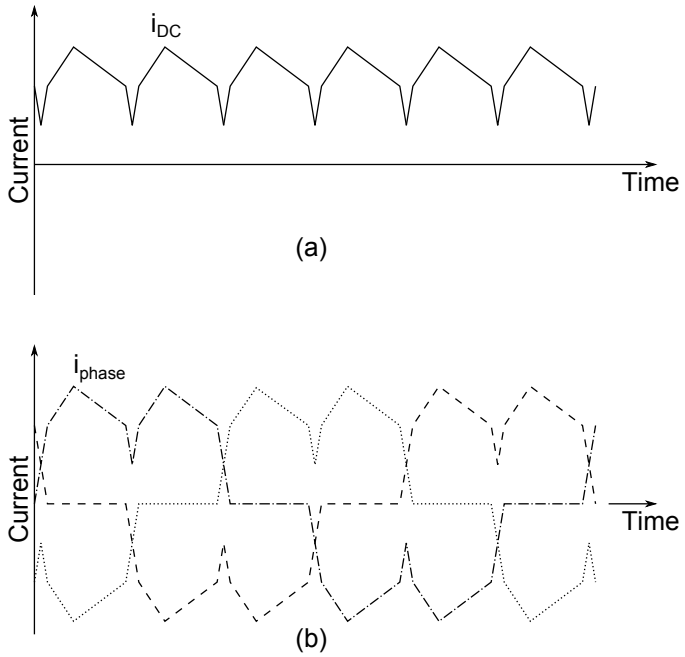

Figure 2.10. Currents within a BLDC drive, (a): DC-bus current i_{DC}, (b): phase currents i_{phase}

Besides torque and current, speed control can be of interest as well. A conventional cascaded speed and current/torque control scheme is depicted in Fig. 2.12. The rotor speed is measured with an encoder, but it can be replaced by a self-sensing speed estimation algorithm. Once the rotor speed information is known, the switching signals for the power stage are generated by the control algorithm. The magnetic field, produced by the stator windings, is guided in such a way that it is approximately perpendicular to the magnetic field produced by the rotor. At that instant, the produced torque is proportional to the current in the DC-bus.

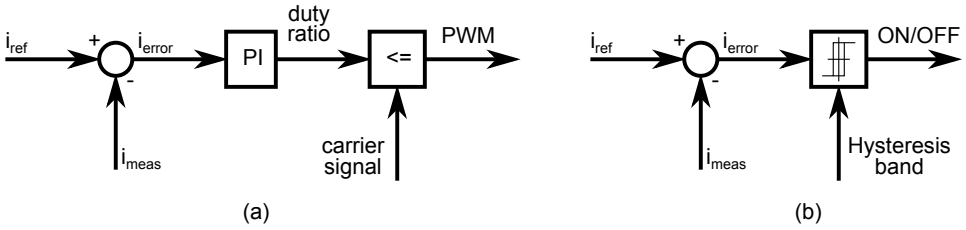

Figure 2.11. Current control, (a): PWM PI controller, (b): Hysteresis control

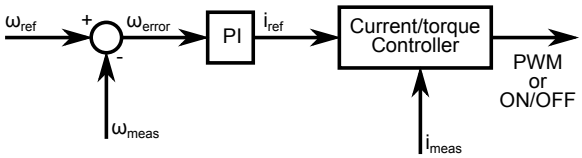

Figure 2.12. Cascaded speed control

The speed of the BLDC machine is controlled by a PI controller. This speed controller generates the reference value for the DC-bus current, which determines the required electromagnetic torque. The current in the DC-bus can also be controlled by a PI or an hysteresis controller. The current controller determines the duty ratio and is applied to the switches of the power stage. In case of a PWM the output of the PI current controller is compared with a triangular carrier signal to generate the pulsed signals to drive the switches, Fig. 2.13. A PWM provides a fixed switching frequency on the other hand implementation of the hysteresis control is more simple that can be realised by multi purpose ICs in case of using no processing units (micro processor, DSP, FPGA, ...) within the drive.

The duty ratio δ determines the on time of a switch related to the switching period. During the on time supply voltage V_s is connected to the machine phases. Different switching strategies exist to apply δV_s to the machine phases. Three important scheme that are often applied to BLDC machines are listed below:

Bus clamped switching strategy In the six-step control of BLDC machines, a conduction path is formed by closing one of the upper switches and one of the bottom switches of the inverter. In the bus clamped switching strategy, the upper switch remains closed at all times. When the PWM signal is OFF,

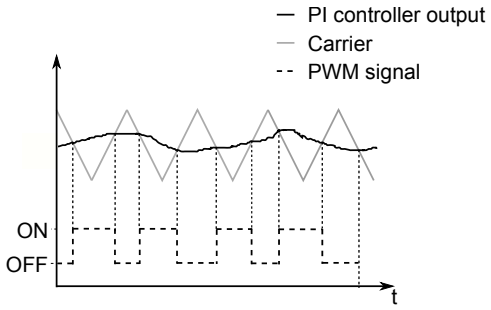

Figure 2.13. Working principle PWM

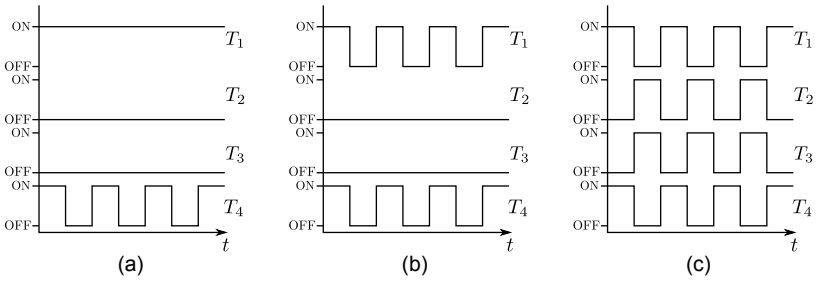

Figure 2.14. PWM switching strategy for the conduction path in Fig. 2.9 and a duty ratio of 50%, (a): Standard, (b): independent and (c): complementary.

the bottom switch is opened and the current starts flowing through the upper anti-parallel diode of the same inverter leg. The terminals of the two motor phases that conduct current are attached to each other, i.e. the motor phases are now fed with a voltage of 0V. The current decays due to the resistance of the motor phases. The PWM switching signals, for the conduction path shown in Fig. 2.9, are depicted in Fig. 2.14(a) for a duty ratio of 50%.

Independent switching strategy The conduction path is altered by opening both of the conducting switches. Due to the inductance of the motor windings, the direction of the current remains the same and decays by flowing through the diodes (D_2 and D_3 for Fig. 2.9). The polarity of the voltage applied to the active phases of the machine reverses when opening the conduction path and it forces the current to drop to zero. While the current decays, power is delivered to the DC supply (the DC supply must be able to deal with a reversed power flow). The PWM switching signals, for the conduction path shown in Fig. 2.9, are depicted in Fig. 2.14(b) for a duty ratio of 50%.

Complementary switching strategy In the complementary switching strategy the conducting switches of the same inverter legs have an opposite switching mode (T_2 and T_3 in Fig. 2.9). When the conducting switches are opened, the polarity of the voltage applied to the active phases of the machine again changes sign. The current in the motor phases decreases while delivering power to the DC supply (the DC supply must be able to deal with a reversed power flow). The difference with previous switching strategy is that, the current can now change sign as it can flow through the switches that are steered in a complementary way. Hence, in this strategy reversing the electromagnetic torque is possible. In such a case, as long as the rotor speed remains positive, the mechanical energy of the machine is reduced while taking energy from the supply (counter-current braking). The PWM switching signals, for the conduction path shown in Fig. 2.9, are depicted in Fig. 2.14(c) for a duty ratio of 50%.

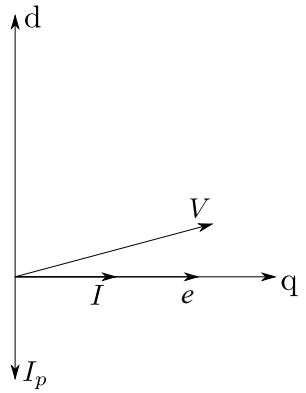

Figure 2.15. Vector diagram for situation where stator current I is in phase with the produced back-EMF e in a d-q reference frame

2.2.2 Field-Weakening Operation of a BLDC Machine

The speed of a BLDC machine using six-step control method is limited. When the speed rises, the back-EMF rises along with it. At a certain rotor speed, the back-EMF approximates the supply voltage. The vector diagram in the six-step control method is depicted in Fig. 2.15 in a synchronous reference frame fixed to the rotor. The variable I_p is the equivalent excitation current that produces a

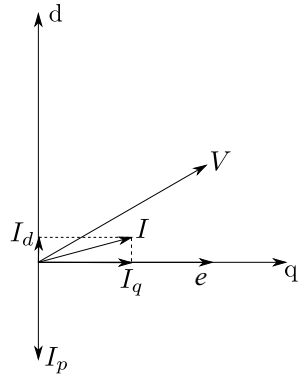

Figure 2.16. Vector diagram for the situation where the stator current I leads the back-EMF e in a d-q reference frame

magnetic field equal to that produced by the permanent magnets. The variable e is the induced back-EMF in the stator winding. The stator current I is in phase with e. Due to the inductance of the stator winding, the stator voltage V leads the stator current I. In Fig. 2.15, the stator current I does not influence the produced magnetic field by the rotor. As back-EMF e approximates supply voltage V the current I reduces, hence affecting the maximum torque achievable. It also limits the speed as e is proportional to the speed.

In regular DC machines, the rotor speed is increased by lowering the current in the field winding, allowing higher rotor speeds for the same back-EMF value. The magnetic field in BLDC machines is produced by permanent magnets, to reduce this magnetic flux a stator current component should be injected opposing the permanent magnet field. This means that, the stator current I should lead the back-EMF e.

2.3 Conclusions

The basic operation principles of BLDC drives is introduced in this chapter as well as the current, torque and speed controlling techniques. These basic knowledge about BLDC drives is required to understand the coming chapters.

Chapter 3

Analytical Model for BLDC Drives

3.1 Introduction

In this chapter, a mathematical model for BLDC drives is derived. This model is used in continuous-time simulations in order to validate the performance of the proposed algorithms. Later on, in this chapter, the continuous-time model is discretised for several purposes. It is used in computer based off-line simulations to predict the behaviour of the drive and verify the controller or for online emulation of the electrical machines on the processing units such as FPGAs or DSPs. This last technique, known as Hardware-In-the-Loop (HIL) has several features making it a convenient tool for a designer:

- Real time simulation of dynamic systems
- Testing the developed control algorithms before the production of final prototypes (reduced design to market time)
- Avoiding a high risk of damage to the actual system during tests

In the case of this study, the behaviour of the drive will be examined under different operating conditions in real time without the requirement of the actual converters and machines. Moreover, the machine model, together with the adjustable machine parameters, can be used as a HIL platform to examine different control and estimation algorithms.

Moreover, the machine model is also inevitable to predict the future behaviour of the machine in a Model Based Predictive Control (MBPC) strategy.

3.2 Continuous-Time Model of BLDC Machines

3.2.1 Introduction

Modelling a system, in general, is performed in such a way that the obtained model covers the system behaviour and features of interest, while keeping this model mathematically less complicated. On the other hand, this last characteristic should not compromise the required accuracy. Often, some simplifications and assumptions are made in the derivation of the model for a BLDC machine (with respect to the required accuracy for a high performance control system):

- The BLDC machine has a three-phase stator winding that is star connected. This number of phases occurs frequently in BLDC machines, as it suffices for an acceptable torque ripple.
- The machine is three-phase symmetrical. An unbalance in resistance, inductance and back-EMF values is not tackled in this study.
- The magnetic state is assumed invariable. This means magnetic nonlinearities such as magnetic saturation are neglected.
- Skin effect is not considered. This implies also that resistances are assumed to be independent of frequency.
- Slot effects are neglected. This implies that higher harmonics in the airgap flux and inductances [Nandi2004] caused by slots are not taken into account.

Models of conventional induction and synchronous machines are often derived in a synchronous reference frame to obtain a linear time invariant model. When deriving these models, the three-phase variables are first transformed to a stationary two phase reference frame using the Clarke or the symmetric component transformation. Then a park transformation is performed. Sinusoidal varying (with respect to the position) inductances become constants in the qd reference frame. Unlike the modelling of conventional induction and synchronous machines, the modelling of a BLDC machine will be done in the stationary reference frame. The inductances in a BLDC machine are assumed here not to vary with the rotor position, so there is little advantage in using a transformation from three phase to a two phase reference frame [Pillay1988].

3.2.2 Continuous-Time Model

The differential equations that describe the machine are derived using Kirchhoff's laws. The terminal voltage vector $\boldsymbol{v} = [v_{an}, v_{bn}, v_{cn}]^T$, referred to the neutral (star) point n of the machine, can be written as:

$$\boldsymbol{v} = \boldsymbol{R} \cdot \boldsymbol{i} + \frac{\mathrm{d}}{\mathrm{d}t} [\boldsymbol{L} \cdot \boldsymbol{i}] + \boldsymbol{e} \tag{3.1}$$

where $\boldsymbol{i} = [i_a, i_b, i_c]^T$ represents the phase-current vector and $\boldsymbol{e} = [e_{an}, e_{bn}, e_{cn}]^T$ is the back-EMF vector. The matrix $\boldsymbol{R}$ contains the phase resistances and the matrix $\boldsymbol{L}$ includes the phase inductances:

$$\boldsymbol{R} = \begin{bmatrix} R_s & 0 & 0 \\ 0 & R_s & 0 \\ 0 & 0 & R_s \end{bmatrix} \tag{3.2}$$

$$\boldsymbol{L} = \begin{bmatrix} L_s & M_s & M_s \\ M_s & L_s & M_s \\ M_s & M_s & L_s \end{bmatrix} \tag{3.3}$$

In these matrices, R_s is the phase resistance and L_s is the phase inductance.

The neutral point or star point n of an electrical machine is often not accessible. The back-EMF signal is often measured with respect to this point potential. Methods exist to create a virtual neutral point n', which behaves similar to the neutral point of the machine. The implementation of a virtual neutral point and th phase voltage values referred to the neutral point V_n will be compared with the ones referred to the virtual neutral point V_n' in Section 4.3.6. The model can, however, be derived without using the neutral point voltage by considering line-to-line voltages:

$$\begin{cases} v_{ab} = R_s(i_a - i_b) + (L_s - M_s)\dfrac{\mathrm{d}}{\mathrm{d}t}(i_a - i_b) + (e_{an} - e_{bn}) \\ v_{bc} = R_s(i_b - i_c) + (L_s - M_s)\dfrac{\mathrm{d}}{\mathrm{d}t}(i_b - i_c) + (e_{bn} - e_{cn}) \\ v_{ca} = R_s(i_c - i_a) + (L_s - M_s)\dfrac{\mathrm{d}}{\mathrm{d}t}(i_c - i_a) + (e_{cn} - e_{an}) \end{cases} \tag{3.4}$$

The back-EMF of the machine is a voltage induced in the stator winding by a time varying magnetic flux as seen by that winding due to the rotation of the rotor. Its waveform depends on the design of the machine as well as operating speed. Its amplitude is proportional to the product of the magnetic flux in the machine

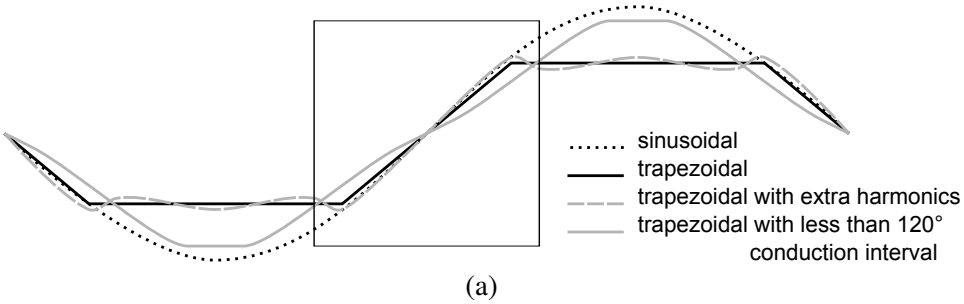

(a)

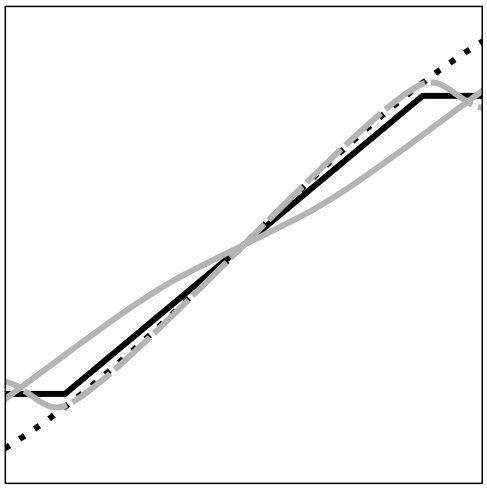

(b)

Figure 3.1. Different back-EMF waveform profiles, (a): electrical $360°$, (b): zoomed view of transition region

and the speed ω_e and it is assumed to have a trapezoidal waveform. However, in practice, for different machine designs, the back-EMF waveform varies between trapezoidal and sinusoidal waveforms (see Fig. 3.1). It can be seen from this figure that the back-EMF waveform is symmetrical around its zero-crossing. This is an important feature of the back-EMF waveform that will be used in Chapter 4 in order to develop back-EMF based self-sensing algorithms.

The back-EMF induced in each phase of the machine related to the neutral point

can be written as:

$$\begin{cases} e_{an} = K_e \omega_e F(\theta_e) \\ e_{bn} = K_e \omega_e F(\theta_e - \dfrac{2\pi}{3}) \\ e_{cn} = K_e \omega_e F(\theta_e + \dfrac{2\pi}{3}) \end{cases} \tag{3.5}$$

where F is the speed normalized back-EMF and reflects the back-EMF waveform characteristics. The parameter K_e is called the voltage constant or back-EMF constant. It is defined as the amount of back-EMF voltage that the machine can produce per each krpm rotation speed $[\frac{\text{v}}{\text{rpm}}]$. It should be mentioned that the speed dependency of the back-EMF is expressed in two ways:

- $[\frac{\text{v}}{\text{rpm}}]$ the amount of back-EMF voltage that the machine can produce per each krpm rotation speed.
- $[\frac{\text{rpm}}{\text{v}}]$ the amount of revolution per minute that the machine can reach per each volt of the supply voltage in unloaded case.

Within the modelling process the variable F is defined as (3.6) in order to model a BLDC machine with an ideal trapezoidal back-EMF waveform. However, the function F can be altered if an open-circuit test shows other back-EMF values. During the experiments different machines will be tested to verify the performance of the proposed algorithms for different F characteristics.

$$F(\theta_e) = \begin{cases} 1, & 0 \leq \theta_e \leq \dfrac{2\pi}{3} \\ 1 - \dfrac{6}{\pi}\left(\theta_e - \dfrac{2\pi}{3}\right), & \dfrac{2\pi}{3} \leq \theta_e \leq \pi \\ -1, & \pi \leq \theta_e \leq \dfrac{5\pi}{3} \\ -1 + \dfrac{6}{\pi}\left(\theta_e - \dfrac{5\pi}{3}\right), & \dfrac{5\pi}{3} \leq \theta_e \leq 2\pi \end{cases} \tag{3.6}$$

If the rotor position and speed are known, the corresponding value of the back-EMF can be calculated. The required line-to-line voltages v_{ab}, v_{bc} and v_{ca} can be applied by a wide variety of PWM techniques. The command signals for the semiconductor switches of the inverter are generated in the processing unit and applied in such a way that a desirable current and hence torque is produced at the

operation point. This torque is determined by the current in the machine stator windings. The electromagnetic torque T_e depends on the magnetic flux in the air gap and the current that flows in the stator. Because the flux depends on the rotor position (as illustrated in Fig. 1.3(a)), T_e also depends on the rotor position. The electromagnetic torque can be expressed in function of F:

$$T_e = K_t \left[F(\theta_e) i_a + F(\theta_e - \frac{2\pi}{3}) i_b + F(\theta_e + \frac{2\pi}{3}) i_c \right] \tag{3.7}$$

Here, K_t is the torque constant. Using (3.4) the instantaneous current in each phase can be calculated.

In addition to the electrical equations, the equation of motion has to be considered as well:

$$J \frac{\mathrm{d}\omega_e}{\mathrm{d}t} = T_e - K_f \cdot \omega_e - T_l \tag{3.8}$$

The variable ω_e represents the speed, J is the inertia of the rotor and load (if any load is coupled to the rotor shaft), T_e is the electromagnetic torque and T_l is the load torque. In (3.8), a frictional torque is also introduced. The frictional torque is assumed here proportional to the speed, with a factor K_f.

Because the sum of the line-to-line voltages is equal to zero, only two of the three equations (3.4) are independent of each other. Therefore, in the rest of the model derivation we will express the model in terms of v_{ab} and v_{bc} only.

As already mentioned, the machine is assumed to be star connected, where the neutral point is not accessible. It follows that zero-sequence currents cannot exist:

$$i_a + i_b + i_c = 0 \tag{3.9}$$

The system (3.4) then becomes:

$$\begin{cases} v_{ab} = R_s(i_a - i_b) + (L_s - M_s) \dfrac{\mathrm{d}}{\mathrm{d}t} (i_a - i_b) + (e_{an} - e_{bn}) \\ v_{bc} = R_s(i_a + 2i_b) + (L_s - M_s) \dfrac{\mathrm{d}}{\mathrm{d}t} (i_a + 2i_b) + (e_{bn} - e_{cn}) \end{cases} \tag{3.10}$$

3.3 Inverter Model

In the previous section, the electrical and mechanical equations governing the stator winding and rotor of the machine are given. A BLDC machine is connected to a DC supply through an inverter. The inverter output serves as an input to the electrical equations. The model of the inverter depends on the switching strategy. In this study, the model is derived for a switching strategy where the state of the semiconductor switches of a given leg are steered complementary. A similar approach can be used for other switching strategies. In the 6-step commutation, two out of the three phases are conducting in each given time instant. The third phase remains unexcited until the next commutation state. If the phase currents are well aligned with the flat part of the phase back-EMF waveforms (considering a trapezoidal back-EMF waveform) the machine can produce its maximum rated torque with minimum current (MTPA). Detailed information about switching strategy and six-step commutation is given in Section 2.2.

Table 3.1 shows the conducting states of the inverter. For the first conduction state we suppose that phases A and B of the machine are connected to the DC-bus and carry the current. During this interval phase C is connected to the DC-bus via freewheeling diode until the residual current from the previous conduction state reaches zero. The sign of this transient current is determined by the previous commutation state and load (the current sign is same or opposite as of the back-EMF sign). In this interval, v_{ab} is assumed equal to the supply voltage, regardless of the currents i_a, i_b and i_c.

$$v_{ab} = V_s \quad , \quad \theta \in \left[0, \frac{\pi}{3}\right] \tag{3.11}$$

If there is a positive transient current in phase C, anti-parallel diode SCb (SCb means bottom switch of inverter leg C, see Fig. 2.9) is conducting. This means that the terminal of phase C is connected with the low voltage side of the supply (negative DC-bus voltage). As both the terminals of phase B and phase C are connected to the low voltage side of the supply, the line-to-line voltage v_{bc} is zero. When the current i_c drops to zero, the current that flows through phase A is identical to that in phase B. The supply voltage V_s can then be expressed in terms of the current i_a, the resistance R and inductances L_s, M_s of the phases A and B, and the speed induced voltages e_{an} and e_{bn}:

$$V_s = 2R_s i_a + 2(L_s - M_s)\frac{\mathrm{d}}{\mathrm{d}t} i_a + (e_{an} - e_{bn}) \tag{3.12}$$

This equation results in the following expression for the voltage drop over the impedance of a conducting phase:

$$R_s i_a + (L_s - M_s)\frac{\mathrm{d}}{\mathrm{d}t} i_a = \frac{1}{2}\left(V_s - e_{an} + e_{bn}\right) \tag{3.13}$$

The line-to-line voltage v_{bc} can now be written as a function of this voltage drop:

$$v_{bc} = e_{bn} - (R_s i_a + (L_s - M_s)\frac{\mathrm{d}}{\mathrm{d}t} i_a) - e_{cn} \tag{3.14}$$

$$= \frac{1}{2}(-V_s + e_{an} + e_{bn}) - e_{cn} \tag{3.15}$$

From this, an expression for $v_{bc} - e_{bc}$ can be derived. If the transient current in phase C is negative, the diode SCt is conducting. The voltage v_{bc} then equals the negative of the supply voltage, so that the following expression holds:

$$v_{bc} - e_{bc} = -V_s - e_{bn} + e_{cn} \tag{3.16}$$

Similar calculations can be performed for the other switching states of the inverter. The expressions for the voltages $v_{ab} - e_{ab}$ and $v_{bc} - e_{bc}$ of the six conducting states of the inverter are summarized in Table 3.1.

Table 3.1. Voltages $v_{ab} - e_{ab}$ and $v_{bc} - e_{bc}$ for the conducting states of the invertor

θ_e	Transient current	$v_{ab} - e_{ab}$	$v_{bc} - e_{bc}$
$0 - \frac{\pi}{3}$	$i_c > 0$	$V_s - e_{an} + e_{bn}$	$-e_{bn} + e_{cn}$
	$i_c = 0$		$\frac{1}{2}(-V_s + e_{an} - e_{bn})$
	$i_c < 0$		$-V_s - e_{bn} + e_{cn}$
$\frac{\pi}{3} - \frac{2\pi}{3}$	$i_b > 0$	$V_s - e_{an} + e_{bn}$	$-e_{bn} + e_{cn}$
	$i_b = 0$	$\frac{1}{2}(V_s - e_{an} + e_{cn})$	$\frac{1}{2}(V_s - e_{an} + e_{cn})$
	$i_b < 0$	$-e_{an} + e_{bn}$	$V_s - e_{bn} + e_{cn}$
$\frac{2\pi}{3} - \pi$	$i_a > 0$	$-V_s - e_{an} + e_{bn}$	$V_s - e_{bn} + e_{cn}$
	$i_a = 0$	$\frac{1}{2}(-V_s + e_{bn} - e_{cn})$	
	$i_a < 0$	$-e_{an} + e_{bn}$	
$\pi - \frac{4\pi}{3}$	$i_c > 0$	$-V_s - e_{an} + e_{bn}$	$V_s - e_{bn} + e_{cn}$
	$i_c = 0$		$\frac{1}{2}(V_s + e_{an} - e_{bn})$
	$i_c < 0$		$-e_{bn} + e_{cn}$
$\frac{4\pi}{3} - \frac{5\pi}{3}$	$i_b > 0$	$-e_{an} + e_{bn}$	$-V_s - e_{bn} + e_{cn}$
	$i_b = 0$	$\frac{1}{2}(-V_s - e_{an} + e_{cn})$	$\frac{1}{2}(-V_s - e_{an} + e_{cn})$
	$i_b < 0$	$-V_s - e_{an} + e_{bn}$	$V_s - e_{bn} + e_{cn}$
$\frac{5\pi}{3} - 2\pi$	$i_a > 0$	$-e_{an} + e_{bn}$	$-V_s - e_{bn} + e_{cn}$
	$i_a = 0$	$\frac{1}{2}(V_s + e_{bn} - e_{cn})$	
	$i_a < 0$	$V_s - e_{an} + e_{bn}$	

3.4 Discretisation of the BLDC Machine Model

The dynamic model derived above is described in continuous time. The result is a set of differential equations. These equations are solved numerically in Simulink/Matlab. Implementing the model in digital processing units (DSPs, FPGAs,...), used to control BLDC machines, requires the model to be discrete. In this section, the derived continuous model will be discretised. A zero-order hold discretisation method [DeCooman2012] will be used for this purpose. The differential (3.10) can be written as of the following form:

$$\frac{\mathrm{d}\boldsymbol{x}}{\mathrm{d}t} = \boldsymbol{A}\boldsymbol{x} + \boldsymbol{B}\boldsymbol{u} \tag{3.17}$$

A general solution for this differential equation is given by:

$$\boldsymbol{x}(t) = e^{\boldsymbol{A}(t-t_0)}\boldsymbol{x}(t_0) + \int_{t_0}^{t} e^{\boldsymbol{A}(t-\tau)}\boldsymbol{B}\boldsymbol{u}(\tau)\mathrm{d}\tau \tag{3.18}$$

The solution $\boldsymbol{x}$ at time kT_s is denoted by $\boldsymbol{x_k}$. If the solution is sampled at time kT_s and at time $(k+1)T_s$ and the input $\boldsymbol{u}$ is kept constant in between two samples (T_s is the sampling period), it follows that:

$$\begin{aligned}\boldsymbol{x}_{k+1} &= e^{\boldsymbol{A}T_s}\boldsymbol{x_k} + \int_0^{T_s} e^{\boldsymbol{A}(T_s-\tau)}\boldsymbol{B}\mathrm{d}\tau\boldsymbol{u_k} \\ &= \boldsymbol{A_{SH}}\boldsymbol{x_k} + \boldsymbol{B_{SH}}\boldsymbol{u_k}\end{aligned} \tag{3.19}$$

The vector $\boldsymbol{u_k}$ is the value of the input $\boldsymbol{u}$ in the time interval $[kT_s, (k+1)T_s]$. Applying (3.19) to the (3.10), results in the following matrices of the discretised system:

$$\boldsymbol{A_{SH}} = \begin{bmatrix} e^{-\frac{R_sT_s}{L}} & 0 & 0 & 0 \\ 0 & e^{\frac{-R_sT_s}{L}} & 0 & 0 \\ 0 & 0 & 1 & 0 \\ 0 & 0 & T_s & 1 \end{bmatrix} \tag{3.20}$$

$$\boldsymbol{B_{SH}} = \begin{bmatrix} \frac{2}{3}\frac{1-e^{-\frac{R_sT_s}{L}}}{R_s} & \frac{1}{3}\frac{1-e^{-\frac{R_sT_s}{L}}}{R_s} & 0 \\ -\frac{1}{3}\frac{1-e^{-\frac{R_sT_s}{L}}}{R} & \frac{1}{3}\frac{1-e^{-\frac{R_sT_s}{L}}}{R} & 0 \\ 0 & 0 & \frac{T_s}{J} \\ 0 & 0 & \frac{T_s^2}{2J} \end{bmatrix} \tag{3.21}$$

3.5 Discretisation of PID Controller

To control the speed of electrical drives conventional cascaded PI(D) controllers are used. One PI(D) controller for the speed and another for the current. In each stage the parameter to be controlled is measured or estimated and compared with its set-point. The error signal e is the input to the PI(D) controller:

$$e(t) = r(t) - y(t) \tag{3.22}$$

The set-point at time t is represented by $r(t)$ and $y(t)$ is the measurement of the controlled variable at time t. The PI(D) controller translates this error e into a control action u:

$$u(t) = K_p e(t) + K_i \int_0^t e(\tau)\mathrm{d}\tau + K_d \frac{\mathrm{d}e}{\mathrm{d}t} \tag{3.23}$$

The parameters K_p, K_i and K_d are chosen in such a way that the error e approaches zero in an acceptable way. Taking the derivative of equation (3.23), we get the following expression:

$$\frac{\mathrm{d}u}{\mathrm{d}t} = K_p \frac{\mathrm{d}e}{\mathrm{d}t} + K_i e + K_d \frac{\mathrm{d}^2 e}{\mathrm{d}t^2} \tag{3.24}$$

We can discretise this equation using the backward Euler method:

$$\frac{u(t_k) - u(t_{k-1})}{T_s} = K_p \frac{e(t_k) - e(t_{k-1})}{T_s} + K_i e(t_k) + K_d \frac{\frac{\mathrm{d}}{\mathrm{d}t}e(t_k) - \frac{\mathrm{d}}{\mathrm{d}t}e(t_{k-1})}{T_s} \tag{3.25}$$

Where $\frac{\mathrm{d}e}{\mathrm{d}t}$ represents the first derivative to time of e:

$$\frac{u(t_k) - u(t_{k-1})}{T_s} = K_p \frac{e(t_k) - e(t_{k-1})}{T_s} + K_i e(t_k) + K_d \frac{\frac{e(t_k) - e(t_{k-1})}{T_s} - \frac{e(t_{k-1}) - e(t_{k-2})}{T_s}}{T_s} \quad (3.26)$$

Hence, the control effort at time $t = t_k$, $u(t_k)$, can be written as:

$$u(t_k) = u(t_{k-1}) + K_p \left[e(t_k) - e(t_{k-1})\right] + K_i T_s e(t_k) + \frac{K_d}{T_s} \left[e(t_k) - 2e(t_{k-1}) + e(t_{k-2})\right] \quad (3.27)$$

3.6 Simulation of the BLDC Machine Model Using Simulink

3.6.1 Implementation of the Model in Simulink

In the previous sections, a continuous-time and a discrete-time model for BLDC machine and inverter are given. The back-EMF results from the product of the function F, which depends on the variables θ_e and ω_e. The generated electromagnetic torque T_e depends on the product of current (i_a and i_b) and the function F. The set of (3.10) is a set of nonlinear differential equations. By considering the nonlinear components, the back-EMF and the electromagnetic torque, as external inputs (illustrated in Fig. 3.2), the resulting system was discretised using a procedure for linear systems, based on the matrix exponential. Simulation results at the end of this chapter (Figs. 3.6 and 3.7) show that the discretised model approximates the continuous-time model well if the discretisation period is sufficiently small when compared with the carrier frequency of the PI current controller.

3.6.2 Simulated Waveforms Using the BLDC Model

The model outlined in Sections 3.2 and 3.3 is implemented in Simulink/Matlab. The model is first tested without speed and current controller. The waveform of the phase currents for this case are depicted in Fig. 3.3(a). Due to the lack of controllers start-up current is very high and the speed reaches to no-load speed quickly as shown in Fig. 3.3(b). As the back-EMF evolves proportional to the speed, at low speeds, the back-EMF is small and hence the phase currents can become high for

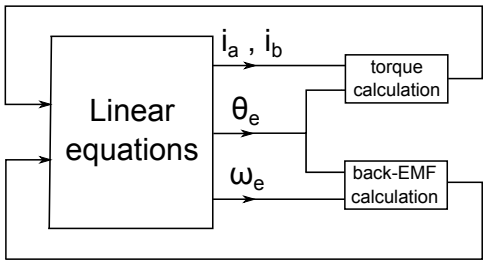

Figure 3.2. Nonlinear components of the derived differential equations are modelled as nonlinear feedback signals

a given supply voltage. Every 60 electrical degrees, the current from one phase commutates to the unexcited phase. The waveform of the electromagnetic torque T_e is depicted in Fig. 3.3(c). The electromagnetic torque is proportional to the phase current in the conducting phases. Without current control, the current is allowed to vary substantially. As a consequence, there is a significant torque ripple.

As a second case, the dynamical behaviour of the BLDC machine using the speed and current PI controllers is studied. The speed set-point is set to 200 rad/s, after 50 ms the setpoint is changed to 100 rad/s. The phase current is now limited to 2 A, Fig. 3.4(a). This limits the obtainable acceleration of the machine, Fig. 3.4(b). The limitation on the current is achieved by using a saturation block in between the speed and current controller, i.e. by limiting the current reference of the PI current controller. The torque ripple is lower than in the uncontrolled case, as shown in Fig. 3.4(c).

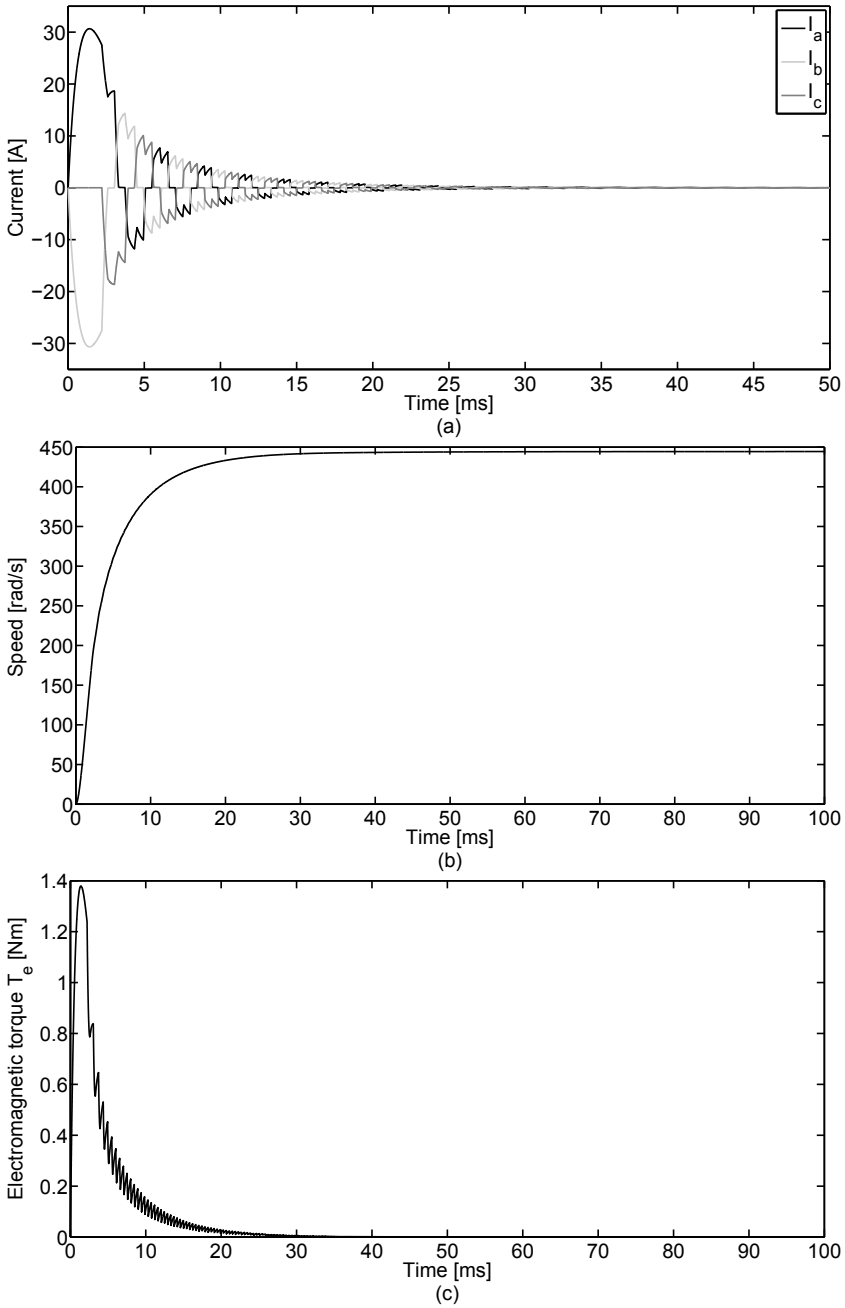

Figure 3.3. Simulation results, (a): Phase currents in function of time for a BLDC machine without speed and current PI controller, (b): rotor speed, (c): electromagnetic torque

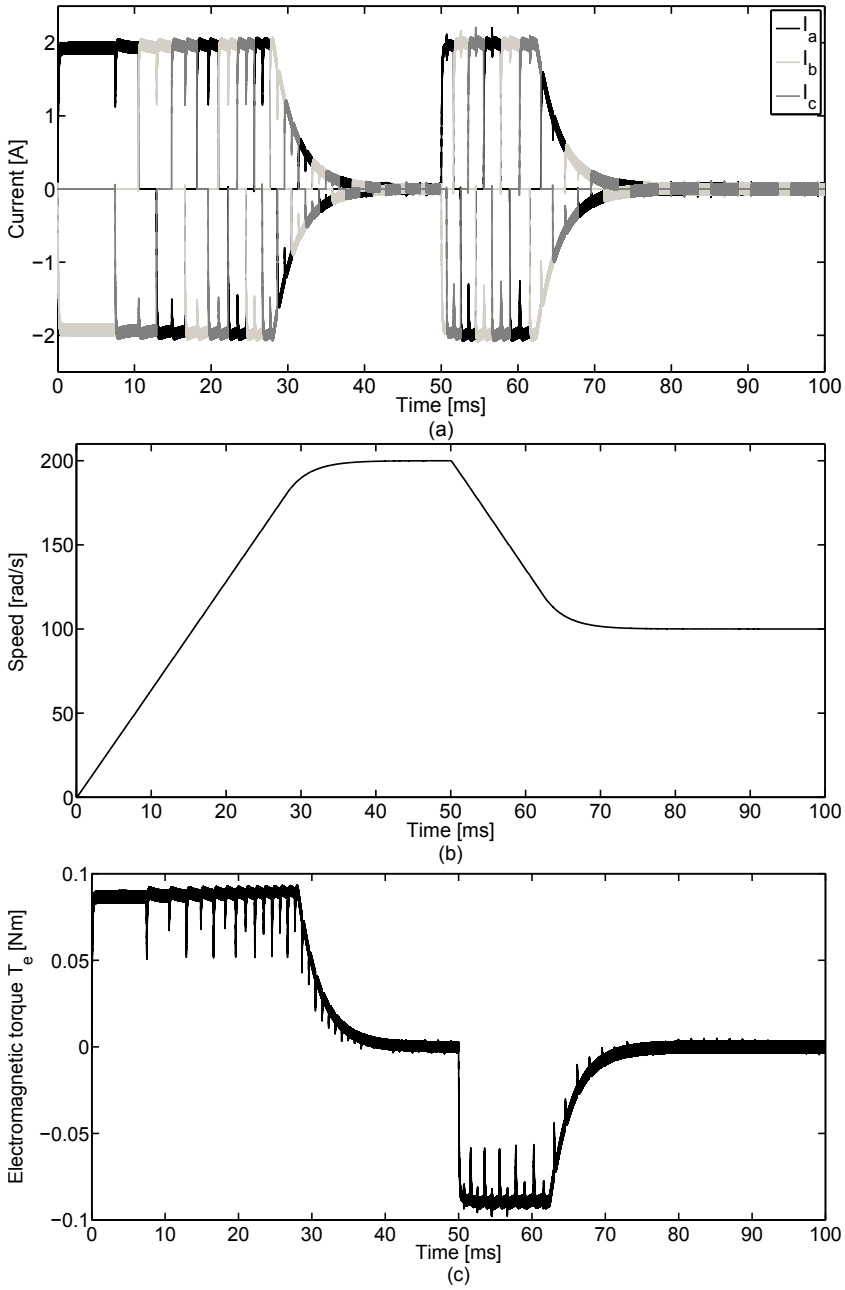

Figure 3.4. Simulation results, (a): Phase currents in function of time for a BLDC machine with speed and current PI controller, (b): rotor speed, (c): electromagnetic torque

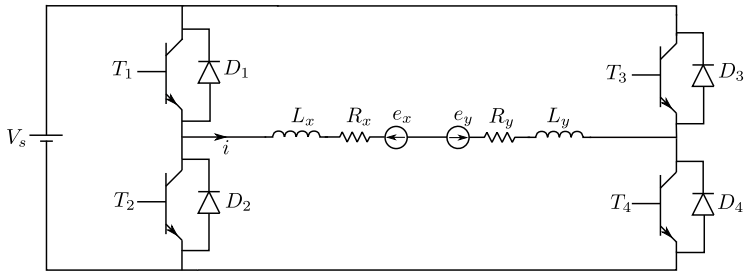

Figure 3.5. Electrical diagram of a BLDC machine and H-bridge after transients

3.7 Derivation of a Reduced Discretised Model for BLDC Machines

In Section 3.2 of this chapter, a model for a BLDC machine is derived. This model takes current commutation and the corresponding transients into account. This provides a detailed model which is suitable for time simulations. To not needlessly complicate the theoretical analysis, a reduced model is derived in this section. This model will be used later in Chapters 5 and 6. After transients, the dynamics are described by the electrical circuit in Fig. 3.5.

Two phases, X and Y, are connected to the supply. Moreover, there is a mathematical relationship between the back-EMF voltages in the phases X and Y, e_x and e_y respectively. In (3.6), the ideal trapezoidal waveform of the back-EMF in a BLDC machine was described. A phase is conducting current when the value of the F function in that phase is 1 or -1. It follows that the back-EMF voltages e_x and e_y are equal in amplitude, but have different signs:

$$e_x = K_e \omega_e \tag{3.28}$$
$$e_y = -K_e \omega_e \tag{3.29}$$

The current flowing in the active phases is controlled using PWM signals (generated according to the complementary switching strategy) to the switches of the H bridge. When the PWM signal is ON, the switches T_1 and T_4 are closed, the other two switches are open. When the PWM signal is OFF, the switches T_2 and T_3 are closed, T_1 and T_4 are open. This means that when the PWM signal is ON, the positive DC-bus voltage is applied to the motor terminals of phases X and Y. When the PWM signal is OFF, X and Y are connected to the negative supply voltage. The level of the PWM reference is denoted by δ. If $\delta = 1$, the

switches T_1 and T_4 are closed during the complete PWM period, while T_2 and T_3 are open. If $\delta = 0$, the switches T_2 and T_3 are closed during the complete PWM period, while T_1 and T_4 are open. If $\delta = 0.5$, the motor terminals are connected to the positive supply voltage for half the PWM period and to the negative supply voltage for the other half of the PWM period, resulting in an average voltage of 0 V over the motor terminals X and Y. The value for δ is controlled by the PI speed and current controllers.

The current in the phases X and Y can be determined by solving the following differential equation (assuming $R = R_x = R_y$ and $L = L_x = L_y$):

$$\frac{\mathrm{d}i}{\mathrm{d}t} = -\frac{R}{L}i + \frac{1}{2L}\delta V_s - \frac{1}{2L}2K_e\omega_e \tag{3.30}$$

A change in the speed ω_e results from the difference between the electromagnetic torque T_e and the load torque T_l. Using equation $T_e = 2K_t i_{DC}$ for T_e leads to the following differential equation for the speed:

$$\frac{\mathrm{d}\omega_e}{\mathrm{d}t} = \frac{1}{J}2K_t i_{DC} - \frac{1}{J}T_l \tag{3.31}$$

Equations (3.30) and (3.31) can be combined in a state-space model:

$$\begin{bmatrix} \frac{\mathrm{d}i}{\mathrm{d}t} \\ \frac{\mathrm{d}\omega_e}{\mathrm{d}t} \end{bmatrix} = \begin{bmatrix} -\frac{R}{L} & -\frac{K_e}{L} \\ \frac{2K_t}{J} & 0 \end{bmatrix} \begin{bmatrix} i \\ \omega_e \end{bmatrix} + \begin{bmatrix} \frac{1}{2L} & 0 \\ 0 & -\frac{1}{J} \end{bmatrix} \begin{bmatrix} \delta V_s \\ T_l \end{bmatrix} \tag{3.32}$$

This model can also be discretised. To achieve the discrete-time equivalent of this derived reduced continuous-time model of the BLDC machine, an approach similar to that of Section 3.4 can be used: a zero-order hold discretisation method is used. Since the differential equation (3.32) is in the form of

$$\begin{cases} \frac{\mathrm{d}\boldsymbol{x}}{\mathrm{d}t} = \boldsymbol{A}\boldsymbol{x} + \boldsymbol{B}\boldsymbol{u} \\ \boldsymbol{y} = \boldsymbol{C}\boldsymbol{x} + \boldsymbol{D}\boldsymbol{u} \end{cases} \tag{3.33}$$

it has a general solution as it is described in (3.18) and (3.19) the following matrices can be derived for the discretised system:

$$A_{SH} = \begin{bmatrix} e^{-\frac{RT_s}{L}} & e^{-\frac{K_e T_s}{L}} \\ e^{-\frac{2K_t T_s}{J}} & 0 \end{bmatrix} \tag{3.34}$$

$$B_{SH} = \begin{bmatrix} \frac{1}{2}\frac{1-e^{-\frac{RT_s}{L}}}{R} & 0 \\ 0 & -\frac{T_s}{J} \end{bmatrix} \tag{3.35}$$

To illustrate the dynamics of the reduced model of the BLDC machine, the responses of the current i and speed ω_e to a step in the voltage δV_s and in the load torque T_l are depicted in Figs. 3.6 and 3.7 for the Maxon Motor BLDC machine, which motor parameters are given in Appendix A.1. In these figures, the discretisation, performed with the Matlab command c2d, is validated. When a step in the voltage δV_s is applied, current will start to flow, electromagnetic torque is produced and the machine starts to accelerate. Due to the increasing speed ω_e, the amplitude of the back-EMF induced in the stator winding increases, which counters the supply voltage and reduces the current flow. At a certain speed, the back-EMF (referred to the neutral point) matches half of the supply voltage (the line-to-line back-EMF then equals the supply voltage), the current drops to zero and the machine stops accelerating.

When a step in the load torque T_l is applied, the machine decelerates. The back-EMF decreases and for a given supply voltage current starts to flow. The machine keeps decelerating until the electromagnetic torque produced by the current in the machine matches the applied load torque.

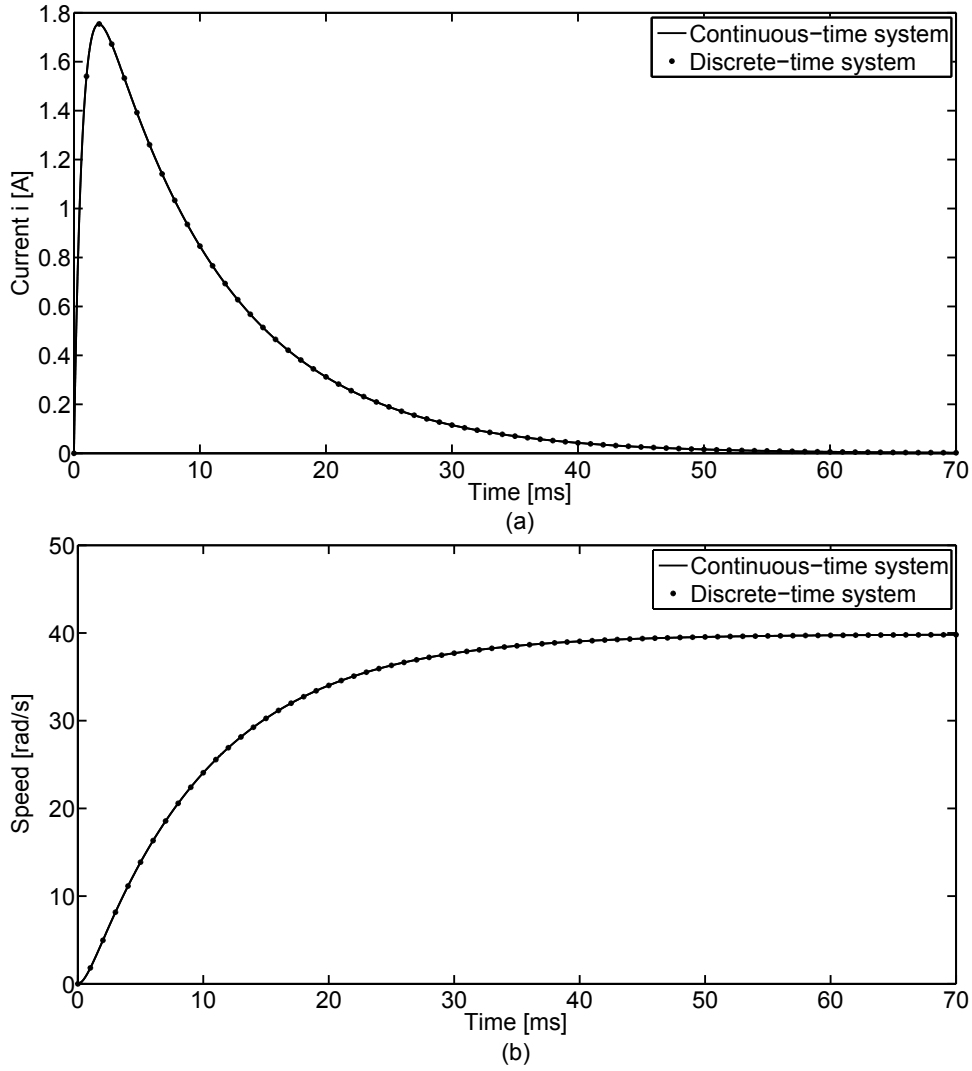

Figure 3.6. Simulation results, response of the current, (a): and the speed, (b): to a step in the voltage δV_s

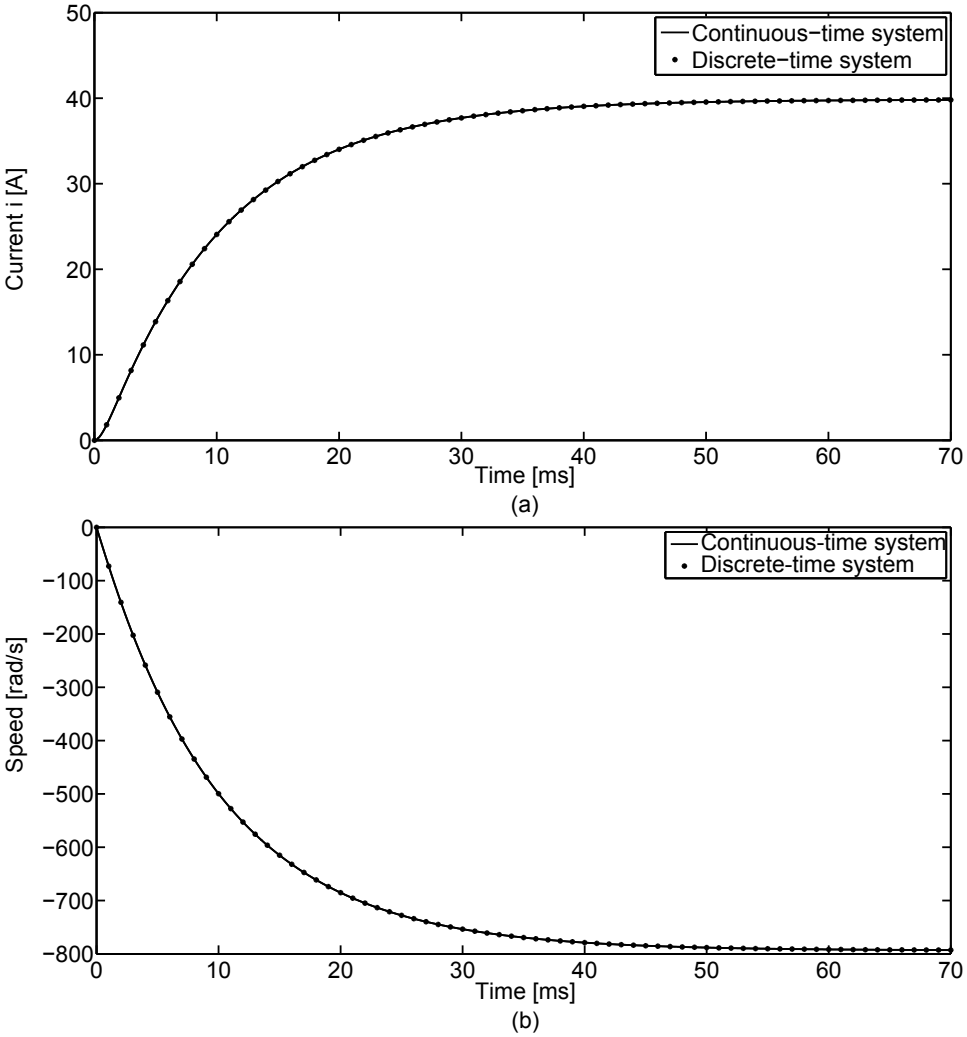

Figure 3.7. Simulation results, response of the current, (a): and the speed, (b): to a step in the load torque T_l

Chapter 4

Self-Sensing Commutation of BLDC Machines Using Back-EMF Samples

4.1 Introduction

To obtain a stable dynamical system that fulfils certain criteria (rise time, overshoot, settling time, ...) a feedback loop like the one in Fig. 4.1 can be implemented. The input to such a system is the signal we want the output to follow. Therefore this signal is referred to as the reference signal. The output of the system is measured using sensors and is compared with the reference signal. The resulting error is used by the controller to correct the input to the process in order to force the output to follow the input closer.

Unfortunately, it is not always possible or desirable to measure all the outputs of the process. Despite that these unmeasured outputs are required to control the process in a stable way. For these cases, observers for state estimation have been

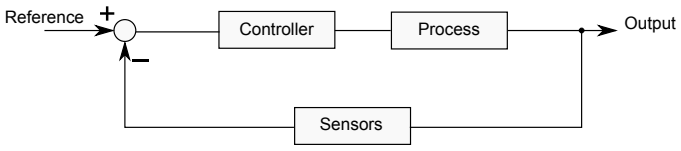

Figure 4.1. Scheme of a controlled system

developed. In BLDC drives, an extra set of position sensors (Hall sensors, for example) is often unwanted. Instead, an estimation of the rotor position is made to determine accurate current commutation instants. Furthermore, if speed control is required the rotor speed will be estimated as well.

Over the last decades, different self-sensing methods have been proposed for a wide range of rotor speeds from standstill to high speeds. In [Perriard2012] B-H hysteresis characteristics of the stator iron are used to detect the rotor position of a BLDC motor at standstill. In [Iepure2012] an observer based method is used for permanent magnet flux estimation. In [DeAngelo2005, Stirban2012] observers are used in order to estimate position and speed of the machine. A three-dimensional coordinate system, often applied in control of AC machine, is used in [Gao2010] to control a BLDC machine. However, due to misalignment of the current with the back-EMF, achieving the nominal efficiency of the machine seems to be difficult. Back-EMF observers are developed in [Genduso2010, Hongryel2011] which avoid the integration drift problem in flux estimators. The convergence of an observer during the state estimation of a self-sensing drive is studied recently in [Hamida2013]. In [DeBelie2010, DeBelie2012] the response on a high-frequency test-signal injection is used to estimate the position of the rotor of BLDC as well as permanent-magnet synchronous machine (PMSM). In this method the average-current samples are unaffected by the test signals. Another study [Gabriel2013], is carried out to study the influence of the converter on the high frequency test signals. In [Leidhold2011] the high-frequency signal is injected in the zero sequence component. As a result the high-frequency signal does not have interaction with current controllers. In [Zhu2011] the effectiveness of high-frequency signal injection based self-sensing-control methods for brushless alternating current (BLAC) motors has been investigated. In [Dadashnialehi2014] the back-EMF signal is used in order to estimate the speed of a BLDC machine using a wavelet transformation.

Many observers and filters have been used in order to estimate the states of a controlled drive system (e.g. rotor speed and position, load torque, ...). However, in this section before introducing the back-EMF based commutation methods two observers will be introduced which are widely used in self-sensing control algorithms of electrical drives.

The conventional back-EMF based techniques will be evaluated and the advantages and drawbacks will be discussed. Based on this discussion two different back-EMF based algorithms, showing improved performance of the back-EMF based algorithms, will be explained in more details.

4.1.1 Luenberger Observer

A fundamental observer for time-invariant linear systems is the Luenberger observer [DeCooman2012]. In what follows, the Luenberger observer will be derived for the following discrete-time system:

$$\begin{cases} \boldsymbol{x}(k+1) & = \boldsymbol{A}\boldsymbol{x}(k) + \boldsymbol{B}\boldsymbol{u}(k) \\ \boldsymbol{y}(k) & = \boldsymbol{C}\boldsymbol{x}(k) \end{cases} \tag{4.1}$$

The vector $\boldsymbol{x}$ represents the state vector we want to estimate from measurement vector $\boldsymbol{y}$. The vector $\boldsymbol{u}$ represents the input vector to the system and is considered measurable. A state estimator of the following form was proposed by Luenberger:

$$\hat{\boldsymbol{x}}(k+1) = \boldsymbol{A}\hat{\boldsymbol{x}}(k) + \boldsymbol{B}\boldsymbol{u}(k) + \boldsymbol{L}[\boldsymbol{y}(k) - \hat{\boldsymbol{y}}(k)] \tag{4.2}$$

$$\hat{\boldsymbol{y}}(k) = \boldsymbol{C}\hat{\boldsymbol{x}}(k) \tag{4.3}$$

The estimated state vector is denoted with $\hat{\boldsymbol{x}}$. Introducing the error vector of the estimation $\boldsymbol{e}(k) = \hat{\boldsymbol{x}}(k) - \boldsymbol{x}(k)$, it follows that the dynamics of the error are given by:

$$\boldsymbol{e}(k+1) = (\boldsymbol{A} - \boldsymbol{L}\boldsymbol{C})\boldsymbol{e}(k) \tag{4.4}$$

A discrete-time system is stable if its poles lie within the unit circle. The estimated state $\hat{\boldsymbol{x}}$ will converge to the real state $\boldsymbol{x}$ if the poles of $\boldsymbol{A} - \boldsymbol{L}\boldsymbol{C}$ lie within the unit circle. If a matrix $\boldsymbol{L}$ exists such that this is the case, the system (4.1) is called observable. A disadvantage of the Luenberger observer is that it does not take into account the occurring disturbances in the system and the noise in the measurements $\boldsymbol{y}$.

4.1.2 Kalman-Bucy Filter

For linear systems which are influenced by noise, often a Kalman-Bucy filter is used. The Kalman-Bucy filter will be explained for a discrete-time system:

$$\begin{cases} \boldsymbol{x}(k+1) & = \boldsymbol{A}(k)\boldsymbol{x}(k) + \boldsymbol{B}(k)\boldsymbol{u}(k) + \boldsymbol{w}(k) \\ \boldsymbol{y}(k) & = \boldsymbol{C}(k)\boldsymbol{x}(k) + \boldsymbol{v}(k) \end{cases} \tag{4.5}$$

The vectors $\boldsymbol{v}$ and $\boldsymbol{w}$ represent the measurement noise and disturbance inputs, respectively. It is assumed that $\boldsymbol{v}$ and $\boldsymbol{w}$ have a mean value of zero, that successive values of $\boldsymbol{v}$ and successive values of $\boldsymbol{w}$ are uncorrelated and that $\boldsymbol{v}$ and $\boldsymbol{w}$ are uncorrelated (white Gaussian processes). Under these conditions, it is possible to derive an optimal (in the class of linear systems and nonlinear filters) state estimator [DeCooman2012]:

$$\hat{\boldsymbol{x}}(k+1) = \boldsymbol{A}(k)\hat{\boldsymbol{x}}(k) + \boldsymbol{B}(k)\boldsymbol{u}(k) + \boldsymbol{H}(k)(\boldsymbol{y}(k) - \boldsymbol{C}(k)\hat{\boldsymbol{x}}(k)) \tag{4.6}$$

Where $\boldsymbol{H}(k)$ is determined as:

$$\boldsymbol{H}(k) = \boldsymbol{A}(k)\boldsymbol{P}(k)\boldsymbol{C}(k)^T(\boldsymbol{V}(k) + \boldsymbol{C}(k)\boldsymbol{P}(k)\boldsymbol{C}(k)^T)^{-1} \tag{4.7}$$

The matrix $\boldsymbol{P}(k)$ is the covariance matrix of the estimation error at time $t = k$ and is updated as follows:

$$\begin{aligned}\boldsymbol{P}(k+1) = \boldsymbol{A}(k)\boldsymbol{P}(k)\boldsymbol{A}(k)^T - \boldsymbol{A}(k)\boldsymbol{P}(k)\boldsymbol{C}(k)^T(\boldsymbol{V}(k) \\ + \boldsymbol{C}(k)\boldsymbol{P}(k)\boldsymbol{C}(k)^T)^{-1}\boldsymbol{C}(k)\boldsymbol{P}(k)\boldsymbol{A}(k)^T + \boldsymbol{W}(k)\end{aligned} \tag{4.8}$$

Here, $\boldsymbol{V}(k)$ and $\boldsymbol{W}(k)$ represent the covariance matrices at time $t = k$ of $\boldsymbol{v}$ and $\boldsymbol{w}$, respectively.

A similar filter, the Extended Kalman Filter (EKF), exists for nonlinear systems of the form:

$$\boldsymbol{x}(k+1) = f(\boldsymbol{x}(k), \boldsymbol{u}(k)) + \boldsymbol{w}(k) \tag{4.9}$$

$$\boldsymbol{y}(k) = h(\boldsymbol{x}(k)) + \boldsymbol{v}(k) \tag{4.10}$$

The functions f en h are nonlinear and differentiable. In the EKF, the functions f and h are linearized around the last estimated state $\hat{\boldsymbol{x}}$:

$$\boldsymbol{A}(k) = \left.\frac{\partial f}{\partial \boldsymbol{x}}\right|_{\hat{\boldsymbol{x}}(k-1),\boldsymbol{u}(k-1)} \tag{4.11}$$

$$\boldsymbol{C}(k) = \left.\frac{\partial f}{\partial \boldsymbol{x}}\right|_{\hat{\boldsymbol{x}}(k-1),\boldsymbol{u}(k-1)} \tag{4.12}$$

Disadvantages of the Kalman-Bucy filter are:

- The computational complexity of the algorithm (the calculation of the inverse of a matrix required).
- The variables $\boldsymbol{v}$ and $\boldsymbol{w}$ are assumed to be white noise processes, in practice this is not always the case.
- Information about $\boldsymbol{V}(k)$ and $\boldsymbol{W}(k)$ is necessary to obtain good observer dynamics.

4.1.3 Back-EMF Based Algorithms

The back-EMF in electric AC machines depends on the rotor position as well as on the rotor speed. By using these dependencies it could be possible to estimate the position and speed of the rotor by measuring and processing the back-EMF. An overview of measured back-EMF based self-sensing methods for BLDC drives can be found in [Acarnley2006]. These methods can be fitted into one of the following categories:

- back-EMF zero-crossings detection: (section 4.2)
- back-EMF integration
- back-EMF third-harmonic voltage component
- back-EMF threshold detection: (sections 4.3 and 4.4)

4.2 Conventional Zero-Crossing Detection Methods

In conventional back-EMF zero-crossing detection techniques for BLDC with 120° electrical conduction mode, a zero-crossing event of the back-EMF signal occurs 30° electrical before each commutation instant, Fig. 4.2. The back-EMF signal of the unexcited phase is compared to a sample of the neutral point voltage. Different methods are proposed to obtain a good measurement of the back-EMF signal [Lai2008, Darba2013b, Shao2003, Shao2006]. The back-EMF zero-crossing instant occurs when the back-EMF voltage value equals the voltage of the star point of the stator windings. For delta connected windings and machines where the star point is not available a virtual neutral point is used. In [Lai2011] it is shown that the back-EMF detection depends upon the PWM techniques and an approach to

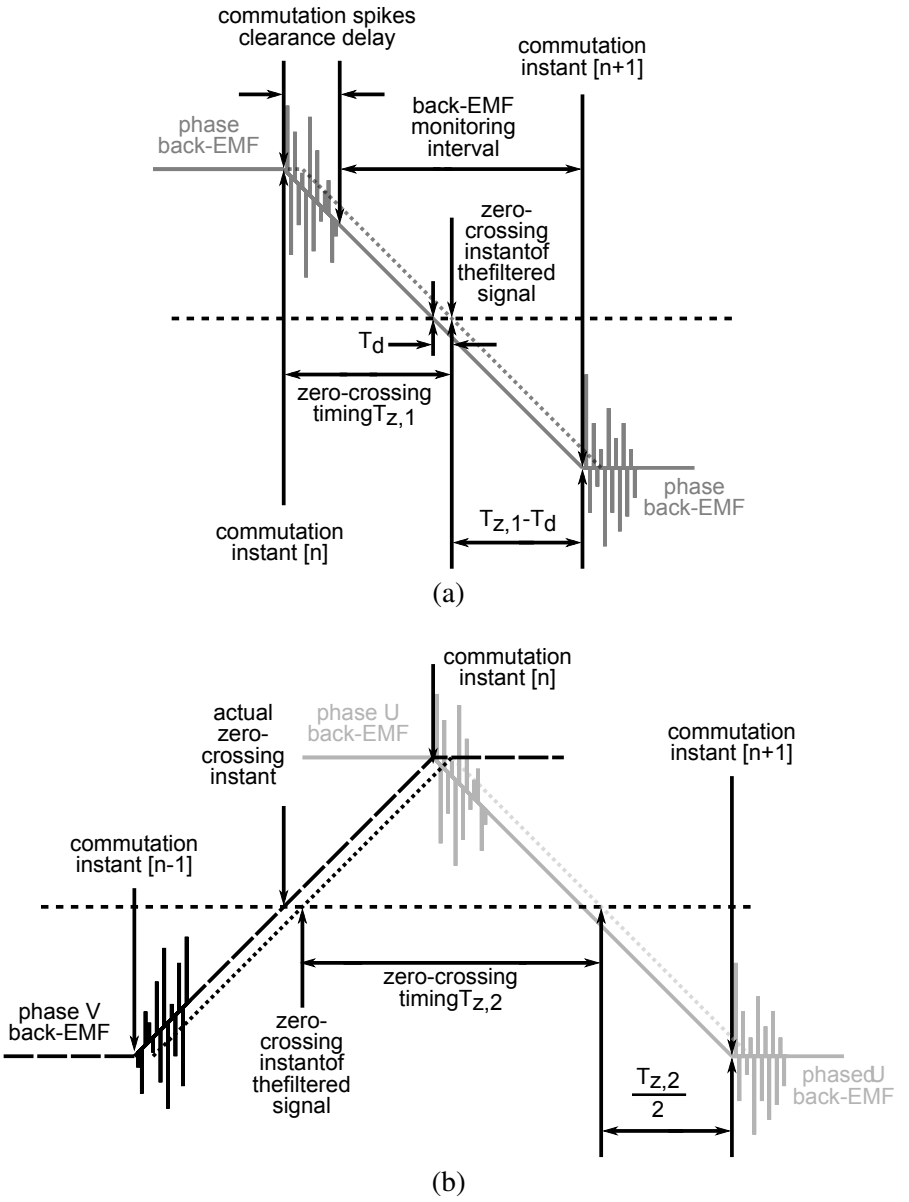

Figure 4.2. Different methods to determine commutation instants using back-EMF zero-crossing detection, (a): by using time difference between commutation and zero-crossing instant, (b): by time difference between successive zero-crossing instants

detect the zero-crossing points is explained in detail. Counting from the back-EMF zero-crossing detection, the commutation instants can be triggered 30° after

each zero-crossing. When the previous commutation instant [n] occurs, a timer starts to count and the time interval between this instant and the zero-crossing of the back-EMF is measured, Fig. 4.2(a). This time $T_{z,1}$ is often assumed to be the time interval during which the rotor position has changed by 30° electrical. With this assumption, the commutation instant $[n+1]$ is triggered a time $T_{z,1}$ after the back-EMF zero-crossing event. In another method the time interval $T_{z,2}$ between two successive commutations is measured and half of this time $\frac{T_{z,2}}{2}$ is used as an equivalent of the 30° electrical position Fig. 4.2(b).

In [Iizuka1985], this has been implemented on a microprocessor where a low-pass filter is used to remove the high-frequency components in the measured back-EMF signal. These high frequency components are the results of the switching actions of the power converter in order to control the average value of the voltage applied to the machine. However, the time delay of the low-pass filter has a constant value for different speeds (as indicated in Fig. 4.2 by T_d) and hence this limits the speed range.

Different improvements have been implemented for the zero-crossing method. For example in [Kim2011] a zero-crossing detection of the line-to-line measurement of the back-EMF signal is implemented but it shows the same problems of conventional zero-crossing methods. In [Shao2003, Shao2006] an alternative back-EMF zero-crossing detection is proposed using the negative terminal voltage of the DC-bus instead of the neutral point of the machine. It uses the zero-crossing detection concept so adding a fixed 30 degree delay is still necessary. In [Damodharan2010] the terminal voltages measured with respect to the negative DC-bus voltage are used to determine the zero-crossing instant of the back-EMF. In [Tsotoulidis2015] zero-crossings of the filtered zero sequence voltage (ZCV) are used. This method also uses a filter to obtain a more smooth ZCV. Another method to detect the commutation instants of a BLDC machine using the back-EMF zero-crossing concept is the integration of the back-EMF of the unexcited phase as it results in the rotor flux and hence position as discussed in [Becerra1991]. This method is less sensitive towards switching noise so it does not use any filter but it has some offset errors arising from the integration action.

In the aforementioned studies [Iizuka1985, Kim2011, Shao2003, Shao2006, Damodharan2010, Tsotoulidis2015, Becerra1991] obtaining the instant of commutation is realised by adding a 30° electrical delay to the zero-crossing instants of the back-EMF and show therefore the same inherent problem.

If the motor phase windings are star connected and the star point is available for measurements, summation of the three phase voltages results in a third harmonic voltage. Integration of the third harmonic voltage results in an estimation of the third harmonic flux of the motor. Zero-crossing instants of the third harmonic flux correspond to the commutation instants [Moreira1996]. This method shows the exact instant of commutation and solves the problem of calculating exactly 30°

electrical, but the noise-to-signal ratio in the lower speed range is more critical compared to other methods because of the relatively low amplitude of the third harmonic component. Moreover, the access to the neutral point of the motor is required which is not always the case and the drift can be an issue for the integration. In [Shen2006] integration of the third harmonic is proposed for ultra high speed self-sensing BLDC drives. The performance of the proposed method is not evaluated for speeds lower than 40 krpm which makes it suitable only for very specific high speed applications.

Another indirect method to detect the zero-crossing is obtained by using the conduction state of the free-wheeling diode as proposed in [Ogasawara1991]. This method works well in a wide range of speed but requires additional and complex electronic circuits to detect the current of the free-wheeling diodes and extra isolated power supplies. In [Cheng-HuChen2007] the commutation signals are directly detected from the average line-to-line voltages obtained from filtered PWM waveforms and machine model which solves the 30° electrical shift problem but deals with the disadvantages of the filter delay.

To conclude, using the zero-crossing instants of the back-EMF results in inaccurate estimations of the current commutation instants. This is a result of the assumption of a constant rotor speed during which the variation in rotor position is proportional to the corresponding time interval. However, during speed transients such as acceleration and deceleration, using $T_{z,1}$ or $\frac{T_{z,2}}{2}$ results in an inaccurate or faulty estimation of the 30° electrical position. Such an error can have a great influence in the speed estimation and could result in unstable behaviour of the drive during generator or braking mode. Fig. 4.3 shows the operation condition for a BLDC machine in generator mode in open-loop speed control. When a sudden speed increase occurs a lower braking torque is generated by the self-sensing generator drive due to incorrect commutation instant detection (Fig. 4.3(b)). This loss in braking torque results in a monotonous increase in the speed, Fig. 4.3(c) which on its turn causes future incorrect commutation instant detections [DeBelie2015].

In [Darba2013a], the authors proposed a self-sensing method that detects the commutation instants more accurately referred to as threshold technique. It uses the back-EMF voltage variation instead of time differences to detect the 30° electrical shift as it is done in most of the conventional methods. Simulation results published in [Darba2013a] show the advantages of this method. Experimental results are published in [Darba2013b, Darba2015b]. The basic principles of this method and the results of simulations and experimental tests are explained in Section 4.3. In [Darba2014, Darba2015a] another back-EMF based self-sensing commutation technique is proposed which also provides an accurate estimate of rotor position information. In Section 4.4 this method will be explained and simulation results as well as experimental validations will be used to prove the performance of the proposed method.

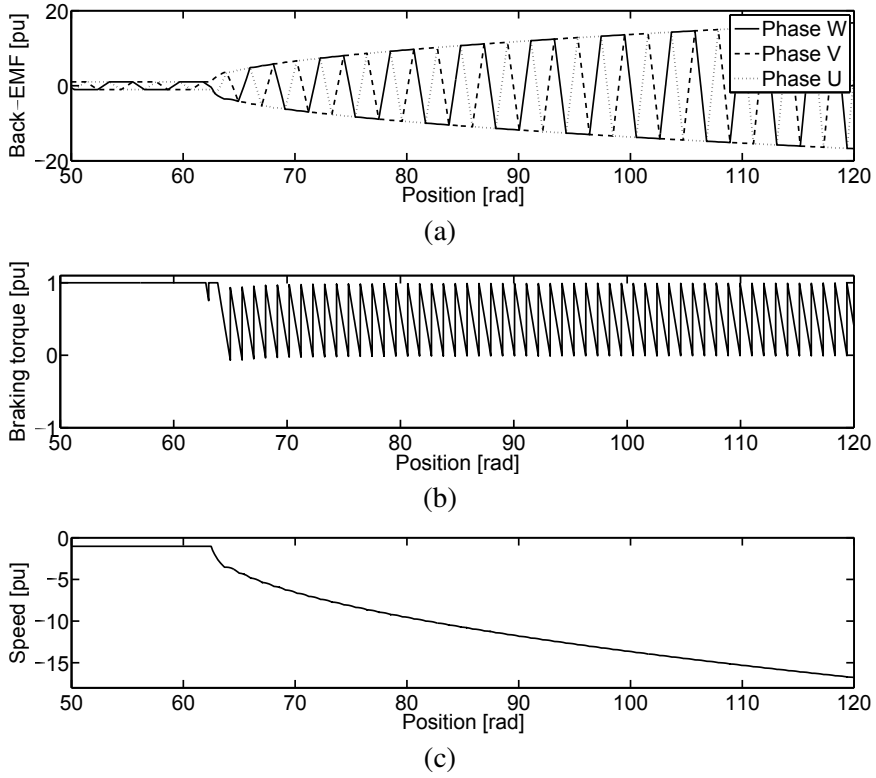

Figure 4.3. Simulation results, continuous increase in the rotor speed of a self-sensing BLDC generator during a sudden increase in the driving mechanical power

4.3 Back-EMF Threshold Commutation Method

4.3.1 Principles

To solve the problem of inaccurate estimations with respect to the 30° electrical position, we propose a method based on the back-EMF magnitude instead of its zero-crossings. After a commutation instant t_0 in Fig. 4.4 the back-EMF magnitude decreases and reaches its former absolute value again at the next commutation instant t_4 during constant speed operation. This relationship is the basis of the symmetrical threshold-tracking method presented in [Darba2013a]. In this method, the unexcited phase voltage is sampled at t_1. As the phase is unexcited this sample corresponds to the back-EMF as has been proven in [Shao2003, Shao2006]. It results in a back-EMF measurement and is then monitored, Fig. 4.4. After each commutation instant, a threshold is computed firstly (eg. at t_1 in the case of Fig. 4.4). This

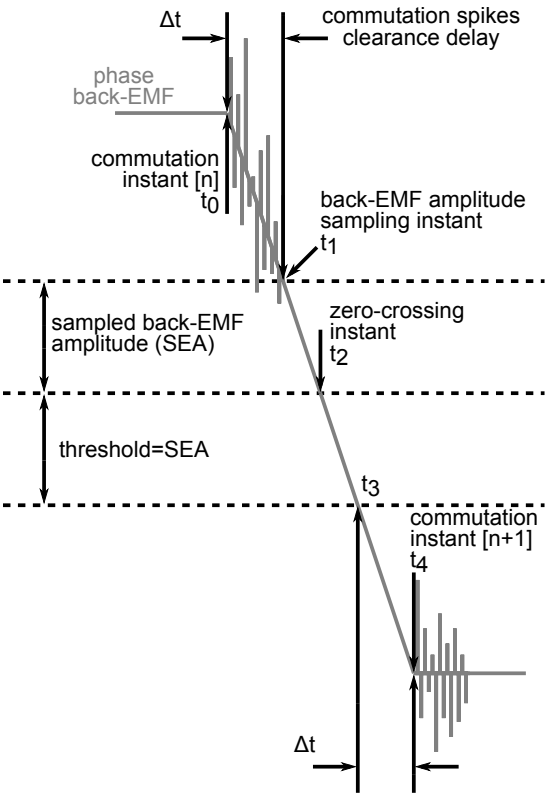

Figure 4.4. Proposed self-sensing method including the timings and important events

threshold is made based on a sample of the back-EMF taken at a time Δt after the previous commutation instant. A minimum Δt is used in order to avoid measuring the switching noise and other purposes to be explained later in this section. The sign of this sampled back-EMF is modified and the resulting value will be used as a threshold that will detect the next commutation instant. Indeed, a comparison is made between the threshold and the back-EMF of the unexcited phase. As soon as the back-EMF voltage intersects with the threshold value t_3 a time delay equal to Δt is applied. The end of this time delay is considered as the instant for the next phase commutation t_4. Here, the occurrence of back-EMF zero-crossing t_2 has not been used.

4.3.2 Indirect Measurement of the Speed and Peak Back-EMF

In this section, speed and peak back-EMF estimations are discussed in order to improve the performance of the self-sensing method as will be discussed later. The

peak back-EMF is the maximum value of back-EMF waveform before reaching to its flat part if a trapezoidal back-EMF is considered. At each commutation instant the estimation of the speed and peak value of the back-EMF are updated. These estimations are performed by measuring the time interval between two estimated current commutation instants. The detection procedure of the commutation instants is described in more detail in 4.3.1. The absolute value of the mechanical rotor speed in rpm is estimated by the following equation:

$$|\hat{\omega}_r| = \frac{60}{N_p.[6.N_{\text{clk}}.T]} \tag{4.13}$$

where T is the clock period of the processor, N_{clk} is the number of processor clock periods elapsed during two commutation instants and N_P is the number of pole pairs. The back-EMF peak value is then estimated based on the estimated $|\hat{\omega}_r|$ as follows:

$$|\hat{e}| = K_e|\hat{\omega}_r| \tag{4.14}$$

where K_e is the voltage constant of the BLDC machine, often given in the data-sheets or measured before.

4.3.3 Determining and Limits of Δt

The value of Δt needs to be adapted with respect to the different operating conditions of the machine. The capability of modifying this parameter gives more flexibility to deal with different operating conditions of the drive compared to the conventional back-EMF zero-crossing methods.

A. Maximum and Minimum Values of Δt

The method as illustrated in Fig. 4.2(a), is a special case of the symmetrical threshold-tracking method. For a Δt equal to $T_{z,1}$ or $\frac{T_{z,2}}{2}$ as given in Fig. 4.2 the proposed method will operate as the conventional back-EMF zero-crossing method. This means that the value of $T_{z,1}$ or $\frac{T_{z,2}}{2}$ is the maximum limit for Δt a non-zero minimum limit should be defined as well. With a decrease in the speed of the machine the value of the back-EMF decreases. Hence, the threshold magnitude has to be limited in order to obtain an intersection with the back-EMF. This means that a minimum has to be imposed on the Δt as higher Δt lowers the threshold magnitude. The behaviour of the back-EMF during a speed reduction is illustrated in Fig. 4.5. The drop in back-EMF signal is exaggerated to explain the problem more clearly. The light grey line represents the amplitude of the back-EMF before a speed drop. The dark grey solid line represents the value of back-EMF at lower

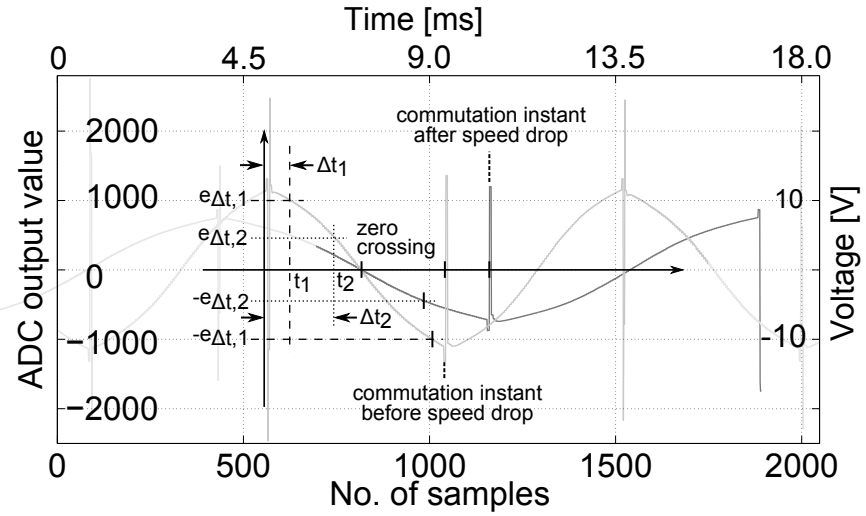

Figure 4.5. Variation of the measured back-EMF signals due to a speed change and different threshold values due to the different values of Δt (back-EMF waveforms are measured from experimental tests)

speed. The value of the back-EMF before the speed drop sampled at t_1 is referred to as $e_{\Delta t,1}$ and the value of the back-EMF after the speed drop sampled at t_2 is referred to as $e_{\Delta t,2}$. The time interval between the last commutation instant and the sampling time of the back-EMF value before and after speed drop is denoted by Δt_1 and Δt_2. The value of the back-EMF after a speed drop (solid dark grey line) has no intersection with the horizontal dashed black line $-e_{\Delta t,1}$ as illustrated in Fig. 4.5. An intersection with the threshold can be obtained if the threshold is sufficient low. For this, a new threshold sample such as $e_{\Delta t,2}$ for which $\Delta t_1 < \Delta t_2$ must be taken. The new threshold value guarantees the intersection with the back-EMF value. Determining the value for the threshold is controlled by Δt. This example shows the importance of Δt in this algorithm.

B. Maximum Back-EMF Decrease During Load Increase

The problem which is described in previous paragraph poses a minimum to Δt and depends on how fast the back-EMF can vary between commutation instants. For this we will compute firstly the largest back-EMF decrease due to a sudden load increase. Then the minimum Δt can be obtained in order to guarantee an intersection between the back-EMF and the threshold. To determine the minimum value of Δt the speed-torque characteristic of the machine should be calculated. Assuming that the back-EMF e and current I are in phase and $\omega L \ll R$ [Kenjo1985] then

the BLDC machine can be analysed using magnitudes of e, I and V only. The electromagnetic torque can be calculated using the electromagnetic power (output power plus all mechanical losses) of the machine as:

$$P_{em} = 3|e||I| = 3\omega|\lambda_m||I| \tag{4.15}$$

$$T_{em} = \frac{P_{em}}{\omega_r} = \frac{3\omega|\lambda_m||I|}{\omega_r} \quad , \quad T_{em} = T_l + T_{\text{losses}} \tag{4.16}$$

where T_l is the load torque, ω_r is the mechanical speed of the rotor and λ_m is the flux linkage of the stator winding per phase due to the permanent magnets. By neglecting the absolute signs and using $\omega_r = 2\omega/N_p$ we have:

$$T_{em} = \frac{3}{2}N_p\lambda_m I \quad , \quad e = \frac{N_p}{2}\omega_r\lambda_m \tag{4.17}$$

and then the voltage equation can be rewritten as:

$$V = e + RI = \frac{N_p}{2}\omega_r\lambda_m + \frac{2}{3}\frac{R}{N_p\lambda_m}T_{em} \tag{4.18}$$

From (4.17) the mechanical speed is computed as follows:

$$\omega_r = \frac{2V}{N_p\lambda_m} - \frac{4}{3}\frac{R}{(N_p\lambda_m)^2}T_{em} = K_1 - K_2T_{em} \tag{4.19}$$

$$K_1 = \frac{2V}{N_p\lambda_m} \quad , \quad K_2 = \frac{4}{3}\frac{R}{(N_p\lambda_m)^2} \tag{4.20}$$

The maximum speed difference between the no-load case and the full-load case for a given speed direction can be determined by:

$$\begin{aligned} |\Delta\omega_r| &= |\omega_{r,\text{nl}} - \omega_{r,\text{fl}}| \\ |\Delta\omega_r| &= |(K_1 - K_2T_{em,\text{nl}}) - (K_1 - K_2T_{em,\text{fl}})| \end{aligned} \tag{4.21}$$

where nl and fl subscripts are the indicators for no-load and full-load conditions. The torque at no-load is assumed to be zero.

By assuming T_{losses} equal for unloaded as well as loaded case, the maximum speed decrease during the loading of the machine can be estimated as:

$$|\Delta\hat{\omega}_r| = K_2T_{l,\text{max}} = \frac{4}{3}\frac{R}{(N_p\lambda_m)^2}T_{l,\text{max}} \tag{4.22}$$

During the maximum speed decrease, computed in (4.22), a maximum decrease in the back-EMF can be observed given by the voltage constant:

$$|\Delta e_{\text{max}}| = |\Delta\omega_{r,\text{max}}|K_e \tag{4.23}$$

knowing the maximum back-EMF decrease, the minimum value of Δt can be computed. For this, the waveform of e has to be known.

Note Assume that the minimum measurable back-EMF (sufficient signal-to-noise ratio) is given by e_{min}, corresponding to a minimum speed value $\omega_{r,\text{min}} = e_{\text{min}}/K_e$. Given the maximum back-EMF decrease (4.23) due to loading, the minimum back-EMF at which the symmetrical threshold-tracking method could work is given by $e_{\text{min}} + \Delta e_{\text{max}}$, corresponding to the speed $\omega_{r,\text{min}} + \Delta\omega_{r,\text{max}}$. This mechanical rotor speed value determines the boundary at which the open-loop start-up method ends and the closed-loop current control begins.

C. Minimum Δt to Detect Commutation Instants

The waveform of $e(t)$ during the unexcited time interval can have different profiles. Often this function is assumed to be linear as in the case of a machine designed to have a trapezoidal back-EMF profile. The BLDC-machine model which is used in this study has also a linear profile as illustrated in Fig. 4.16. However, most BLDC machines show a more sinusoidal back-EMF profile.

Fig. 4.6(a) shows the measured terminal voltages of a BLDC machine with respect to the negative side of DC-bus. This measurement is done while the machine was working with the proposed self-sensing method. It shows the nonlinearity in the back-EMF signal. Fig. 4.6(b) shows samples used by the self-sensing method, all taken in the unexcited intervals of different phases. Vertical spikes are results of the commutation actions. Differences in back-EMF waveforms between machines are related to different machine design parameters such as winding configuration, pole shape and magnet strength.

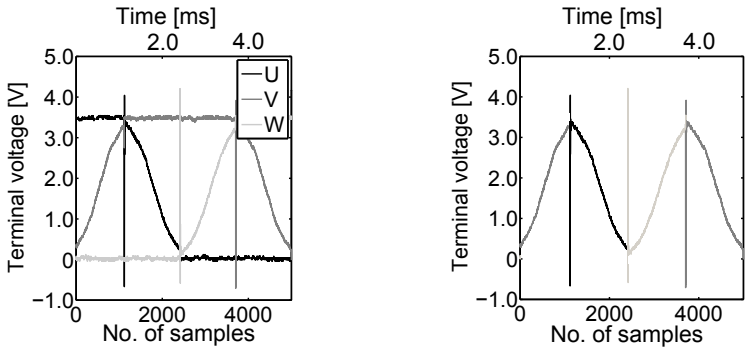

Figure 4.6. Nonlinear back-EMF during unexcited interval, (back-EMF waveforms are measured from experimental tests)

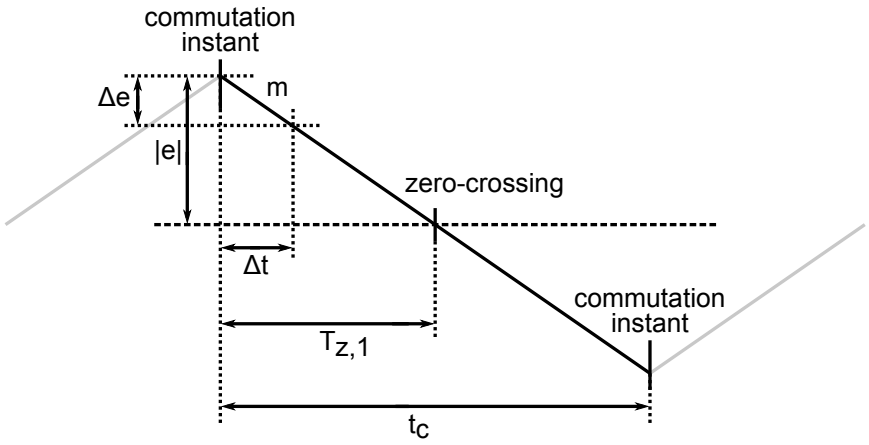

Figure 4.7. Linear back-EMF signals taken during the unexcited interval of the phases only

Linear Case By assuming $e(t)$ to be a linear function of time, Fig. 4.7, Δt can be computed as follows:

$$\Delta t_{\text{min}} = \frac{|\Delta e|}{m} \tag{4.24}$$

where m is the slope of the back-EMF and a variable related to the speed of the machine as shown in Fig. 4.7. It can be derived from the following equations:

$$m = \frac{|e|}{T_{z,1}} = \frac{6N_P\omega_r|e|}{\pi} \tag{4.25}$$

$$t_c = \frac{\pi}{3N_P\omega_r} = 2T_{z,1} \tag{4.26}$$

where t_c is the time interval between two successive commutation instants, ω_r is the mechanical speed of the machine expressed in rad/s.

Nonlinear Case The waveform of the back-EMF signal during the unexcited time interval can be approximated by a cosine function as shown in Fig. 4.8. By using this approximation and by considering $|e|$ as a reference value for the back-EMF voltage. Δt, shown in Fig. 4.8, is obtained as follows:

$$|\Delta y| = \frac{|e| - |\Delta e|}{|e|} \quad , \quad \beta = \sin^{-1}\left(|\Delta y|\right)$$
$$\Delta t_{min} = \frac{t_c}{2}\cos\left(\beta\right) \tag{4.27}$$

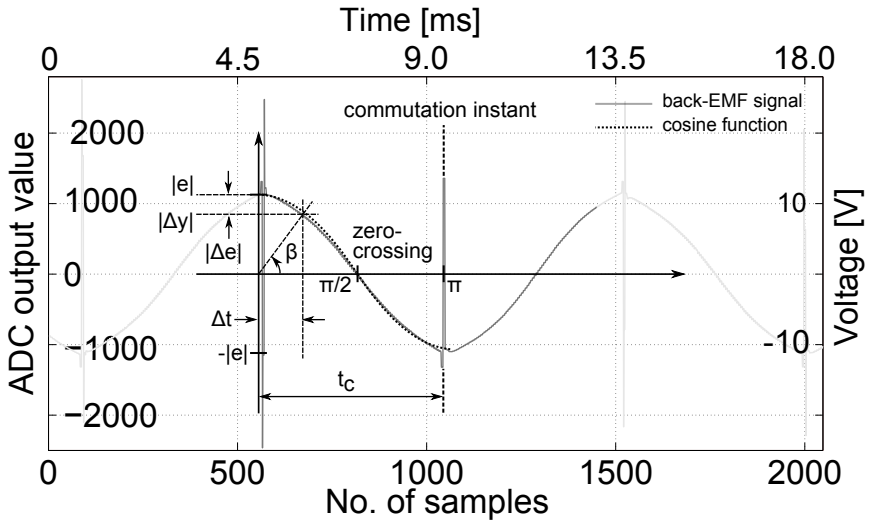

Figure 4.8. Nonlinear (cosine) function to describe a measured back-EMF signal during the unexcited interval of the phases, (back-EMF waveforms are measured from experimental tests)

4.3.4 Adaptation of Δt for the Nonlinear Case

The time Δt should be adapted to the working speed of more importance to machines showing a nonlinear back-EMF function. The time gradient of the back-EMF during instants just after commutation is smaller than during instants closer to the zero-crossing. At low speed operation condition the threshold is determined with a small value of Δt to measure a high back-EMF value and to keep the signal-to-noise ratio high. However in that case the back-EMF is rather slowly varying around the threshold value and detection of the intersection instant will be sensitive to noise. Therefore, Δt should be chosen corresponding to an instant at which the back-EMF value as well as the back-EMF gradient are sufficient high. This on its turn means that the value of Δt should be sufficient large in order to determine a threshold closer to the zero-crossing instant for which the time gradient is high. As it can be seen from Fig. 4.8 the slope of the back-EMF signal is increasing from 0 to $\frac{\pi}{2}$. In other words,

$$\frac{\mathrm{d}}{\mathrm{d}t}(e(t_1)) < \frac{\mathrm{d}}{\mathrm{d}t}(e(t_2)) \quad \text{if} \quad t_1 < t_2 \quad \text{for} \quad t_1, t_2 \in [0, \frac{\pi}{2}] \tag{4.28}$$

Hence, an optimal Δt has to be found. At high speed Δt should be tuned as low as the minimum value of Δt. This helps the algorithm to sample the back-EMF at a

high value and with a sufficient time gradient. Sampling near the zero-crossing at high speed, the time gradient turns out to be too large. To conclude, Δt is adapted to the speed by as follows:

$$\Delta t = \Delta t_{\text{min}} + t_a \quad , \quad t_a = \frac{K_a}{{\omega_r}^3} \tag{4.29}$$

Where Δt_{min} is the minimum Δt as given before and ω_r is the mechanical rotor speed and given in rpm. The parameter K_a is a constant and for the tested machine it is chosen to be 1.6×10^4 rad^3/s^2. For this value of K_a at 416 rpm operation speed $t_a = 2.22 \times 10^{-4}$s. This value for t_a is approximately 11% of the commutation period. For a higher speed such as 2000 rpm $t_a = 2 \times 10^{-6}$s. This value for t_a here is 0.5% of the commutation period. This method will result in a more accurate detection of the threshold-intersection and less sensitive to the measurement noises within the back-EMF signal.

4.3.5 Performance Analysis During Transients

During a rotor speed variation, the amplitude and the frequency of the back-EMF signal are both related to the value of the rotor speed ω_r. Assume that the behaviour of the phase back-EMF during an unexcited interval can be approximated by a cosine function as follows:

$$e(t) = K_e |\omega_r| \cos(\omega_r t) \tag{4.30}$$

Then the value of $e(t)$ at a specific time instant such as t_1 (where $t_1 = \Delta t_1$ as it is mentioned in Fig. 4.5) is equal to $e(t_1) = e_{\Delta t,1} = K_e |\omega_r| \cos(\omega_r t_1)$. If the speed value is considered to be constant, the intersection instant where the back-EMF value becomes equal to the threshold value $e(t) = -e(t_1) = -e_{\Delta t,1}$ will be reached at the time $\pi - \omega_r t_1$. However, if the speed changes after sampling $e(t_1)$, the intersection $e(t) = -e(t_1)$ will occur at $\pi - \omega_{r,\text{new}} t_1$. For an increase in the speed, with $\omega_{r,\text{new}} > \omega_r$, $e(t) = -e(t_1)$ will occur earlier than expected and vice-versa. It should be mentioned that an increase in the speed results in a sooner commutation instant. Hence, an advantage of this method is that by using this feature of the back-EMF signal, the error in the estimation of commutation instant always decreases compared to the conventional back-EMF zero-crossing method. During a variable speed operation, a significant error can occur in the commutation instant (e.g. when speed increases). Fig. 4.9 shows the significant difference in determining the accurate commutation instant in the proposed method and in the conventional method as explained earlier in this paragraph. Consider that the motor is at steady-state at time 0 a sudden speed drop occurs at the zero-crossing instant of the back-EMF. The back-EMF waveform changes from the light grey trace (with higher magnitude) to the darker trace (with lower magnitude) due to the reduction in the rotor speed. For the zero-crossing technique the determined

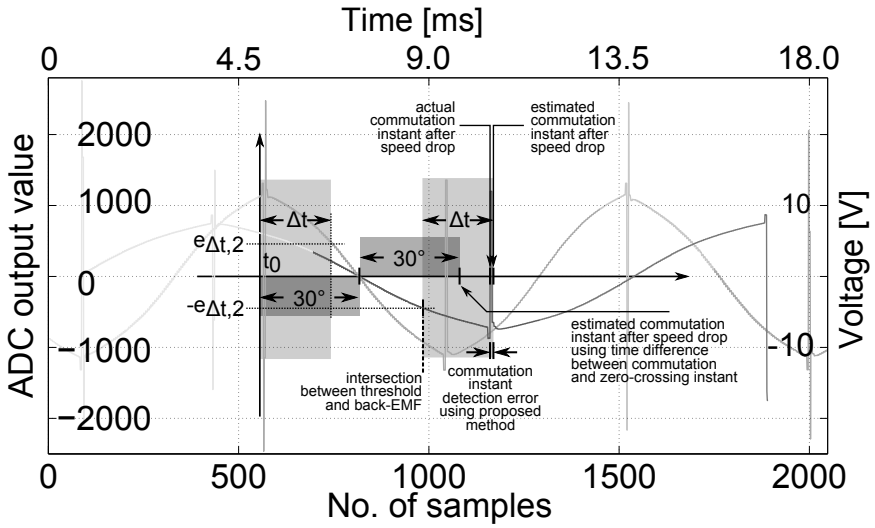

Figure 4.9. Comparison of the error in the commutation instants between the proposed method and a conventional back-EMF zero-crossing detection method, (back-EMF waveforms are measured from experimental tests)

30° (the time interval from t_0 to zero-crossing instant) is applied after zero-crossing event to determine the commutation instant. From Fig. 4.9 a large error can be observed between the actual and estimated commutation instants. However, for the threshold technique by a reduction in the speed the intersection occurrence instant is happening later that is resulting in a more accurate estimation of the commutation instant.

4.3.6 Measurement Techniques

A. Current Measurements

The current measurement for each phase is provided by sampling the DC-bus current only. The performance of using a single DC-bus current sensor in self-sensing drives has already been evaluated in [Carpaneto2012, DeBelie2012]. The value of the sampled current is assigned to the energized phases of the motor with respect to the direction of the current. The commutation sequence determines the direction of the speed. The sign of current then determines the semiconductor components conducting the phase currents.

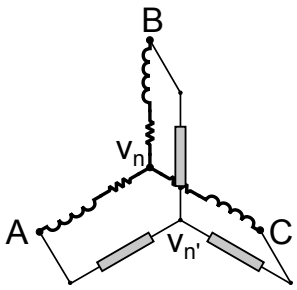

Figure 4.10. Virtual neutral point

B. Back-EMF Measurements

For all back-EMF based self-sensing methods, accurate and less noisy back-EMF measurement improves the drive performance [Lai2008, Lai2011]. If the back-EMF is measured directly between the unexcited phase terminal V_T and virtual neutral point V_n', every time a switching action occurs in the active phases, the potential change over active phases appears as voltage spikes on V_n'. On the other hand, measurements are also affected by grid frequency interferences. In the proposed method both the terminal V_T and virtual neutral point voltages V_n' are sampled referred to the negative DC-bus potential. By subtracting $V_T - V_n'$ most of the common mode voltages and spikes are cancelled out. To guarantee a smooth back-EMF during all operation conditions the sampling of the V_T and the V_n' is done synchronously with the PWM signal. Implementation of a virtual neutral point is illustrated in Fig 4.10. Fig. 4.11 shows a signal including the measure-

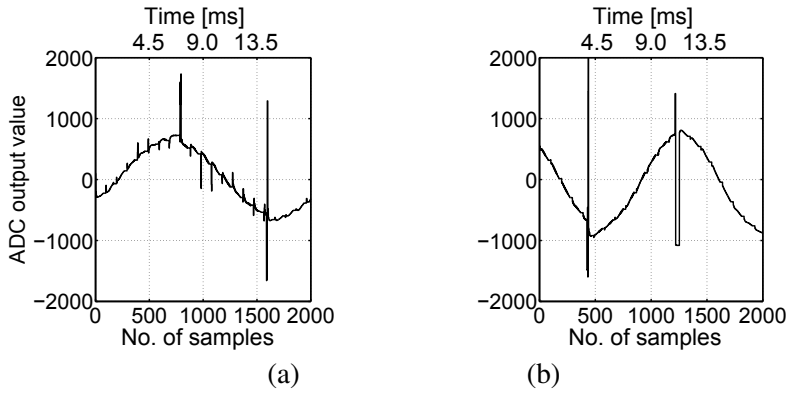

Figure 4.11. Measurement results, (a): independent sampling, (b): synchronous sampling with PWM

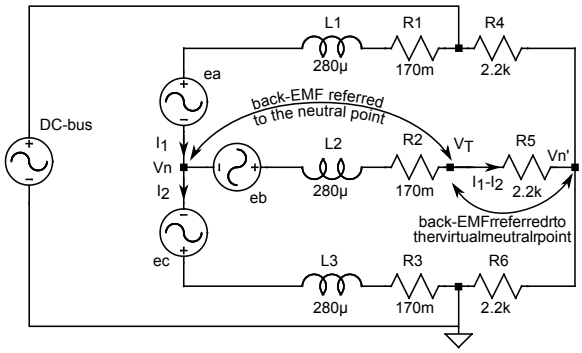

Figure 4.12. Electrical circuit used for simulation

ments of the phase voltages of a BLDC machine during their unexcited intervals. These signals contain useful information of the back-EMF for all three phases. In order to remove the effects of the switching actions, sampling instants are only chosen after a short clearance delay after the PWM switching action. For the measurement shown in Fig. 4.11(b) this delay equals 30μs which is sufficient to avoid sampling a switching transients.

A static circuit analysis is carried out to show the difference between the measurement of the back-EMF referred to the neutral point and referred to the virtual neutral point. The schematic is shown in Fig. 4.12. The back-EMF voltages referred to the neutral and to the virtual neutral points can be calculated using the following equations:

$$V_n = (R_s + L_s s)(I_2 - I_1) - e_c \quad , \quad s = j\omega \tag{4.31}$$

$$V_{n'} = R_5(I_1 - I_2) \tag{4.32}$$

where R_s and L_s are the stator resistance and inductance of the machine Fig. 4.13 illustrates the simulation results from LTSPICE software. The simulation results support the measurement results illustrated in Fig. 4.14. The spikes in Fig. 4.14 result from the current controller switching action which is not included in the static simulations. The grey areas in Fig. 4.13 and Fig. 4.14 show the phase unexcited intervals. From the simulation results, the zero-crossing instants are occurring at the same time for both measuring methods. Therefore, the zero-crossing of $V_T - V_n'$ can be used instead of $V_T - V_n$. The only difference is in the amplitude of the back-EMF voltage which has no effect on the proposed method neither on the conventional back-EMF zero-crossing based methods.

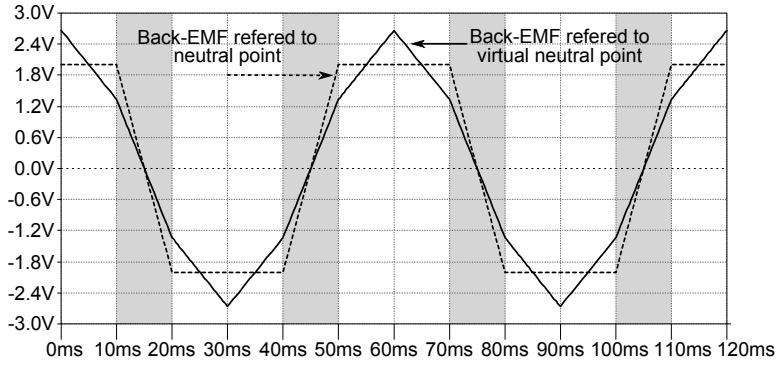

Figure 4.13. Simulated back-EMF waveform referred to the neutral point and referred to the virtual neutral point

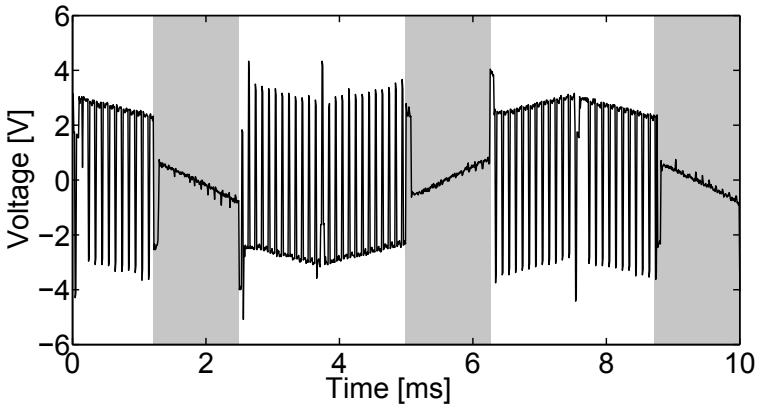

Figure 4.14. Experimental result, The terminal voltage of the self-sensing BLDC-machine drive. The back-EMF measurement intervals are indicated in grey

4.3.7 Simulations

Simulations are performed by using Matlab/Simulink and the BLDC machine simulation model is provided by PLECS® (a tool for high-speed simulations of power electronic systems). Using this tool allows modelling including cogging torque and higher harmonic components. Self-sensing commutation can be achieved within simulations at very low speed because of the availability of a noise free back-EMF signal measurement in simulation, but this is not possible in reality due to noise within the back-EMF samples. The maximum time step for discrete-time simulation within the speed and current controllers is chosen to be 10μs. The main goal is to control the speed of the BLDC machine in a relatively wide speed range

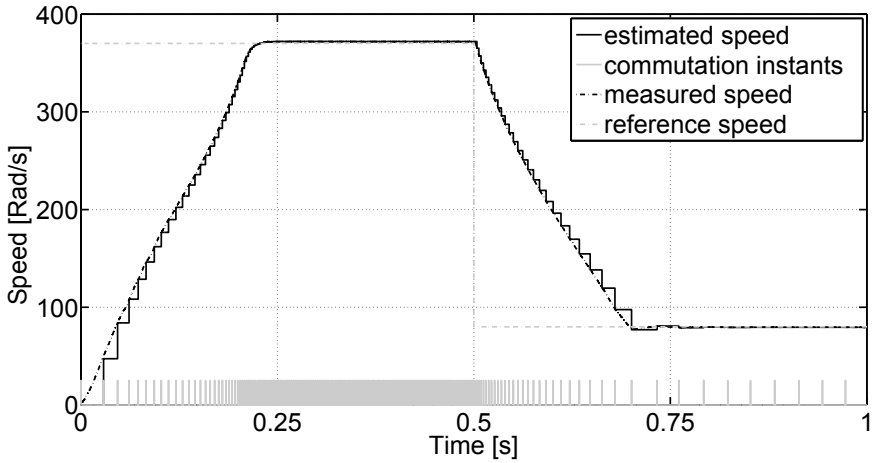

Figure 4.15. Simulation result, speed control: acceleration and deceleration

(from $0.33\omega_{r,\text{nom}}$ to nominal speed $\omega_{r,\text{nom}}$). Successful speed control can verify the application and transient performance of the proposed self-sensing method. A discrete-time PWM-PI-controller at a fixed frequency is implemented to control the current. The speed controller is a conventional discrete-time PI-controller. The speed controller is working at a variable sampling time based on the update frequency of the speed indirect measurement. Each time the speed value is updated the controller gives a new control command and holds it until the next speed update. The update of the back-EMF as well as of the speed is done by using the commutation instants. This means that the update of all parameters (e.g. position, speed, back-EMF and Δt) is done each 60° electrical position. Simulation starts with an open-loop startup scheme from zero to 10 rpm. After which the proposed closed-loop self-sensing technique is used until reaching the rated speed of the machine. Fig. 4.15 shows a simulation at no-load start-up, acceleration and deceleration. It can be seen that the motor can be driven smoothly both in transients as well as steady state using the proposed self-sensing method. Performance of the speed controller as well as the self-sensing method are examined with this simulation. It verifies the performance of the drive on sudden variations in the speed reference. Fig. 4.16 shows the operation of the threshold intersection together with the triggering of the commutation pulses. Notice the difference in time over the Δt. It should be mentioned that the back-EMF signal shown in Fig. 4.16 is generated by combining the back-EMF signals of three phases during unexcited intervals. The conduction sequence of the phases is determined by a switching pattern (which is generated by a finite-state machine). The main parameters of the machine used in simulations are presented in Appendix A.5.

The performance of the proposed self-sensing algorithm is evaluated in Fig. 4.17

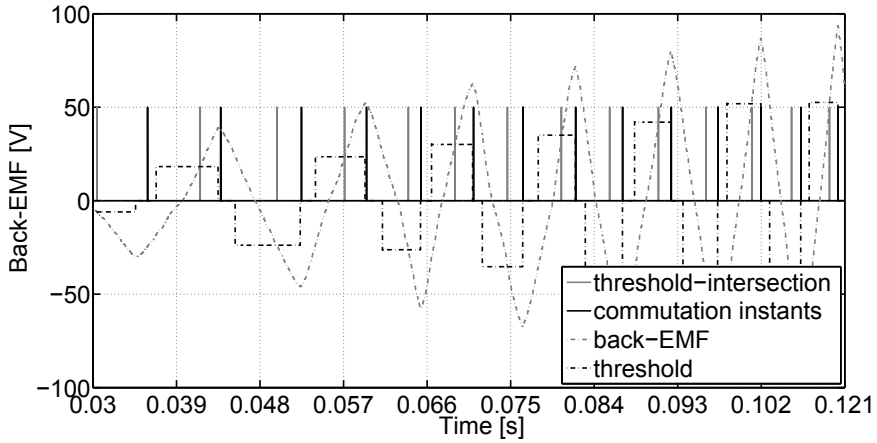

Figure 4.16. Simulation result, demonstration of the threshold-intersection instants of back-EMF and added Δt delay for generating real switching pulses during acceleration of the machine

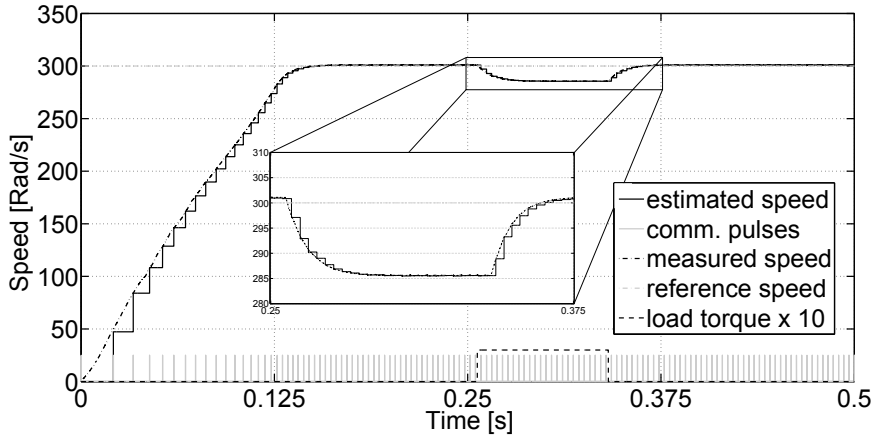

Figure 4.17. Simulation result, loading condition: loading and unloading with sudden load 3N.m

by applying a step load torque of 3Nm to the machine shaft. This load is removed after 0.1 s. In Fig. 4.18 a fan torque proportional to ω^2 is applied. The fan torque factor is tuned in such a way to reach the nominal load torque of the machine at its rated speed. These results verify the performance of the proposed method in loading and unloading conditions with different load torque.

In practice often an open-loop start-up sequence is used in order to start the ma-

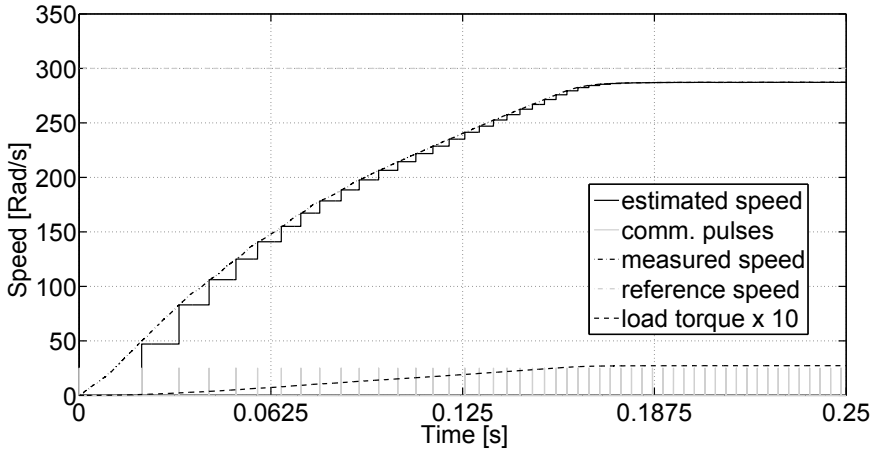

Figure 4.18. Simulation result, loading condition: start-up with fan load

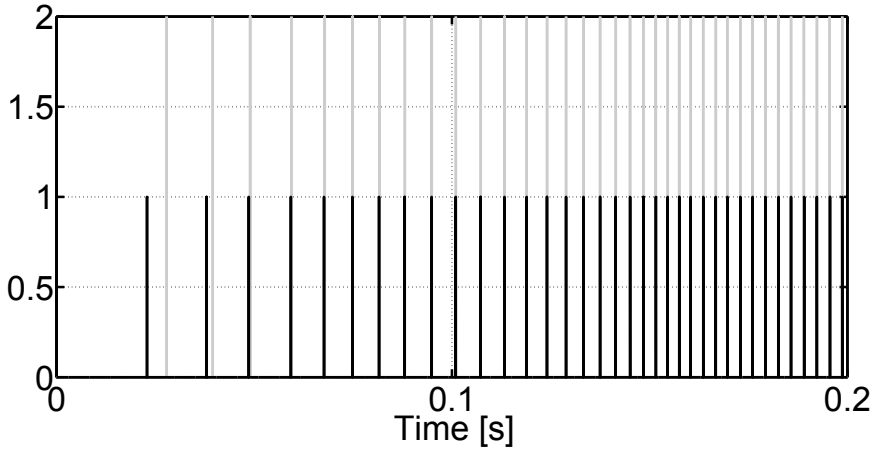

Figure 4.19. Simulation result, comparison of pulses generated by the proposed self-sensing method and correct switching pulses, (grey) commutation pulses generated by the proposed self-sensing method, (black) actual commutation pulses generated by position sensors

chines driven by the back-EMF based self-sensing methods. Fig. 4.19 gives the comparison between switching pulses determined by the proposed self-sensing method and the correct switching pulses. It can be seen that besides the first pulses generated at very low speed the estimated pulses are perfectly aligned with the correct ones.

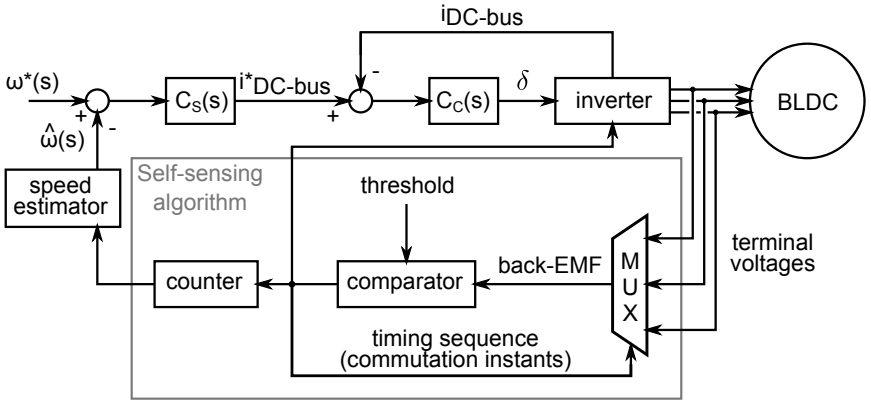

Figure 4.20. Self-sensing speed and current control diagram

4.3.8 Experimental Results

A. Steady-State Tests

A cascaded speed and current control loop is implemented to control the speed and current of the machine. The current controller is the inner control loop while the speed controller is the outer control loop. The control diagram is shown in Fig. 4.20 where $C_S(s)$ and $C_C(s)$ are the transfer functions of the speed and current controllers respectively. The speed controller does not use the actual speed of the machine, instead the speed is estimated using the terminal voltages and referred to as $\hat{\omega}(s)$. The reference speed is noted by $\omega^*(s)$. The speed error is used to compute a DC-bus current reference and the measured current of the inverter DC-bus is compared with the reference current. The current controller generates a duty ratio which is applied to the inverter PWMs corresponding to the excited phases.

The self-sensing algorithm uses terminal voltages of the machine to extract the back-EMF. By sampling the back-EMF a threshold is defined from which the commutation instants are generated. A counter is used to measure the time interval between successive commutation instants from which the rotor speed is estimated.

To verify the performance of the proposed method the internal states of the controller and drive are shown in Fig. 4.21. The machine is driven at no-load for a wide speed range without speed controller. Different speeds are achieved by varying the supply voltage. It can be seen how Δt varies during a variation of the speed. The back-EMF signal is shown in solid grey and the detected threshold in solid black line, The intersection of the threshold and the back-EMF signals are shown with dash-dot lines and the detected commutation instants by dotted lines. It must be

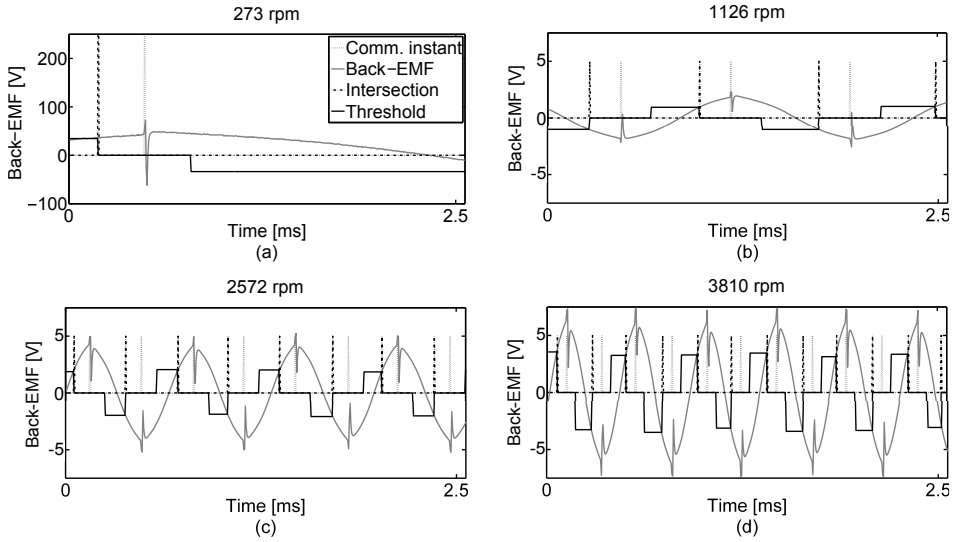

Figure 4.21. Experimental results, internal signals of the controller and measured value of the back-EMF for different rotation speeds

mentioned that in order to avoid unexpected commutations the intersection detection is disabled during the instants that the threshold value is zero. It can be seen from Fig. 4.21(a) and (b) at low speed operation a voltage spike on the measured back-EMF signals crosses the threshold signal which is set to zero. These spikes come from the residual currents in the commutated phases injected to the DC-bus through anti-parallel diodes of the inverter switches. Therefore, the threshold is set to zero and disabled as soon as an intersection is detected.

All variables in Fig. 4.21 are calculated within the FPGA hardware based on measured variables. The control performance of the proposed algorithm during steady state is plotted in Fig. 4.22(a) and (b). The speed controller is realised using a PI controller cascaded with the internal PI current control loop. The oscilloscope time is set to 1ms/div. Parameters of the machine are measured at two different speeds. For example phase U terminal voltage V_T, virtual neutral point voltage V_n' are measured both referred to the negative side of the DC-bus, $V_T - V_n'$ voltage and the phase V current. From Fig. 4.21 it can be seen that the speed and current controllers are working properly within the drive and the current and voltage signals are stable. The speed of the machine during each commutation period can be calculated using the time interval between two successive commutations and the number of poles of the machine. Parameters of the tested machine in this experiment can be found in Appendix A.2.

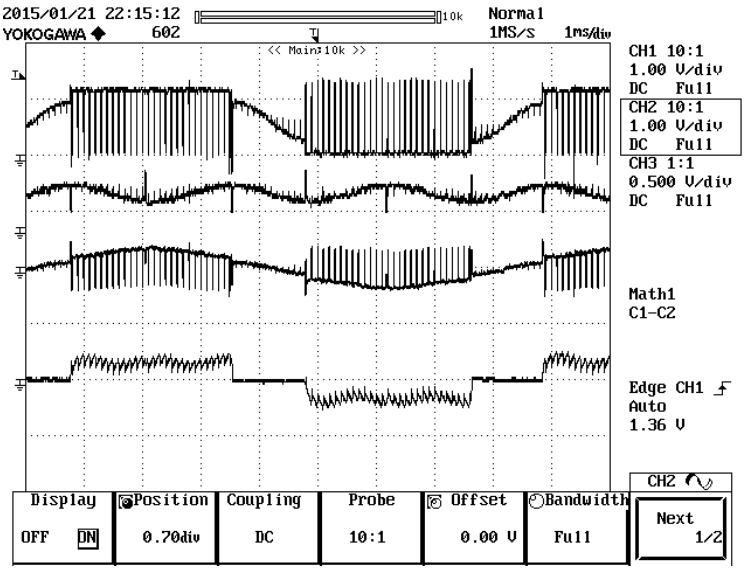

(a): the scales are 2.5 A/Div for current measurement and 2 V/Div for the voltage measurements

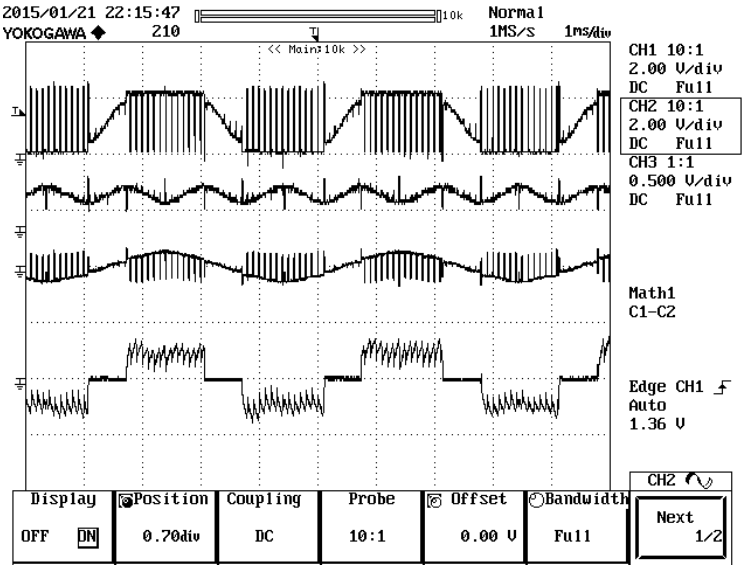

(b): the scales are 2.5 A/Div for current measurement and 4 V/Div for the voltage measurements

Figure 4.22. Experimental results, oscilloscope screen shot, speed control, the traces are terminal voltage (V_T), virtual neutral voltage (V_n'), $V_T - V_n'$ and phase current from top to bottom respectively. (a): $\omega_m = 500$ rpm and DC-bus current of $I = 0.8$ A, (b): $\omega_m = 1000$ rpm and DC-bus current of $I = 1.7$ A.

B. Transient Behaviour

Different tests are carried out to evaluate the transient behaviour of the proposed algorithm. The PI speed controller is tested for a uniform acceleration as well as step change in the rotor speed reference. The control scheme is shown before in Fig. 4.20. For the loading and unloading tests the machine is coupled with a second BLDC machine that acts as a generator.

Uniform Acceleration A triangular ramp speed reference is used and the machine is loaded with a frictional load. The results are plotted in Fig. 4.23 showing the speed and the value of Δt during the speed variation. The time Δt is shown by the number of clock pulses of the FPGA. (For example $\Delta t = 2\mu$s when the related signal shows the value of 10000). It can be seen that the speed is falling in the beginning of the measurement and after reaching to a certain speed the value of Δt is reduced to 7000 that is equal to 140μs and reduced one more time at 2500 rpm from 7000 to 5000. There are some oscillations around 2000 rpm which result from a resonance frequency of the machine and coupled load which are not quite precisely aligned.

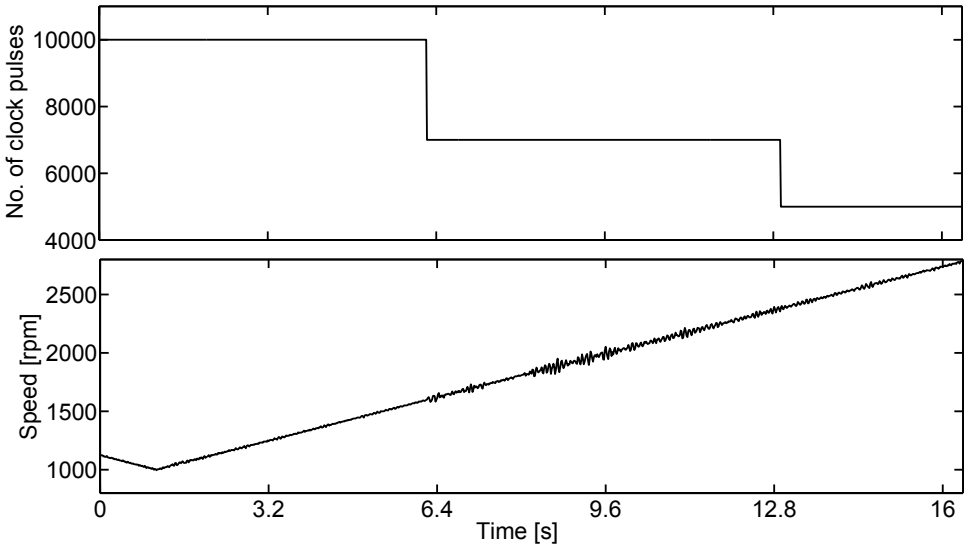

Figure 4.23. Experimental results, (top figure): Δt value, (bottom figure): Measured rotor speed of the machine for a ramp speed command

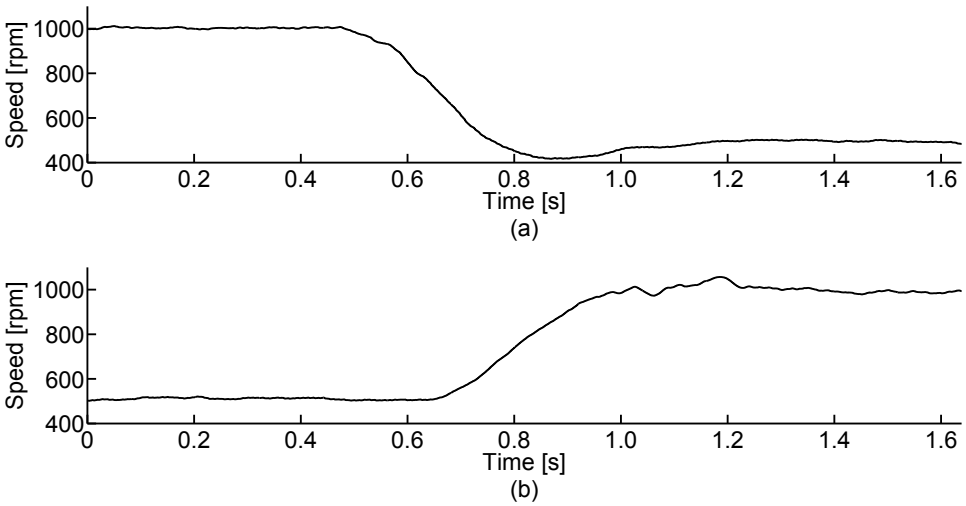

Figure 4.24. Experimental results, measured rotor speed due to a step change in the speed reference, (a): from 1000 rpm to 500 rpm, (b): from 500 rpm to 1000 rpm

Step Change in the Speed Reference The performance of the self-sensing algorithm is also tested during step changes of the speed reference. A load torque proportional to the speed is used for this test. The speed set point can change between 500 rpm and 1000 rpm. The gains of the speed and current PI controllers have been tuned in an heuristic way. The proportional and integral gains of the speed and current controllers are $G_{S,p} = 6.6 \times 10^{-5}$, $G_{S,i} = 1 \times 10^{-5}$, $G_{C,p} = 5 \times 10^{-3}$ and $G_{C,i} = 2.5 \times 10^{-3}$ respectively.

The speed variations are shown in Fig. 4.24(a) and (b) for a step change from 1000 rpm to 500 rpm and from 500 rpm to 1000 rpm respectively. The measured speed controller bandwidth is approximately 1Hz. The gains of the PI speed and current controllers are tuned to have a fast speed response an overshoot of 15% can be seen in the speed response.

Loading and Unloading The performance of a drive during loading transients is one of the main characteristics of a drive system. This performance is evaluated using a proper setup including a mechanical load torque. In order to see the effects of the loading and unloading on the rotor speed, the speed controller is disabled in this set of tests. In this way the effects of transients are studied with special attention to the self-sensing detection of the commutation instants without the effects of the speed controller. The current controller is kept active in order to protect the machine against over current and possible demagnetization of the rotor magnets. Fig. 4.25 shows a snapshot of the oscilloscope screen. As it can be seen from this

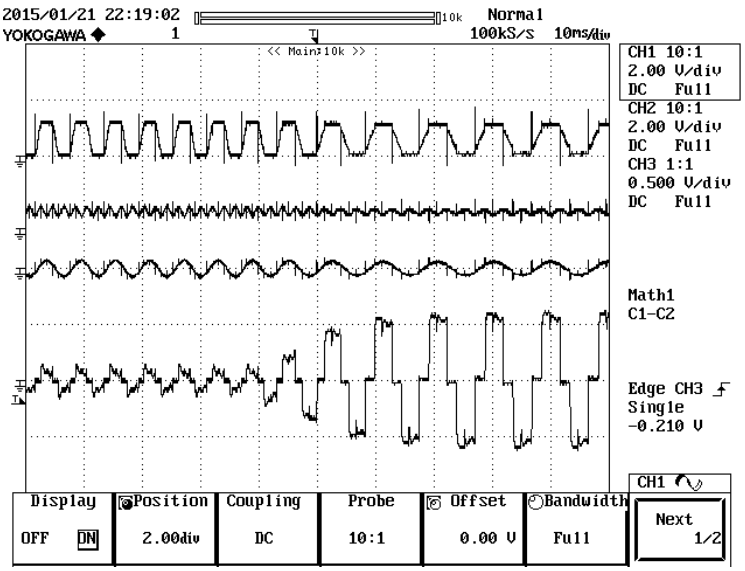

(a): the scales are 2.5 A/Div for current measurement and 4 V/Div for the voltage measurements

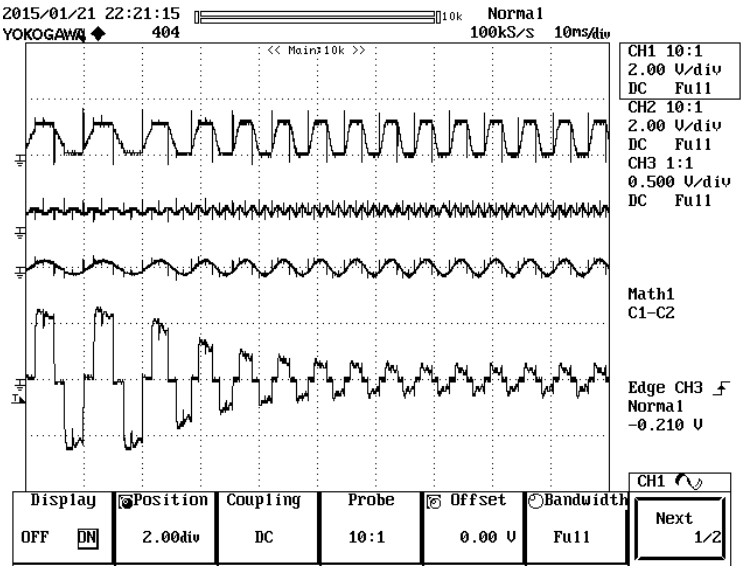

(b): the scales are 2.5 A/Div for current measurement and 4 V/Div for the voltage measurements

Figure 4.25. Experimental results, oscilloscope screen shot, traces from top to bottom: terminal voltage V_T, virtual neutral point voltage V_n', $(V_T - V_n')$ and phase current i, (a): loading transients (rotor speed and phase current during the loaded condition are $\omega_m = 470$ rpm and $I = 2.6$ A), (b): unloading transients (rotor speed and phase current during the no-load condition are $\omega_m = 765$ rpm and $I = 0.4$ A)

figure the proposed method results in successful current commutation during the loading and unloading cases. From the upper traces it can be seen that the commutation occurs at the correct instants as a symmetric trapezoidal waveform measured at the terminal voltages (upper traces in Fig. 4.25(a) and (b)).

4.4 Rotor Speed and Position Estimation Based on Successive Back-EMF Samples

In the previous section a self-sensing method is proposed referred to as the symmetric-threshold-tracking method. It is an enhanced estimation method based on the monitoring of the back-EMF signal. As discussed before for a safe and stable operation a maximum limit for the applied load torque should be defined for the self-sensing algorithm to determine the minimum value of Δt parameter. In this section the theoretical background of speed and position estimation methods based on back-EMF measurement will be discussed. The method that will be presented in this section uses the idea of tracking a threshold and utilizes the rotor speed information to overcome the complexities of the technique described in 4.3 such as determining the maximum and minimum values of Δt. The simulation and experimental results will be presented in Chapter 5 together with the results of the load torque estimation and will be discussed in detail.

4.4.1 Speed and Position Estimation from the Back-EMF Measurements

To estimate the speed and position, the back-EMF is measured firstly. The method to obtain a reliable back-EMF measurement has been explained in detail in Section 4.3. The back-EMF measurements contain information about both the electrical position θ_e (through $F(\theta_e)$) and the speed ω. An estimation of the speed is obtained by comparing the value of the measured back-EMF for successive samples $e[k-1]$ (measured back-EMF at sample $k-1$) and $e[k]$ (measured back-EMF at sample k). Starting from (3.5), the following equations can be derived from $\Delta e[k] = e[k] - e[k-1]$ and linearisation

$$\begin{aligned}\Delta e[k] &= K_e(F(\theta_e[k]) - F(\theta_e[k-1]))\omega[k] + K_e F(\theta_e[k])(\omega[k] - \omega[k-1]) \\ &= K_e m_L(\theta_e[k] - \theta_e[k-1])\omega[k] + K_e F(\theta_e[k])(\omega[k] - \omega[k-1]) \quad (4.33)\end{aligned}$$

where m_L is the slope of the linear part of the back-EMF signal. $\Delta\theta_e[k]$ can be written in terms of speed as $T_s\omega[k]$. Here T_s is the time between two back-EMF measurements (back-EMF sampling time). By considering a small T_s compared to the mechanical time constant of the machine an approximation of $\Delta e[k]$ can be

derived from (4.33) as follows:

$$\Delta e[k] = K_e m_L T_s \omega^2[k] + K_e F(\theta_e[k])(\omega[k] - \omega[k-1]) \tag{4.34}$$

It is assumed that at the instant of the back-EMF measurement in the unexcited phase, the electrical angle θ_e is in the linear part of $F(\theta_e)$. Furthermore, assuming $\tau_m \gg \tau_e$ mechanical and electrical time constants of the machine, the rotor speed variations can be neglected in (4.34) ($\omega[k] \approx \omega[k-1]$). We then obtain the following equation to estimate the rotor speed at sample time k:

$$\hat{\omega}[k] = \sqrt{\frac{e[k] - e[k-1]}{K_e m_L T_s}} \tag{4.35}$$

From this estimation and the back-EMF measurement $e[k]$ it is possible to get an estimate of the value of the function F at sample time k:

$$\hat{F}(\theta_e[k]) = \frac{e[k]}{K_e \hat{\omega}[k]} \tag{4.36}$$

As there is a one-to-one relationship between F and θ_e, an estimate of F implies an estimation of the rotor-position, $\hat{\theta}_e[k]$.

As it is mentioned in Section 3.2, the function $F(\theta_e)$ determines the back-EMF waveform as a function of θ_e. The parameters $\hat{\omega}_m$, $F(\theta_e)$ and θ_e are all dependent on the voltage constant K_e. Important factors that influence K_e are related to the machine design such as number of turns, parallel branches of the windings and the flux of the permanent magnets. However, we may assume that a variation of $\pm 15\%$ in the back-EMF constant K_e is common. For instance, we suppose the temperature dependence of the back-EMF to be included in K_e. Hence, if (4.35) is used for speed estimation in the drive, the temperature change will affect the precision of the speed estimation. However, during the simulations, the value of K_e is assumed to be exact. While in the experimental implementation, as the value of K_e can change related to the temperature of the machine, (4.36) is used for calculation of F but for the speed control we have used a speed estimation technique based on the measurement of the time interval between successive commutations which is not dependent on the temperature and K_e. As F is defined as a function of $\hat{\omega}$ and K_e, it depends on the temperature changes as well. The sensitivity of $\hat{\omega}$, F, to the parameter K_e is evaluated later in Chapter 5.5.

4.4.2 Simulation Results of Rotor Speed and Position Estimator

The simulation results of the speed and position estimation from the Back-EMF measurements will given in Section 5.2.1. It will include the load torque estimation, discussed in Chapter 5.

4.4.3 Experimental Results of Rotor Speed and Position Estimator

A. Evaluation of the Speed Estimation

A speed controller is implemented on an FPGA platform using the speed information provided by the speed estimation algorithm. The speed set point is programmed to change between 100, 150, 1000 and 1500 rpm. A PI controller is used to reduce the speed error by generating a proper set value for the current. The maximum value for current is set to 2.5 A. The current set point is compared with the measured DC-bus current and its error is reduced using a second and faster PI controller. The output of the current PI controller is compared with a sawtooth signal to generate the switching pulses for inverter switches. The frequency of the sawtooth signal determines the PWM frequency which is 10 kHz in this study. Phase current, DC-bus current and related phase voltages of a BLDC machine are illustrated in Fig. 4.26(a). For very high or very low duty ratios, Fig. 4.26(b) a technique is implemented which is called *Alternating-Edge-Sampling*. It provides switching noise immunity described in [VanDeSype1999].

The gains of the PI controllers are tuned in a heuristic way. The speed controllers gains are set to:

$$K_{p,\omega} = 1 \times 10^{-5}$$
$$K_{i,\omega} = 0.5 \times 10^{-5}$$

the inner current controller loop gains are:

$$K_{p,i} = 1 \times 10^{-3}$$
$$K_{i,i} = 18 \times 10^{-3}$$

Different tests have been carried out to evaluate the performance of the interaction of the speed estimation and the speed controller. Fig. 4.27(a) demonstrates the speed estimation and speed control results at steady-state condition. When a BLDC machine operates at very low speed the developed torque has the same variable content as the back-EMF of the machine. Theoretically 15% torque ripple at lower speeds is always present. Another cause of speed ripple is due to the very low inertia of the system which makes the tuning of the PI controller difficult for a wide speed range. Fig. 4.27(b)shows the dynamic results while applying a sudden change to the speed set point. As it can be seen in Fig. 4.27(a) and (b) it is possible to control the machine at very low speeds (eg. 100 or 150 rpm) by using the proposed self-sensing algorithm. The characteristics of the speed control (rise time, overshoot and etc.) performance can be easily changed according to the application demands.

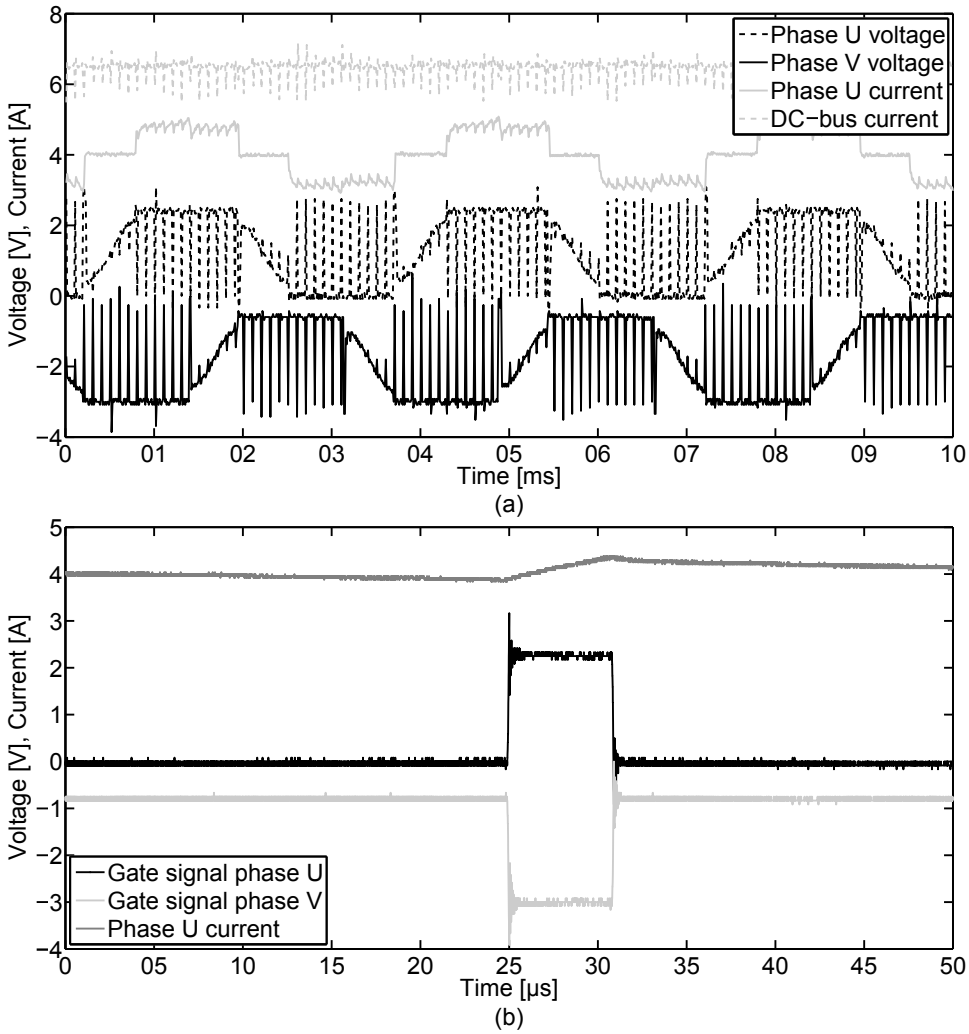

Figure 4.26. Experimental results, measured values of a BLDC machine with trapezoidal back-EMF waveform, (a): terminal voltages v_U, v_V referred to the negative side of the DC-bus, Phase current measured using current probe and DC-bus current measured using shunt resistor which is used for current control, (b): very short pulse (the current is measured using a current probe)

Bandwidths of the Controllers In order to determine the bandwidth of the current and speed controllers experimentally, the following procedure can be used.

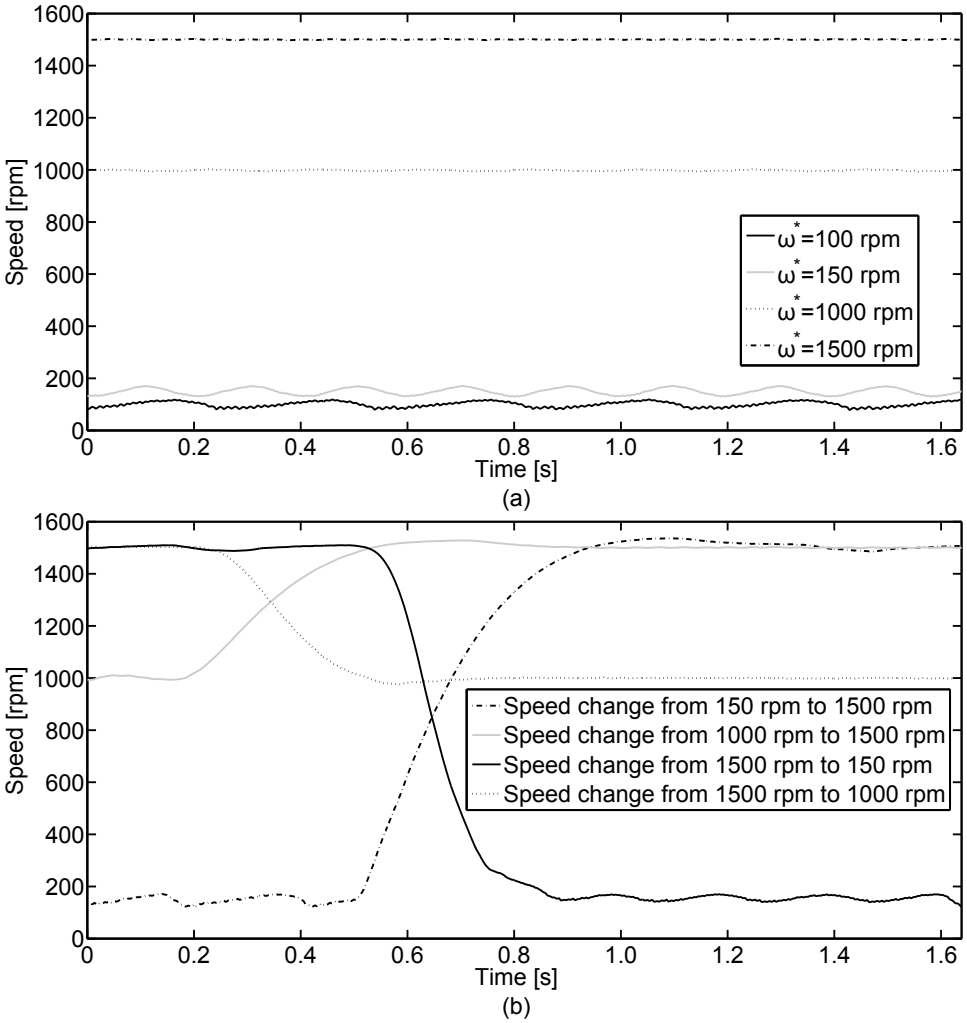

Figure 4.27. Experimental results, speed estimator and controller, (a): steady-state, (b): different speed set points

The general exponential step response of a first order system can be written as:

$$V(t) = V_F - (V_F - V_I)e^{-t/\tau} \tag{4.37}$$

Where V_I, V_F are the initial and final values of the system output for a step change in the input and τ is the system time constant. The bandwidth f_{BW} can also be

written in terms of the time constant τ as

$$f_{BW} = \frac{1}{2\pi\tau} \tag{4.38}$$

Rise time t_r is defined as the time for the output to rise from 10% to 90% of its final value. Subtracting the following term

$V_F + 0.1(V_F - V_I) = V_F - (V_F - V_I)e^{-t_{10}/\tau}$

from $V_F + 0.9(V_F - V_I) = V_F - (V_F - V_I)e^{-t_{90}/\tau}$ the relation between f_{BW} and t_r is

$$f_{BW} = \frac{0.35}{t_r} \tag{4.39}$$

Using (4.39) and Fig. 4.27(b) the bandwidth of the speed controller is approximated by 1.75 Hz. The gains of the speed and current controllers are tuned in a way to have a fast speed response. Using the same approach the bandwidth of the current controller is approximated by 230 Hz.

B. Evaluation of the Rotor Position Estimation

The rotor position estimator and the corresponding self-sensing method are implemented for the Maxon Motors BLDC machine as well as three other machines with different back-EMF profiles. The Maxon machine is equipped with Hall sensors (specifications of the machines are in Appendix A.1). The position estimator requires a division of the measured back-EMF and the estimated rotor speed. A division of two variables can be implemented in the System Generator programming environment using the CORDIC DIVIDER block from the Xilinx Reference Blockset.

For this BLDC machine driven using Hall sensors and a converter supplied by a DC-bus voltage of 2.8 V, the measured terminal voltage U of the machine is illustrated Fig. 4.28. In this figure, two successive commutation instants are indicated by arrows. The back-EMF voltage at the first commutation instant is approximately equal to the supply voltage of 2.8 V. The back-EMF value at the second mentioned commutation instant is approximately 0.4 V lower than that at the first mentioned commutation instant. It can thus be noted that the machine is not driven with the maximum possible efficiency due to a misalignment of the Hall sensors to the PM rotor field.

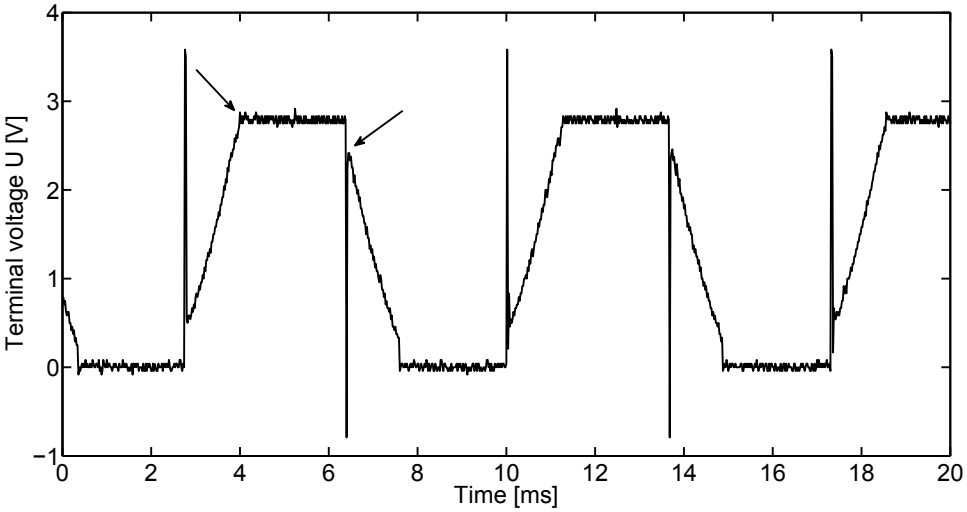

Figure 4.28. Experimental result, measured terminal voltage U referred to the ground of the power stage when the machine is driven with a voltage of 2.8V, using the Hall sensors to drive it

The open-circuit back-EMF waveform of the Maxon BLDC machine is measured on its terminals by driving it by a second machine. The line-to-line back-EMF is recalculated to the phase back-EMF by dividing the amplitude by $\sqrt{3}$. The resulting phase back-EMF is given in Fig. 4.29. The machine has a more sinusoidal line-to-line back-EMF than a trapezoidal one. The correct and incorrect conducting intervals are indicated by a dashed and a dash-dot line, respectively. In the situation where there is an incorrect commutation timing, the absolute value of the back-EMF at successive commutation instants is different. An inaccurate commutation timing results in a stator current which is not in phase with back-EMF waveform. The sensors could have been aligned in this way to have good performance for a specific loading conditions. However, this results in an inefficient operation during other operating conditions.

Figs. 4.28 and 4.29 point out one of the disadvantages of using the Hall sensors. They allow to drive the machine, however not always in an optimal way. A better performance of the machine is obtained when using the self-sensing commutation methods proposed in this chapter. The terminal voltage of phase U for the same machine is given in Fig. 4.30 when the machine is driven using the self-sensing method presented in Section 4.4. The absolute value of the back-EMF at successive commutation instants is approximately the same.

The same test is done one more time with another machine and the results are

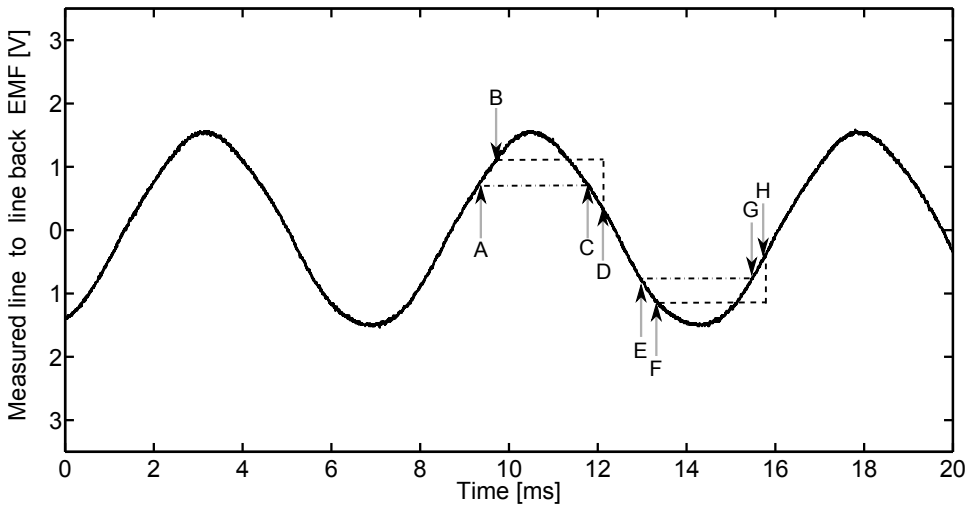

Figure 4.29. Experimental result, measurement of the phase back-EMF. The correct conducting intervals are indicated by a dash-dot line (A, C, E and G). The conducting intervals using the Hall sensors are indicated by a dashed line (B, D, F and H)

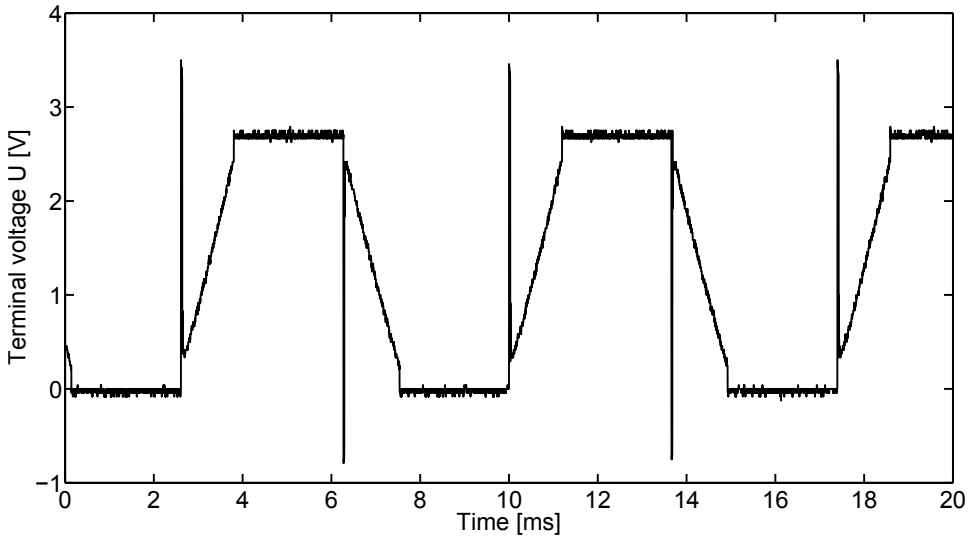

Figure 4.30. Experimental result, the measured terminal voltage U referred to the ground of the power stage when the machine is driven with a voltage of 2.8V, using the self-sensing algorithm to drive it

plotted in Fig. 4.31. The first evaluation criterion for any BLDC self-sensing algorithm is to determine the performance of the commutation instant estimation.

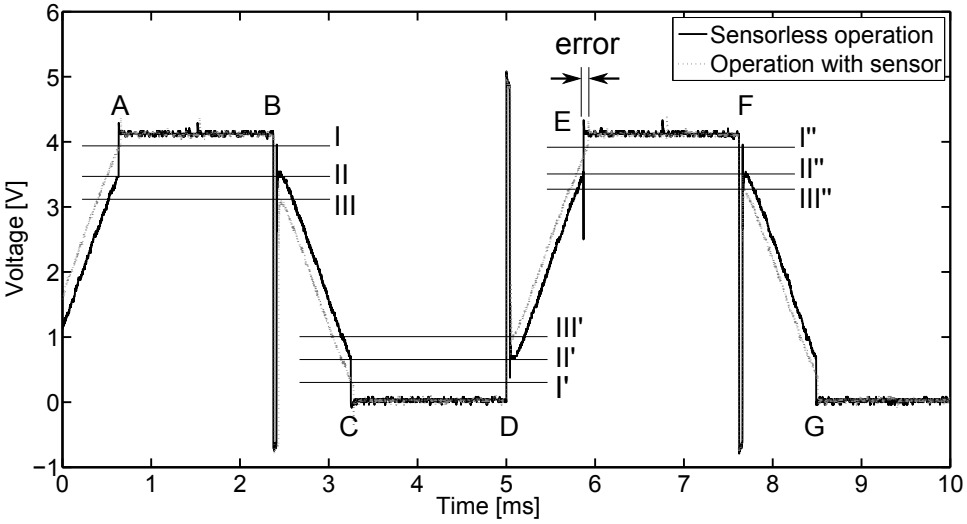

Figure 4.31. Experimental result, the voltage levels indicated by II, II′, II″ show the back-EMF voltage at commutation instants for the black trace using the proposed self-sensing algorithm. The grey trace is the back-EMF signal of the same machine but driven by Hall-effect sensors and it can be seen that the level of two successive commutations are not equal (I,III or I′,III′ or I″,III″)

Measurement results from Figs. 4.30 and 4.31 show that the self-sensing method has better performance in detecting the exact commutation instant compared to the Hall sensors. Fig. 4.31 compares the terminal voltage of the machine while working in steady-state condition with two different commutation methods: first, self-sensing operation, second, operation with Hall sensors. By comparing the values of the back-EMF signal at instants of successive commutations, it can be seen that the commutations occur at almost equal back-EMF voltage trajectory (level II for instants A and B, II′ for C and D, II″ for E and F) during the self-sensing operation. However, during operation with the Hall-effect sensors, commutation occurs with a time error compared to the optimal commutation instant. In commutation instants A, C and E the back-EMF voltage value is at levels I,I′ and I″ and at the next commutation instants B, D and F the back-EMF voltage is at quite different levels III, III′ and III″. The error in the commutation instant detection while using sensors comes from little misalignment of the sensors. The effect of this misalignment is a reduction in the generated electromagnetic load torque. For the same supply voltage, the measured speed for the self-sensing operation was 1433 rpm with a supply current of 556 mA and for the operation with sensors it was 1425 rpm and 570 mA. This means that, by having better commutation it will be possible to produce more output power with less input

power.

An accurate commutation instant detection improves the BLDC drive performance in two ways:

- **By decreasing the torque ripple**: If the commutation occurs at the optimum instant, the electromagnetic torque ripple will be minimized.
  - Lower torque ripple decreases the vibrations of the drive system.
  - Another effect of the lower torque ripple is the lower audible noise.
- **By increasing the efficiency**: According to the equation $T_{em} = \frac{3|e|.|I|}{\omega_m}$ the electromagnetic torque in a BLDC machine is proportional to $|e|.|I|$. By an accurate commutation the current and the back-EMF waveforms will be in-phase resulting in a more efficient performance of the machine.

C. Tests on Different Machines with Different Back-EMF Profiles

The back-EMF of a BLDC machine has been considered as a trapezoidal function (3.6) in simulations. However, in practice, it can vary between a trapezoidal and a sinusoidal waveform. The proposed algorithm has been tested with BLDC machines regardless of their back-EMF waveform profiles and the results are illustrated in Fig. 4.32. The algorithm is adapted to the different motors by modifying the parameter K_e. Different control characteristics is observed for the different machines because the parameters of the controllers are not tuned for each. For example by fine tuning the current controller for each machine a smooth back-EMF signal can be obtained from $V_T - V_n'$ trace for the cases (c), (d) and (e) as it is done for the case (a).

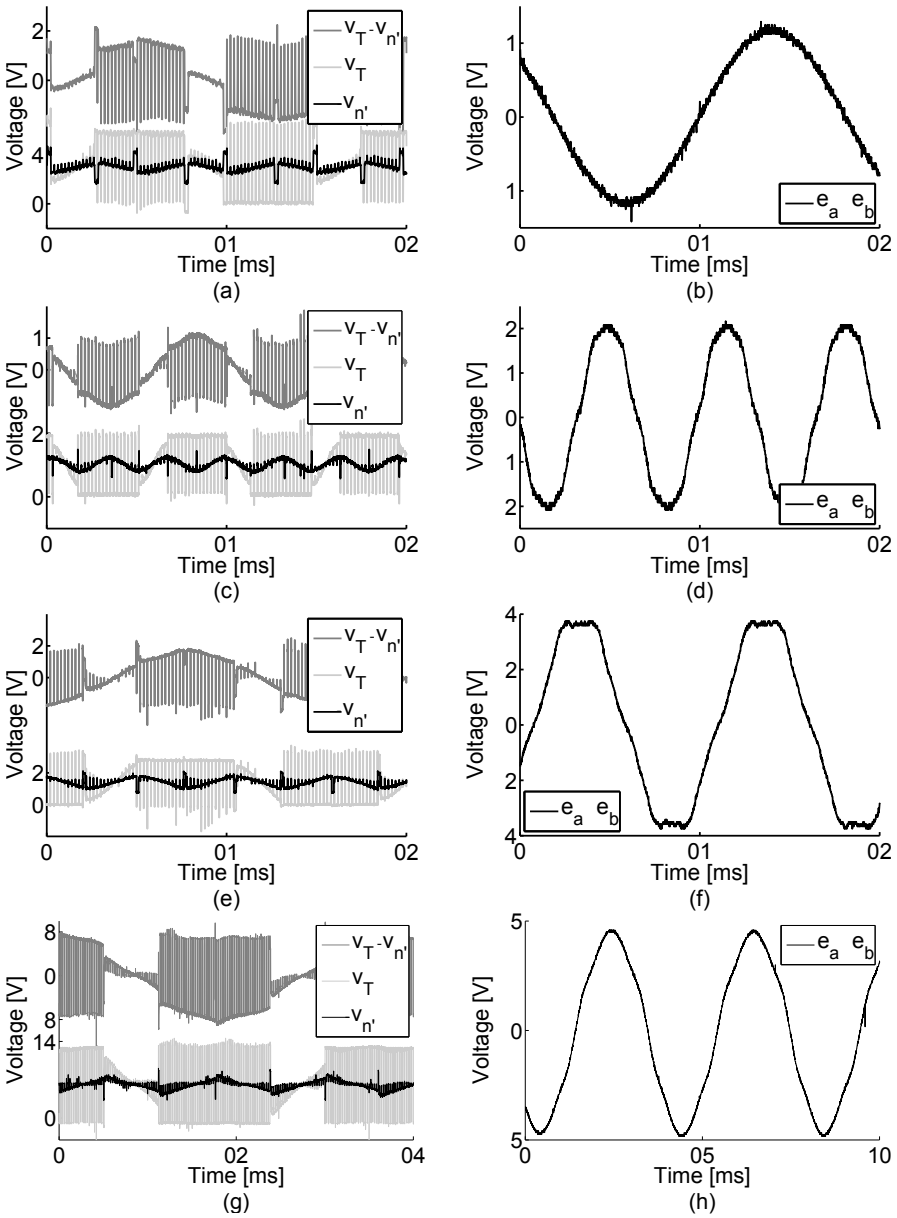

Figure 4.32. Experimental results, measured values of BLDC machines with different back-EMF waveforms, (a,c,e and g): voltages V_T, V_n' referred to the negative side of the DC-bus and $V_T - V_n'$, (b,d,f and h): line-to-line (coupled) back-EMF waveform measured in generator mode (Specifications in Appendix A)

D. Evaluation of the Behaviour of the Self-Sensing Commutation Algorithm During a Load Transient

When driving a BLDC machine, it is important that commutation instants are skipped. To test this in dynamical circumstances, A BLDC machine is loaded by mechanically coupling it to another BLDC machine. The results are shown in Fig. 4.33 where the commutation state sequence resulting from the self-sensing method is compared with the results from the Hall sensors. The load torque is applied to the motor at 22 ms after starting the measurement. The Hall effect sensors produce a reliable commutation state which can be used as a benchmark for the proposed self-sensing commutation algorithm. The switching sequence of the Hall sensors is shown in grey.

With every change of the commutation state determined by the Hall sensors, there should be a corresponding change of the switching state determined by the self-sensing method. In Fig. 4.33, it can be observed that this is indeed the case. Furthermore, it can also be noticed that the commutation sequence determined by the self-sensing method leads that determined by the Hall sensors at all times. This is due to the inaccurate positioning of the sensors that is studied before in Section 4.4.3.B.

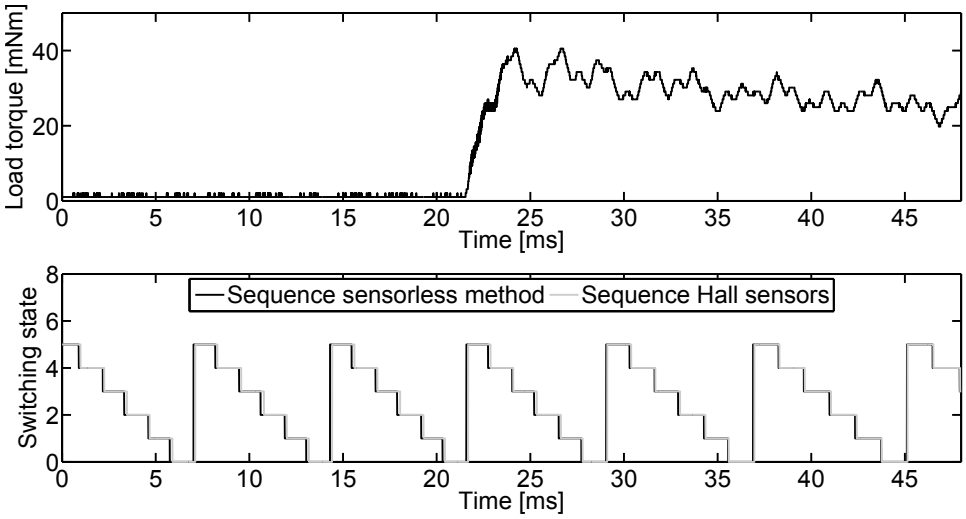

Figure 4.33. Measurement results, (upper figure): load torque variation, (lower figure): commutation states resulting from the self-sensing method and resulting from the Hall sensors is given in

Even though the provided Hall sensors allow to detect missing steps from the switching sequence, they do not allow to investigate the accuracy of the commutation instants computed by the self-sensing method. This is due to the misalignment of the Hall sensors on the stator of the machine. Because of the misalignment, the optimal commutation instants differ from those determined by the sensors. From the back-EMF measurement in Fig. 4.28, it follows that the length of each conduction interval is correctly determined by the Hall sensors as 60° non-conducting – 120° conducting positive current – 60° non-conducting – 120° conducting negative current for each phase. It can be concluded that the three Hall sensors are shifted from the correct position on the stator of the machine by the same angle. This error angle was calculated to be 7.422° electrical. This implies that in steady state, there will be a fixed time error between the commutation instants determined by the Hall sensors and the optimal commutation instants. The self-sensing method is capable of keeping the switching instants closer to the correct switching instants in steady-state ($\approx 0^\circ$ error). There is only a small influence of noise in the speed estimation. This can be verified by the back-EMF waveform as was depicted in Fig. 4.31.

The performance of the self-sensing detection of the commutation instants during steady state and transient state is studied using an encoder (specifications in Appendix B.5). The encoder that is used here has a high resolution (20,000 pulses per revolution) and permits to verify the correctness of the commutation timing under different conditions. To test this, the Maxon Motor BLDC machine is loaded with an square wave load torque with a period of 400 ms. The commutation timing will be investigated in two situations: when the external load torque is applied to the machine, and when the load torque is removed.

The commutation sequence that is determined by the Hall effect sensors and the one that is determined by the self-sensing method when the load torque is applied are given in Fig. 4.34. The commutation sequence that is determined by the self-sensing method leads the sequence that is determined by the Hall sensors by 7.422° (the error of the Hall sensors) during steady-state as mentioned before. The electrical angle between these two is denoted by ϕ shown in Fig. 4.34 (bottom). In steady-state, ϕ was determined to be 7.422° indicated by a dashed line. When the load torque is applied, ϕ falls to approximately 5°. After 10 ms, the angle ϕ evolves back to 7.422° later.

The switching sequence determined by the Hall sensors and that determined by the self-sensing method for decreasing load are shown in Fig. 4.35. The angle ϕ is also shown in this figure. It can be observed that the angle ϕ now stays around its steady-state value of 7.422°, i.e. there is no visible effect of the decreasing load torque on the commutation timing. This points out that the deviating ϕ in Fig. 4.34 could be due to noise in the speed estimation.

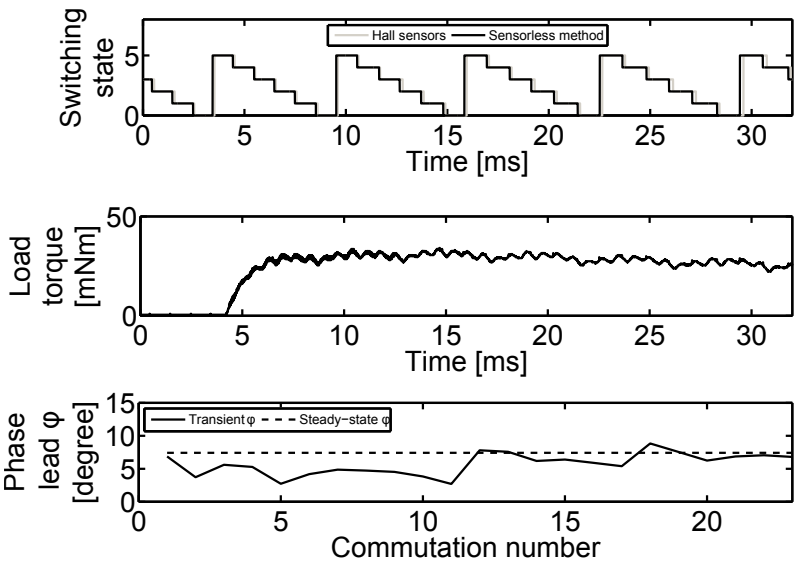

Figure 4.34. Experimental results, (top): Measurement of the switching state, (mid): the external applied load torque and (bottom): the phase lead angle ϕ when the machine is loaded

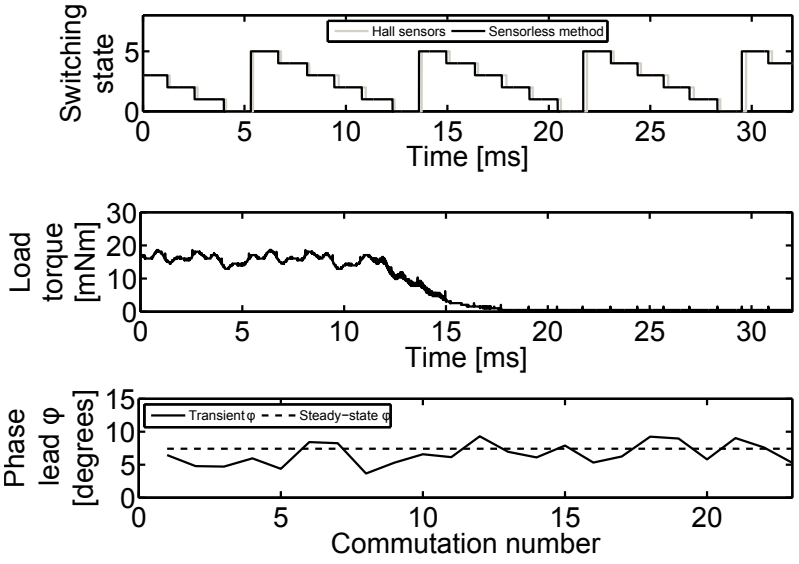

Figure 4.35. Experimental results, (top): Measurement of the switching state, (mid): the external applied load torque and (bottom): the phase lead angle ϕ when the machine is unloaded

4.5 Open-Loop Behaviour of Back-EMF Based Self-Sensing BLDC Drives

Brushless dc machines (BLDC machines) are often used in low cost applications where speed control can be obtained by using a low resolution rotor position sensor only. This sensor, such as based on an array of Hall sensors, indicates the moments at which the stator current should commutate between stator phases, [Miller1989]. Steering the stator current amplitude determines the electromagnetic torque and hence the acceleration of the rotor to a new speed that can be sensed by the position sensor also. Setting the current amplitude is often done by using a power converter in which semiconductor switches are steered. By computing a set value for the switch duty ratio, the dc input voltage is chopped to deliver a steerable stator voltage.
In modern BLDC drives, self-sensing methods are used to replace the position sensor, [Acarnley2006]. Whereas the requirement on the resolution of such methods is low (six-step commutation: 60 electrical degrees), the accuracy required in detecting the correct current commutation instants is much higher (several degrees to less than 1 degree depending on torque, speed and inertia). Even a small phase misalignment of the current waveform with respect to the back-EMF waveform will result in a reduction of electromagnetic torque generation, Fig. 4.36. Such reduction can be compensated for by increasing the stator current amplitude as is often done by adding a speed control loop to the drive. Nevertheless, it would be of interest to study methods that detect the commutation instants sufficiently accurate, avoiding the requirement of an increase in current amplitude and corresponding Joule losses.

To discuss the feasibility of self-sensing methods in detecting the commutation instants accurate, in this section, the open loop behaviour of such drives is studied in which the stator current amplitude is held constant. Note that the open-loop stability study in [Wu2014] is different as a V/f strategy is applied instead. Stability of speed controlled BLDC machines is discussed in [Tashakori2012]. We focus our study towards methods wherein the commutation instants are detected by measuring or observing the speed-induced back-EMF. The reduction in electromagnetic torque due to wrongly estimated commutation instants and the effect on the speed and hence commutation instants will be discussed. In the next section, the torque reduction will be studied first as a function of the estimation error in the commutation instants. Then the equation of motion is taken into account to compute the speed variation as a consequence of this torque reduction and the resulting variation in the current commutation instant. To conclude this study, the variation of the rotor speed will be considered as a method to determine regions of zero acceleration. It will follow that such regions depend on inertia, speed and torque as well as on the self-sensing method chosen.

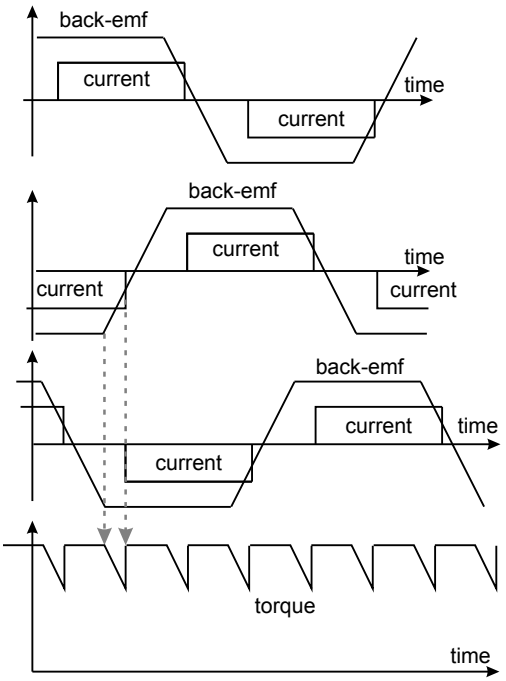

Figure 4.36. Incorrect current commutation instants result in torque loss

4.5.1 Behaviour of Back-EMF Self-Sensing Methods

A. Rotor Speed Variations

Consider a BLDC machine with a trapezoidal back-EMF waveform as function of the rotor position when driving at constant rotor speed, Fig. 4.36. In a single period of the back-EMF waveform, two successive zero-crossing moments t_n and t_{n-1} can be detected. In a zero-crossing back-EMF based self-sensing method, these successive zero-crossing moments are used to compute the moments to commutate the current from one phase to another. The time difference between two successive zero-crossing moments is given by $T_n = t_n - t_{n-1}$. The average rotor speed taken over a time between these two zero-crossing moments is then given by

$$\widehat{\omega}_n = \frac{\pi/3}{T_n}, \tag{4.40}$$

as the angular difference in rotor position between two succeeding crossing moments is given by $\pi/3$ electrical radians and where $\widehat{x}_n$ denotes the average of the variable x_n over the time between two zero-crossing moment t_n and t_{n-1}. As the

rotor speed changes, a speed step $\Delta\widehat{\omega}_n$ can be observed in the average rotor speed at each zero-crossing moment t_n:

$$\widehat{\omega}_{n+1} = \widehat{\omega}_n + \Delta\widehat{\omega}_n. \tag{4.41}$$

Between periods, the following relation holds:

$$T_n\widehat{\omega}_n = T_{n-1}\widehat{\omega}_{n-1} = \pi/3,$$

or

$$T_n = T_{n-1}\big(1 - \frac{\Delta\widehat{\omega}_{n-1}}{\widehat{\omega}_n}\big) \tag{4.42}$$

giving the period duration T_n as a function of the previous period duration T_{n-1}.

B. Torque Loss in a Zero-Crossing Self-Sensing Method

In a back-EMF zero-crossing based self-sensing BLDC drive, the time difference between past back-EMF zero-crossing moments is used to compute the next current commutation moments. Using previous zero-crossing moments to detect a future current commutation moment, a prediction time error $\Delta T = 0,5 \cdot (T_n - T_{n-1})$ is made in the next current commutation moment when the rotor speed ω is varying. When the current commutation moment is shifted in time over ΔT from the correct moment, a lower average electromagnetic torque will be generated. Indeed, when introducing a time shift ΔT, a phase current flows when the rotor flux coupled with the stator winding decreases. As the instantaneous torque is proportional to the product of this flux and current, a decrease in the average torque can be noticed as well. As a result of a time shift in the commutation instant from the correct moment, the generated torque is reduced by, Fig. 4.37,

$$\Delta T_n^{em} = -\frac{\widehat{T}^{em}}{2}\frac{1}{\pi/3}\int_0^{\Delta T}\frac{\theta}{\pi/6}\mathrm{d}\theta \tag{4.43}$$

where the time shift in the commutation instant

$$\Delta T = \frac{1}{2}(\widehat{\omega}_n T_{n-1} - \pi/3) \tag{4.44}$$

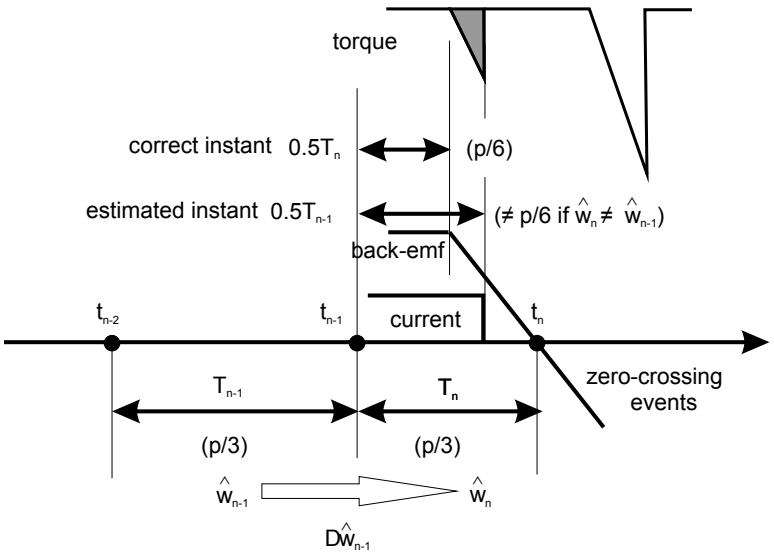

Figure 4.37. Torque loss during sensorless operation using back-EMF zero crossings

and where $\widehat{T}^{em}$ denotes the average electromagnetic torque generated when current commutates at the correct moments. Solving this integration results in

$$\Delta T_n^{em} = -\frac{9\widehat{T}^{em}}{8\pi^2}(\widehat{\omega}_n T_{n-1} - \pi/3)^2. \tag{4.45}$$

Using (4.40) and (4.41), this torque drop can be written as function of variables at the previous period $n-1$

$$\Delta T_n^{em} = -\frac{9\widehat{T}^{em}}{8\pi^2}\Delta\widehat{\omega}_{n-1}^2 T_{n-1}^2. \tag{4.46}$$

The torque drop results in a speed variation $\Delta\widehat{\omega}_n$ computed from the equation of motion

$$\Delta T_n^{em} = J\frac{\Delta\widehat{\omega}_n}{T_n}. \tag{4.47}$$

Combining the two previous expressions and by using (4.42) as well, the speed variation during two succeeding zero-crossing moments t_{n-1} and t_n of the back-EMF is given by

$$\widehat{w}_n = \frac{T_n}{J\widehat{\omega}_n}\Delta T_n^{em} = -K_0\frac{\widehat{w}_{n-1}^2}{(1-\widehat{w}_{n-1})^2}, \tag{4.48}$$

where the factor

$$K_0 = \frac{\pi}{24} \cdot \frac{T^{em}}{J\widehat{\omega}_n^2} \tag{4.49}$$

depends on mechanical quantities only and where $\widehat{w}_n = \Delta\widehat{\omega}_n/\widehat{\omega}_n$ is the per unit rotor speed. A region can now be defined to which the speed difference $\widehat{w}_n$ should be bounded. As, for a given K_0, (4.48) is a monotone function of $\widehat{w}_{n-1}$, a zero average rotor acceleration can be guaranteed when the next speed difference $\widehat{w}_n$ remains smaller than the previous one $\widehat{w}_{n-1}$. This condition is given by the dashed line in Fig. 4.38 wherein (4.48) is shown as well for $K_0 = 1000$. When $\widehat{w}_n$ is higher than this dashed line, speed increases continuously at a nonzero acceleration as is illustrated by the grey arrows.

C. Torque Loss in Back-EMF Symmetrical Tracking Sensorless Methods

To estimate the next current commutation instant more accurately, a measurement e of the back-EMF is used additional to the back-EMF zero-crossing instants. In most BLDC drives, and during intervals of 60 electrical degrees, one phase is without current excitation. During such open-circuit intervals the phase back-EMF can be observed directly at the phase terminal by using a voltage probe. An estimation of the next current commutation instant can be made by considering the negative of the sampled back-EMF as discussed in [Darba2015b]. To avoid measuring switching transients in the back-EMF, this voltage is measured at an instant $\alpha T_{n-1}/2$ before the zero-crossing, Fig. 4.39. The sampled magnitude is again observed after the zero-crossing at a moment $\alpha T_{n-1}\widehat{\omega}_{n-1}/\widehat{\omega}_n$ taking into account the possible speed variation over time. Starting from this instant and assuming steady-state operation, the next commutation instant occurs after a time $(1-\alpha)T_{n-1}/2$. To conclude, the estimated commutation instant counted from the last back-EMF zero-crossing instant is given by

$$\frac{\widetilde{T}_n}{2} = \big(\alpha\frac{\widehat{\omega}_{n-1}}{\widehat{\omega}_n} + (1-\alpha)\big)T_{n-1}. \tag{4.50}$$

Computing the torque drop is done by using the previous estimation and by adapting accordingly the upper integration limit in (4.43) to

$$\Delta T = \frac{1}{2}(\widehat{\omega}_n\big(\alpha\frac{\widehat{\omega}_{n-1}}{\widehat{\omega}_n} + (1-\alpha)\big)T_{n-1} - \pi/3) = \frac{1-\alpha}{2}(T_{n-1}\widehat{\omega}_{n-1} - \pi/3), \tag{4.51}$$

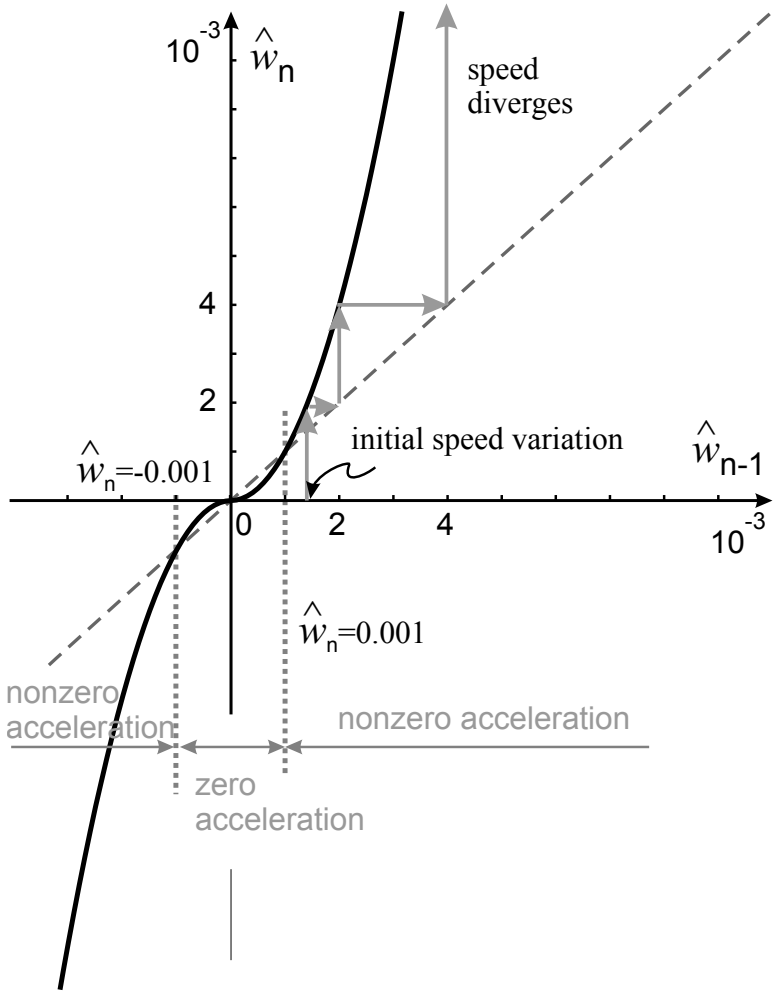

Figure 4.38. Speed variations by using (4.48) at $\widehat{\omega}_n = 500$rpm and $T^{em} < 0$

hence resulting in a reduction in torque loss compared to the zero-crossing method over $(1-\alpha)^2$. As a result, the characteristics (4.43) describing the behaviour of a zero-crossing method, shown in Fig. 4.40 as a function of $\widehat{w}_n$ and for different values of K_0, decrease, meaning the robustness of the sensorless method against speed variations increases. This is illustrated in Fig. 4.40 also. Applying $\alpha = 0.5$ means that K_0 reduces to a quarter of its former value. As an example, it can be seen in this figure that for $K_0 = 400$ at $\alpha = 0$ the stability region extends from $\widehat{w}_n = 0.25\%$ to $\widehat{w}_n = 1.1\%$ when increasing α to 0.5. It is observed that values for α close to one are of interest. Nevertheless, such a value means sampling the back-EMF close to a commutation moment, hence introducing switching noise in

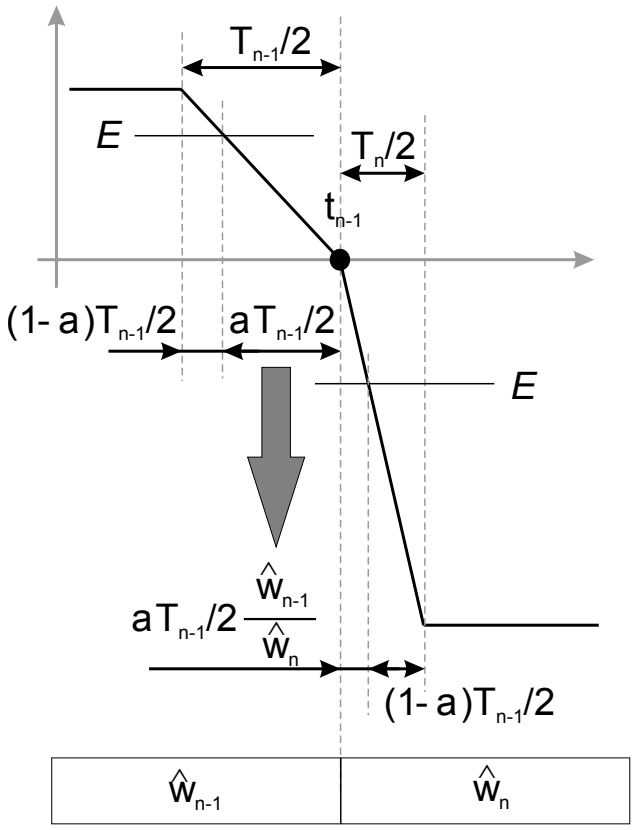

Figure 4.39. Symmetrical back-EMF tracking self-sensing method

the sample. Moreover, as speed drops can occur, the value of α should be sufficient different from one, [Darba2015a]. Hence, a trade off has to be made, for instance by using $\alpha = .5$.

4.5.2 Simulation Results

The control scheme used to simulate the behaviour of the open-loop self-sensing BLDC drive is shown in Fig. 4.41. From the voltages measured at the terminals of the three-phase machine, the voltage is taken that corresponds to the open-circuited phase. This voltage equals the back-EMF and is used to estimate the current commutation moments. With the observation that the zero-crossing self-sensing method is a particular case of the symmetrical threshold tracking method wherein $\alpha = 0$, the aforementioned methods can be described by the same control scheme. Besides the commutation moments, the set value for the stator current is

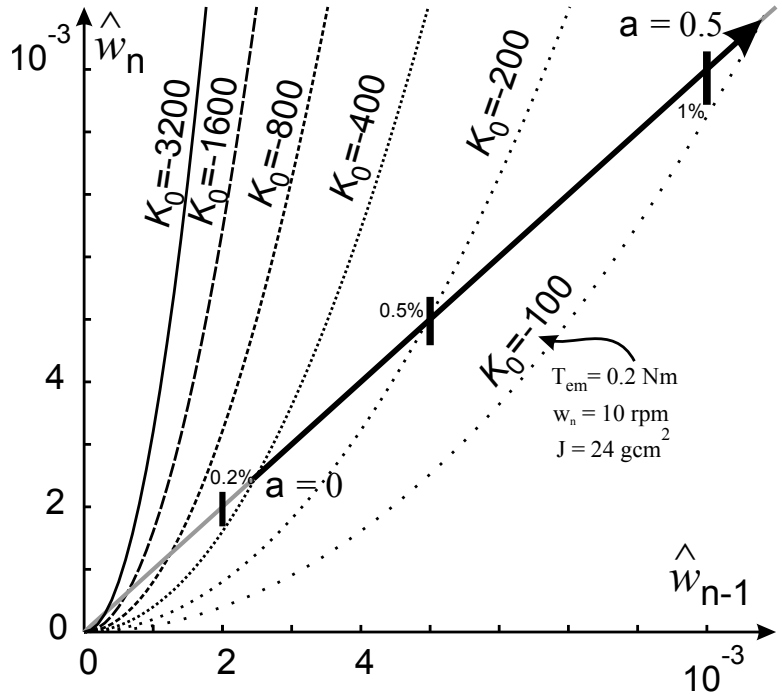

Figure 4.40. Stability regions by using (4.48) for different K_0

given to the power converter steering module. For the simulations, the current is generated by a current source inverter and time delays in generating the current are neglected. The BLDC machine shown in Fig. 4.41 is used in generator mode. It rotates at a negative speed of -500 rpm and is driven by a second motor at a constant positive torque, independent of the rotor speed in order to keep the stator current amplitude constant. The inertia of the system is assumed low, 25 gcm^2. The time simulation in Simulink^{TM}/Matlab^{TM} is started with position sensors and at a certain moment (after 0.5 s) the self-sensing method is activated, replacing the position information of the sensors by estimations. After each simulation run, the average speed $\widehat{\omega}_n$ is computed by postprocessing the simulation results.

A. Zero-Crossing Back-EMF Self-Sensing Method

For $\alpha = 0$, and hence for the zero-crossing self-sensing method, the speed difference $\Delta\widehat{\omega}_n$ and speed $\widehat{\omega}_n$ are shown in Fig. 4.42 for $K_0 = 1000$. The speed difference is given for succeeding periods, each period bounded in time by succeeding zero-crossings in the three-phase back-EMF waveform. By using simulations and assuming sensors are used (before 0.5 s), zero differences $\Delta\widehat{\omega}_n$ in speed are ob-

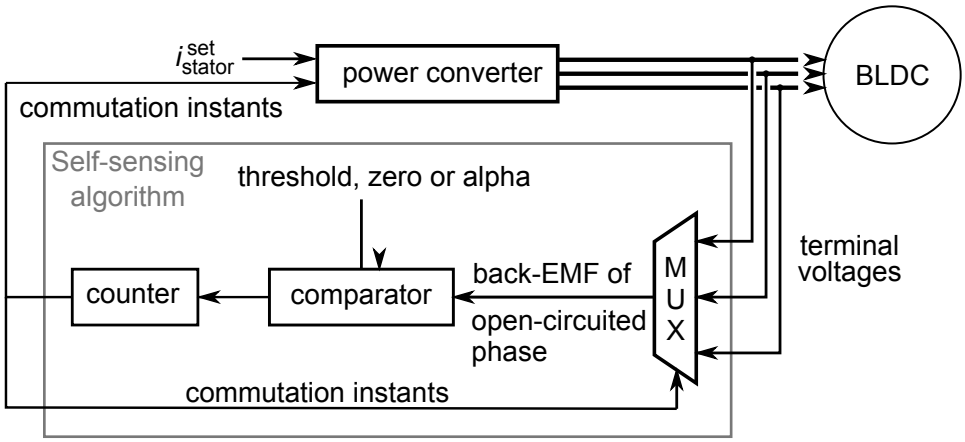

Figure 4.41. Control scheme of BLDC machine with back-EMF self-sensing method

served as all is modelled ideal. When activating the self-sensing method (after 0.5 s), the detection algorithm of the zero-crossing moments in the back-EMF introduces small time delays within the simulation, acting as distortions in the estimated commutation moments. Indeed, when activating the self-sensing method after 70 periods ($n \geq 70$), a nonzero speed difference $\Delta\widehat{\omega}_n$ can be observed that stays within the stable region of 0.51 rpm that can be derived from Fig. 4.38 at 500 rpm. As the speed control loop is open, a slow varying drift in the rotor speed can be observed however at a rate that can be compensated for by a speed control loop with a low bandwidth (several 10 Hz). However, in the case the speed difference $\Delta\widehat{\omega}_n$ has crossed the threshold of 0.51 rpm, Fig. 4.43 the torque of the generator decreases too much as a result of estimation errors in the commutation instants and the rotor speed changes more rapidly at a nonzero acceleration as is shown from period n=102 in Fig. 4.43.
Note, in case the speed differences are within the boundaries set by the threshold it is expected that any speed difference $\Delta\widehat{\omega}_n$ reduces to zero when considering the analytical expression (4.48) or Fig. 4.38. Nevertheless, simulations show nonzero speed differences all times as the source of these speed differences remains, such as discretisation of the machine model in Simulink over time as well as quantification of signals, small time delays and interpolation of samples.

B. Back-EMF Symmetrical Tracking Self-Sensing Method

With a back-EMF symmetrical tracking self-sensing method the value of K_0, for a given speed, torque and inertia is a factor $(1-\alpha)^2$ lower than for a zero-crossing self-sensing method. A reduction of K_0 corresponds with a higher threshold for

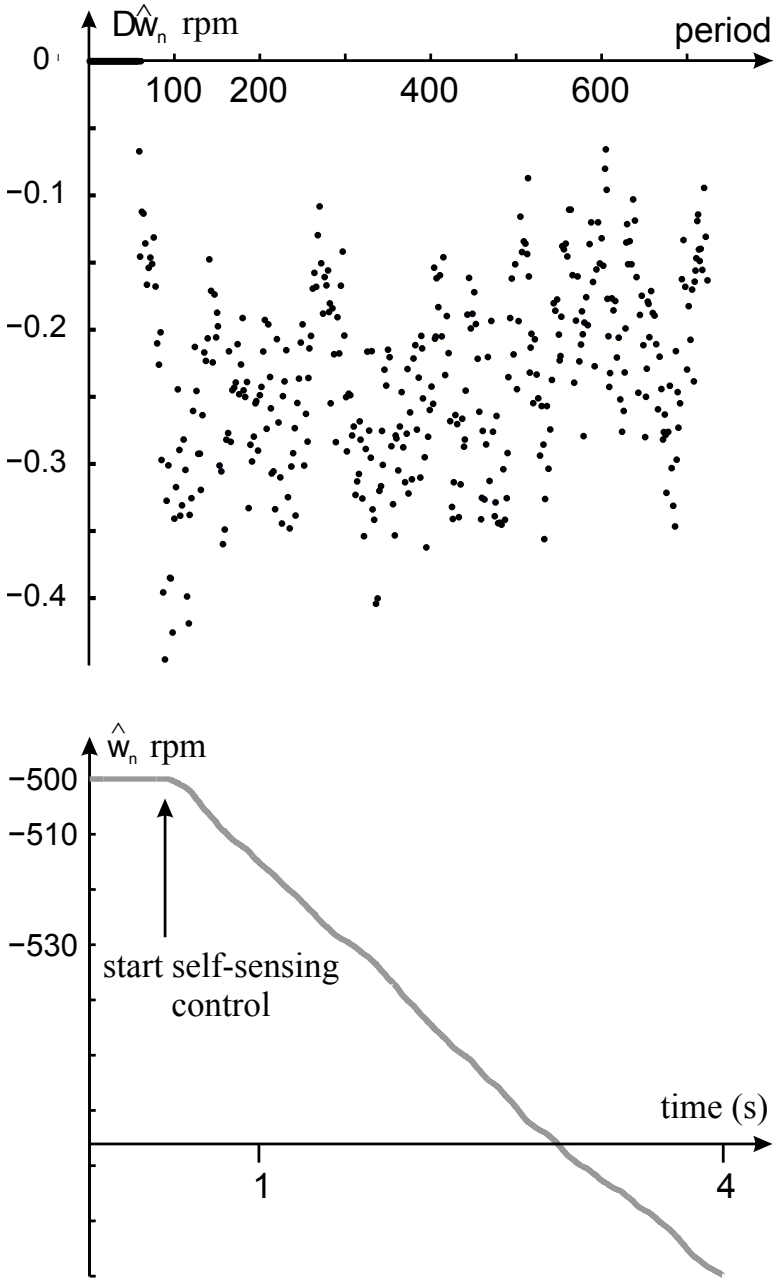

Figure 4.42. Simulation results at $\widehat{\omega}_n = 500$rpm for zero-crossing method: rotor speed differences stay within the region of stability of 0.51 rpm

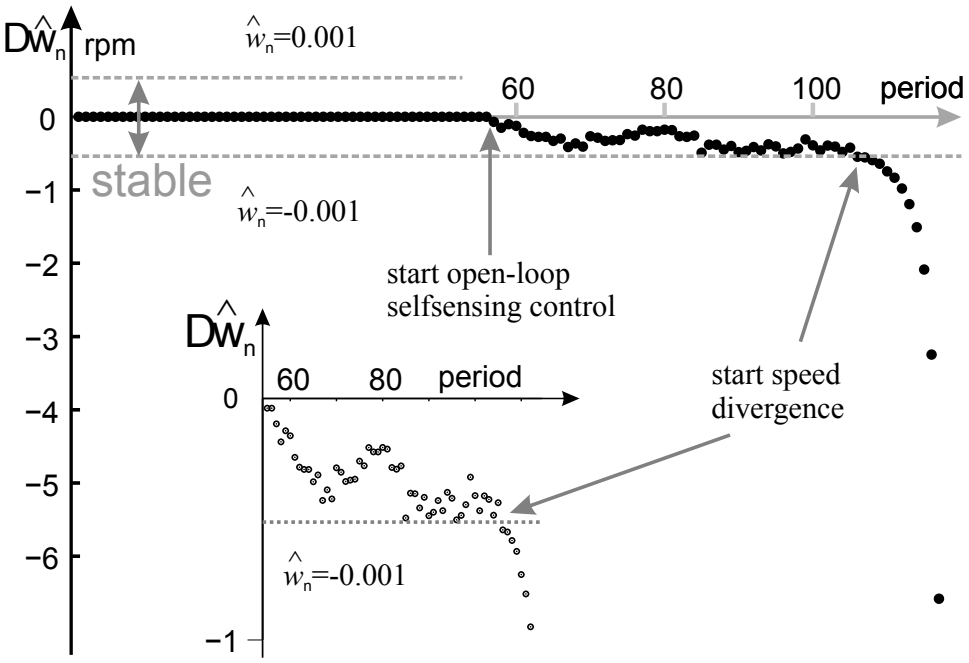

Figure 4.43. Simulation results at $\widehat{\omega}_n = 500$rpm for zero-crossing method: rotor speed diverges when crossing the region of stability of 0.51 rpm

the speed difference above which this difference starts to diverge. For $\alpha = 0.2$, and for the same torque, speed and inertia as used to obtain Fig. 4.43, the speed differences stay within the new threshold limit of 0.825 rpm. Fig. 4.44 shows results for this case: this time, speed differences are used higher than the threshold of 0.51 rpm as computed for the zero-crossing method but lower than 0.825 rpm valid for the symmetrical tracking self-sensing method with $\alpha = 0.2$. From this simulation it follows that by using a symmetrical threshold tracking method the robustness against speed variations increases. This means also that the effort of a speed control loop to keep the BLDC drive operation stable is lower when using the threshold tracking method.

4.6 Conclusions

Conventional self-sensing commutation methods based on the back-EMF signals are widely used in different industrial and low-power applications with their own drawbacks. Two enhanced self-sensing commutation method based on the back-EMF measurement are proposed in this chapter and the theoretical

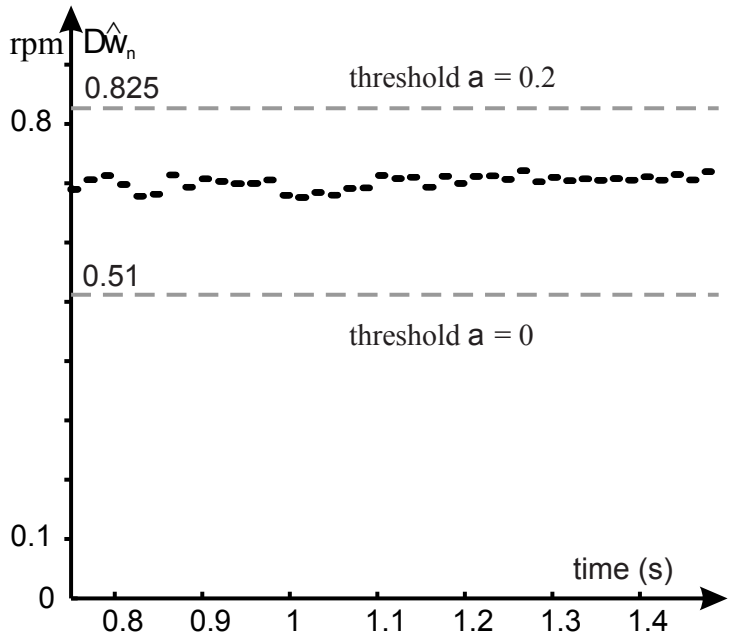

Figure 4.44. Simulation results at $\widehat{\omega}_n = 500$rpm for symmetrical tracking method: rotor speed differences stay within the region of stability of 0.825 rpm

background and experimental results are given. The results show a satisfactory performance can be achieved with the proposed self-sensing commutation methods. The advantages of the proposed methods are: better performance during transients, a more accurate commutation at higher speed owing to the use of the low slope part of the back-EMF. Using back-EMF samples also results in an increased control performance with the speed as higher the back-EMF value are used.

The rotor speed of BLDC drives for several back-EMF based self-sensing methods is studied when operating the drive in an open speed control loop. The effect of estimation errors in the current commutation instants on the rotor speed is analysed and verified with simulations. With the analysis given in this book, the dynamical behaviour of a back-EMF based self-sensing method can be studied and improved before the design and tuning of the speed control loop. Analytical expressions are derived that consider average speed values over periods between succeeding zero-crossing occurrences in the back-EMF waveforms. When operating the drive in open speed control loop, a drift in the rotor speed can be expected. However, from the analytical expressions, it follows a speed drift at zero acceleration occurs when the difference in the average speed between succeeding periods crosses a threshold. Such speed variations should be avoided as these demand a higher steering force

of the speed control loop. The aforementioned threshold can be computed and increases with the drive inertia as well as rotor speed and decreases with the electromagnetic torque. Hence, achieving low speed operation with back-EMF based self-sensing methods is more difficult not only due to the low signal-to-noise ratio of the speed-induced back-EMF, but also due to a less robust dynamical behaviour of the self-sensing method at lower speed. However, for a given speed, torque and inertia, a better dynamical behaviour can be obtained by using a back-EMF symmetrical tracking method instead of a zero-crossing back-EMF self-sensing method.

Chapter 5

Load Torque Estimation

5.1 Introduction

In a robust BLDC drive for a wide variety of applications, load torque is a disturbance within the control loop. Coupling the load to the motor shaft may cause variations of inertia and alters the viscous friction coefficient besides the load variation [Kyeong-Hwa2002]. Even for a drive with known load torque characteristics there are always some unmodelled components that can affect the performance of the drive system. In self-sensing controlled drives, these disturbances are more critical due to the limitations of the self-sensing algorithms compared to drives equipped with position sensors. To compensate or reject torque disturbances, control algorithms need information of these disturbances. The direct measurement of the load torque on the machine shaft would require another expensive and sensitive mechanical sensor. An estimation algorithm can be a good alternative.

If the control algorithm can use estimates of the load torque disturbances, then the dynamics of the drive can greatly be improved [Darba2015a]. As another possible application, in [Guzinski2009, Guzinski2010] the load torque estimation is used for mechanical fault detection in high-speed trains. However, the estimated load torque has large errors during dynamic operation. In [Buja1995] different observer based estimation algorithms are proposed wherein the machine model has to be chosen carefully to reduce parameter sensitivity. Robustness against model uncertainties and noise in the disturbance load torque estimations are studied in [Grignion2014] for constant load torque disturbances. In [Wale2004] the current profile is used to generate a signal related to the load torque. However the dynamic performance of the method has not been studied. The asymmetries of machines are

another source of torque disturbances which must be considered in high performance drives. An observer based algorithm is proposed in [Ruderman2013] to eliminate periodic torque disturbances. In [Harke2008] the disturbance rejection properties of a vector-tracking observer for BLDC machines is evaluated and the drive is equipped with low resolution Hall-effect sensors. In [Harke2006, Harke2007] an analytical approach in frequency as well as in time domain is used in order to investigate the dynamic properties of AC permanent magnet synchronous machines for both sensor-based and self-sensing techniques. The self-sensing control is implemented using an observer based algorithm. It is shown that by using a proper construction of the observer and including appropriate feedforward paths the dynamic properties can be improved. In this book, the main focus is on BLDC machines and the authors propose a self-sensing speed control method together with a load torque feedforward. Experimental and simulation results support the theoretical analysis which has been performed in [Harke2006, Harke2007] for AC PMSM machines.

In Section 4.3 a self-sensing method is explained, referred to as the symmetric-threshold-tracking that is an estimation method based on the monitoring of the back-EMF signal. For a safe and stable operation the applied load torque should be limited within the self-sensing algorithm to determine the minimum value of Δt parameter. Having an estimation of the load torque value even only once every 60 electrical degrees will improve the performance of this method during transients Where based on load torque information Δt can be adapted. In this chapter the theoretical background of the load torque estimation will be discussed. Later on, the simulation and experimental results of the rotor speed and position estimation which are explained in 4.4 together with the results of load torque estimation will be shown. Finally, the positive effect of a load torque estimator to increase the dynamic stiffness of the drive will be presented and discussed in detail. In Section 5.5 the sensitivity of the proposed algorithms to variation of important parameters will be analysed.

5.2 BLDC Machine Load Torque Estimation

In this section by neglecting friction, rotor speed ω_m can be described by the following differential equation:

$$J\frac{\mathrm{d}\omega_m}{\mathrm{d}t} = T_e - T_l \tag{5.1}$$

where T_e represents the electromagnetic torque produced by the BLDC machine and T_l the load torque. It expresses that change in speed over time is a result of difference between electromagnetic torque and load torque. By considering (3.7), T_e is proportional to the measured DC-bus current i_{DC}. Moreover, as in a BLDC drive one of the phase currents i_a, i_b or i_c is zeroed the following estimation for the electromagnetic torque T_e can be made from a sample $i_{DC}[k]$ of the dc-current:

$$\hat{T}_e[k] = 2K_t i_{DC}[k] \tag{5.2}$$

In order to estimate the load torque T_l at a given instant $t_k = kT_s$, referred to as $\hat{T}_l[k]$, an update of the load torque estimation $\hat{T}_l[k-1]$ computed at the previous time instant t_{k-1} will be made.

In Section 4.4 computing the estimated speed value $\hat{\omega}_m$ has been discussed where a measurement of the back-EMF was used. Besides this estimated value $\hat{\omega}_m$, a predicted value $\hat{\omega}_{m,\text{pred}}$ can be obtained as well by discretising (5.1) and assuming that the electromagnetic torque and load torque remain constant during the next sample period:

$$\hat{\omega}_{m,\text{pred}}[k+1] = \hat{\omega}_m[k] + T_s\frac{\hat{T}_e[k] - \hat{T}_l[k]}{J} \tag{5.3}$$

Notice that combining equations (5.2) and (5.3), makes it possible to get a prediction using the measured current $i_{DC}[k]$:

$$\hat{\omega}_{m,\text{pred}}[k+1] = \hat{\omega}_m[k] + T_s\frac{2K_t i_{dc}[k] - \hat{T}_l[k]}{J} \tag{5.4}$$

Remark also that the rotor position can be predicted in a similar way using the discretised model:

$$\hat{\theta}_{e,\text{pred}}[k+1] = \hat{\theta}_e[k] + T_s\hat{\omega}_m[k] + \frac{T_s^2}{2J}\left(2K_t i_{dc}[k] - \hat{T}_l[k]\right) \tag{5.5}$$

Returning this discussion to the estimation of the load torque, the predicted speed value $\hat{\omega}_{m,\text{pred}}[k]$ at instant t_k is required and is obtained from (5.3) as

$$\hat{\omega}_{m,\text{pred}}[k] = \hat{\omega}_m[k-1] + T_s\frac{\hat{T}_e[k-1] - \hat{T}_l[k-1]}{J} \tag{5.6}$$

where the estimated values of speed and load torque computed at the previous time instant t_{k-1} are used.

Assuming no variations in T_e then the difference between the estimated rotor speed $\hat{\omega}_m$ and the predicted rotor speed $\hat{\omega}_{m,\text{pred}}$ results from a variation in the load torque over the sample time T_s. Hence this difference is an indication for the load torque variation and, by considering (5.6), an update of the estimated load torque value can be made by using the difference $\hat{\omega}_{m,\text{pred}}[k] - \hat{\omega}_m[k]$:

$$\hat{T}_l[k] = \hat{T}_l[k-1] + \frac{J}{T_s}\left(\hat{\omega}_{m,\text{pred}}[k] - \hat{\omega}_m[k]\right) \tag{5.7}$$

5.2.1 Simulation Results

To test the algorithm outlined above, we will use the model which was discussed in Chapter 3. The method will be applied with the motor parameters of the Maxon Motor BLDC machine, given in Appendix A.1.

For the first set of simulations, the machine is driven without any speed or current control loop. The speed and current controllers which were build in the model are disabled. The machine starts with an initial rotor speed of 50 rad/s. Without speed controller, the motor will speed up to its maximum no-load speed, $\omega_m = 400$ rad/s. Without current controller, the machine will accelerate very fast. At $t = 0.06$ s, a load torque of 0.06 Nm is applied. At every instant, the back-EMF can be measured at one of the motor terminals. In steady-state, the back-EMF measured in the unexcited phase varies linearly in time, with an alternating positive and negative slope, forming a triangular waveform. The simulated back-EMF signal is depicted in Fig. 5.1. During start-up, the peak-to-peak value of the simulated back-EMF signal increases due to the increase in rotor speed. When the load torque is applied, this peak-to-peak value decreases again due to a decrease in the speed (there is no controller to return the speed to set point of 400 rad/s).

By using (4.35), the rotor speed can be estimated from the measured back-EMF. Both the actual rotor speed and the rotor speed estimation are shown in Fig. 5.2. When the machine is commutated to the next commutation state, the slope of F, m_L, changes from $\frac{6}{\pi}$ to $-\frac{6}{\pi}$, or vice versa. At the commutation instant, the measured back-EMF exhibits a singularity: the derivative does not exist at these points. At these instants, the estimated rotor speed is not updated. In the zoomed section of Fig. 5.2, it can be seen that the estimated rotor speed $\hat{\omega}_m$ deviates from the actual rotor speed. The estimated rotor speed is equal to the actual rotor speed

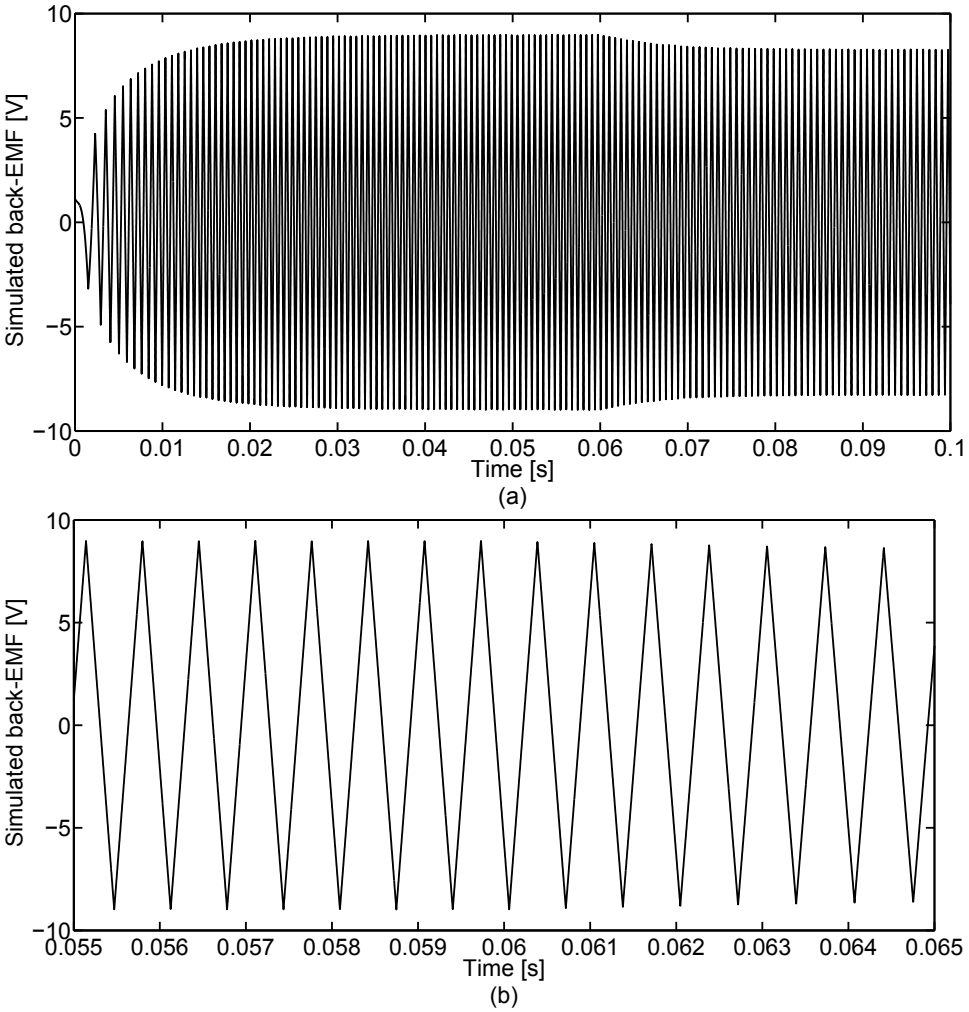

Figure 5.1. (a): Simulated back-EMF at the motor terminals, (b): zoomed view

approximately halfway in between two commutation instants.

By using (4.36), it is possible to estimate the value of the function F at each time sample. The results of this equation are depicted in Fig. 5.3(a) and (b). In Fig. 5.3(a), the estimation of F is shown when the BLDC machine accelerates from $\omega_m = 50$ rad/s to $\omega_m = 400$ rad/s. After 0.0025 s, most of the transients due to acceleration in this estimation have died out. In Fig. 5.3(b), the estimation of the function F is represented in case the machine is loaded with 0.06 Nm. There is no noticeable transient in the estimation because the parameters of the machine

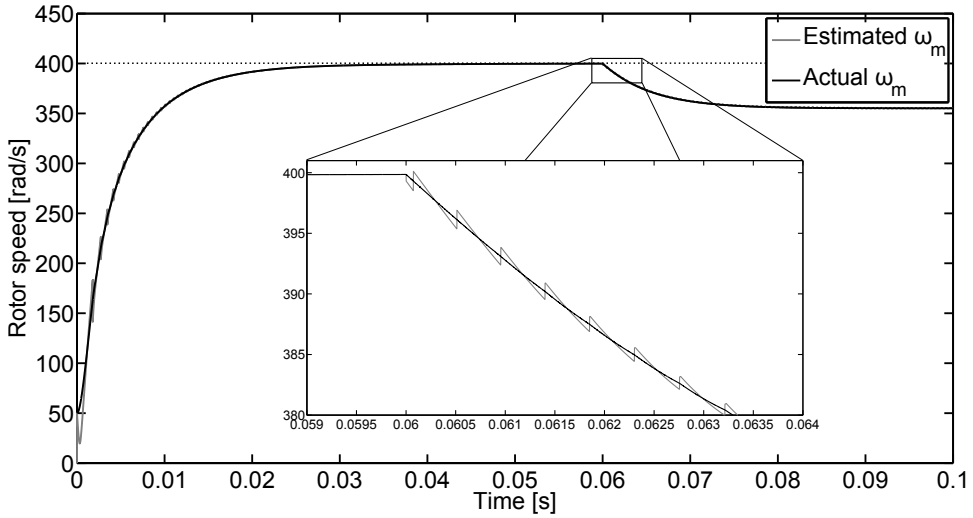

Figure 5.2. Simulation result, estimated rotor speed from back-EMF samples and the simulated actual rotor speed

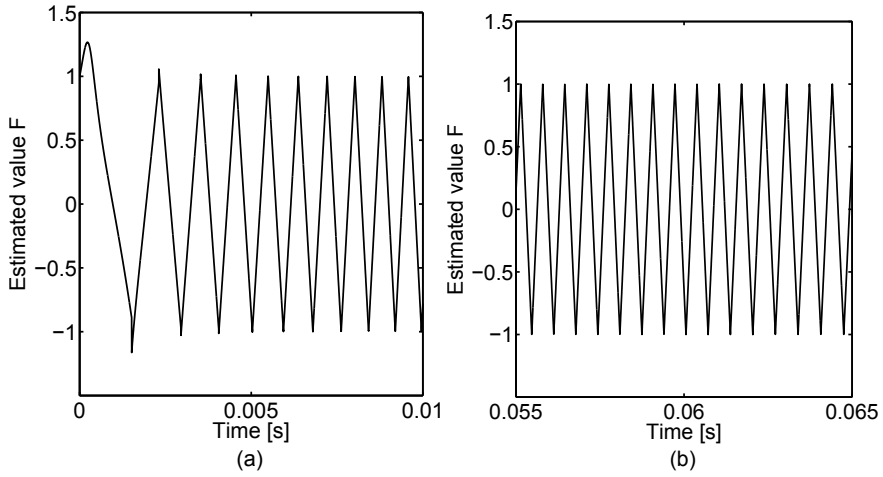

Figure 5.3. Simulation results, (a): estimated value for the function F during acceleration from 50 rad/s to 400 rad/s, (b): estimated value for the function F, machine is loaded with $T_l = 0.06$ Nm at $t = 0.06$ s

are accurate and the speed variation is small.

From the estimation of F, the rotor position can be estimated using (3.6). The results are shown in Fig. 5.4(a) and (b). The electrical angle θ_e is calculated

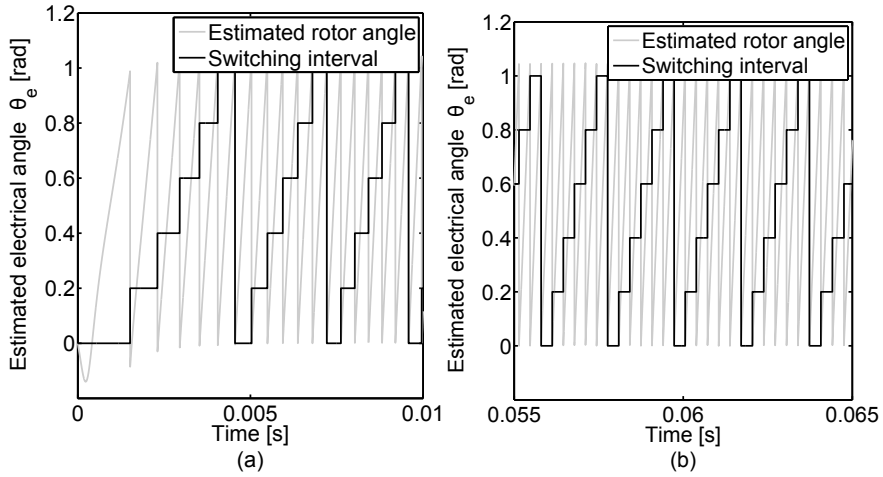

Figure 5.4. Simulation result, (a): estimated rotor position from back-EMF measurements during acceleration of the machine from 50 rad/s to 400 rad/s, (b): estimated rotor position from back-EMF measurements when a load torque $T_l = 0.06$ Nm is applied at $t = 0.06$ s

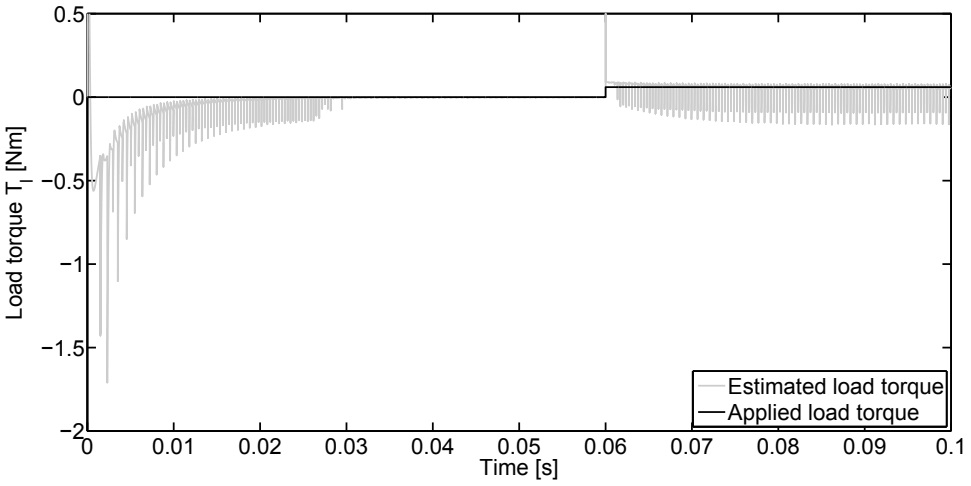

Figure 5.5. Simulation result, estimated load torque T_l from back-EMF measurements

in such a way that it lies between 0 and $\frac{\pi}{3}$. In this way the signal reaches to its maximum value at each commutation instant and hence in these figures, the commutation interval is represented as well. Every level of this staircase function corresponds to a certain conduction state.

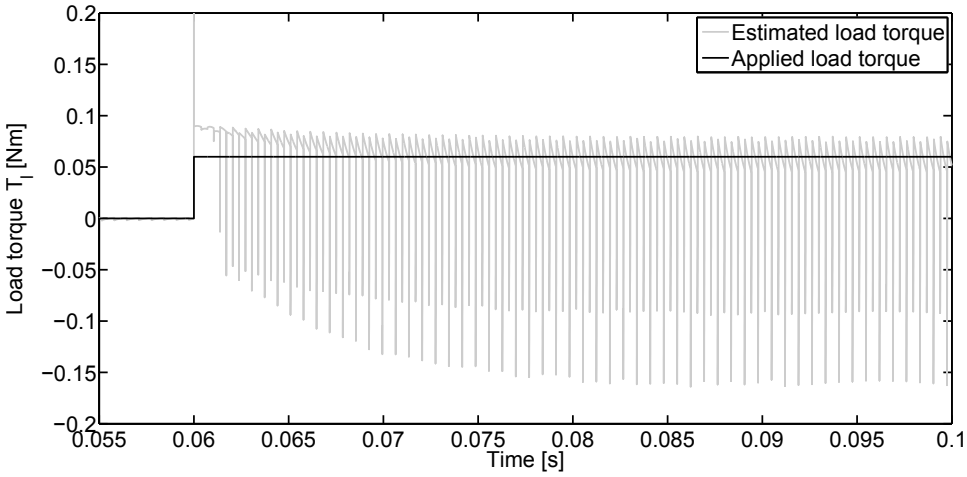

Figure 5.6. Simulation result, estimated load torque T_l from back-EMF measurements

The load torque can be estimated using (5.7). The simulation results for the machine without the speed and current controllers are depicted in Figs. 5.5 and 5.6. During transients, the speed estimation, used in the algorithm to estimate the load torque, differs from the actual rotor speed. This causes the estimated load torque to differ from the actual load torque during transients. When the machine accelerates from $\omega_m = 50$ rad/s to 400 rad/s, the slope of the estimated rotor speed in between two commutations is more positive than the slope of the actual rotor speed. As a result there is an underestimation of the load torque. Notice a negative load torque corresponds to a torque that accelerates the rotor.

After transients, the slope of the estimated speed is approximately equal to that of the actual rotor speed. The estimated load torque then converges to 0 Nm. When the load torque is applied to the BLDC machine, an immediate response can be noticed in the estimated load torque. There is a small overestimation when applying the load torque at $t = 0.06$ s. This is, again, due to a different slope between the actual rotor speed and the estimated rotor speed, as the slope of the estimated rotor speed is more negative Fig. 5.2. The estimated load torque then converges to 0.06 Nm. There are spikes present in the estimation $\hat{T}_l$ after applying the load torque. These spikes are the result of the spikes in the phase currents (which are used to get an approximation of the electromagnetic torque T_{em}). The estimated load torque will be improved in the next section in order to have more accurate results.

5.2.2 Origin of the Speed Estimation Error During Transients

In the previous section, it was noted that the estimated rotor speed deviates from the actual rotor speed during acceleration of the BLDC machine. This speed difference occurs during transients. In the derivation of (4.35) speed variation in between successive time samples ($\omega_m[k] = \omega_m[k-1]$) is neglected. When this difference is taken into account (4.34) is rewritten to obtain:

$$K_e m_L T_s \omega_m[k-1]\omega_m[k] \approx \\ e[k] - e[k-1] - K_e F(\theta_e[k])(\omega_m[k] - \omega_m[k-1]) \quad (5.8)$$

In which, the second term is omitted when neglecting speed transients. During acceleration of the machine, it holds that:

$$\omega_m[k] - \omega_m[k-1] > 0 \quad (5.9)$$

The measured back-EMF signal e consists of rising and falling edges. It is a triangular waveform that is deformed by transients. For a falling edge, the difference between successive back-EMF measurements is negative:

$$e[k] - e[k-1] < 0 \quad (5.10)$$

and the corresponding value for the slope m_L is $\frac{-\pi}{6}$. As a result, for positive speed, the left hand side of (5.8) is negative. The first term of the right hand side of this equation is also negative. As the case of a falling edge for the measured back-EMF signal is considered, the F function varies from positive $(+1)$ to negative values (-1). If the value of F is positive, the value of the right hand side is more negative than assumed by the estimation method (4.35). The resulting estimated rotor speed is lower than the actual rotor speed. The opposite holds when the function F takes on negative values. This means that, at a certain time in between two commutation instants, the estimated rotor speed becomes equal to the actual rotor speed. This point corresponds to the case where the value of F equals to 0. Indeed, for this value, the second term of the right hand side of (5.8) is zero, showing the same result when neglecting the speed difference. A similar approach can be used to interpret the difference between the estimated rotor speed and the actual rotor speed for a rising edge of the measured back-EMF signal.

5.2.3 Improvement of the Rotor Speed and Load Torque Estimation through the Rotor Position and Acceleration Feedback

In the previous section, it was explained how neglecting a variation in the rotor speed influences the rotor speed and load torque estimation, $\hat{\omega}_m$ and $\hat{T}_l$ respectively. In this section, it is shown that using the rotor position and speed taken at previous sample moments can enhance the rotor speed and load torque estimation. Referring back to (5.8), the following estimation rule can result in better rotor speed estimations:

$$\hat{\omega}_m[k] \approx \sqrt{\frac{e[k] - e[k-1] - K_e\hat{F}(\theta_e[k-1])(\omega_m[k-1] - \omega_m[k-2])}{K_e m_L T_s}} \tag{5.11}$$

It was explained by (4.36) how the rotor position $\hat{\theta}_e$ was estimated using back-EMF measurements and the already obtained rotor speed estimation $\hat{\omega}_m$. Because a delay is required to calculate the rotor speed $\theta_e[k-1]$ instead of $\theta_e[k]$ is used in (5.11). A similar manipulation is done with the speed difference $\omega_m[k] - \omega_m[k-1]$. In (5.11), the speed difference based on time measurement between commutation instants is used instead of the estimated speed difference.

The load torque estimation can be improved by using the average acceleration a_{avg} of the BLDC machine. The term of average acceleration relates to the acceleration of the rotor over one commutation cycle. It is derived from counting the clock cycles of the controller between successive commutation instants and is updated at each commutation instant.

To see the influence of speed feedback, two cases are considered. In the first case, the acceleration derived from the actual rotor speed is used. In the second case, the acceleration used in (5.11) is the actual acceleration multiplied by 0.5 to show the influence of a less accurate acceleration value. In both cases, the speed and current controllers are enabled. The current controller reduces the ripple in the electromagnetic torque, thereby reducing the spikes in the load torque estimation.

The results for the estimated rotor speed are depicted in Fig. 5.7. By using the actual rotor acceleration in (5.11), the spikes in the estimated rotor speed at the commutation instants are eliminated. The estimated rotor speed that results from using only half of the actual rotor acceleration results in estimation errors but is a better approximation than the one that results from (4.35). Fig. 5.7 shows the spikes are reduced using acceleration feedback at the commutation instants.

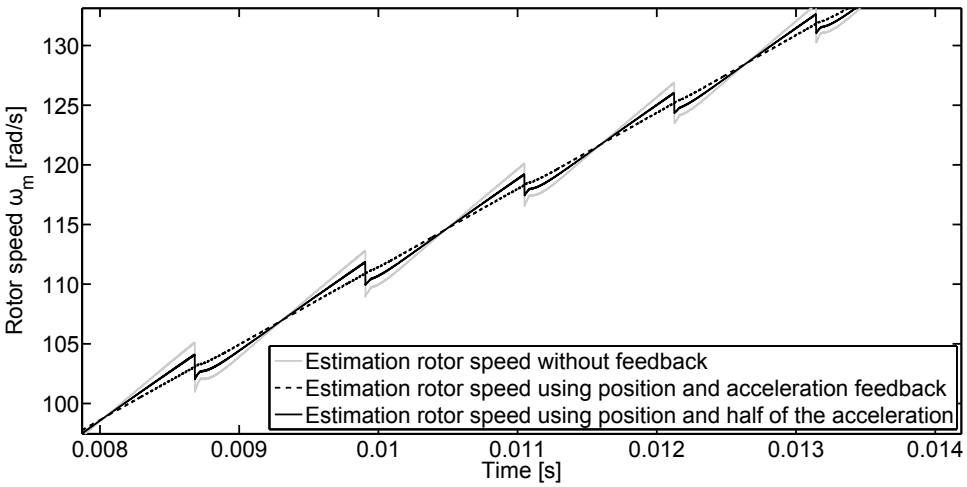

Figure 5.7. Simulation result, influence of rotor position and acceleration feedback on the rotor speed estimation

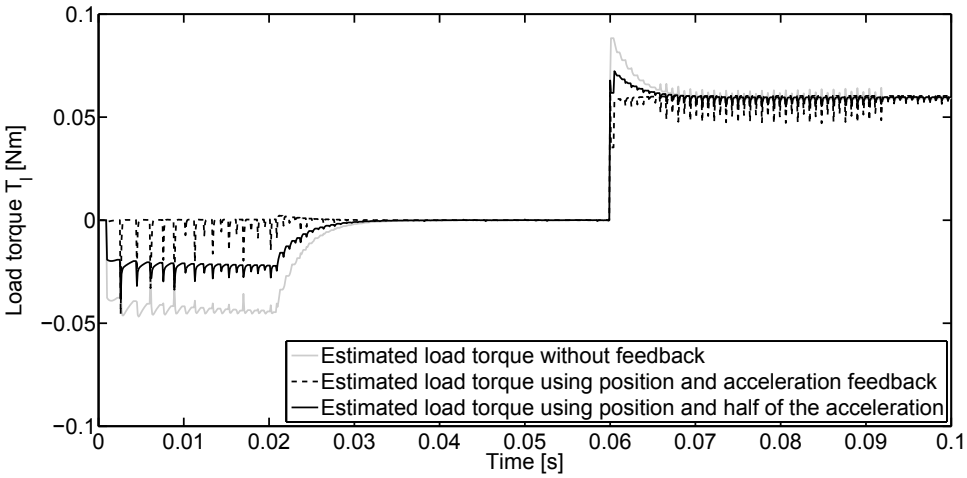

Figure 5.8. Simulation result, influence of rotor position and acceleration feedback on the load torque estimation

Using acceleration and position feedback improves the estimation of the rotor speed. As a consequence, the slope of the estimated rotor speed bears close resemblance to the slope of the actual rotor speed. This is important for a good load torque estimation. The influence of the acceleration and position feedback on the load torque estimation is shown in Fig. 5.8. During start-up of the machine, the load torque is wrongly estimated from the estimated rotor speed that results from

(4.35). In this case, an average deviation of -0.04 Nm from the actual applied load torque is observed. When a sudden load torque of 0.06 Nm is applied, an overestimation of 47% occurs. When half of the actual rotor acceleration is used to estimate the rotor speed, the deviation from the actual load torque becomes -0.02 Nm during start-up. The load torque estimation error is reduced to 19% when a sudden load torque is applied. If the actual rotor acceleration is used to estimate the rotor speed, the deviation during start-up is approximately 0 Nm. There is almost no load torque estimation error when a sudden load torque is applied.

5.2.4 Dynamical Behaviour of the Rotor Speed and Load Torque Estimation

In this section, the rotor speed and load torque estimation methods are tested under variable load torque conditions. To test the performance of the estimation methods under such circumstances, two types of load torque waveforms are used. The first one is a sawtooth waveform, with a period of 0.01 s. This load torque waveform first increases linearly up to 0.06 Nm and then suddenly drops to 0 Nm. The second waveform is a sinusoidal one with an amplitude of 0.06 Nm and a frequency of 25 Hz. The speed and current controller are enabled in both tests. The varying load torques are applied after the machine has reached its steady state.

Firstly, the behaviour of the estimation methods for the load torque of the first case is investigated, without position and acceleration feedback. The estimated rotor speed is shown in Fig. 5.9. The estimated rotor speed matches the actual rotor speed. The spikes in the estimated rotor speed that are due to neglecting speed variations in the rotor speed are present here as well.

The estimated load torque is depicted in Fig. 5.10. The initial transients were discussed earlier. The estimated load torque deviates from the actual applied load torque, even in steady state. This is because no acceleration feedback is used in this set of simulations. When the applied load torque does not change abruptly, the transients in the estimation are absent and only a steady-state error exists.

The average acceleration for this test is depicted in Fig. 5.11. It approximates the actual rotor acceleration quite well in regions where the acceleration does not change (e.g. between $t = 0.03$ s and 0.04 s). In regions where the acceleration changes (e.g. between $t = 0.02$ s and 0.03 s), a_{avg} lags behind the actual acceleration. It can be expected that this lagging will cause a deviation in the load torque estimation.

The estimated load torque using a_{avg} is plotted in Fig. 5.12. The error in the load

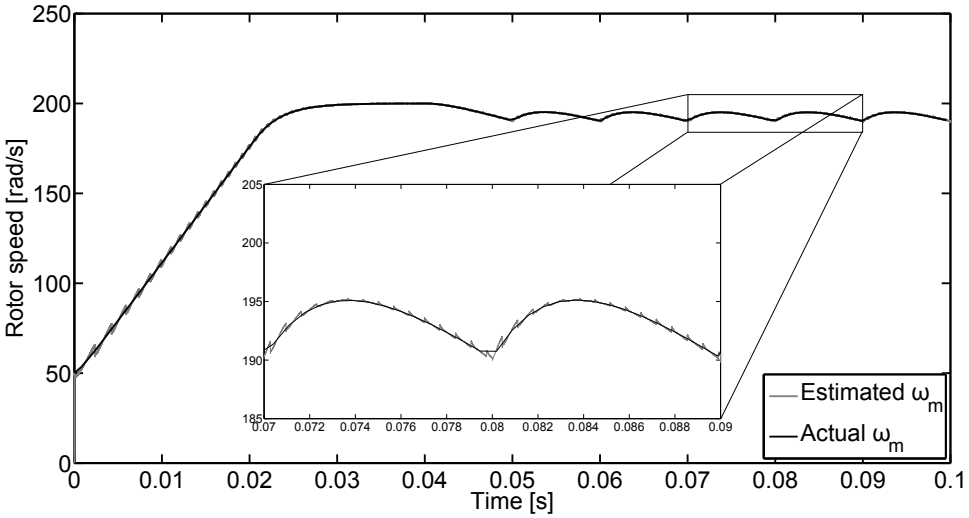

Figure 5.9. Simulation result, estimated rotor speed under sawtooth load torque

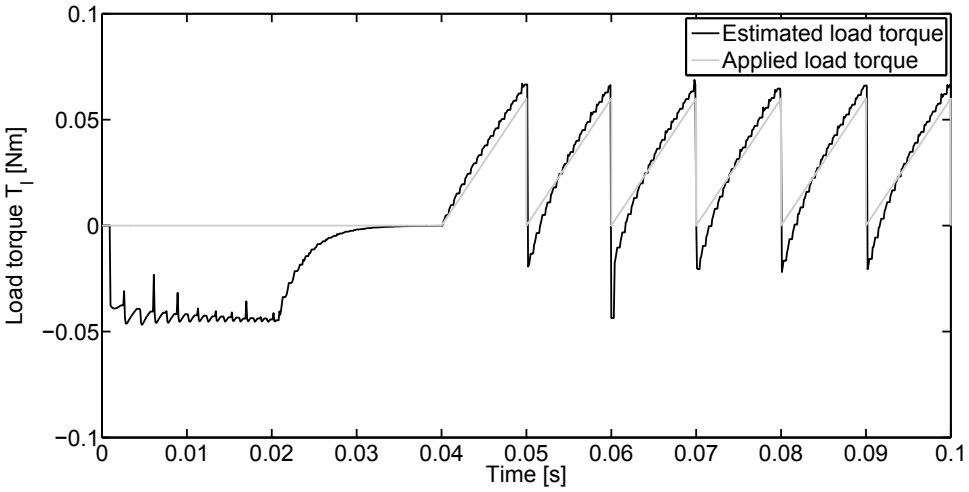

Figure 5.10. Simulation result, estimated load torque under sawtooth load torque without acceleration and position feedback

torque estimation has become smaller. The steady-state error at the linear parts of the applied load torque has disappeared. When the acceleration was approximated well, the load torque estimation has improved remarkably.

As a second test of the dynamical performance of the estimation algorithms,

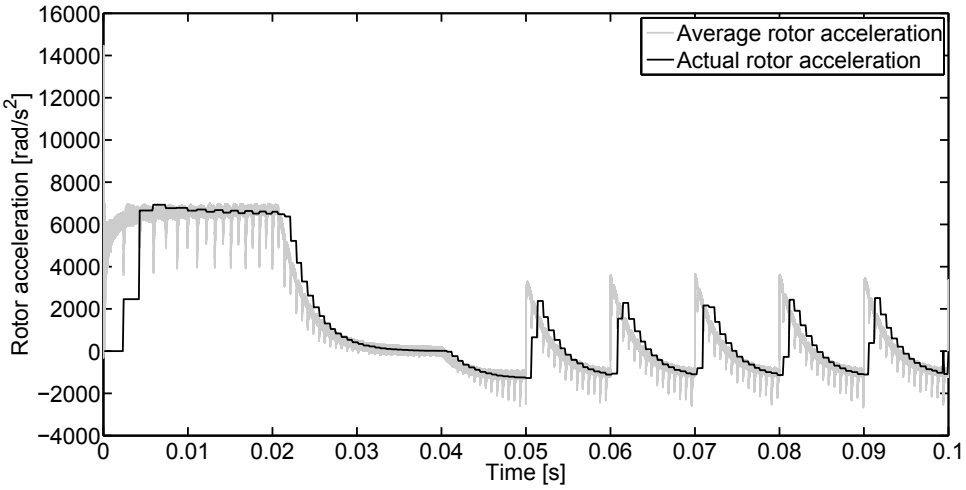

Figure 5.11. Simulation result, average acceleration for BLDC motor under sawtooth load torque

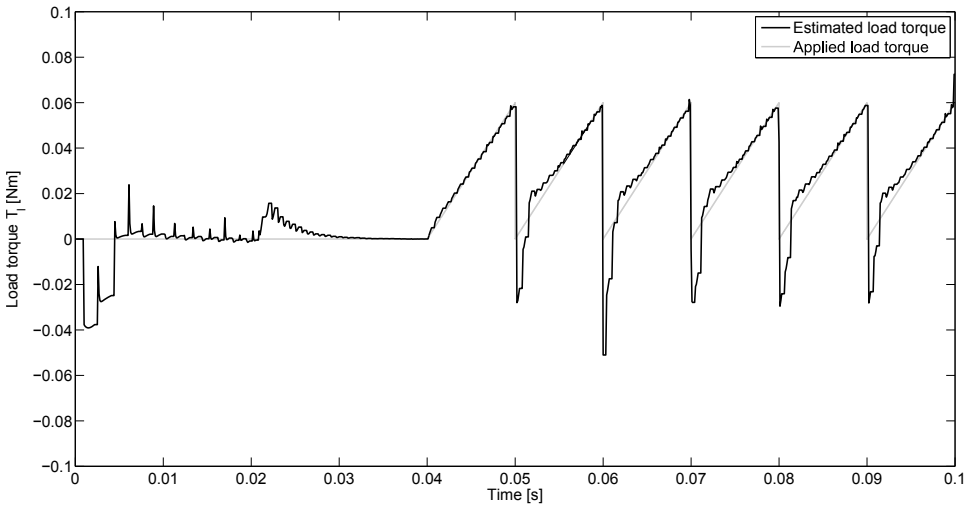

Figure 5.12. Simulation result, estimated load torque using the average acceleration of the BLDC machine

the BLDC machine is loaded with a sinusoidal load torque during steady-state operation of the machine. The estimated rotor speed when applying a sinusoidal load torque, without acceleration feedback is shown in Fig. 5.13. Using this rotor speed estimation, the corresponding estimation for the load torque is performed, Fig. 5.14. The resulting estimated load torque is smooth when the sinusoidal

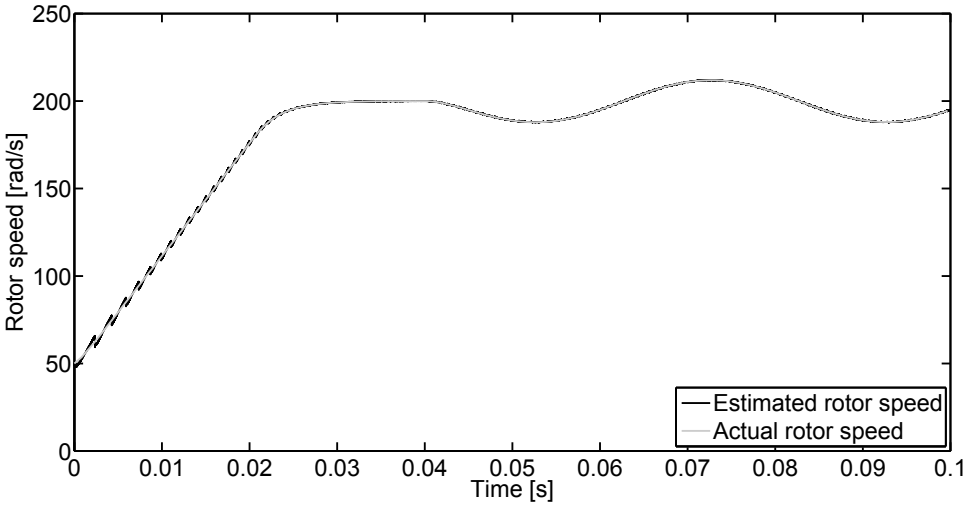

Figure 5.13. Simulation result, estimated rotor speed when applying a sinusoidal load torque, without acceleration feedback

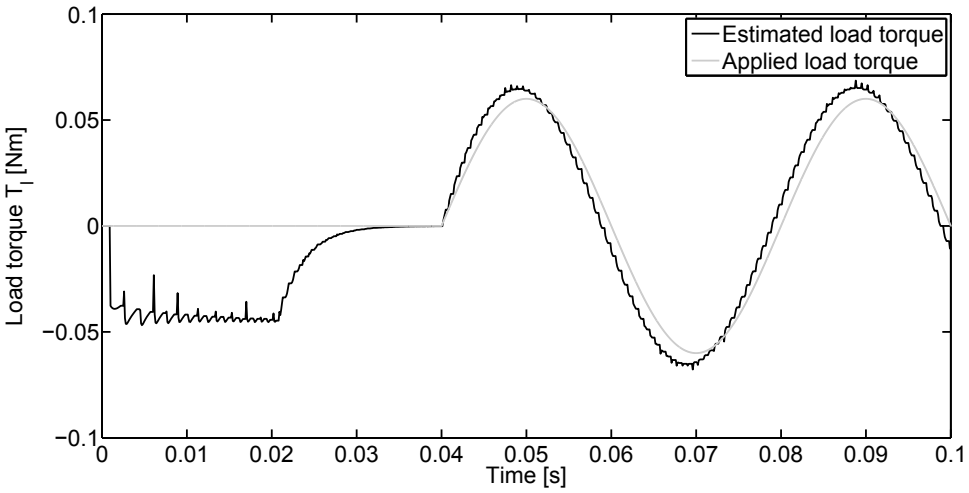

Figure 5.14. Simulation result, estimated load torque when applying a sinusoidal load torque, without acceleration feedback

load torque is applied. However, the amplitude and phase differ from the actual amplitude and phase.

For this case of load torque, the influence of a feedback of a_{avg} is also checked.

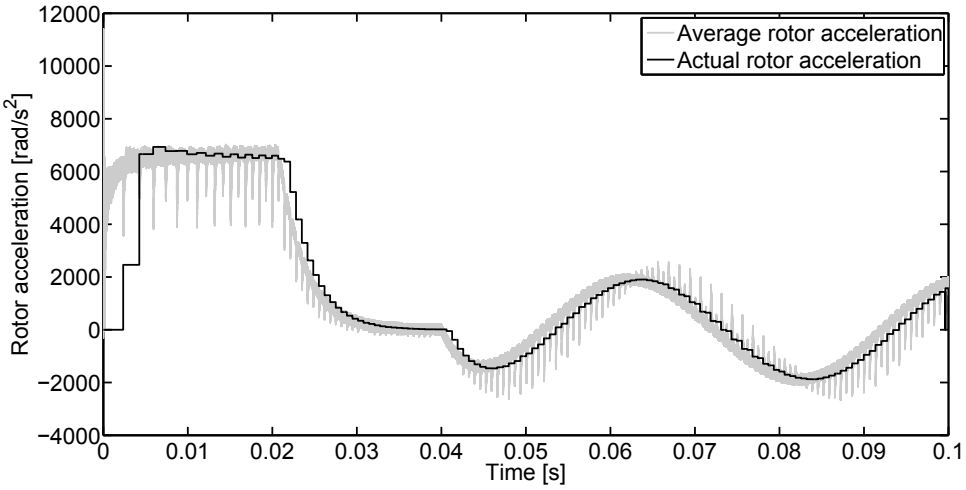

Figure 5.15. Simulation result, average acceleration of the BLDC machine when applying a sinusoidal load torque

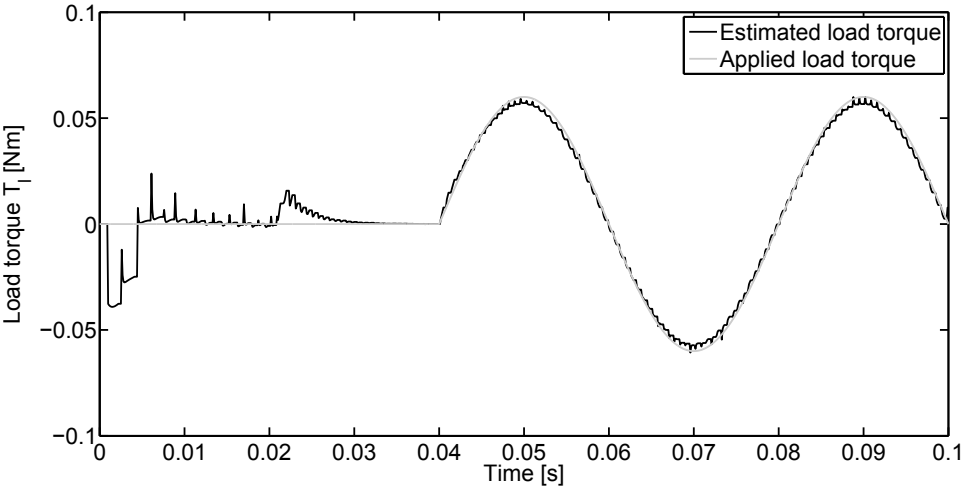

Figure 5.16. Simulation result, estimated load torque when applying sinusoidal load torque, using average acceleration

The average acceleration a_{avg} for this simulation is depicted in Fig. 5.15. The effect on the estimated load torque is illustrated in Fig. 5.16. It can be seen that the estimated load torque follows the applied torque when the speed reaches to its set point. There are small deviations in the beginning of the simulation that is due to the low update rate of the acceleration feedback at lower speeds.

5.3 Programmable Load Torque

To evaluate the performance of the load torque estimation, a test bench is set up in order to provide the required mechanical load torque profile to test the proposed load torque estimation algorithm on the actual BLDC machines. A BLDC machine (as load) is mechanically coupled to the tested motor shaft (the parameters of the machine can be found in Appendix A.2). The load machine provides the required mechanical load torque profiles which are chosen to evaluate the performance of the estimation algorithm.

The programmable load torque consists of a BLDC machine with its terminals connected to a conventional three-phase diode rectifier. The output of the rectifier is connected to a power resistor (as the electrical load for the BLDC generator) via a first-quadrant DC chopper. The DC chopper is implemented on a Atmel MC300 BLDC/stepper motor driver, see Appendix B.1. The DC-bus current of the chopper is measured using a shunt resistor. This current is then used as a feedback to a PI current controller. The switches of the DC chopper are controlled using an FPGA (see Appendix B.2) to control the average applied voltage to the power resistors. By this way the current and torque of the generator is controlled. The generated mechanical braking torque of the BLDC generator is proportional to the stator currents of the machine. The required load torque profile is generated within the FPGA and applied to the current control loop as the current reference. The output of the current controller provides the duty ratio of the applied voltage which is realised using a PWM technique. A fixed 10 kHz frequency is chosen for the PWM triangular carrier.

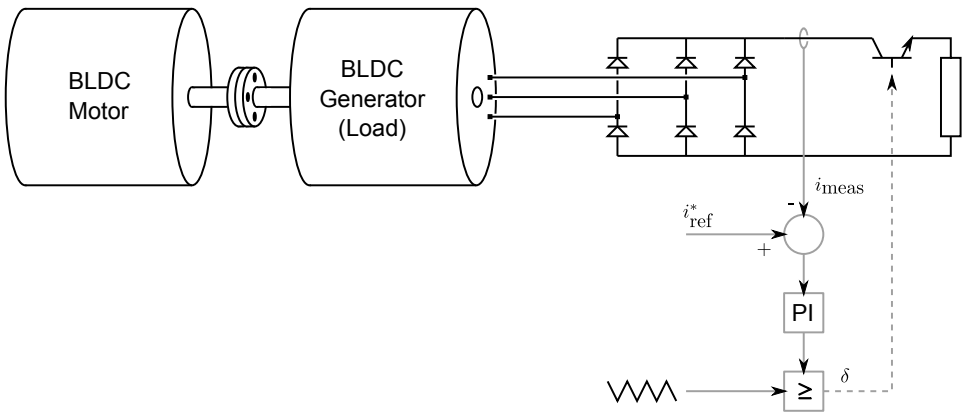

Figure 5.17. Schematic diagram of the practical realisation of programmable load torque using a BLDC machine as generator

Another topology for the programmable load torque using a BLDC machine would be possible by using a six-step current commutation for the BLDC generator. This technique also provides a controlled current and hence also a controlled braking torque for the coupled motor. However, the first technique is chosen for its simplicity.

By measuring the load current of the BLDC generator which is equal to the DC-bus current of the first quadrant DC chopper the mechanical braking torque on the rotor shaft of the BLDC generator can be determined. The only difference between the DC-bus current profile of the first quadrant chopper and the actual load torque applied to the BLDC motor is the friction that is neglected in this study.

A schematic digram of the programmable load torque is illustrated in Fig. 5.17. The measured current information is fed to the FPGA using an analog-to-digital converter (more information in Appendix B.3) and a digital isolator (see Appendix B.4). The duty ratio which is generated within the FPGA is applied to the driver circuit of the DC chopper IGBT switch using a digital isolator as well.

5.3.1 Experimental Results

The evaluation procedure of the load torque estimation will be discussed in this section. To test and verify the algorithm, a programmable load torque is implemented. The estimated load torque can then be compared with a measurement of the external applied load torque which is represented by the measured DC-bus current of the BLDC generator.

5.3.2 Evaluation of the Load Torque Estimation

The load torque estimation algorithm is implemented on a Spartan-3E XC3S1600E FPGA board. The algorithm to drive the load machine (BLDC generator) in order to provide the programmable load torque is implemented on a Spartan-3E XC3S500E FPGA board. The current that flows through the DC-bus of the first quadrant DC chopper shown in Fig. 5.17 is also sampled by the XC3S1600E FPGA board. The load torque estimation is especially important during transients. In steady-state, the estimated load torque will be equal to the electromagnetic torque, which can be derived from measurements of the DC-bus current that flows to the motor. The schematic diagram of the entire test setup is depicted in Fig. 5.18.

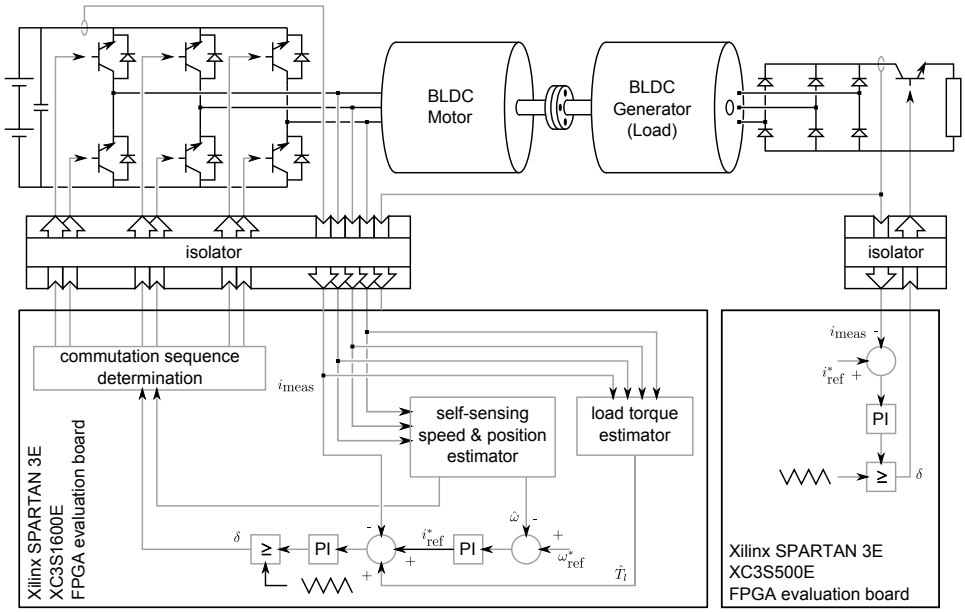

Figure 5.18. Schematic diagram of the practical realisation of programmable load torque using a BLDC machine as generator

The behaviour of the load torque estimator is tested for rectangular and sinusoidal loading of the drive. The estimated load torque, when the machine is loaded with a rectangular load torque profile with a period of 400 ms, is depicted in Fig. 5.19(a):

- Disregarding the high-frequency noise, it can be noticed that the estimated load torque exhibits the same waveform (low-high) as that of the external applied load torque.
- There exist a difference in the average values of the estimated load torque and the generator current (referred to as externally applied load torque). This deviation can be caused by the presence of friction, which is not visible via monitoring of the generator current. The externally applied load torque refers to the torque generated by the current in the phases of the BLDC generator only. It is measured that the friction results in a 0.5 A phase current in no-load conditions (where the externally applied load torque is zero) of the motor, when the machine rotates at 1000 rpm.
- The noise on the load torque estimation follows from noise on the speed estimation. If necessary, a filter can be used to reduce the noise on the load estimation. However, this also implies that a time delay would be introduced in the load torque estimation.

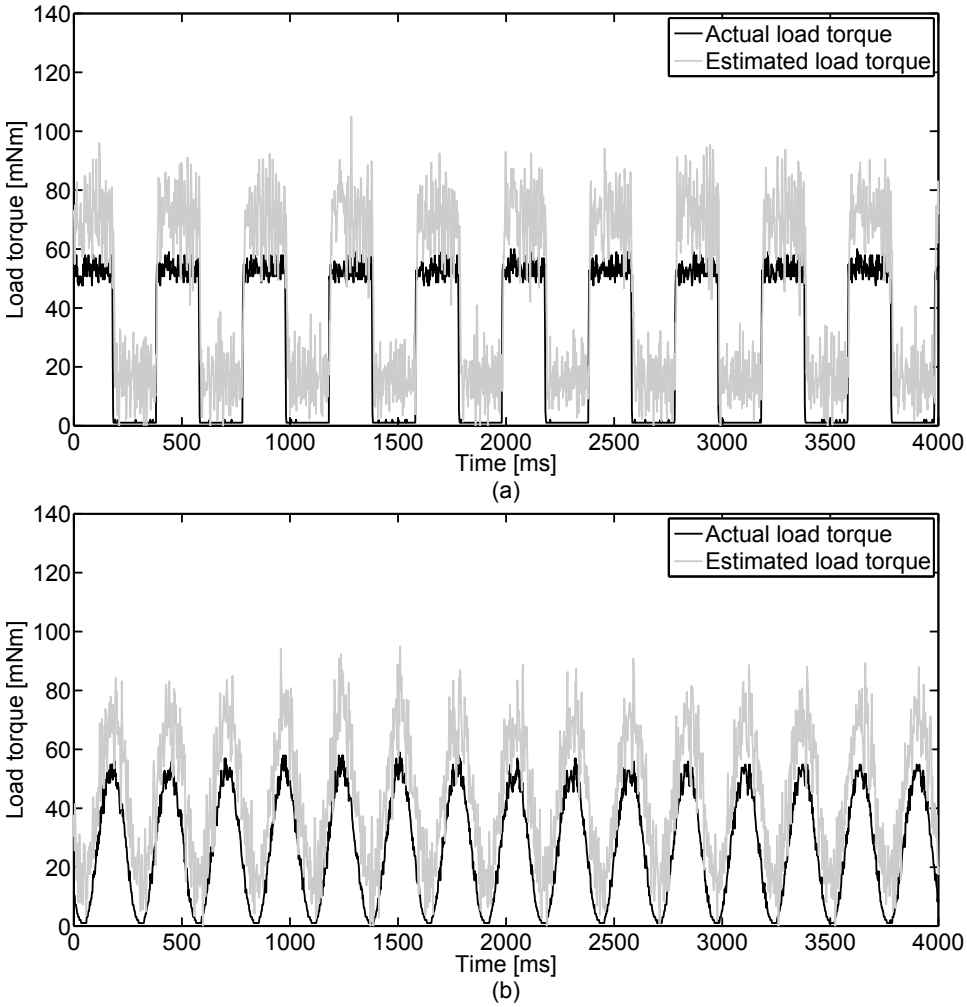

Figure 5.19. Experimental results, load torque estimator: Rotor speed set-point $\omega_m^* = 1000$ rpm, (a): pulsed load torque, (b): sinusoidal load torque

The load torque estimation, when the machine is loaded with a sinusoidal load torque, is shown in Fig. 5.19(b) (period of 270 ms) and Fig. 5.20 (period of 2314 ms). Similar conclusions can be drawn as those mentioned above.

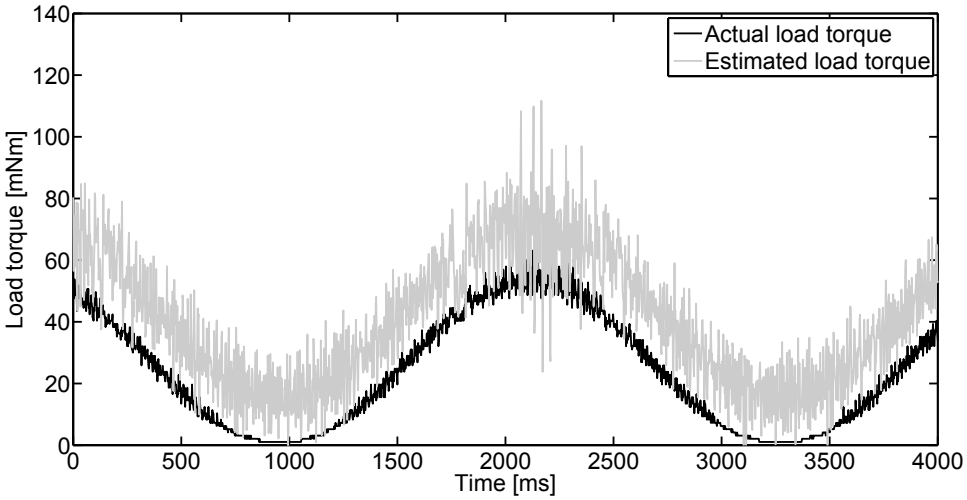

Figure 5.20. Experimental results, load torque estimator, Rotor speed set-point $\omega_m^* = 1000$ rpm.

5.4 Application of the Load Torque Information to Improve the Dynamic Stiffness

Previously, in this chapter, a load torque estimator was described and implemented on an FPGA. The results has verified the performance of the proposed algorithm. In this section, an application of the load torque information is presented. A load torque variation often result in a variation of the rotor speed. In applications where a constant rotor speed is important, a speed controller is applied and speed variations due to load torque variations are to be avoided. By using the load torque information, it is possible to improve the speed control characteristics of the drive during load transients. This is achieved in a BLDC drive with the proposed self-sensing algorithm as described hereafter. The positive effect of load torque feedforward is proven by implementing it on an FPGA and testing it at different loading conditions.

5.4.1 Dynamic Stiffness and Load Torque Feedforward

Possible applications that use estimated load torque are described in [Guzinski2009, Guzinski2010] where the load torque information is used to detect and diagnose the mechanical failures of the load torque coupled to the machine. In this section, the load torque estimation is used to improve the dynamic

stiffness of the drive.

In terms of control theory, the load torque T_l is an external disturbance for electrical drive systems. For example in a cascaded speed and current control strategy of electrical machines (see Fig. 5.18) the load torque and the speed reference are two different inputs to the control system.

In [Lorenz1994, Schmidt1992] the authors have proposed two basic measures for improving the motion control performance:

- command tracking (how well the output state follows the input set point)
- disturbance rejection

where the latter can also be called dynamic stiffness The term "dynamic stiffness", citing [Lorenz1994, Schmidt1992], has been introduced as "The act of providing restoring torques to attenuate motion error response [which can be speed or position error] to process disturbances is equivalent to providing dynamic stiffness. From a state controller perspective this is achieved via the stiffness gain on position feedback and damping gain on velocity feedback". In this study, a load torque feedforward is used in order to increase disturbance rejection performance (or dynamic stiffness) of the control-loop.

The transfer function $\frac{\omega_m(s)}{T_l(s)}$ or $\frac{\theta_m(s)}{T_l(s)}$ reflect the output speed or position sensitivity to applied load torque disturbances. The transfer function $\frac{\omega_m}{T_l}$ relates to the frequency domain of the system output ω_m and the load torque T_l. In the ideal condition the transfer function of $\frac{\omega_m}{T_l}$ should be equal to zero. Systems with the transfer function from disturbance to output close to zero are referred to as rigid or stiff, reflecting the fact that the disturbance inputs (in this case T_l) of the control system, have little or no influence on the controlled variable (in this case machine speed ω_m).

The load torque affects the output speed ω_m of the machine and introduces speed errors $(\omega_m^* - \widehat{\omega}_m)$. Conventional PI controllers compromise between settling time, oscillations and steady-state error. When the machine is used to drive a highly varying load torque, maintaining the desired speed using conventional PI controllers is cHallenging. A high-frequency variable load torque in a low inertia system can cause a high speed variation. Achieving a constant speed by only tuning the integral and proportional gains of the PI controller and having a wide bandwidth at the same time is beyond the capabilities of conventional PI

controllers.

5.4.2 Load Torque Feedforward

PI controllers that are tuned to control the rotor speed of BLDC machine try to achieve a specific performance (e.g. overshoot and settling time) while changing the rotor speed set point. These PI controllers are also able to reject disturbances that come from load torque disturbances. There is, however, a fundamental difference in the behaviour of the controller to changing setpoints and to disturbances.

- When the speed reference is changed, the PI speed controller will change the current reference with a certain rate. This rate depends on the gains of the PI speed controller. Subsequently, the PI current controller changes the duty ratio of the switches of the power stage. Assuming that the machine was in steady state before changing the rotor speed, the response of the machine to a changing setpoint is immediate. The speed changes in the desired way.
- When a load torque is applied, the rotor speed will decrease. The PI speed controller will increase the current reference, thereby increasing the generated electromagnetic torque. However, as long as the electromagnetic torque is lower than the applied load torque, the machine will keep decelerating. The machine will accelerate again up to the point where the electromagnetic torque becomes larger than the applied load torque. A similar reasoning can be followed for a sudden decrease in the load torque.

The problem with the PI controllers is that they do not recognize a change in the load torque as a disturbance. They react indirectly on a torque disturbance in the same way that they would to a change of the rotor speed setpoint. To reduce the influence of a load torque disturbance on the rotor speed, the electromagnetic torque must evolve similarly to the applied load torque as it does for the current. In this section, the performance of the drive to load torque disturbances is improved by using the load torque estimator described in earlier in this chapter.

The reference current i^* determines the reference value for the electromagnetic torque. It is thus plausible to adjust i^* based on the load torque estimation, Fig. 5.21. The idea behind this is to eliminate the influence of the disturbance before it has an noticeable effect on the rotor speed. For the considered BLDC machine, the order of magnitude of the numeric value of the load torque in SI units (10^{-3} Nm) is much smaller than the order of magnitude of the numeric value of the DC-bus current in SI units (1 A). To have a perceptible effect of the addition of the load torque estimation $\hat{T}_l$ to the current reference i^*, the gain a_{LT} should bridge the

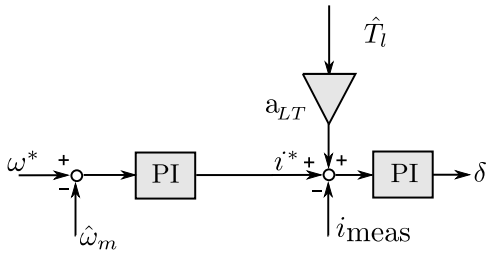

Figure 5.21. Scheme of PI controllers with load torque feedforward

difference in the order of magnitude between them. The electromagnetic torque is related to the DC-bus current by the torque constant K_t.

$$T_e = 2K_t i_{DC} \tag{5.12}$$

Therefore, it makes sense to express a_{LT} in terms of K_t^{-1}:

$$a_{LT} = a_{LT} K_t^{-1} \tag{5.13}$$

In the rest of this chapter, the influence of load torque feedforward on the dynamic stiffness of the machine is described using the dimensionless parameter a_{LT}.

A. *Influence of a_{LT} on the Dynamic Stiffness of a BLDC Drive*

The model equations derived in Section 3.7 can be combined with the scheme from Fig. 5.21 to obtain a transfer function that relates the rotor speed ω_m to the applied load torque T_l:

$$\frac{\omega_m(s)}{T_l(s)} = \frac{-(R + Ls + PI_i V_s) + 2K_t a_{LT} K_t^{-1} PI_i V_s}{(Js + K_f)(R + Ls + PI_i V_s) + 2K_t(PI_i PI_{\omega_m} V_s + 2ke)} \tag{5.14}$$

The variable s represents the Laplace operator. The transfer functions of the PI current and speed controller are represented by PI_i and PI_{ω_m}, respectively. These transfer functions are given by:

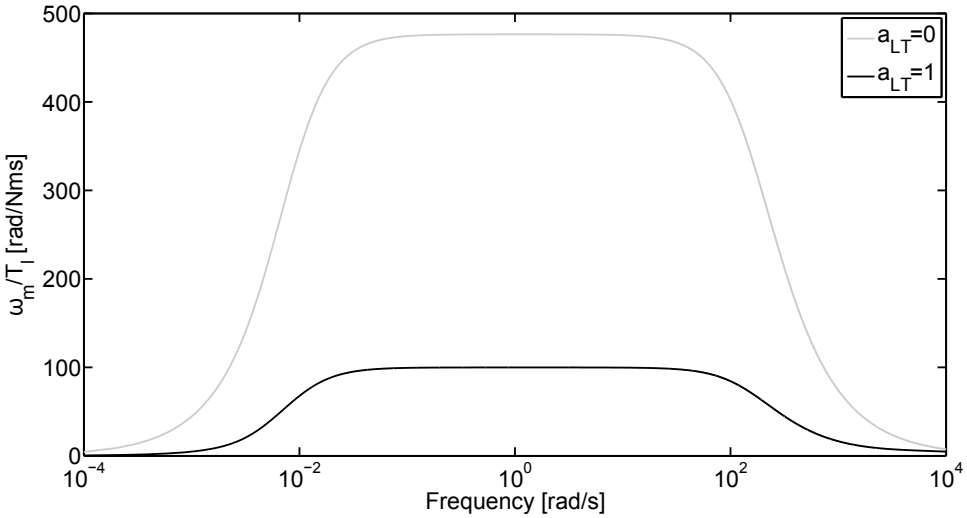

Figure 5.22. Frequency response of the amplitude of the transfer function ω_m/T_l

$$\frac{\delta}{i_{\text{error}}} = PI_i = \frac{K_{p,i}s + K_{i,i}}{s} \qquad (5.15)$$
$$\frac{i^*}{\omega_{\text{error}}} = PI_{\omega_m} = \frac{K_{p,\omega_m}s + K_{i,\omega_m}}{s}$$

Where

$K_{p,i}$: the proportional gain of the PI current controller

$K_{i,i}$: the integral gain of the PI current controller

K_{p,ω_m} : the proportional gain of the PI speed controller

K_{i,ω_m} : the integral gain of the PI current controller

The frequency response of the amplitude of the transfer function ω_m/T_l is depicted in Fig. 5.22. The gains for the PI controllers are: $K_{p,i} = 0.2$, $K_{i,i} = 1 \times 10^{-3}$, $K_{p,\omega_m} = 0.1$ and $K_{i,\omega_m} = 1 \times 10^{-3}$ in 5.14. The parameters of the machines which are used here are given in Appendix A.1. In Fig. 5.22, the effect of a_{LT} is clear. There is a significant reduction in the rotor speed frequency response over the considered frequency range.

5.4.3 Experimental Results

The estimated load torque feedforward is implemented on the XC3S1600E FPGA. The PI speed and current controllers are already implemented for the proposed self-sensing algorithm, explained in Section 4.4, as well as the load torque estimation algorithm explained earlier in this chapter. The FPGA is programmed in such a way that the value for a_{LT} is tunable by using the rotary encoder which is provided by the FPGA evaluation board. In this way, it is possible to check the influence of a_{LT} gain in real time. The influence of a_{LT} on the dynamic behaviour of the drive can be studied using aforementioned process. The performance of load torque feedforward is described for different load torque profiles in this section.

A. Influence of the Gain a_{LT}

The influence of the gain a_{LT} is analysed for three different types of load torque waveforms. As a first test, the behaviour of the drive under a step load change is examined. Secondly, a load torque with rectangular waveform is applied. As a last test, the dynamical behaviour of the drive under a sinusoidally varying load torque is studied. The tested machine operates with a self-sensing current commutation algorithm and PI speed and current controllers.

Step loading and unloading In Section 5.3, it is described how to implement a variable load using a three-phase passive rectifier and a DC chopper. The BLDC machine is now loaded with a fixed load. This is achieved by connecting a resistor of $1.36\ \Omega$ directly to the DC-side of the three-phase passive rectifier. The response of the machine to such a loading of the machine is given in Fig. 5.23. Once the machine reaches its setpoint of 1000 rpm, the machine is unloaded again. The response of the rotor speed to the unloading of the machine is depicted in Fig. 5.24. It can be seen that the effect of load torque feedforward is twofold:

- By using load torque feedforward, the deviation from the speed reference is reduced with 42% when the machine is loaded, and with 61% when the machine is unloaded.
- Because the deviation from the speed reference is limited, it is easier for the PI current and speed controllers to bring the rotor speed back to its setpoint. This leads to a reduction of the settling time[1] with 754 ms when the machine is unloaded, and with 1316 ms when the machine is loaded.

[1] A 5% settling time is used. The settling time is then defined as the time needed to get back within 5% of the speed reference.

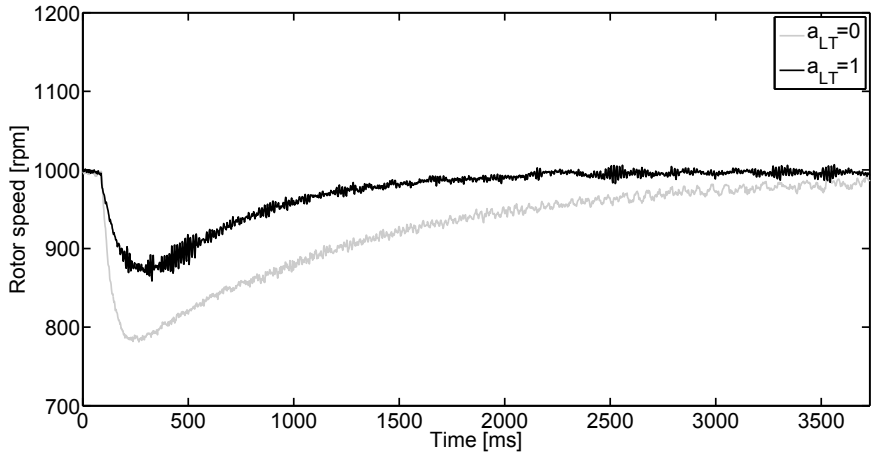

Figure 5.23. Experimental results, influence of a_{LT} on the rotor speed response to a sudden loading of the machine

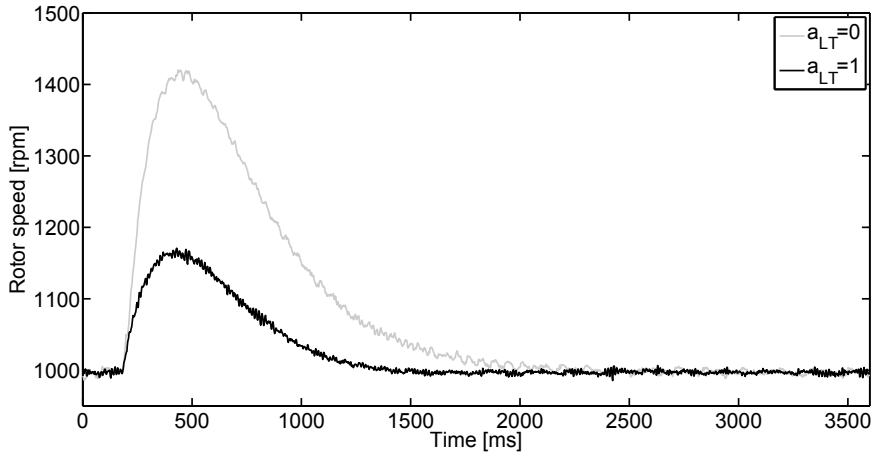

Figure 5.24. Experimental results, influence of a_{LT} on the rotor speed response to a sudden unloading of the machine

Rectangular load torque waveform The effect of a_{LT} on the dynamical behaviour of the drive to a rectangular load torque waveform with a period of 418 ms is examined. The BLDC machine is fed with a DC-bus voltage of 4 V. The speed reference is 1000 rpm. The effect of a_{LT} on the amplitude of the rotor speed oscillation is depicted in Fig. 5.25. In this figure, the minimum and maximum rotor speeds that occur for a certain value of a_{LT}, are shown.

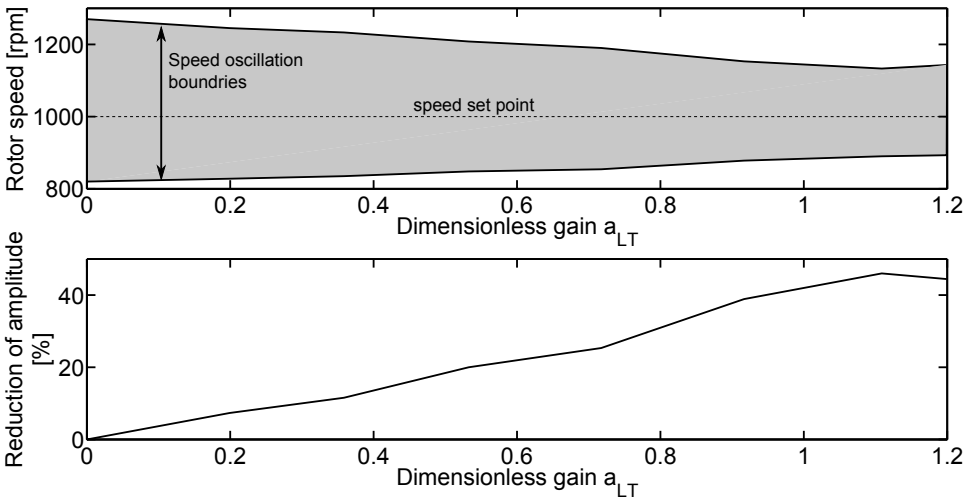

Figure 5.25. Experimental results, influence of a_{LT} on the amplitude of the oscillation, when the machine is loaded with a load torque with rectangular waveform (top). The corresponding reduction in the amplitude is also given (bottom)

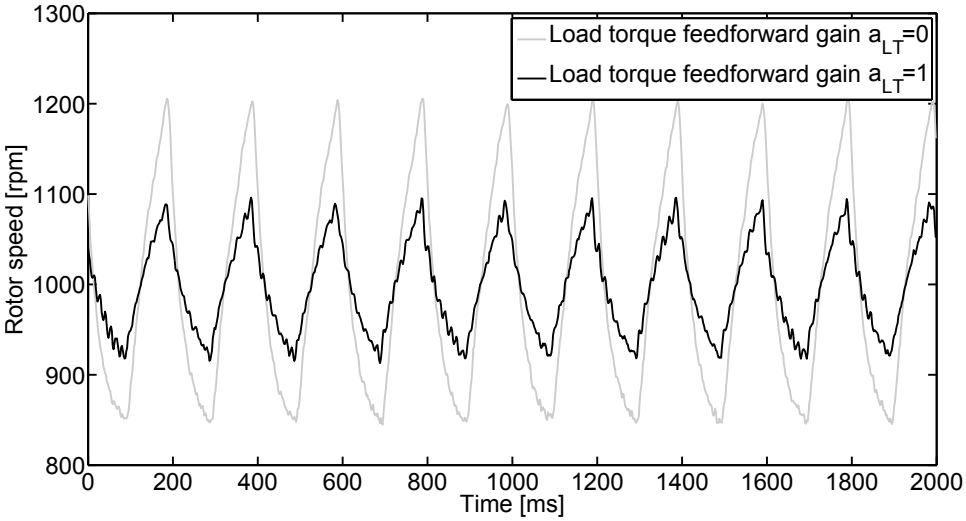

Figure 5.26. Experimental results, comparison of a_{LT} influence on the amplitude of the oscillation, when the machine is loaded with a load torque with rectangular waveform

It can be noticed that the effect of load torque feedforward is significant. When $a_{LT} = 0$, i.e. in the case where there is no load torque feedforward,

the rotor speed oscillates between 820 rpm and 1270 rpm. The amplitude of the oscillation is 225 rpm. When a_{LT} is increased, the amplitude of the oscillation decreases. The reduction of the oscillation amplitude, in terms of percentage, is also given in Fig. 5.25. When $a_{LT} = 1$, the amplitude of the oscillation is reduced with 46 % when compared with the case where $a_{LT} = 0$. The amplitude reduction varies semi-linearly with a_{LT}. However, a full elimination is not possible. Further increase in a_{LT} gain results in higher oscillations.

A comparison of two different a_{LT} gains are given in Fig. 5.26 which illustrates the effect of a_{LT} gain on a variable rectangular load torque.

Sinusoidal load torque waveform The effect of a_{LT} on the dynamical behaviour of the drive with a sinusoidal load torque waveform with a period of 474 ms is examined. The BLDC machine is fed with a DC-bus voltage of 6 V. The load torque is generated by controlling the current flowing through the mechanically coupled BLDC machine working as generator. The reference speed is increased to 1500 rpm. The influence of a_{LT} on the oscillation amplitude is shown in Fig. 5.27. When $a_{LT} = 0$, the rotor speed oscillates between 1078 rpm and 1922 rpm. Increasing a_{LT} again results in a decrease of the oscillation amplitude. When a_{LT} is close to 1, the oscillation amplitude is reduced by approximately 65 %. Also for sinusoidal loading conditions, the amplitude reduction varies about linearly with a_{LT}. A comparison of three different a_{LT} gains is given in Fig. 5.28 illustrating the effect of a_{LT} gain on variable sinusoidal load torque.

B. Influence of the Frequency of the Applied Load Torque

The effect of the load torque frequency on the performance of the load torque feedforward is analysed in this section. Rectangular and sinusoidal waveforms for the load torque are considered in this study. The highest period in the experiments is 680 ms, the lowest period is 18 ms. When the period becomes smaller than 18 ms, the variation in the rotor speed of the BLDC machine, due to the applied load torque, becomes very small (smaller than the noise in the speed estimation). The reason is that due to the mechanical time constant of the system including two mechanically coupled BLDC machines filters the frequencies higher than 55 Hz and it appears as a constant load torque.

Rectangular load torque waveform In this experiment, a DC-bus voltage of 4 V is used. The rotor speed reference is 1000 rpm. Rectangular waveforms with periods of 418 ms, 198 ms, 84 ms, 42 ms and 18 ms are used as external applied load torques. The results are given in Fig. 5.29. For low-frequency

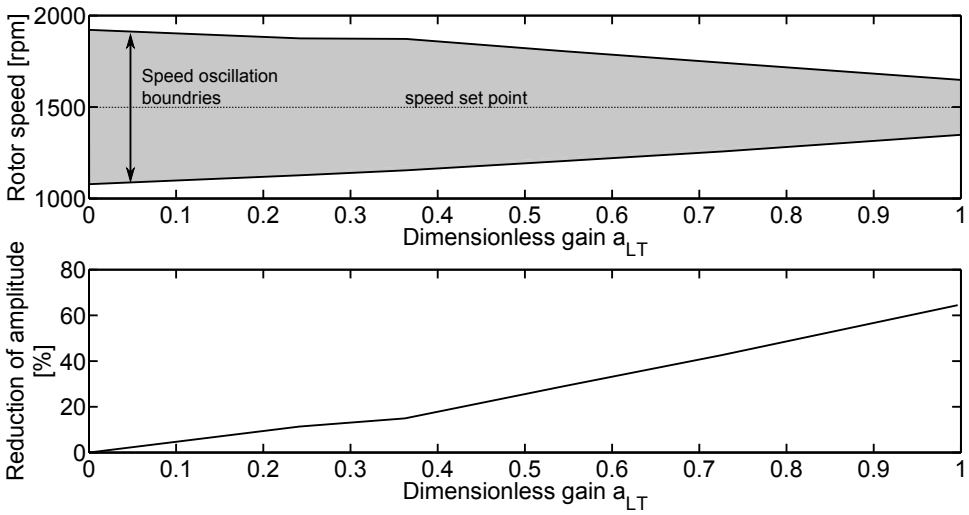

Figure 5.27. Experimental results, influence of a_{LT} on the amplitude of the oscillation, when the machine is loaded with a load torque with sinusoidal waveform (top). The corresponding reduction in the amplitude is also given (bottom)

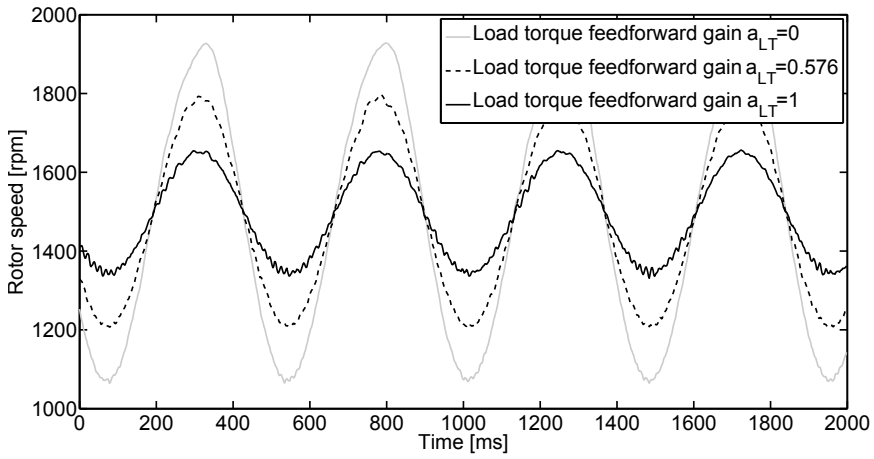

Figure 5.28. Experimental results, comparison of a_{LT} influence on the amplitude of the oscillation, when the machine is loaded with a load torque with sinusoidal waveform

load torques (waveforms with periods 418 ms, 198 ms and 84 ms) there is a clear and large reduction of the oscillation period (a reduction of 47 %, 50 % and 55 %, respectively).

For a load torque with higher frequency (waveforms with periods 42 ms and 18 ms), there still is a reduction in the oscillation period. For the waveform with a period of 18 ms, there is a reduction of the oscillation period, which is smaller than that for the other waveforms. However, for these two high frequency varying load torque tests, load torque reference appears as a constant torque to the motor and generator and it is eliminated by speed and current controllers of the motor in "*steady state*".

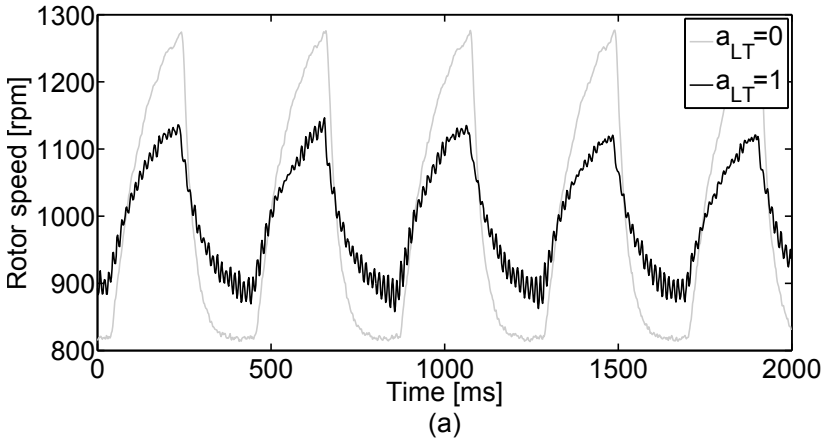
1300
1200
1100
1000
900
800
Rotor speed [rpm]
0
500
1000
1500
2000
Time [ms]
a_LT=0
a_LT=1
(a)

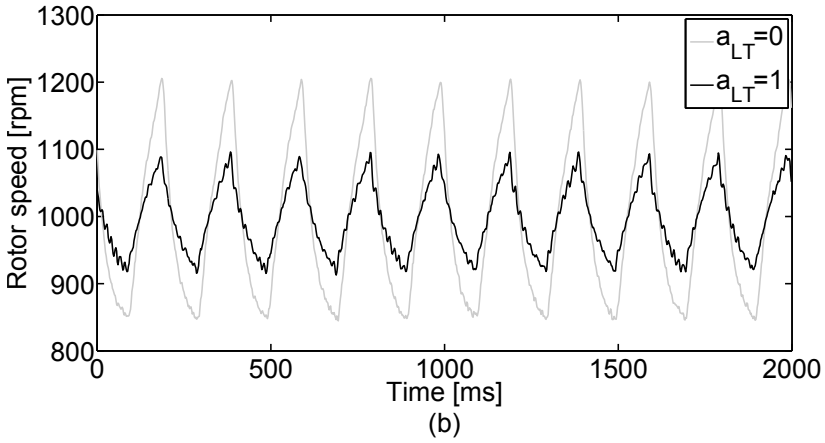
1300
1200
1100
1000
900
800
Rotor speed [rpm]
0
500
1000
1500
2000
Time [ms]
a_LT=0
a_LT=1
(b)

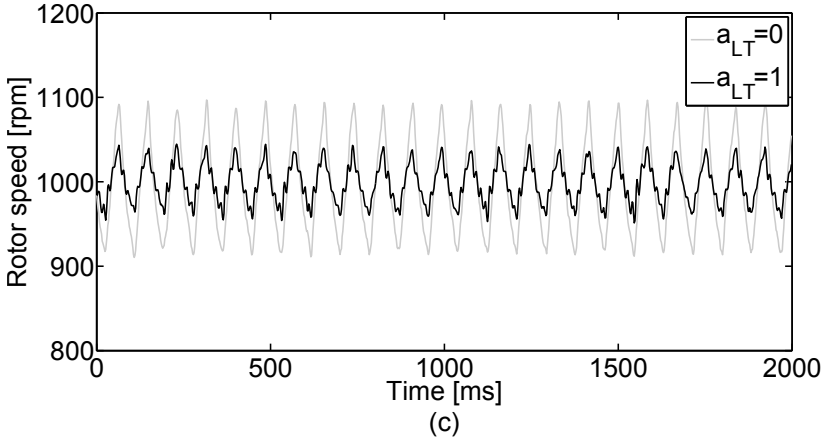
1200
1100
1000
900
800
Rotor speed [rpm]
0
500
1000
1500
2000
Time [ms]
a_LT=0
a_LT=1
(c)

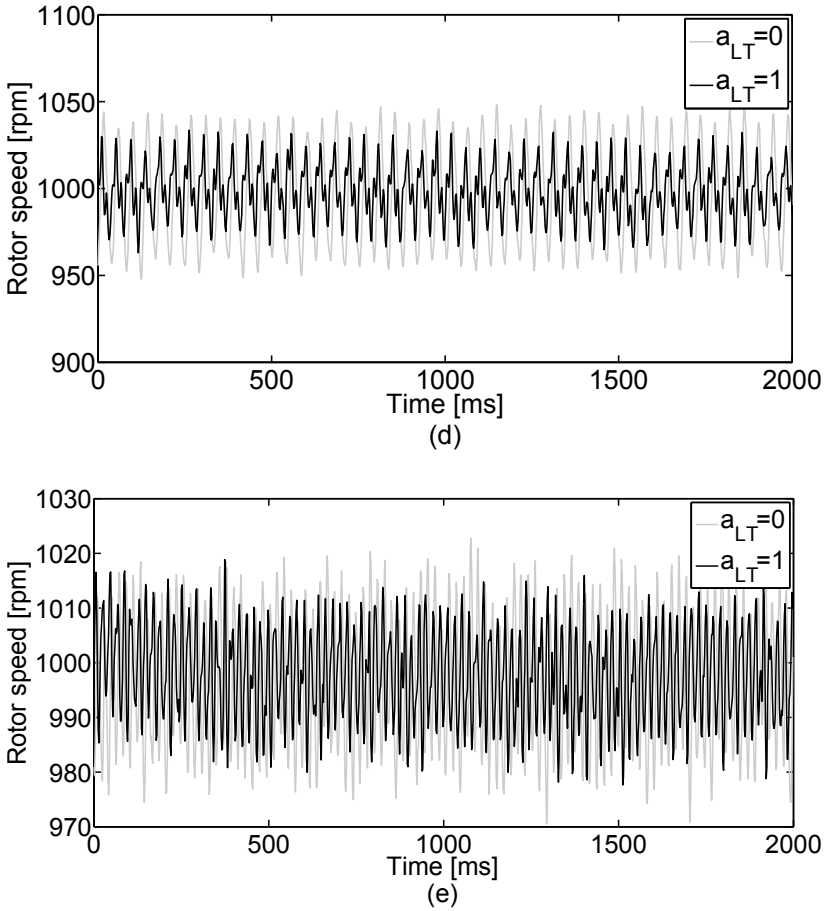

Figure 5.29. Experimental results, the effect of a_{LT} on the rotor speed when applying a load torque with rectangular waveform with a period of (a): 418 ms, (b): 198 ms, (c): 84 ms and (d): 42 ms and (e): 18 ms

Sinusoidal load torque waveform The larger the periods of the sinusoidal loading, the more significant is the effect of load torque feedforward on the dynamic stiffness of the drive for both high-frequency loading (tested by rectangular load torques) and for low-frequency loading (tested by sinusoidal load torques). The tests are carried out for sinusoidal load torque waveforms with a period of 680 ms, 474 ms and 220 ms. The results are given in Fig. 5.30.

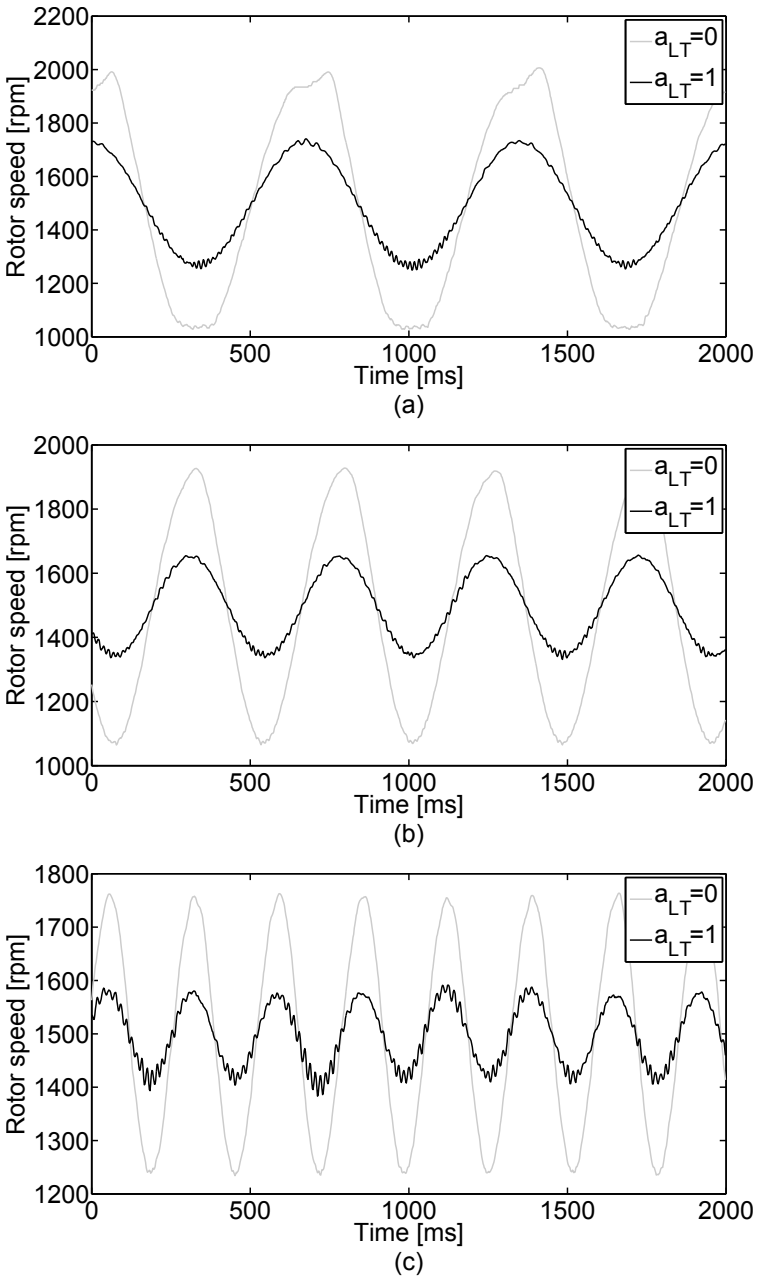

Figure 5.30. Experimental results, the effect of a_{LT} on the rotor speed when applying a load torque with sinusoidal waveform with a period of (a): 680 ms, (b): 474 ms and (c): 220 ms

5.5 Parameter Sensitivity Analysis

In the previous chapters, the proposed speed, position and load torque estimators are explained and discussed. The proposed algorithms are simulated in Matlab/Simulink and the results are verified by experiments on BLDC machines. To evaluate the parameter sensitivity of the algorithms, the influence of parameter uncertainties on the estimation results are examined in this section. In this section, the influence of two parameters will be studied: the back-EMF constant K_e and the inertia J.

The reason for choosing these two parameters is that the parameter K_e can vary up to 15% due to a change in the working temperature of the machine. The parameter J can change by changing the coupled load to the machine.

In this paragraph, the influence of an inaccurate back-EMF constant K_e is studied. The back-EMF constant K_e is used in equations (4.35) and (4.36) to estimate the rotor speed and the function F of the BLDC machine, respectively. The speed estimation is used to obtain a load torque estimation. This implies that a wrong value for K_e may have an influence on the load torque estimation as well. The back-EMF constant varies according to the temperature. Therefore, the effect of errors in K_e on the speed, F and load torque estimation will be examined.

The effect of K_e on the speed estimation is depicted in Fig. 5.31(a). The nominal value for K_e is represented by $K_{e,n}$. Small as well as large values for K_e are considered in the simulations. The rotor speed estimation $\hat{\omega}$ is inversely proportional with the square root of K_e. This entails that $\hat{\omega}$ becomes larger for smaller values of K_e, and vice versa. Increasing K_e with a factor 1.15 leads to a decrease of $\hat{\omega}$ with a factor of 0.9325. Decreasing K_e with a factor 0.85 leads to an increase of $\hat{\omega}$ with a factor of 1.085.

The effect of K_e on the load torque estimation is depicted in Fig. 5.31(b). The effect of K_e on the load torque estimation is rather small, especially when compared with the influence of the inertia J on the load torque estimation, which is described in next paragraph.

The effect of K_e on the function F is shown in Fig. 5.31(c). The voltage constant K_e depends on the permanent magnets flux hence it depends on temperature.

In order to test the effects of the temperature on the performance of the load torque

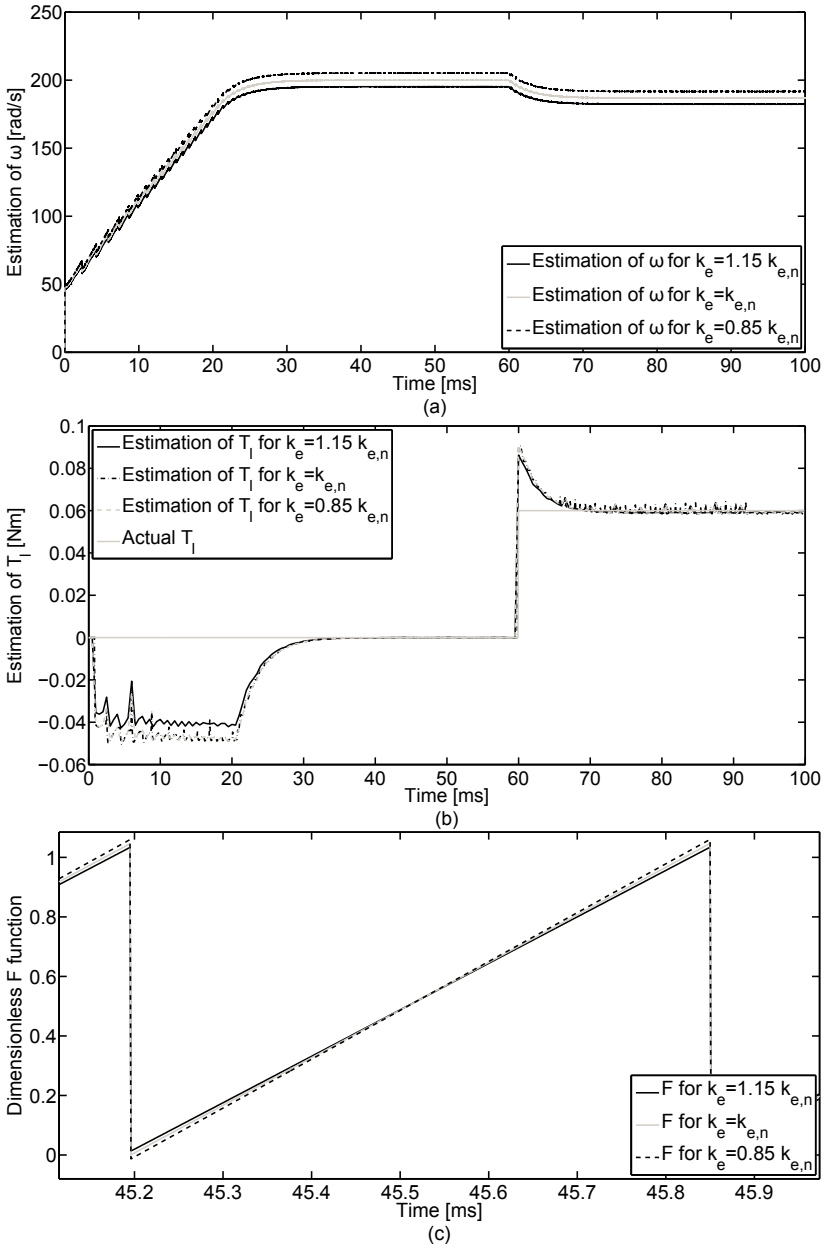

Figure 5.31. Simulation results, (a): Influence of errors in the value of K_e on the speed estimation, (b): Influence of errors in the value of K_e on the load torque estimation, (c): Influence of errors in the value of K_e on the F function (the slope parts of each phase are merged together and negative slopes are changed to positive)

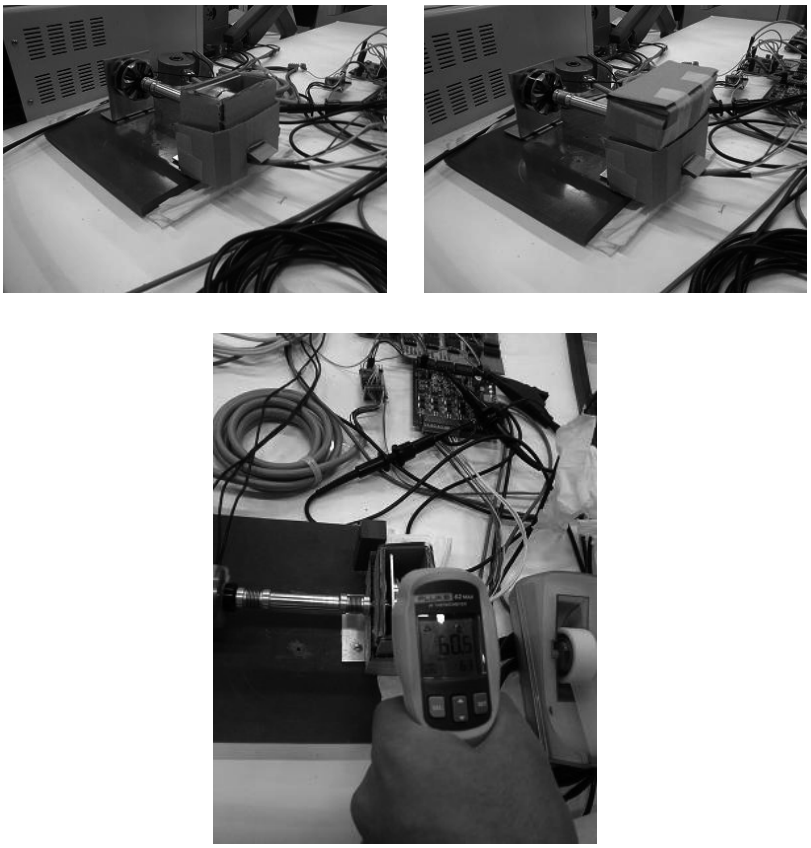

Figure 5.32. Increasing the machine temperature

feedforward an experiment is carried out as follows:

A loaded BLDC machine is driven for a while with a tight enclosure to avoid cooling caused by the air flow (see Fig. 5.32). The temperature of the rotor yoke (the tested motor is a cup-motor with external rotor, see the specifications in Appendix A.1) is monitored using an infrared thermometer. The surface of the rotor yoke is coated with a plastic tape in order to reduce the reflection for more precise temperature measurement. When the temperature of the rotor reaches 60 degree Celsius different tests are carried out in order to evaluate the performance of the proposed algorithm.

In Fig. 5.33 the variation of the speed due to a sudden increase in the load torque is

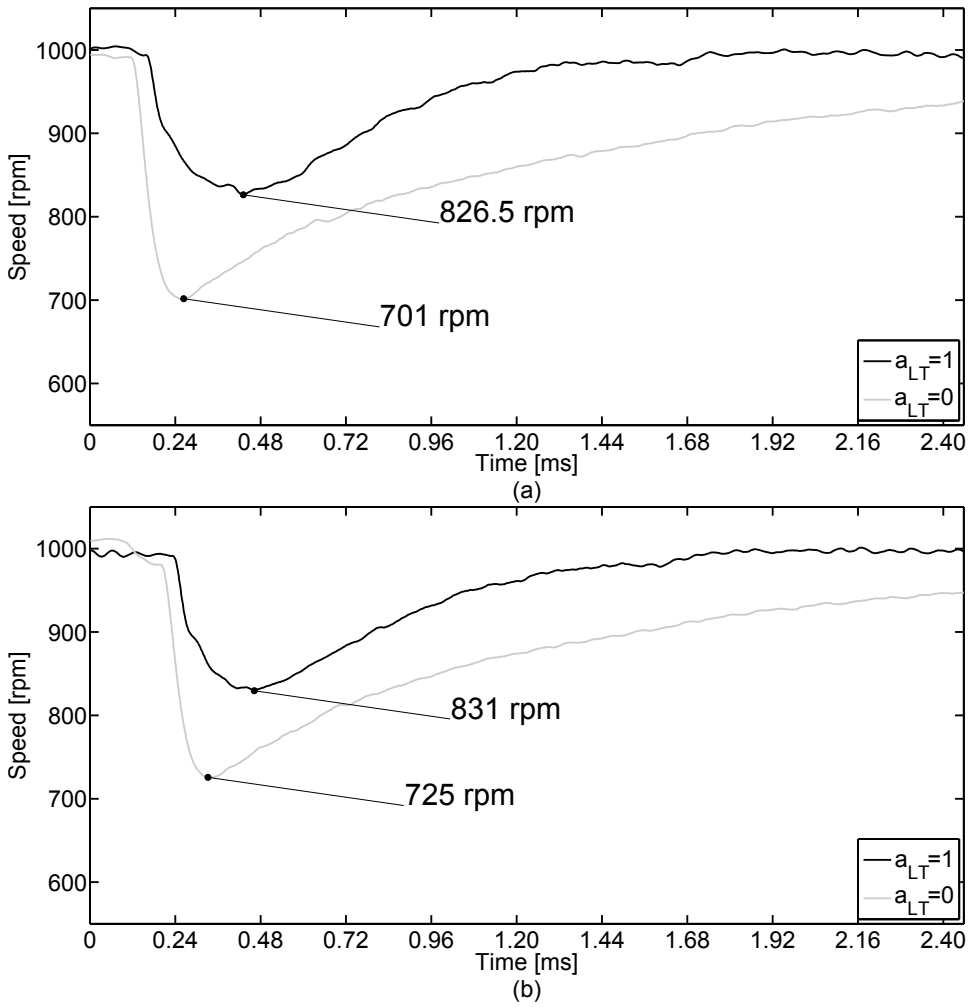

Figure 5.33. Experimental results, performance evaluation of the load torque feedforward during loading of the machine, (a): ≈ 24 degree Celsius 41.9% reduction in the overshoot, (b): ≈ 60 degree Celsius 38.5% reduction in the overshoot, tested machine: Trapezoidal back-EMF

compared with and without load torque feedforward. In a similar way, In Fig. 5.34 the variation of the speed due to a sudden decrease in the load torque is compared with and without load torque feedforward. These figures show that the performance of the load torque feedforward during the changes of K_e due to the temperature change in rejecting the disturbances slightly degrades. Figs. 5.33(b) and 5.34(b) show a decrease in the speed overshoot reduction compared to Figs. 5.34(a) and

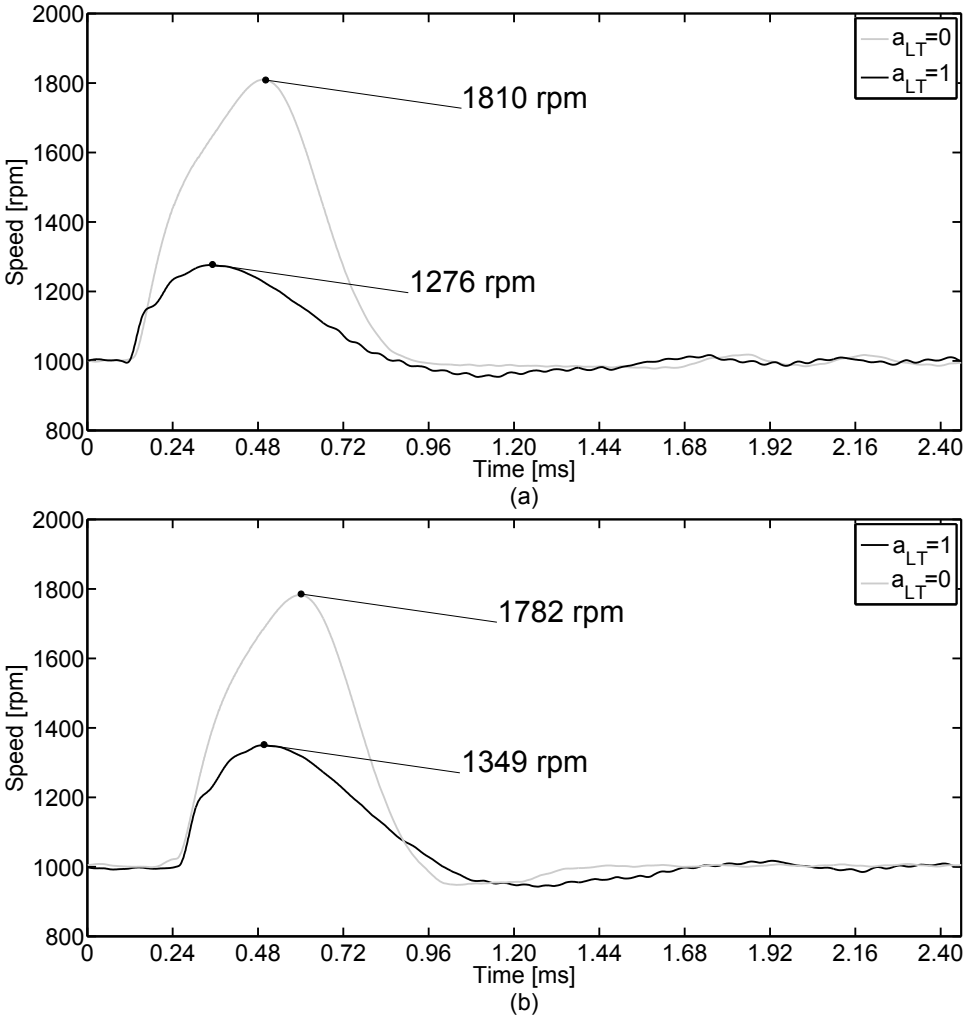

Figure 5.34. Experimental results, performance evaluation of the load torque feedforward during unloading of the machine, (a): $\approx$ 24 degree Celsius 65.9% reduction in the overshoot, (b): $\approx$ 60 degree Celsius 55.3% reduction in the overshoot, tested machine: Trapezoidal back-EMF

5.33(a) which could be explained by the effect on the estimated torque of a decrease in K_e due to the temperature rise. Although the temperature increase has a bad influence on the load torque feedforward performance, applying this feedforward path improves dynamic stiffness of the control loop greatly.

The test is done one more time to evaluate the performance of the self-sensing

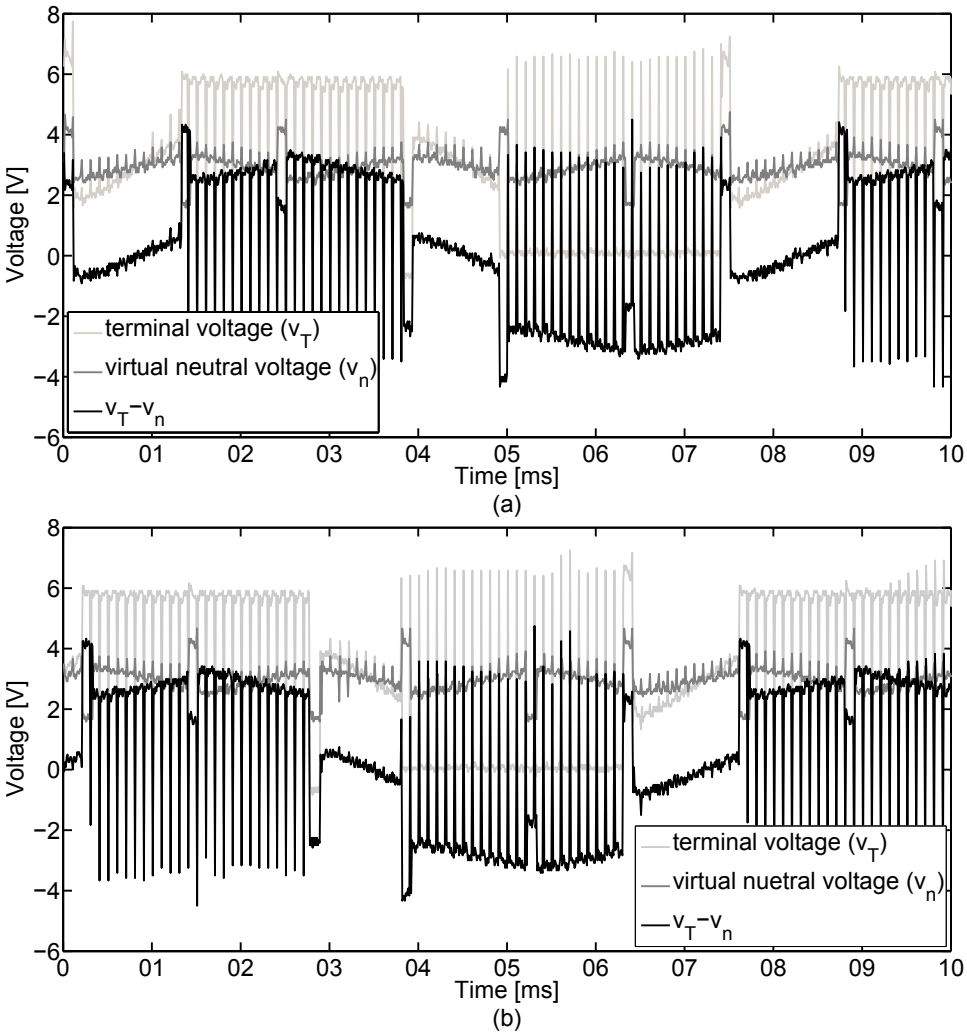

Figure 5.35. Experimental results, performance evaluation of the commutation during (a): low temperature (25 degree Celsius) and (b): high temperature ($\approx$ 60 degree Celsius)

detection of the commutation instants. First the machine is coupled with full load torque and is driven at 1000 rpm. The results are captured using an oscilloscope. Then after a few minutes working inside the enclosure when the temperature of the rotor reaches 60 degree Celsius the terminal voltage (v_T), virtual neutral voltage (v_n) and ($v_T - v_n$) are measured again using an oscilloscope. The results are plotted from the oscilloscope and shown in Fig. 5.35. In Figs. 5.33 and 5.34 a speed evolution in loading and unloading transients is presented and in Fig. 5.35

a more detailed view of the commutation instants and PWM pulses are shown at steady state.

5.5.1 Effect of Uncertainties in J on the Load Torque Estimation

The inertia J is involved only in estimating the load torque from speed estimations. The measurement results for different values of J within the estimation algorithm are given in Fig. 5.36. The load torque estimation results are low-pass filtered in order to make the results more visible. The nominal value for J is represented by J_n. The inertia J is changed over a wide range, from $0.25J_n$ to $4J_n$.

The load torque estimation and its performance strongly depend on the estimation of the value for J. The value for J could be estimated for more critical applications which need accurate value of load torque estimation. However, the effect of an increased J value can be lowered by decreasing the feedforward gain g_{TL} and vice versa.

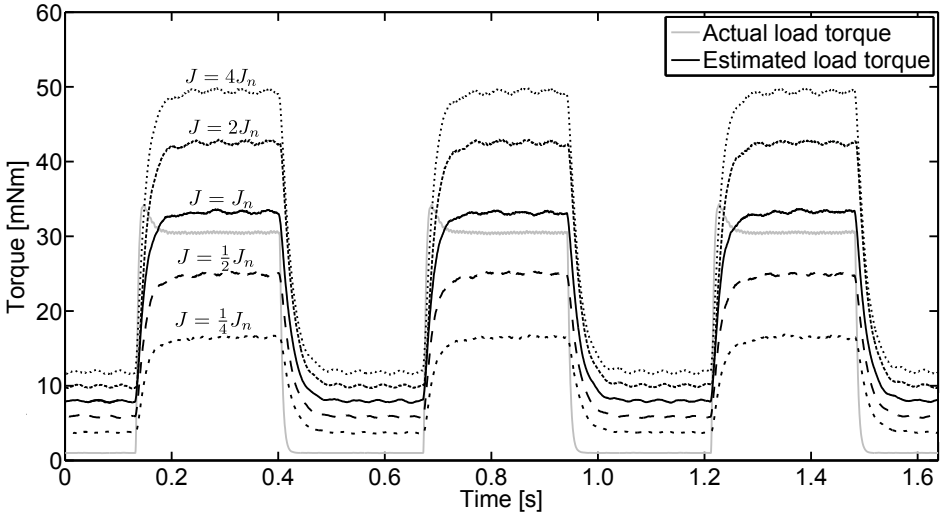

Figure 5.36. Experimental results, influence of errors in the value of J on the load torque estimation

5.6 Conclusions

In this section, load torque estimation feedforward is proposed as a way to improve the dynamic stiffness of a self-sensing BLDC drive. The focus is on the influence of load torque disturbances on the rotor speed. The positive effect of load torque feedforward on the dynamic stiffness was proven theoretically, by means of the frequency response of the transfer function that describes the relation between the rotor speed and the load torque. The algorithm is then tested on an experimental setup using an FPGA. The following conclusions are then drawn:

- The influence of load torque feedforward is studied for several loading conditions. For a load torque that varies periodically in time, a reduction of around 55 % in the rotor speed oscillations is achieved. For load torque disturbances that occur occasionally (modelled as a step load), there is an additional advantage of a reduced settling time.
- The frequency band at which the load torque feedforward is beneficial was studied. From the theoretical results, it can be concluded that the effect is positive over the complete frequency band that is of importance in practical applications. This is also observed in the practical implementation. For higher frequencies (the limit is determined based on the mechanical time constant of the system), a varying load torque appears as a constant load torque. The rotor speed does not vary with the load torque variation frequency due ot the inertia. This averaged load torque (due to the inertia) can be eliminated using conventional speed controllers.

Chapter 6

Model Based Predictive Control for BLDC Machines

6.1 Introduction

In conventional speed controlled BLDC drives, two PI(D) controllers can be used to control the rotor speed and the current/torque of the drive. They allow to control the rotor speed to its set-point, by producing the maximum possible electromagnetic torque while keeping the current within allowed limits. The parameters of the PI(D) controllers can be determined in several ways: using a trial and error approach, using auto tuning algorithms (e.g. Åström-Hägglund, Kaiser-Chiara, Kaiser-Rajka and Ziegler-Nichols) or by using root locus and frequency response techniques to determine the gain and phase margin of the PI(D) controllers. These techniques require a model of the process. The inherent disadvantage of the PI(D) controllers is that they only use historical information of the error between the set-point and the measurement. Using a model of the drive system to predict future process outputs and optimizing future control actions often leads to a better performance of the controlled drive. This class of control strategies is referred to Model Based Predictive Control (MBPC) or shorter Model Predictive Control (MPC).

An MPC strategy is computationally more demanding than PI(D) controllers. However, by rapid improvement and decrease in the price of powerful stand alone computational units such as FPGAs, implementation of model based predictive control algorithms is becoming more and more of interest in the fields of control of power electronics converters and electrical drive systems. MPBC is already applied for a wide variety of applications in the field of power electronics and drives. In [ChangliangXia2013] a finite state model predictive control (FS-MPC) scheme is used in order to reduce the torque ripple in BLDC machines as a result of current

commutation actions. Speed ripple reduction in a PMSM drive is investigated using a cascade MPBC structure in [ShanChai2013]. In [Vyncke2013] the use of an FS-MPC is investigated in order to control the voltage of flying capacitor converters by a proper cost function design method and efficient FPGA implementation. An MPC scheme is suggested [Lim2013] in a drive system consisting of two PMSM machines. In such a case, power supply is often realised by using two separate three phase inverters. However, by using MPC, a single inverter with less switches could be used, reducing the amount of hardware. so that they are supplied and controlled via this inverter. Another important application field of MPC is in the development of fault tolerant drives and diagnostics of power electronics and drive systems [Lim2014a, Druant2015, Guzman2014, Guzman2015].

During the last five years, model predictive direct torque control (MPDTC) and model predictive current and speed control techniques have drawn attention in the area of high performance control of electrical drives. A comparison between PI and three different MPC current controllers is made in [Lim2014a] for a two motor drive supplied by a five leg inverter. However, the improvement in the dynamic behaviour of the speed control is not studied. In [Lim2014a] a finite control set model predictive control (FCS-MPC) based current controller is compared with a PI PWM current controller for a five phase induction machine. Experimental results verify that the MPC is faster than PI PWM in reference current tracking for both of the applications. In [Rodriguez2012] a comparative study has been carried out between field oriented torque control (FOC) and predictive torque control (PTC) and it verifies that PTC has better performance during transients compared to the FOC. The design and implementation of the MPC for electrical drives is discussed in [Bolognani2009] and a more detailed design of the predictive speed controller is given in [Fuentes2014, Preindl2013a] to overcome the drawbacks of the cascade speed controllers. Experimental results on PMSMs and induction machines under different operating conditions verify the capabilities of MPC algorithms to control electrical drives. Different direct torque controllers based on model predictive algorithm are mentioned in [Geyer2009a, Geyer2009b, Geyer2012, Geyer2013, Papafotiou2009, Riveros2013]. In [Barrero2009a, Barrero2009b, Barrero2011, Duran2011] different model predictive current control algorithms are implemented. However, the speed control algorithm is not studied in these latter studies. In [Preindl2013b, Preindl2013c], a cascaded control strategy is used. First a speed error is calculated and a PI controller is used to generate the torque reference which is used to control the torque by the MP-DTC algorithm. The dominant term of the MPC cost function in these studies is the torque. A contribution of the work presented in this thesis compared to the literature such as [Preindl2013b, Preindl2013c] is the effort to improve the dynamic behaviour of drives with low inertia machines for which the cascaded control strategies fail to provide a high performance in the dynamic behaviour. As for low inertia machines the electrical and mechanical time constants have values of the same order so that these systems cannot be treated as two independent first order systems, one for mechanical and one for electrical sub-

systems. To deal with this problem the proposed methodology takes the mechanical subsystem of the machine into account during tuning of the current controller. This is done by including the speed error term in the cost function of the proposed MPC algorithm. In this section a six step current commutation is applied to drive a BLDC machine. Using the proposed MPC the influence of different parameters of the proposed algorithm on the improvement of the controlled system dynamic behaviour is also analysed.

In Section 6.2 a short introduction about the BLDC machine model is given. In Section 6.2 the effects of the machine inertia on the cascaded PI controllers are studied and the dynamic performance is evaluated. In Section 6.5 a model based predictive controller is introduced and the effects of different parameters of the proposed algorithm in the improvement of the dynamic behaviour of low inertia BLDC machines is investigated. In Section 6.6 different implementation aspects of the proposed method on an FPGA evaluation board are studied. In 6.7 a comparison is made in order to show the difference of the speed control performance between a conventional PI controller and the proposed MPC. Within the paper the performance of the proposed algorithm is evaluated by simulation and verified by experimental results as well. Additionally, the improvement on the disturbance rejection properties of the proposed algorithm during the load torque variations is studied. In the second part of this chapter the proposed MPC is implemented together with the self-sensing commutation method which is introduced in 4.4. Then, the advantages of the infusion of MPC and self-sensing commutation is studied in 6.9.

6.2 BLDC Drive Model

The electrical and mechanical equations to simulate the behaviour of a BLDC machine are described in details in [Darba2014, Darba2015a]. The system of time differential equations is represented using a state space model. It is then discretised by using a zero order hold technique to be suitable for digital representation.

The continuous time machine model together with the inverter model will be used to simulate the process outputs of the real system. A discrete-time model, described later, is used for practical implementation on a digital controller in order to predict the future outputs of the system within the MPC algorithm. Fig. 6.1 shows the schematic diagram of a BLDC machine connected to a three-phase inverter. The BLDC machine is connected to a DC supply through the inverter. This inverter serves as an input to the electrical equations of the machine. The model of the inverter depends on the switching strategy. A PWM technique is used to control the inverter output voltage V_{out} to the machine and to maintain the maximum current. The output voltage of the inverter applied to the machine terminals (V_T) is then

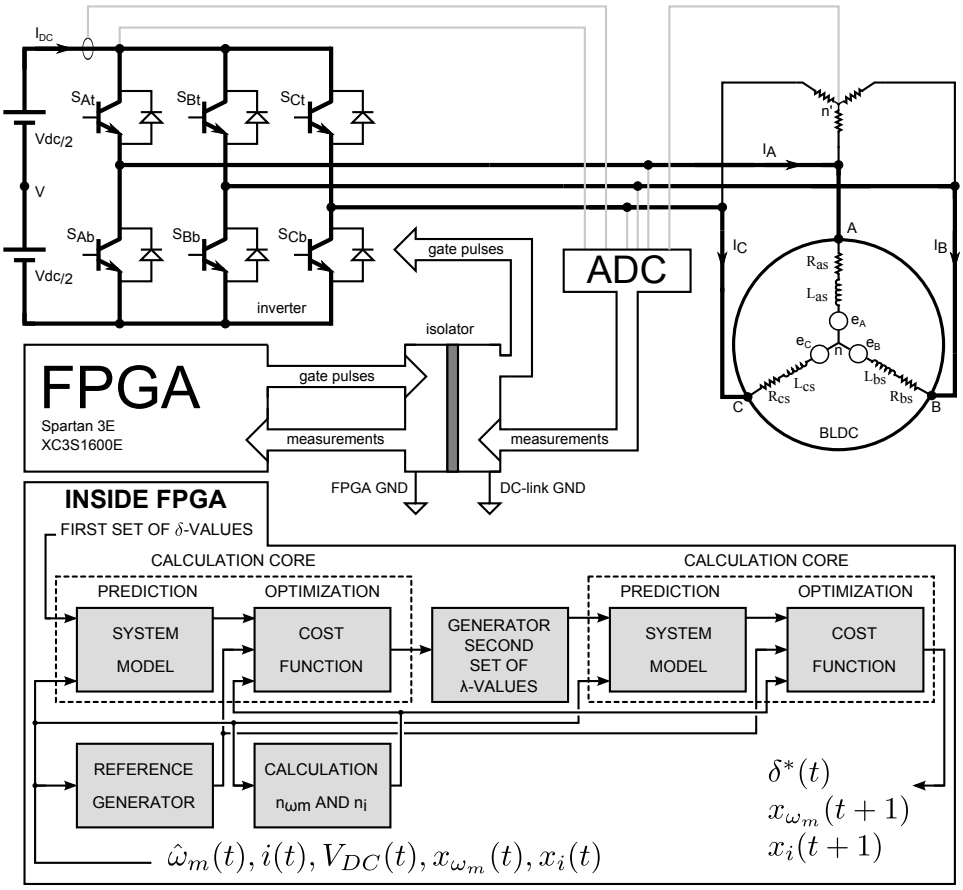

Figure 6.1. Schematic diagram of the test setup

controlled by a duty ratio δ for which:

$$V_{\text{out}} = V_T = \delta V_{DC}; \quad 0 \leq \delta \leq 1 \tag{6.1}$$

V_T could be equal to $V_A - V_B$ or $V_A - V_C$ or $V_B - V_C$ based on the commutation state of the BLDC machine. Fig. 6.2 shows the duty ratio δ, output voltage of the inverter and phase current of the machine (T_s is the PWM period). The produced electromagnetic torque by the machine is proportional to the phase currents of the machine.

$$T_{em} = K_t \phi i \tag{6.2}$$

where K_t is the torque constant of the machine. By considering parameter K_e as

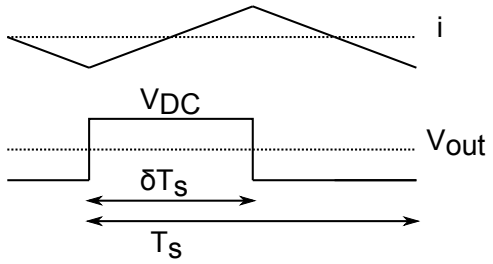

Figure 6.2. Inverter output voltage, definition of the duty cycle δ, phase current

voltage constant of the machine, the speed induced EMF of the machine is proportional to the speed and it can be written as

$$E = K_e \phi \omega \tag{6.3}$$

The model of the inverter depends on the switching strategy. A PWM technique is used to control the inverter output voltage V_{out} to the machine and to maintain the maximum current. In this study, the model is derived for a switching strategy in which the state of the semiconductor switches of the same leg are complementary. A similar approach can be used for other switching strategies.

6.3 Parameter Tuning of Cascaded Controller

6.3.1 Subsystems with Large Difference in the System Time Constants

The electromagnetic torque in an electrical machine is determined by the stator current. When considering the dynamical behaviour, the response time of this torque on a stator voltage variation depends on the electric time constant, while the time response of the mechanical system depends on the mechanical time constant. In most cases, the time delays in the electric subsystem are negligible compared to the response time of the mechanical subsystem. In such cases, the speed control loop analysis and tuning can be performed under the assumption that the current controller has a very high bandwidth.

The current control loop controls the stator currents by changing the duty ratio δ within the PWM and hence steers the average value of the applied voltage. A change in the value of the current reference changes the produced electromagnetic torque. Considering the block diagram in Fig. 6.3(a) that models the cascaded speed and current controller together with the electrical and mechanical subsystems

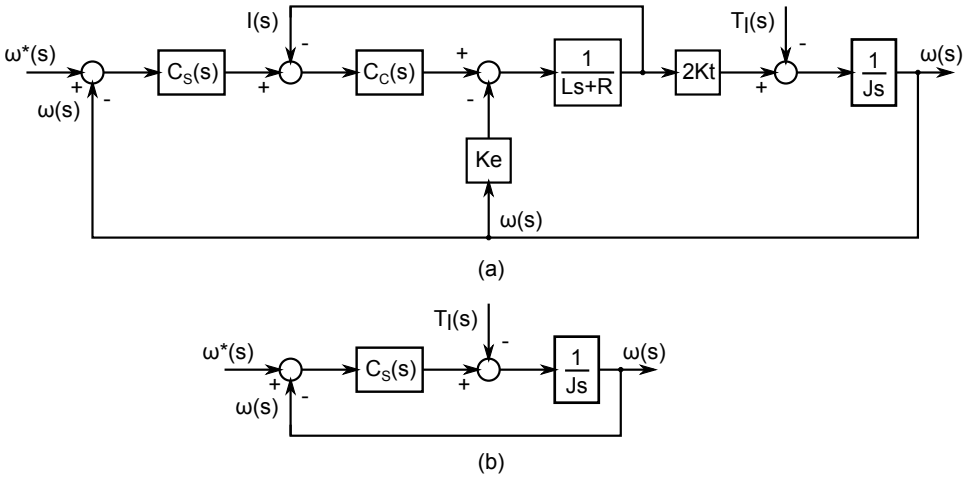

Figure 6.3. Schematic diagram for (a): representation of the system model (6.6), (b): representation of the system model (6.9) and (6.11).

of a BLDC machine under PI control. The transfer function from the reference current to the current is given as:

$$\frac{I(s)}{I^*(s)} = \frac{JsC_c(s)}{Js(Ls + R + C_c(s)) + K_eK_t} \tag{6.4}$$

where I and I^* are the output current and reference current respectively, $C_c(s) = K_{p,c} + \frac{K_{i,c}}{s}$ is the transfer function of the PI current controller and L, R and J are the stator inductance, resistance and total inertia of machine. If the mechanical time constant is considered much larger than the electrical time constant ($\tau_m \gg \tau_e$) the gains of the current controller can be tuned by using the transfer function in (6.4) assuming a constant rotor speed. Tuning the gains using Matlab results in:

$$C_c(s) = 0.82 + \frac{0.95}{s} \tag{6.5}$$

Fig. 6.3(b) models the drive in case the dynamical behaviour of the inner and faster current control loop as well as electrical subsystem is considered to be negligible compared to the dynamical behaviour of the outer and slower speed control loop and mechanical subsystem. The transfer functions from speed reference and load torque to the rotor speed can be expressed as:

$$\begin{cases} \dfrac{\omega(s)}{\omega^*(s)}\Big|_{(T_L(s)=0)} = \dfrac{K_{p,s}s + K_{i,s}}{Js^2 + K_{p,s}s + K_{i,s}} \\ \dfrac{\omega(s)}{T_L(s)}\Big|_{(\omega^*(s)=0)} = -\dfrac{s}{Js^2 + K_{p,s}s + K_{i,s}} \end{cases} \tag{6.6}$$

where $K_{p,s}$ and $K_{i,s}$ are the proportional and integral gains of the PI speed controller $C_s(s) = K_{p,s} + \frac{K_{i,s}}{s}$ and T_L is the load torque, ω and ω^* are the mechanical output speed and reference speed values respectively. Using Matlab the gains of the speed controller, neglecting the electrical subsystem are tuned to: (speed controller bandwidth is 70.1 Hz)

$$C_s(s) = 0.06 + \frac{0.06}{s} \tag{6.7}$$

By using (6.6), the output speed $\omega(s)$ can be approximated by:

$$\omega(s) = \frac{\omega(s)}{\omega^*(s)}\Big|_{(T_L(s)=0)}.\omega^*(s) + \frac{\omega(s)}{T_L(s)}\Big|_{(\omega^*(s)=0)}.T_L(s) \tag{6.8}$$

where it can be used to calculate the speed response of the system.

6.3.2 Subsystems with Small Difference in the System Time Constants

When the inertia J is very low the mechanical and electrical time constants of the system are in the same order of magnitude. In such case the speed and current control loops cannot be described independently in order to tune the controller gains. Instead, the current controller and the electrical subsystem should be included in the transfer functions (6.6).

The schematic diagram of such a system is illustrated in Fig. 6.3(a) and the transfer functions from the reference speed and load torque to the rotor speed are given as:

$$\begin{cases} \dfrac{\omega(s)}{\omega^*(s)}\Big|_{(T_L(s)=0)} = \\ \dfrac{K_t C_s(s) C_c(s)}{Js(Ls + R + C_c(s)) + K_t C_s(s) C_c(s) + K_t K_e} \\ \dfrac{\omega(s)}{T_L(s)}\Big|_{(\omega(s)=0)} = \\ -\dfrac{C_c(s) + (Ls + R)}{Js(Ls + R + C_c(s)) + K_t C_s(s) C_c(s) + K_t K_e} \end{cases} \tag{6.9}$$

In this case the current controller $C_c(s)$ is tuned by taking into account the mechanical subsystem and the speed controller $C_s(s)$ is tuned by considering the electrical subsystem. The control parameters are given by: (speed controller bandwidth is 7.65 Hz)

$$C_s(s) = 0.005 + \frac{0.04}{s} \quad , \quad C_c(s) = 0.5 + \frac{0.5}{s} \tag{6.10}$$

Here, by using (6.9) instead of (6.6), $\omega(s)$ can be calculated by using (6.8).

6.4 Speed and Current Responses for the Cascaded Controllers

Using the model in Fig. 6.3(a), the current response $I(s)$ can be calculated using the following transfer functions from the reference current and load torque to the phase current as:

$$\begin{cases} \dfrac{I(s)}{\omega^*(s)}\Big|_{(T_L(s)=0)} = \\ \dfrac{JsC_s(s)C_c(s)}{Js(Ls+R+C_c(s))+K_tC_s(s)C_c(s)+K_tK_e} \\ \dfrac{I(s)}{T_L(s)}\Big|_{(\omega(s)=0)} = \\ \dfrac{C_c(s)C_s(s)+k_e}{Js(Ls+R+C_c(s))+K_tC_s(s)C_c(s)+K_tK_e} \end{cases} \tag{6.11}$$

hence, $I(s)$ can be approximated by:

$$I(s) = \frac{I(s)}{\omega^*(s)}\Big|_{(T_L(s)=0)}.\omega^*(s) + \frac{I(s)}{T_L(s)}\Big|_{(\omega^*(s)=0)}.T_L(s) \tag{6.12}$$

For the PI controllers, tuned independently and given in (6.5) and (6.7), the speed and current responses are plotted using (6.8) and (6.12) respectively in Fig. 6.4.

A step change in the speed reference from $\omega^* = 0$ rpm to $\omega^* = 1000$ rpm and the machine is considered to be in a no-load condition. The speed and current controllers are tuned considering (6.9) and the responses are given in Fig. 6.4 using (6.10).

The grey traces in Fig. 6.4 show the speed and current responses of the cascaded controller and for the set of controller gain values as given in (6.5) and (6.7). The dashed black traces in Fig. 6.4 show the speed and current responses for the set of controller gain values given in (6.10). The control system gains of (6.5) and (6.7) show a faster speed response then for the controller with the gains of (6.10). However, it can be seen that by tuning the electrical and mechanical controllers independently a maximum current of 7.5 A is drawn that is much higher than the allowable 2 A phase current of the machine. Moreover, due to neglecting the electrical subsystem, the phase margin is smaller than expected. This assumption leads to a less robust controller against parameter uncertainties. When the system is tuned as a second order system taking the electrical and mechanical subsystems

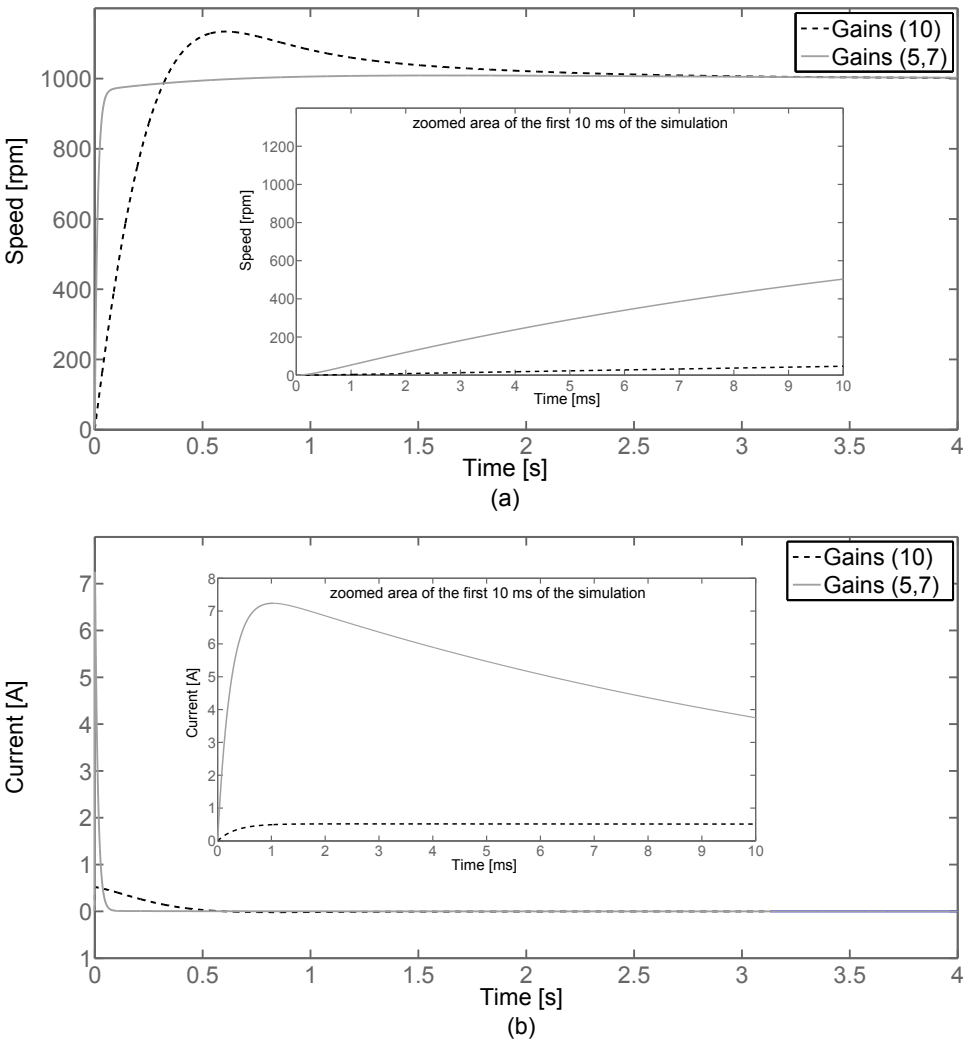

Figure 6.4. Simulation results for a comparison between electro-mechanically coupled and decoupled systems $\omega^*(s) = \frac{1000}{s}$, $T_L = 0$, (a): speed response, (b): current response

dynamics into account the current remains bounded and the speed response is slower, but with a more robust behaviour.

Considering a system with a large difference in the system time constants, if a bandwidth is assigned for the inner control loop (current), the bandwidth of the outer control loop (speed) is made smaller (i.e. 10 times) to have a stable operation. The only constraint that must be taken into account is the limitation of the current

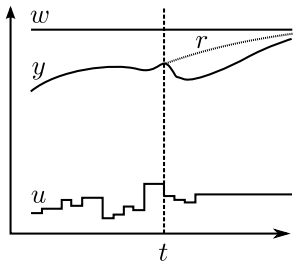

Figure 6.5. Scheme of the evolution of the signals in a MPC strategy

amplitude in this case. However, in the case of a low inertia application, the time constants are of the same order and neglecting the dynamics of the inner control loop when tuning the outer loop can result in unstable operation. Hence, the gains of both control loops must be tuned together taking into account the entire system. In that case, the solution with PI controllers often results in a lower bandwidth of the outer control loop (the bandwidth of 7.65 Hz compared to 70.1 Hz). Instead, in this paper, an MPC algorithm is proposed to control both the current and speed of the machine to obtain a short response time of a low inertia BLDC machine.

6.5 Model Based Predictive Control

In [Rodriguez2012, Bolognani2009, Fuentes2014, Preindl2013a] the advantages of MPC in the speed control of electrical drives over conventional cascaded controllers are described. In this study we consider that at time t a measurement of the system output $y(t)$ is available (Fig. 6.5). The set-point of the system output at time t is $w(t)$. At each time t, a prediction of the future system output $[y(t+1|t), ..., y(t+N|t)]$ is made that depends on the future control actions $[u(t|t), ..., u(t+N-1|t)]$. The parameter N represents the prediction horizon. The vector of the predicted system outputs [$y(t+1|t)$,...,$y(t+N|t)$] is compared with the reference trajectory $[r(t+1|t), ..., r(t+N|t)]$. The reference trajectory starts at $r(t|t) = y(t)$ and evolves towards the set-point $w(t)$. Future control actions $[u(t|t), ..., u(t+N-1|t)]$ are chosen in such a way that a cost function is minimized. This cost function usually depends on the difference between the predicted system outputs and the reference trajectory over the prediction horizon N. In MPC a prediction of future process outputs can be written as

$$y(t+k|t) = x(t+k|t) + n(t+k|t) \tag{6.13}$$

where x is the part of the output that results from applying the input u, to the model of the system. To keep the model manageable, not all aspects of the system are modelled. The output of the process is also susceptible to measurement noise.

These effects are captured in the variable n. The prediction $x(t+k|t)$ results from using the discrete time model of the process:

$$x(t) = \frac{B(q^{-1})}{A(q^{-1})}u(t) \quad , \quad n(t) = \frac{C(q^{-1})}{D(q^{-1})}e(t) \tag{6.14}$$

where $\frac{B(q^{-1})}{A(q^{-1})}$ represents the dynamical behaviour of the model and q^{-1} is the backwards shift operator. The unmodelled part of the output, n, is considered as a coloured noise process. It can be defined as a white noise process e that goes through a filter $\frac{C(q^{-1})}{D(q^{-1})}$.

The disturbance model which is chosen in this study is given as:

$$\frac{C(q^{-1})}{D(q^{-1})} = \frac{1}{1-q^{-1}} \tag{6.15}$$

For this choice of the disturbance model, the prediction of the values for n at future time instants is calculated as:

$$n(t+k|t) = n(t+k-1|t) + e(t+k|t) \tag{6.16}$$

where k varies from $k=1$ up to $k=N$. The value for $n(t)$, which was calculated from the measurement of the process output $y(t)$ and model output $x(t)$, is used over the complete prediction horizon. When the predictions for y are made, they can be compared with the reference signal r in the interval $[t+1, t+N]$:

$$r(t+k|t) = \alpha r(t+k-1|t) + (1-\alpha)w(t+k|t) \tag{6.17}$$

In this way, the reference signal determines how fast the output should evolve to its set-point w. The design parameter that controls this rate is α.

The basic equation used in the MPC scheme is introduced in (6.13). The first part of the right hand side of this equation, $x(t+k|t)$, is the modelled part of the output $y(t+k|t)$.

- The derived BLDC model is used to predict $\{x(t+k|t), k=1..N\}$ over the prediction horizon. The initial value for $x(0|0)$ is the measured/estimated value for $y(0)$. In the iterations thereafter, the initial value for $x(t|t)$ is equal to $x(t|t-1)$, which was predicted in the previous iteration.
- The disturbance model is used to predict $\{n(t+k|t), k=1..N\}$ over the prediction horizon. For the first prediction of an experiment, $\{n(k|0), k=1..N\}$ is zero. For the predictions in the time instants thereafter, each element of $\{n(t+k|t), k=1..N\}$ is equal to $n(t|t)$, which is calculated from the measured/estimated value of $y(t)$ and the value of $x(t|t-1)$ that was predicted in the previous step.

As a BLDC machine can be modelled as a second order system, there are two state variables: the rotor speed ω_m and the phase current i. The equation stated above is applied to both state variables, the used notation for the variables y, x and n remain the same. An index is used to indicate the difference between the two equations. The variable x_{ω_m} is used to denote x in the equation stated above applied for the rotor speed. The variable x_i is used to denote x for the phase current equation. Using this procedure, the MPC algorithm keeps track of its own internal state variables x_{ω_m} and x_i.

6.5.1 Design of the Cost Function

The most general form for the cost function is a weighting of the whole state and the actuation. This cost function then expresses that the state must evolve to a predefined reference for each state and also takes into account the effort of the actuation. A BLDC machine can be expressed as a second order system with a state that is composed out of the rotor speed ω_m and the phase current i. The actuation is determined by the duty cycle δ that is applied to the switches of the inverter connected to the active motor phases. The phase current i is directly proportional with the electromagnetic torque. This means that the phase current determines how fast the machine accelerates or decelerates. The reference path for the rotor speed is therefore related with the reference path for the current. As a result using one of the state variables is sufficient in the expression of the cost function. There is only one output variable of the machine we are interested in as a controlled variable, the rotor speed. The current serves as an internal motor variable that accomplishes the rotor speed. The value for the actuation (duty cycle) is limited by the duty cycle generation scheme between 0 and 1. Adding an additional term for the actuation would limit the change of the actuation between two successive time instants. This term as such does not have an added value, it would only prevent the rotor speed to follow its reference at some time instants. Furthermore, changes in the actuation are allowed as long as they do not imply a sudden high current in the motor phases. For this reason, a term that limits the current to a predefined value was preferred by the authors over a term that directly impacts the actuation itself.

In this section, the influence of the cost function onto the speed control performance of the BLDC machines will be studied. The cost function is one of the design parameters that will determine how the control method will behave. The goal is to control the rotor speed ω_m of the BLDC machine. Therefore, the cost function must contain a term with the difference between the predicted rotor speed ω_m and the rotor speed reference r. In an FPGA, implementation of absolute values is possible by sign detection and constant multiplication which is less demanding compared to the sum of squared signals which is realized by multipliers. To further reduce the computational effort required to minimize the cost function, it is

possible to only consider the error between the reference r and the predicted rotor speed ω_m at $t+N$. If the cost function is reduced to $|r-\omega_m|$ at the future time $t+N$, The cost function can be written as

$$J = |r(t+N|t) - \omega_m(t+N|t)| \tag{6.18}$$

The optimal value for the duty cycle δ will be $\omega_m(t+N|t) = r(t+N|t)$. However, this cost function (6.18) disregards the cost of the phase currents in terms of Joule power losses and risk of permanently demagnetizing the magnets against torque generation.

In the cost function (6.18) the current is not limited and hence it is not practical. When the absolute value of the current becomes larger than the maximum allowable current i_{max} the cost function should increase. This increase will reduce δ and force the current to be within its limits. This is achieved by adding a second term to the cost function of (6.18) that is a function of the current resulting in:

$$J = |r(t+N|t) - \omega_m(t+N|t)| + \mu \sum_{k=1}^{N} a_i(k) \tag{6.19}$$

where a_i is defined as:

$$a_i = \begin{cases} |i| & \text{if } |i| > i_{max} \\ 0 & \text{if } |i| \leq i_{max} \end{cases} \tag{6.20}$$

In the simulations, the parameter μ is chosen to be $1\frac{\text{rad}}{\text{As}}$. The influence of μ on the current limitation will be experimentally examined. As the current i should stay below i_{max} at every instant, a summation over the prediction interval is used in (6.19). Using the value of the current at the instant $t+N$ would undesirably allow the current to rise above i_{max} between t and $t+N$.

To compare the speed control performance of the MPC algorithm to the results of conventional cascaded PI controllers as shown in Fig. 6.4, a step change in the speed setpoint from 0 rpm to 1000 rpm is applied to MPC simulation model and the speed and current responses are plotted in Fig. 6.6. Here, due to the complexity of the MPC algorithm a time stepping simulation is carried out instead of using transfer functions to simulate the drive behaviour. The results are shown in Fig. 6.6 and can be compared with the results of the cascaded PI controllers as shown in Fig. 6.4. As it can be seen the time to reach steady state is approximately 50 ms during which the current is bounded to 2 A illustrating the advantage of MPC in speed control of BLDC machines.

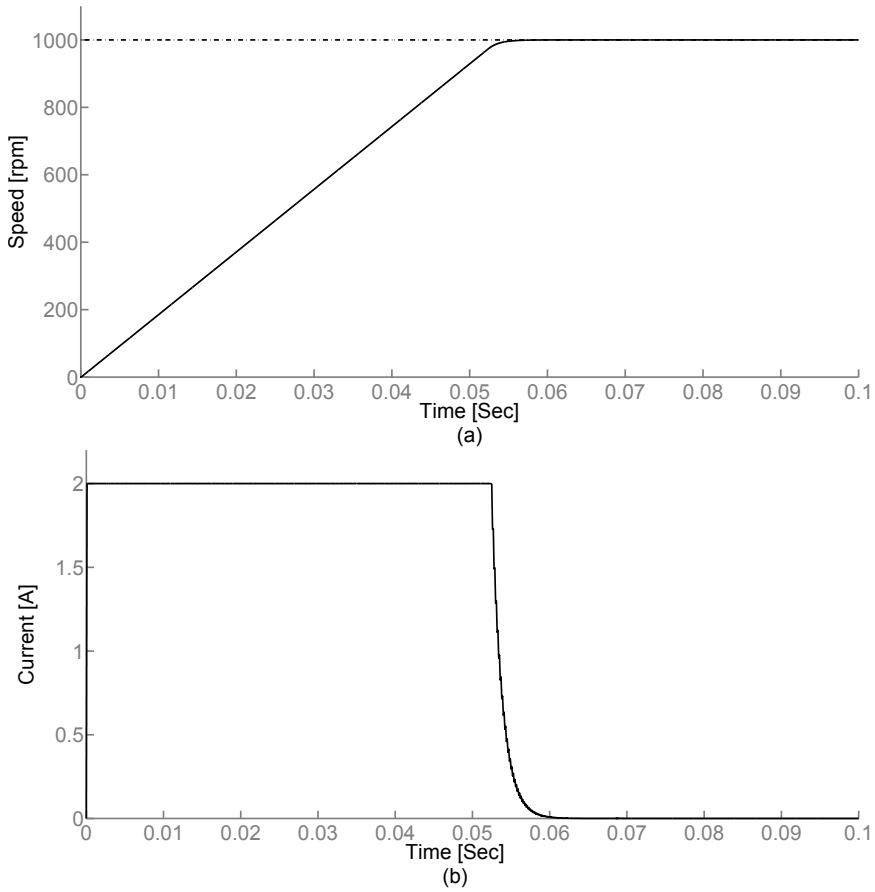

Figure 6.6. Simulation result, a step response for MPC algorithm, (a): speed response, (b): current response

6.5.2 Influence of the Design Parameter α

The parameter α, introduced in (6.17), determines the reference signal r that is used in the cost function. It acts as a filter between the actual measured system output and the set-point for this output. When an MPC algorithm is used to control the rotor speed of a BLDC machine, the parameter α determines the reference path for the rotor speed. The lower the value for α, the larger the weight of the set-point in determining the reference path. The rotor speed, current and the PWM duty cycle δ are depicted in Fig. 6.7 for different values of α. Before $t = 0.05$ s, during the start-up, the acceleration is limited by the current limitation ($i_{\max} = 2$ A). When the rotor speed gets closer to its set-point 200 rad/s, the reference path can be followed with a lower current than 2 A. For small α, the reference is steep,

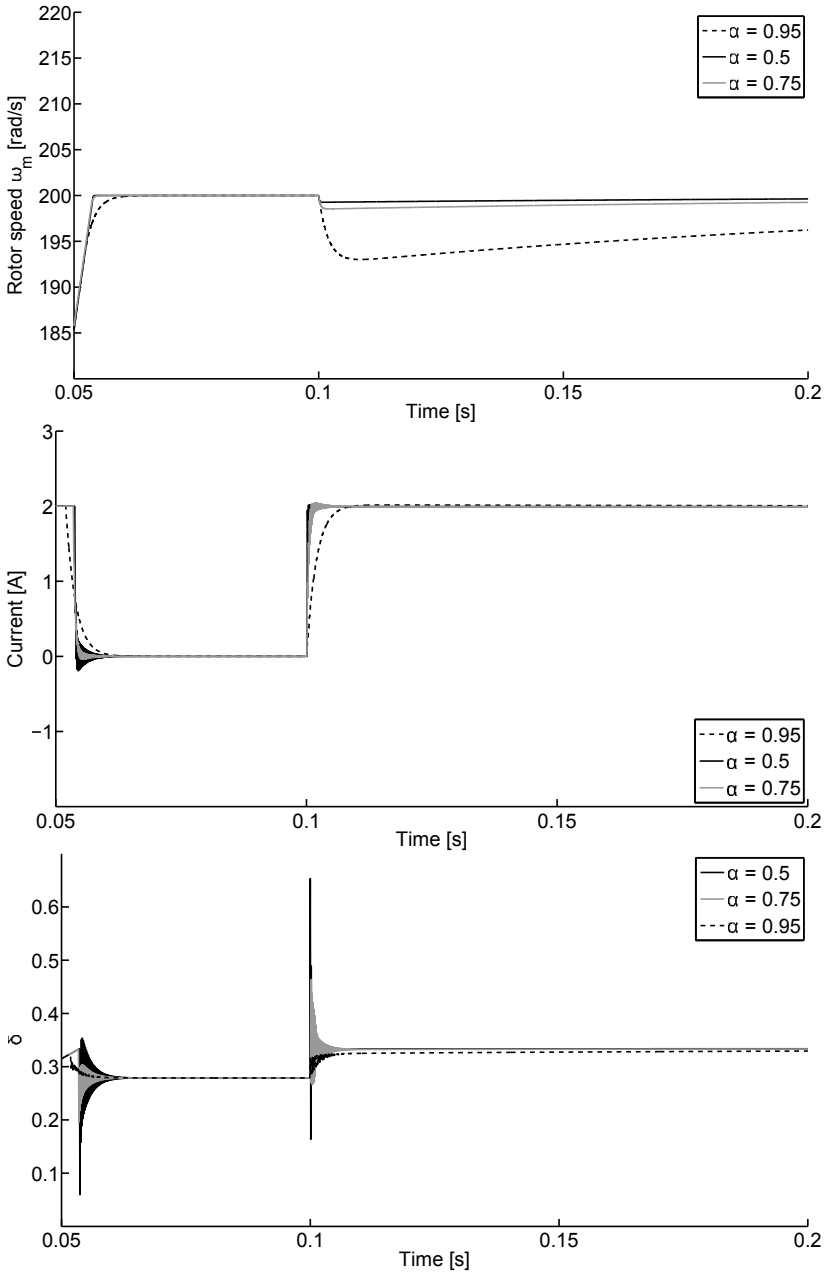

Figure 6.7. Simulation results for the influence of the parameter α on a step change in the speed reference and loading transients, (a): Rotor speed ω_m, (b): Current i, (c): PWM duty cycle δ, using the cost function (6.19). The value for N is 1.

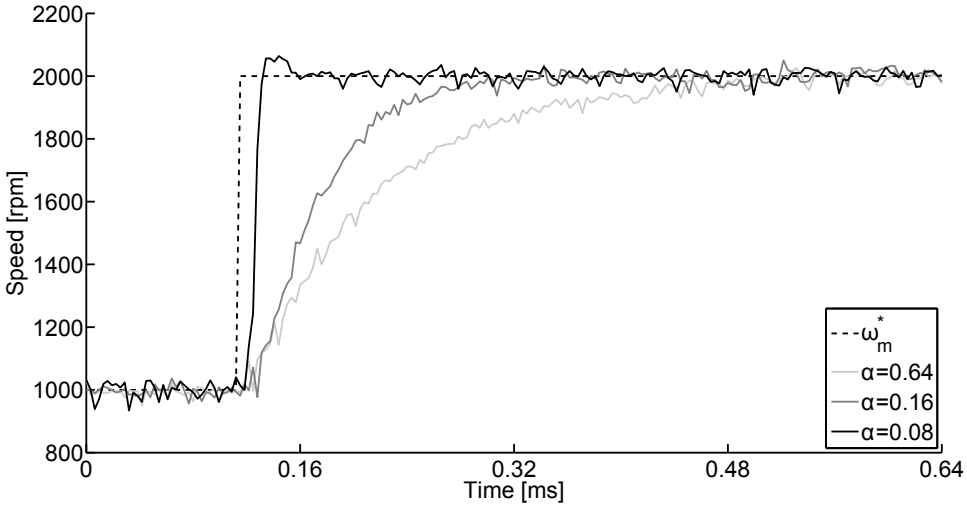

Figure 6.8. Experimental results, a comparative test between the effects of different values of α on a step change in the speed reference, a no-load machine

even when the rotor speed is close to its set-point. This results in a current that remains at maximum of 2 A for a longer time. A clear difference between the start-up behaviour (around $t = 0.055$ s) is noted when either using $\alpha = 0.5$ or $\alpha = 0.95$ in Fig. 6.7(a). For a high value, $\alpha = 0.95$, the rotor speed is allowed to evolve more slowly to the speed set-point and the current decreases more gradually.

When a load torque is applied, the parameter α determines the sensitivity of the control strategy to this disturbance. For instance, at $t = 0.1$ s a load torque step of 0.05 Nm is applied. For $\alpha = 0.95$, the speed drops from 200 rad/s to approximately 193 rad/s until it starts returning to the set-point. This speed drop is due to the reaction time of the current controller on the speed variation. For $\alpha = 0.5$ and $\alpha = 0.75$, the control strategy reacts more strongly to the disturbance, limiting the speed drop when applying the load torque. Using $\alpha = 0.5$ allows the fastest change in the current and the rotor speed decreases slightly to no less than 199 rad/s. By controlling α an adjustable dynamic stiffness could be achieved in the drive system. The influence of α can also be noticed in the behaviour of the PWM duty cycle δ in Fig. 6.7(c). When the rotor speed approaches its set-point, the current is forced to rapidly drop to zero when using low values of α (e.g. $\alpha = 0.5$ and $\alpha = 0.75$). This results in larger variation of δ. When applying the load torque is applied, the lower values of α imply a fast reaction of the current to counteract the load torque. The current rises quickly, again leading to larger variation in δ.

In Fig. 6.8 the effects of α on a step change in the speed reference is evaluated and the results matches the simulation results given in Fig. 6.7. By reducing α the

response of the speed to a step change in the reference speed becomes faster. However, too low values of α can result in a response that could result in an unstable behaviour of the drive.

The influence of the parameter α on the disturbance rejection property of the proposed algorithm will be studied in section 6.6.7 in more detail.

6.5.3 Influence of the Prediction Horizon N

In previous section the prediction horizon N was equal to 1. Two sets of simulations will be performed one at $N = 1$ and one at $N = 3$. in case $N = 3$, the algorithm predicts the current and rotor speed over three PWM periods. For the simulations that are performed here, α is taken 0.95 to study the influence of the prediction horizon on the proposed MPC algorithm performance.

Applying a load torque the model is not sufficient in order to obtain correct predictions due to the lack of load torque information. Due to the application of the load torque, the measured rotor speed at the start of a PWM period deviates from the rotor speed that was predicted in the previous PWM period. An error n_{ω_m} arises between the internal state x and the actual state of the machine y. The algorithm will bring the internal state for the rotor speed to a higher value to compensate for the load torque disturbance. However, the current could be predicted wrongly as no information regarding the current error is used. Feedback of the error n_i is not strictly necessary when $N = 1$. It is assumed that the speed control algorithm is reacting fast enough to keep the system stable without controlling the current (besides keeping its amplitude under a predefined maximum value). When the prediction horizon is changed to a higher value, the speed control algorithm reacts less strongly and the system could become unstable. Using the error n_i in the control algorithm can solve such a stability problem.

The influence of N on the rotor speed is depicted in Fig. 6.9(a) and (b). There is a slight difference between the rotor speed for $N = 1$ and $N = 3$. For $N = 1$, the rotor speed restores faster from the load torque that is applied at $t = 0.1$ s. As the control algorithm neglects the load torque, the predictions of current and rotor speed are with error when a nonzero load torque is applied. For a larger $N = 3$, in the determination of the optimal input, the algorithm does not only take the first PWM period into account, but also the second and the third. Therefore, the control input will be more smooth and the control algorithm is reacting less strongly compared to the case of $N = 1$. This explains the difference in the rotor speed response to a load torque disturbance for $N = 1$ and $N = 3$. The evolution of the current i for $N = 1$ and $N = 3$ is shown in Fig. 6.9(c) and (d). The PWM duty cycle δ as function of time is shown in Fig. 6.9(e) and (f). In contrast with Fig. 6.9(a) and (b) and 6.9(c) and (d), where the difference between the algorithm using $N = 1$ and $N = 3$ was rather small, a large difference in δ can be noted. For

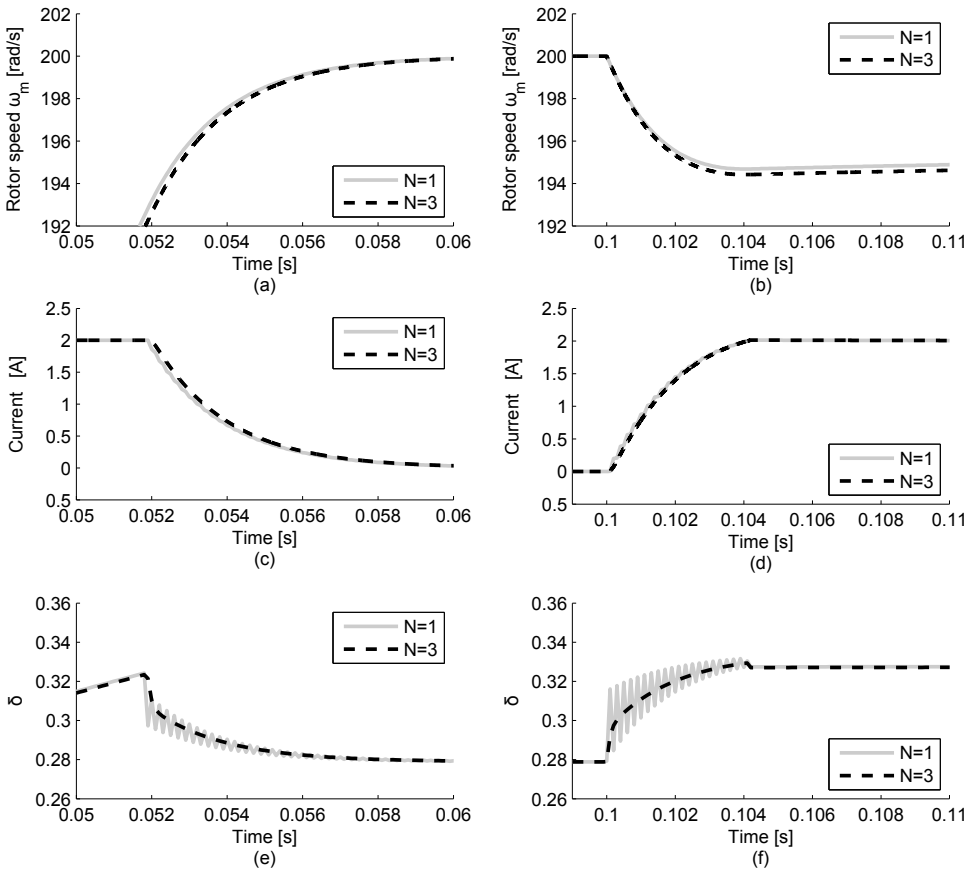

Figure 6.9. Simulation results for the MPC using the cost function from (6.19). The value of α is 0.95. (Left column): transients during startup, (right column): loading transients. (a and b): rotor speed ω_n, (c and d): current i, (e and f): PWM duty cycle δ.

$N = 3$, the PWM duty cycle evolves smoothly when it tries to bring the current to its new value as the rotor speed approaches its set-point. When a load torque is applied, the variation in δ is again smooth. For $N = 1$, an oscillation appears in δ. This is due to a strong control action for this low value of N. If $N = 1$, the algorithm calculates the optimal δ for the next PWM period without taking into account what will happen after that period. The current increase in the first PWM period can be too high. In the next PWM period the algorithm will try to lower this current, often resulting in an oscillating δ.

6.6 Implementation of the MPC on an FPGA

The proposed algorithm is implemented on the SPARTAN 3E XC3S1600E FPGA board. The implemented algorithm differs slightly from the one that is used in the simulations. The differences and reasons are explained in detail in this section.

6.6.1 Discretized BLDC Machine Model

To predict the future outputs of the system a discretised model is used as is described in this section. The waveform of the back-EMF in a BLDC machine is described in [Darba2014]. It can be seen that the back-EMF voltages in the active phases are equal in amplitude, but have different signs

$$e_x = K_e\omega_m \quad , \quad e_y = -K_e\omega_m \tag{6.21}$$

Using a PWM duty cycle δ then an average voltage of δV_s is applied to the motor terminals.

Then the current in the active phases can be determined by solving the following differential equation:

$$\frac{\mathrm{d}\boldsymbol{i}}{\mathrm{d}t} = -\frac{\boldsymbol{R}}{\boldsymbol{L}}\boldsymbol{i} + \frac{1}{2\boldsymbol{L}}\delta V_s - \frac{1}{2\boldsymbol{L}}2K_e\omega_m \tag{6.22}$$

The following differential equation can be written for the BLDC machine motion:

$$\frac{\mathrm{d}\omega_m}{\mathrm{d}t} = \frac{1}{J}2K_t\boldsymbol{i} - \frac{1}{J}T_l \tag{6.23}$$

The system (6.22)-(6.23) can be combined in a state space model:

$$\begin{bmatrix} \frac{\mathrm{d}\boldsymbol{i}}{\mathrm{d}t} \\ \frac{\mathrm{d}\omega_m}{\mathrm{d}t} \end{bmatrix} = \begin{bmatrix} -\frac{\boldsymbol{R}}{\boldsymbol{L}} & -\frac{K_e}{\boldsymbol{L}} \\ \frac{2K_t}{J} & 0 \end{bmatrix} \begin{bmatrix} \boldsymbol{i} \\ \omega_m \end{bmatrix} + \begin{bmatrix} \frac{1}{2\boldsymbol{L}} & 0 \\ 0 & -\frac{1}{J} \end{bmatrix} \begin{bmatrix} \delta V_s \\ T_l \end{bmatrix} \tag{6.24}$$

To implement this on an FPGA a discrete version of (6.24) is needed. A zero order hold discretisation method is used. Since the differential equation (6.24) is in the form of

$$\dot{\boldsymbol{x}} = \boldsymbol{A}\boldsymbol{x} + \boldsymbol{B}\boldsymbol{u} \tag{6.25}$$

it has a general solution:

$$\boldsymbol{x}(t) = e^{\boldsymbol{A}(t-t_0)}\boldsymbol{x}(t_0) + \int_{t_0}^{t} e^{\boldsymbol{A}(t-\tau)}\boldsymbol{B}\boldsymbol{u}(\tau)d\tau \tag{6.26}$$

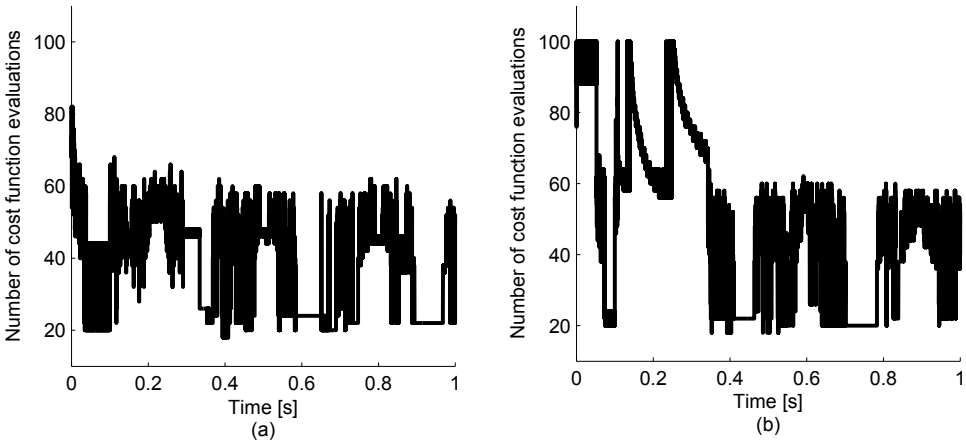

Figure 6.10. Simulated number of function evaluations for the MPC method using the cost function in which $\alpha = 0.95$ and $N = 1$. (a): equation (6.18), (b): equation (6.19)

To discretise (6.25), we consider (6.26) between the time samples $t_0 = kT_s$ and $(k+1)T_s$, where T_s represents the sample period. The corresponding values for the state variable $\boldsymbol{x}$ are $\boldsymbol{x}_k$ and $\boldsymbol{x}_{k+1}$, respectively. The usual procedure in digital control is to hold the control input $\boldsymbol{u}(t)$ constant between sampling times resulting in:

$$\boldsymbol{x}_{k+1} = \underbrace{e^{\boldsymbol{A}T_s}}_{\boldsymbol{A_{SH}}}\boldsymbol{x}_k + \underbrace{\int_0^{T_s} e^{\boldsymbol{A}(t-\tau)}\boldsymbol{B}d\tau}_{\boldsymbol{B_{SH}}}.\boldsymbol{u}_k \tag{6.27}$$

where $\boldsymbol{u}_k$ is the value of the input during the time interval $[kT_s, (k+1)T_s]$. By applying (6.27) to the state space model of the machine, the following matrices can be derived for the discretised system:

$$\boldsymbol{A_{SH}} = \begin{bmatrix} e^{-\frac{\boldsymbol{R}T_s}{\boldsymbol{L}}} & e^{-\frac{K_e T_s}{\boldsymbol{L}}} \\ e^{-\frac{2K_t T_s}{J}} & 0 \end{bmatrix}, \boldsymbol{B_{SH}} = \begin{bmatrix} \frac{1}{2}\frac{1-e^{-\frac{\boldsymbol{R}T_s}{\boldsymbol{L}}}}{\boldsymbol{R}} & 0 \\ 0 & -\frac{T_s}{J} \end{bmatrix} \tag{6.28}$$

6.6.2 Optimization of the Cost Function

To optimize the cost functions introduced in (6.18) and (6.19), the Matlab function `fminunc` is used within the simulations. This is an optimization algorithm that performs a line search. The number of cost function evaluations required to find a solution that lies sufficiently close to the optimal solution is given in Fig. 6.10(a)

and (b) for the two different cost functions. It can be seen from Fig. 6.10(a) that without current limitation the startup transition from 0 s to 0.05 s requires a lower amount of iterations compared to the Fig. 6.10(b). Using (6.10) introduces a constraint to the current and the effect of this constraint on the number of iterations can be seen in Fig. 6.10(b) during the startup transition from 0 s to 0.3 s. The reason of a shorter transition time T_{tran} in Fig. 6.10(a) compared to Fig. 6.10(b) is that by using (6.18) the current is not limited and it produces an unlimited driving torque during the transients. As every cost function evaluation starts with different initial conditions, the time required to find the optimal solution varies in time. Using Matlab function `fminunc` or an other well-known algorithms such as discrete time branch and bound algorithm has two main disadvantages:

- Too much computational effort is required to be implemented on the FPGA
- Too much time to process one iteration of the algorithm
- Uncertain number of iterations are required to find the optimal solution

To avoid this the authors decided to use a more straightforward solution with a guaranteed result after a certain amount of FPGA clock pulses bearing in mind that the solution could be suboptimal. The proposed optimization algorithm tackles the aforementioned implementation problems. The simulation results of using Matlab `fminunc` function of Matlab provides a benchmark for the proposed optimization algorithm.

The interval $[0, 1]$ for δ is divided in 10 smaller and equal intervals. The cost function is evaluated for the discrete values that bound each interval (i.e. for δ equal to 0, 0.1,..., 1). For one of the δ values the cost function becomes minimal. The optimal solution is then searched in one of the neighbouring intervals. For this the two neighbouring intervals are then merged together. The resulting interval is again divided but this time in 12 equal intervals. As two of discrete values of the new intervals are known from the previous iteration. Hence, also in the second iteration, δ has to be evaluated for 11 values. The number of cost function evaluations is in this way limited to 22, while achieving a sufficient resolution of 0.0167 for the optimal value for δ. Fig. 6.11 shows an example in which 0.7 is chosen as the optimal δ value during the first search, to search for a more accurate value δ intervals $[0.6,\ 0.6167,\ 0.633,\ ...,\ 0.6667,\ 0.6833,\ 0.7]$ are chosen and the cost function is evaluated for each value to find a more accurate value for δ.

6.6.3 Calculation of the Optimal δ

The MPC algorithm uses rotor speed measurements ω_m, measurements of the DC-bus voltage V_s and the DC-bus current i_{DC}. These signals are sampled at a PWM

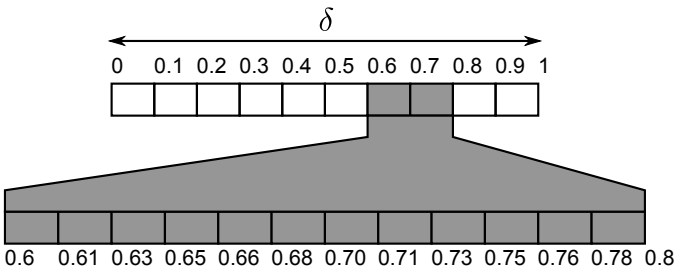

Figure 6.11. An example of cost function optimization

frequency of 10 kHz. The algorithm calculates the optimal δ, and performs a set of calculations as follows:

- Generation of the speed reference r
- Calculation of the error parameters n_{ω_m} and n_i
- First iteration: prediction and cost function evaluation
- Generation of a second set of values for δ
- Second iteration: prediction and cost function evaluation

Execution of the aforementioned steps takes 184 clock cycles to calculate the optimal δ (taking into account that 22 values for δ have to be evaluated). Using the FPGA parallelism and pipelining methods as done in [Vyncke2013, Darba2012] leads to a calculation time that is reduced to approximately 38 clock cycles. This results in a fixed calculation time of 760 ns for an optimal value of δ. The scheme of the MPC algorithm is depicted in Fig. 6.1.

6.6.4 Influence of x_{ω_m} Feedback

Instead of only using the speed measurement ω_m to calculate the optimal δ, the MPC algorithm also takes into account the difference between the predicted rotor speed and the actual rotor speed. The algorithm thus works with an internal state variable x_{ω_m}. It is used for two reasons: to compensate for modelling errors and to improve the disturbance rejection of the drive.

To see the effect of feedback of the state variable x_{ω_m}, the rotor speed reference is set to 1300 rpm. The impact of x_{ω_m} on the rotor speed is shown in Fig. 6.12. When feedback of x_{ω_m} is enabled, the rotor speed stays close to the reference.

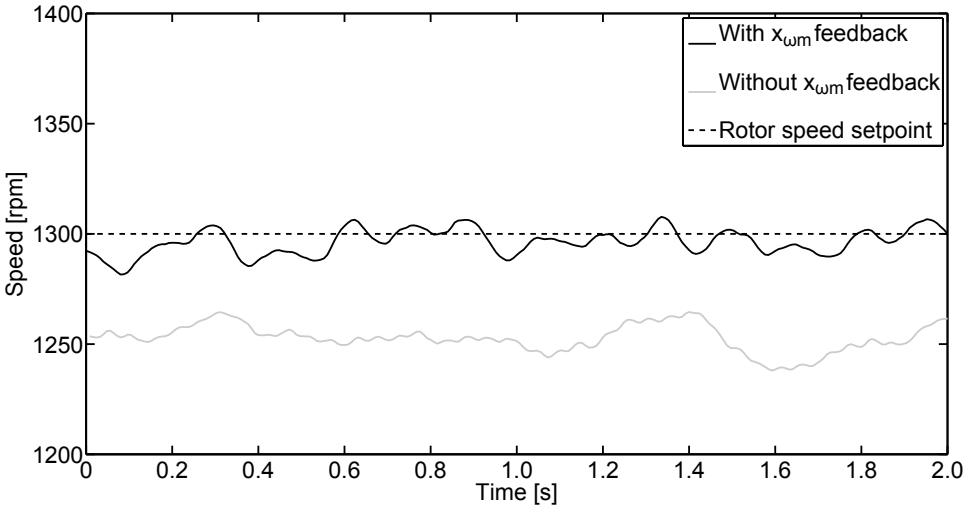

Figure 6.12. Experimental results of the influence of x_{ω_m} feedback on the rotor speed for a no-load machine.

Without feedback of x_{ω_m}, the rotor speed is approximately 1250 rpm. The offset in the rotor speed can be ascribed to modelling errors (friction was not modelled, for example).

To test the influence of the feedback of x_{ω_m} on the disturbance rejection, the machine is loaded with a load torque with square waveform. The improvement in the disturbance rejection that follows from the feedback of x_{ω_m} can be seen in Fig. 6.13.

6.6.5 Effect of μ on the Current Limitation

In (6.19), the parameter μ was used as a weighting factor for the current in the total cost in order to limit this current. In the simulations, μ was chosen as $1\ \frac{\text{rad}}{\text{As}}$. To test the influence of μ on the current limitation the speed set-point is set to 2000 rpm, $\alpha = 0.99$ and $i_{\text{max}} = 2\text{A}$. The machine is then loaded with a load much higher than the nominal load. For this operation condition the required current to produce the electromagnetic torque to reach the speed set-point 2000 rpm is greater than i_{max}. At the moment that the current reaches i_{max} the MPC algorithm tries to limit the current to i_{max} value and the rotor speed will be less than the speed set-point. As (6.19) does not necessarily imply a strict limitation of the current to i_{max}, loading the machine could cause the current to become higher than i_{max}. The effectiveness of the current limitation is characterized by the parameter β (in $\frac{\text{As}}{\text{rad}}$),

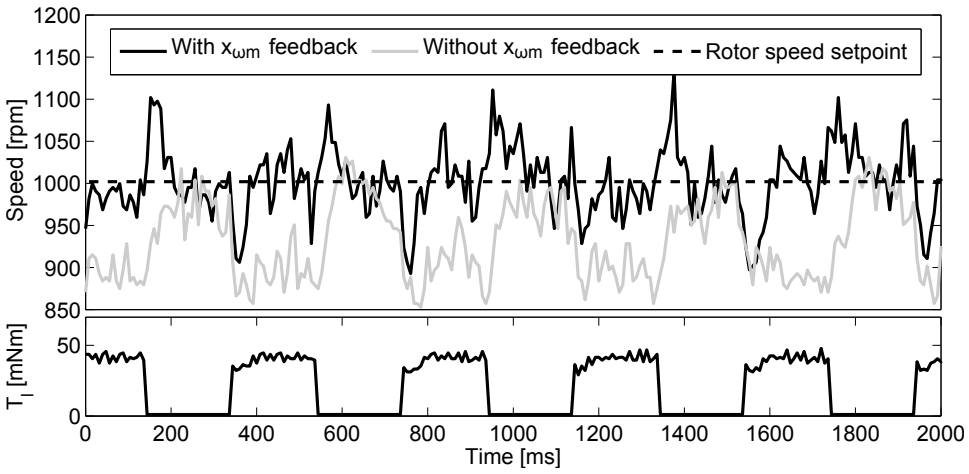

Figure 6.13. Experimental results of the influence of feedback of x_{ω_m} on the disturbance rejection when the machine is loaded with a load torque with a square waveform

which is defined as:

$$\beta = \frac{i - i_{\max}}{\omega_m^* - \omega_m} \tag{6.29}$$

The parameter β is the rate of excess current from its limit to the speed error. Because the speed error has larger values compared to the current, the values of β are small. Within the experimental setup the value of β is calculated for different values of μ during the steady state and the results are plotted in Fig. 6.14.

- For low values of μ, β shows high values. In this region the current can become larger than $i_{\max}$.
- As μ becomes higher, β decreases. The current limitation becomes more strict.

It can be concluded that for applications requiring good speed control with an over-current tolerance (in the machine and inverter), a smaller μ is recommended which can provide faster dynamics and more robust speed reference tracking.

6.6.6 Current Control and Current Limitation

In the practical setup, only the DC-bus current is measured by using a series resistor[DeBelie2012]. A single current sensor reduces the cost of the current

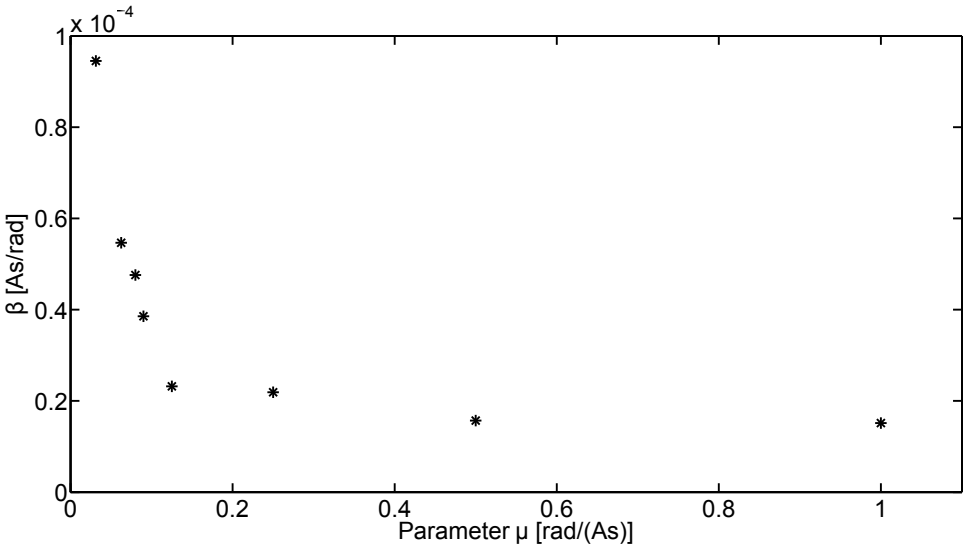

Figure 6.14. Experimental result of the influence of μ on the current limitation of the BLDC drive. $T_l = 1.5T_{l,\text{nom}}$ at $\omega_m = 2000$ rpm

measurement system in the drive. The performance of such a system is evaluated in [Carpaneto2012]. By knowing the switching states within a PWM period and as one of the phases is unexcited, a measurement of the DC-bus current can be used to obtain a sample of the phase currents during each PWM period.

In Figs. 6.15 and 6.16, different oscilloscope measurements are presented in order to show the steady-state and transient behaviour of the proposed algorithm in more detail. Each figure includes four traces: the upper and second traces are terminal voltage (V_T) and virtual neutral point voltage ($V_n^{'}$) referred to the negative DC-bus voltage, the third trace is the subtraction of ($V_T - V_n^{'}$) in order to measure the back-EMF voltage referred to the virtual neutral point during the time intervals that the current of the phase is zero. The bottom trace is the measured phase current using a current transducer. Due to the attenuation factors of the voltage and current probes the scales of interests are given by 2 A/Div for currents in Fig. 6.15 and 3 A/Div for Fig. 6.16 and 2 V/Div for all voltages.

Here, the current control is studied in order to verify its performance in providing the required torque and preventing over current that can damage the machine. In Fig. 6.15 the aforementioned variables of the machine are measured while the rotor speed set-point is set to 1000 rpm. In Fig. 6.15(a) no-load and in Fig. 6.15(b) loaded operation conditions are tested. For the loaded test a torque proportional to the speed of the machine (a three phase BLDC generator is connected to a resistor

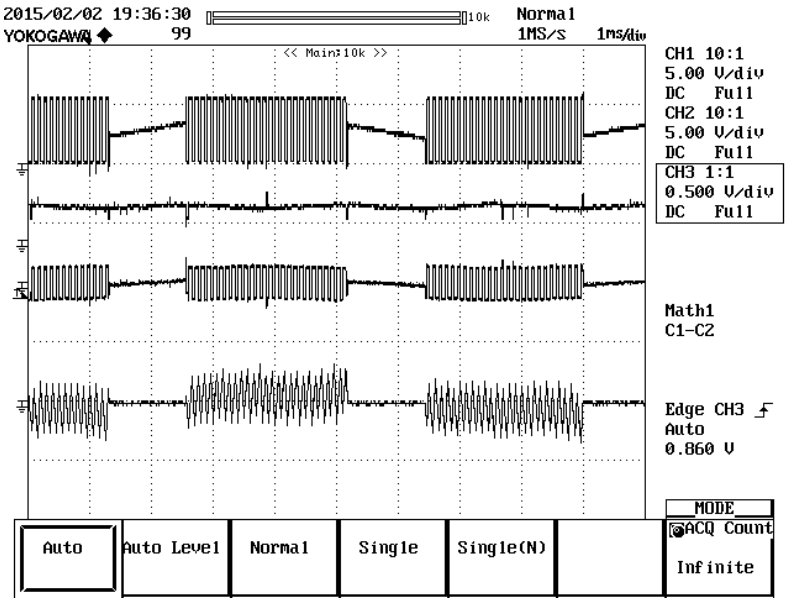

(a): current control at 1000rpm, no-load condition

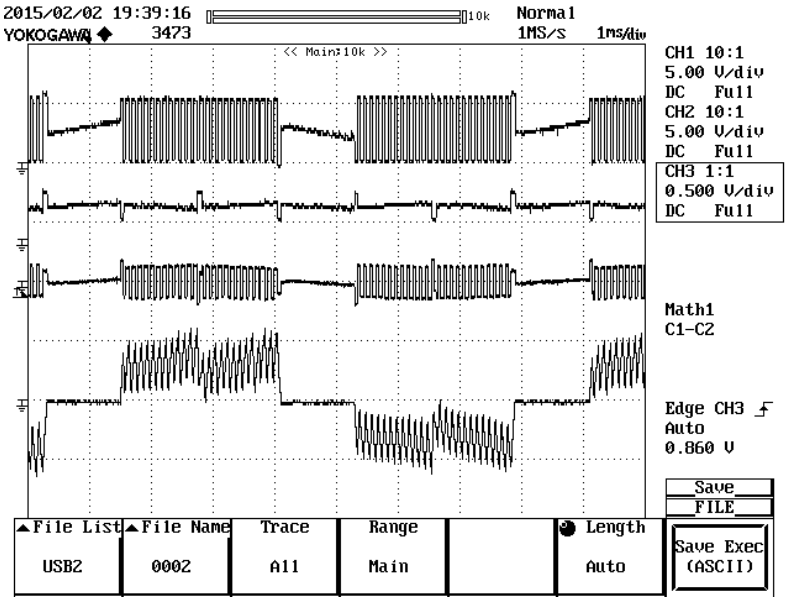

(b): current control at 1000, $T_l = 0.25T_{l,\text{nom}}$

Figure 6.15. Experimental results for the current control using the proposed MPC algorithm, switching frequency 10kHz and $\alpha = 0.9996$

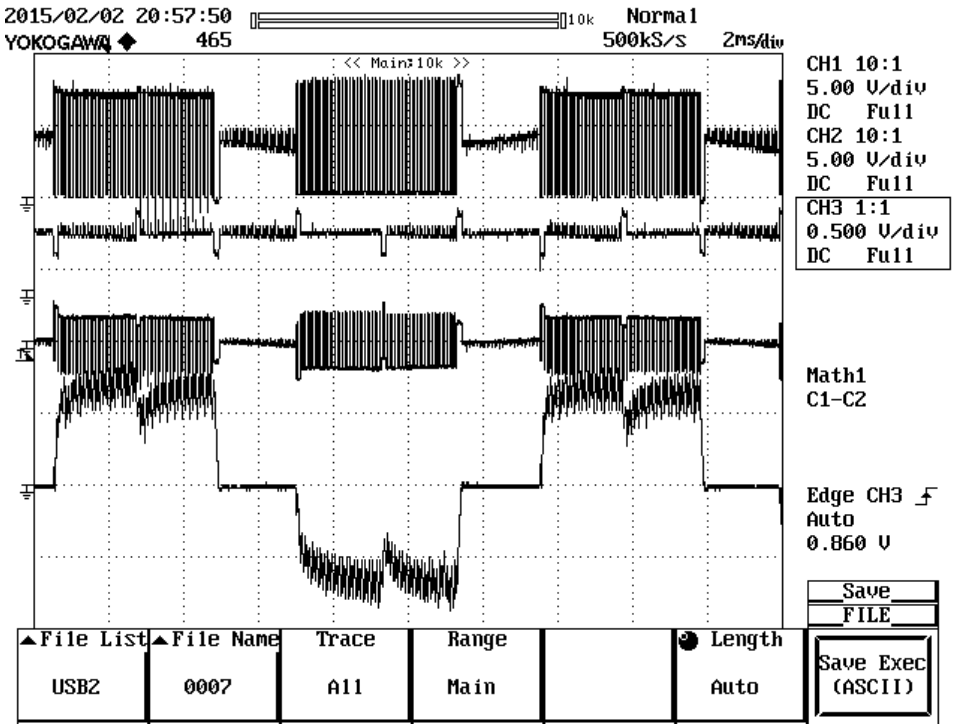

Figure 6.16. Experimental result of the overloaded machine $T_l = 1.5T_{l,\text{nom}}$ at $\omega_m = 1000$ rpm, switching frequency 10kHz and the current is limited to the $i_{\max}$ value

array with star topology) is coupled to the machine to be tested. As it can be seen from Fig. 6.15(a) in no-load condition the current is below $i_{\max}$. The average current is 0.7 A for the loaded operation and similar to the no-load case the rotor speed set-point is equal to 1000 rpm.

In order to evaluate the current limitation performance, the parameter $i_{\max}$ is set to 3.2 A that is the maximum allowable current for the tested machine. Speed set-point is 1000 rpm for this test as well. The machine is then overloaded by a heavy loading of the generator coupled to the machine of interest. As it can be seen from Fig. 6.16 the average phase current does not exceed 3.2 A. As the current reaches its maximum value the electromagnetic torque is limited as well, resulting in a lower rotor speed. The rotor speed is calculated for the case of Fig. 6.16 and it is 568 rpm (each 120° electrical takes ≈ 4.4 ms). Considering the speed set-point equal to 1000 rpm it is shown that the speed set-point tracking performance is compromised when keeping the current bounded to $i_{\max}$.

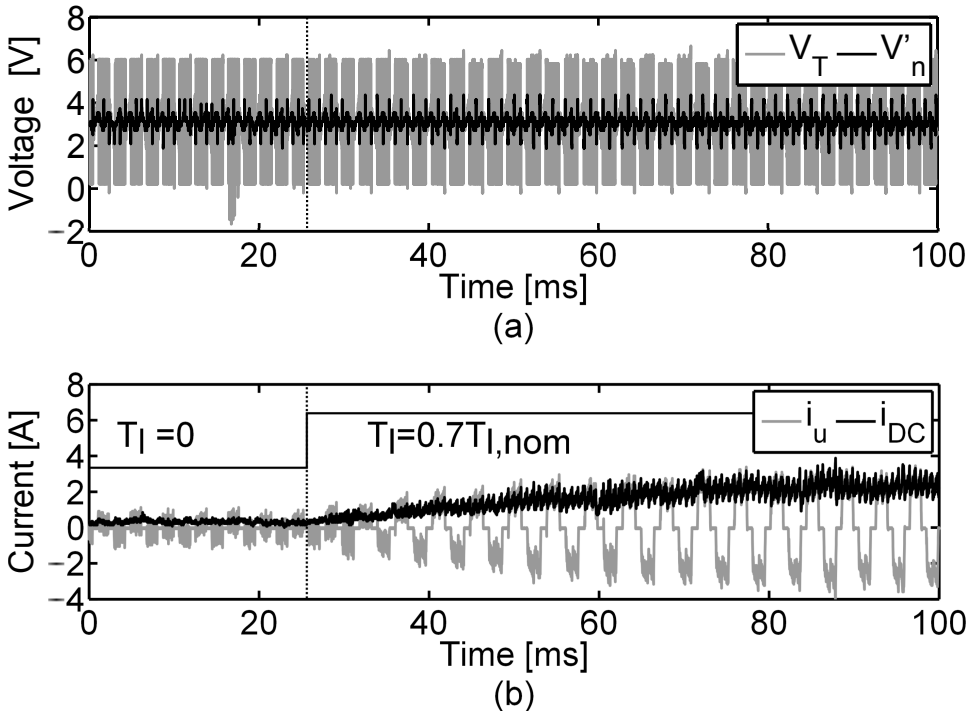

Figure 6.17. Experimental results on the control performance of the proposed MPC algorithm during a step in the mechanical load torque (loading), switching frequency 10kHz, $\alpha = 0.99978$ and $\omega_m = 2000$ rpm, (a): Terminal voltage (V_T), virtual neutral voltage ($V_n^{'}$), (b): phase u current (i_u), DC-bus current (i_{DC}),

By overloading the machine the effectiveness of the parameter μ in limiting the current is evaluated for this operation condition. It shows that by choosing a sufficiently high value for μ the current will remain within the allowable boundaries that guarantees safe operation for the entire drive system. The parameter μ is considered to be 1 during the experimental tests as well as during simulations.

The performance of the proposed MPC algorithm is also evaluated for a step change in the applied mechanical load torque. The loading condition is shown in Fig. 6.17 where Fig. 6.17(a) shows the terminal and virtual neutral voltages and Fig. 6.17(b) shows the phase and DC-bus currents of the machine. The DC-bus current is sampled by a shunt resistor in the DC-bus and the phase current is measured by a current transducer (Hall-effect sensors). The DC-bus current samples are proportional to the electromagnetic torque so these can be used as a representative of the applied load torque as well. It can be seen from Fig. 6.17(b) that the current reaches the steady state value of 2.5 A equal to 70 % of the

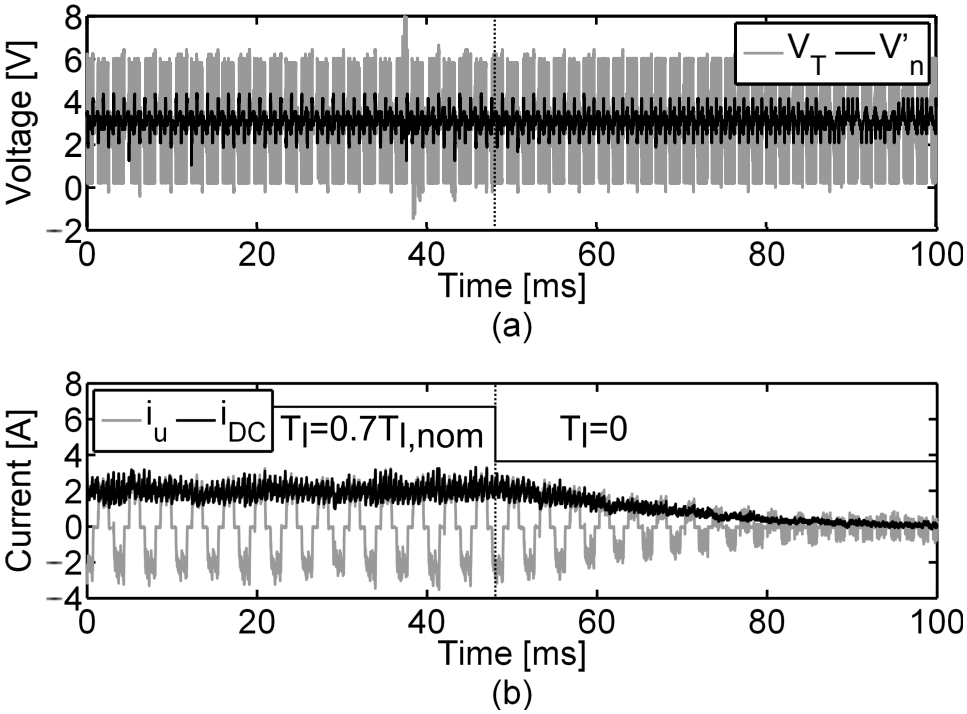

Figure 6.18. Experimental results on the control performance of the proposed MPC algorithm during a step in the mechanical load torque (unloading), switching frequency 10kHz, $\alpha = 0.99978$ and $\omega_m = 2000$ rpm, (a): Terminal voltage (V_T), virtual neutral voltage ($V_n^{'}$), (b): phase u current (i_u), DC-bus current (i_{DC}),

nominal current, 40 to 50 ms after applying the load torque at 25 ms. In Fig. 6.18 the same load is suddenly disconnected from the rotor shaft at 45 ms after starting the measurement. Again, after about 40 to 50 ms, the current reaches the new steady-state value 90 ms after starting the measurement.

6.6.7 Influence of the Parameter α on the Disturbance Rejection

In this section, the impact of α on the load torque disturbance rejection will be discussed. The BLDC machine is loaded with a load torque with a periodic square waveform. The parameter values for α are $\alpha = 0.99$ and $\alpha = 0.999$. From the simulation results in section 6.5.2 and experimental results shown in Fig. 6.8, it is expected that for a lower value of α, the algorithm will react more swiftly. The measurements that result from the FPGA implementation are depicted in Fig. 6.19.

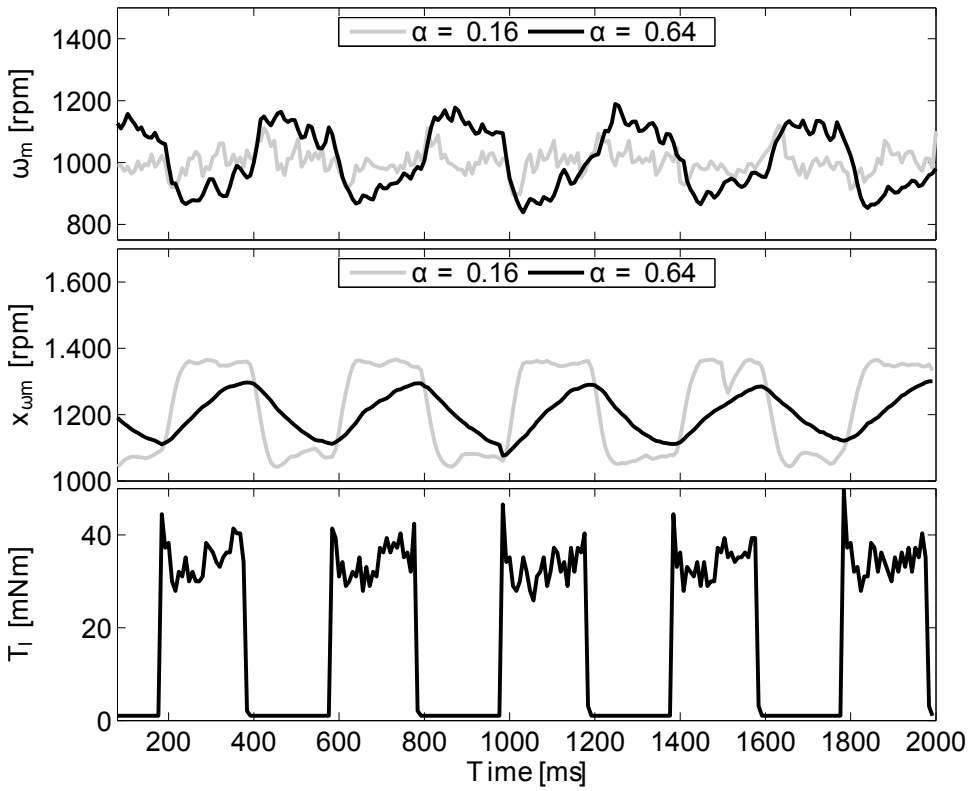

Figure 6.19. Experimental results for the different values of α, (top): Rotor speed ω_m , (mid): the state variable x_{ω_m} and (bottom): the external applied load torque.

Besides the measured rotor speed ω_m, also the state variable x_{ω_m} is shown in this figure.

A smaller α corresponds to less weight on the speed control and allows Δu to take larger values resulting in a faster closed-loop response. It is observed that for lower value of α, the rotor speed measurement ω_m varies between values that are closer to the set-point of 1000 rpm. For $\alpha = 0.99$, the disturbance rejection of the algorithm is thus better than for the case where $\alpha = 0.999$. The effect of α can also be observed in the state variable x_{ω_m}. When the load torque is applied, x_{ω_m} reacts more quickly on the measured deviation in the rotor speed. Lower values of α are thus better for a good disturbance rejection of the drive and control algorithm. However, too low values for α imply an increased susceptibility to measurement noise.

6.7 Speed Control Dynamics

The advantages of using the proposed MPC algorithm can be extended to its possible applications in high dynamic systems. The proposed algorithm can be strongly advised for applications that need rapid and reliable speed changes. Figs. 6.21 and 6.22 show experimental results for a stepwise change in the reference speed (from 1000 rpm to 2000 rpm and from 2000 rpm to 1000 rpm respectively). The rotor speed of a BLDC machine can be calculated using the time difference between commutation instants. For example considering the waveforms of Fig. 6.15, each 120° conduction period that consist of two commutation intervals takes 2.5 ms that is equal to 1000 rpm using an 8 pole machine. A similar approach is used in this section to calculate the speed. In this section the tests are done once for the proposed MPC algorithm and another time for a conventional cascaded PI controller. The PWM carrier frequency of the PI current controller is 10 kHz and all signals within the MPC algorithm are sampled at 10 kHz as well. The gains of the PI controllers are tuned to have a fast dynamic response and the values are presented in section III. As a very low inertia machine is used in this study higher control gains result in an oscillatory behaviour and instability. The minimum achievable experimental settling time for a step change in the speed using conventional PI controllers is ≈ 500 ms. By increasing the gains in order to increase the speed controller bandwidth the speed response overshoot increases and results in an unstable operation. Three different sets of speed controller gains are tested $G_{s,1}$, $G_{s,2}$ and $G_{s,3}$ and the results of speed and current responses are shown in Fig. 6.20(a) and (b). The speed controllers with gain sets of $G_{s,1}$, $G_{s,2}$ and $G_{s,3}$ have 78%, 90% and 96% overshoot respectively. The measured bandwidths are 2.86Hz, 3.03Hz and 3.26Hz respectively. The speed controller gains of $G_{s,3}$ results in an unstable behaviour as it can be seen from Fig. 6.20. On the other hand, for the MPC algorithm the experimental settling time for $\alpha = 0.9996$ is around 35 ms and much faster than for the case with PI controller. Due to the complexity of the system, analytical calculation of the bandwidth is difficult. Therefore, the practical bandwidth of the system is approximated based on the 10% to 90% of the step response settling time using the following equation:

$$f_{BW} = \frac{0.34}{t_r} \tag{6.30}$$

The practical bandwidth of the PI speed controller is 1.33 Hz and for the MPC algorithm 33.32 Hz. It must be mentioned that due to the fact that speed control using MPC is more agile than PI controller, it acts on all speed disturbances very fast. This results in additional high frequency oscillations in the measured speed compared to the PI control. The proposed MPC algorithm could be compared with a PI controller with higher bandwidth where it would provide a faster response but oscillations and instability would become an issue. From Fig. 6.21(b) it can be seen that during steady state and before applying the step up command the

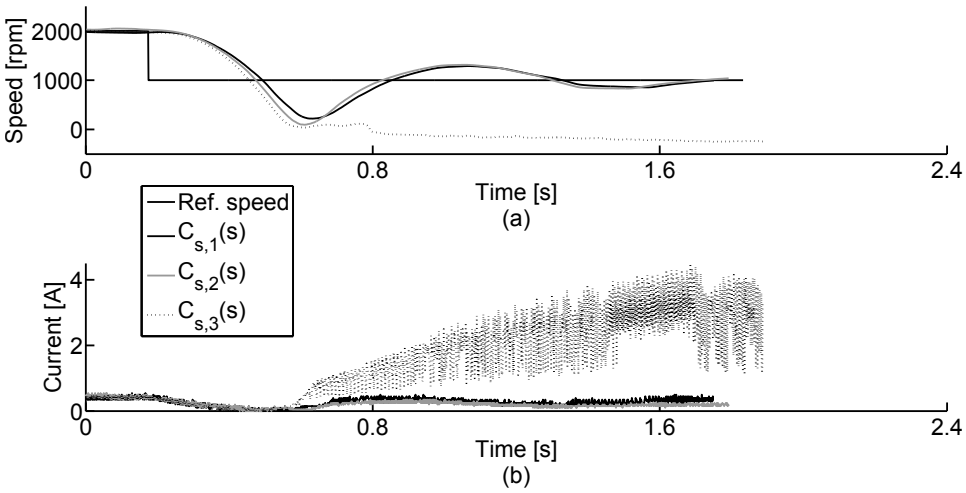

Figure 6.20. Experimental results for high PI speed controller gains in order to increase the speed controller bandwidth that results in an unstable operation in no-load condition, (a): speed response, (b): current response

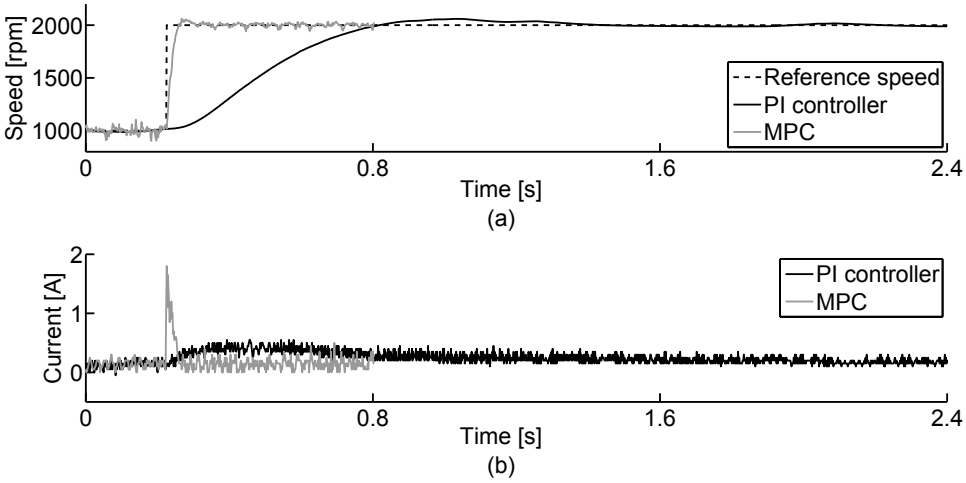

Figure 6.21. Experimental results for a step up change in the speed reference, comparison between the proposed MPC algorithm, switching frequency 10kHz, $\alpha = 0.9996$ and conventional cascaded PI control in no-load condition, (a): speed response, (b): current response

average current of both methods is similar. After the step command the current using the MPC provides a fast acceleration torque and hence the speed is changed immediately to 2000 rpm. However, in the case of a cascaded PI controller the

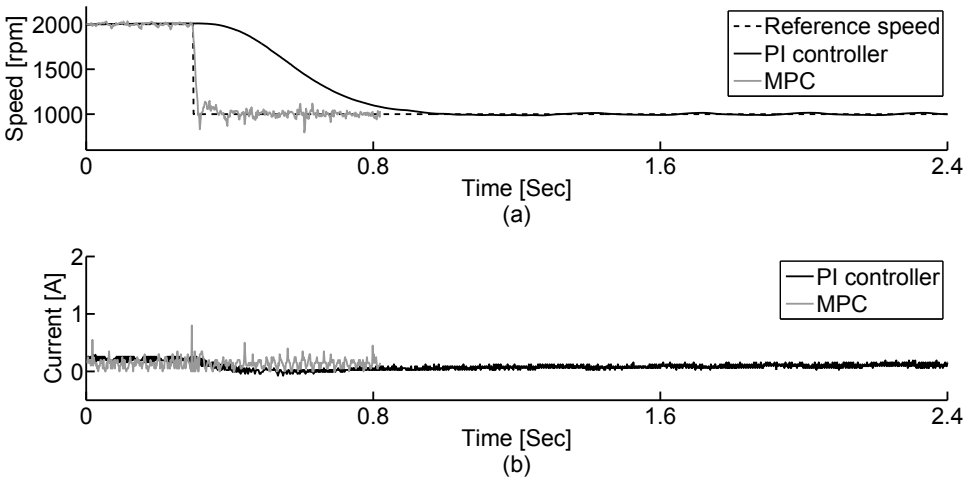

Figure 6.22. Experimental results for a step down change in the speed reference, comparison between the proposed MPC algorithm, switching frequency 10kHz, $\alpha = 0.9996$ and conventional cascaded PI control in no-load condition, (a): speed response, (b): current response

current changes more slowly to maintain stability. In Fig. 6.22(b), after the step down command, the torque reference is reduced to maintain a lower speed. Again, it is occurring more slowly in the case of a PI controller than in the case of MPC.

6.8 Self-Sensing Model Based Predictive Control

The advantages of the combination of a self-sensing and an MPC are not studied widely and not so many papers are published on this topic. However, as examples of the state of the art some of the previous works could be mentioned. In [FengxiangWang2014a] a rotor flux model reference adaptive system (MRAS) is proposed with a Predictive Torque Control algorithm to drive an induction machine. It uses a cascaded speed and torque control based on the estimated torque and flux and an additional PI controller to compensate flux drifts. The cost function defined in the MPC to search for the optimal control output includes terms of torque, flux and switching frequency each multiplied with different weighting factors. In [FengxiangWang2014b] an encoderless full-order sliding mode observer (EFOSMO) is applied to a finite control state predictive torque control (FCS-PTC) to obtain self-sensing control. In [Alkorta2014] a multivariable speed and current control is proposed based on MRAS flux estimation for induction machines. In [Guzinski2013] an observer-based flux/speed estimator is used in order to implement a Field Oriented Control for induction machines. The speed con-

trol is obtained using a cascaded PI speed and a Predictive Current Control (PCC) algorithm. The cost function of the PCC is the current error. In [Preindl2011a] an MPC algorithm is implemented to reduce the switching frequency of the high power voltage source inverters. In [Preindl2011b] a self-sensing PCC is implemented for a PMSM machine, the speed and position is estimated using a second-order PLL observer. One first order and one second order observers are implemented in order to achieve a self-sensing PTC for an induction machine in [Davari2012].

In this section, an MPC algorithm is implemented to control the rotor speed of a low inertia BLDC machine. The MPC provides a simultaneous speed and current control that improves the speed control dynamics. Different features and implementation aspects of the used MPC algorithm are studied earlier in this chapter. The rotor position information which is required for the current commutation is provided by a self-sensing commutation technique based on the back-EMF samples of the machine as presented in Section 4.4.

6.8.1 Modifications of the MPC Algorithm

The basics of the technique to drive a BLDC machine by an MPC algorithm without motion sensors are explained in this section. The proposed technique is based on two main subsystems that seamlessly integrate into each other. The self-sensing subsystem provides speed estimation, commutation sequence and exact commutation instants (see Section 4.4). The estimated speed with current and voltage measurements is fed to the MPC subsystem where the duty ratio of the inverter switches is computed.

To start with, we consider that at the time t an estimation of the rotor speed $\hat{\omega}(t)$ is provided by the self-sensing algorithm. The set-point of the speed at time t is $\omega^*(t)$. Based on the measured current $i(t)$ and DC-bus voltage $V_{DC}(t)$ and duty ratio δ a prediction of the future speed is made at time t,

$$\omega_{\text{pred}} = [\omega(t+1|t), ..., \omega(t+N|t)] \tag{6.31}$$

which depends on the future control action $[\delta(t|t), ..., \delta(t+N-1|t)]$. The parameter N represents the prediction horizon. The vector of the predicted speeds ω_{pred} is compared with the reference trajectory $[r(t+1|t), ..., r(t+N|t)]$. The reference trajectory starts at $r(t|t) = \hat{\omega}(t)$ and evolves towards the set-point $\omega^*(t)$. The future control action $[\delta(t|t), ..., \delta(t+N-1|t)]$ is chosen in such a way that a cost function is minimized. The cost function usually depends on the difference between the predicted process outputs and the reference trajectory over the prediction horizon N. In this MPC algorithm a prediction of the speed can be written as

$$\omega_{\text{pred}}(t+k|t) = x(t+k|t) + n(t+k|t) \tag{6.32}$$

Where x is the part of the output that results from applying the input, that is applied to the real process, to the model of the process. To keep the model manageable, not all aspects of the process output are modelled. The measurement of the output of the process is also susceptible to measurement noise. These effects are captured in the variable n. The prediction $x(t+k|t)$ results from using the discrete time model of the process:

$$x(t) = \frac{B(q^{-1})}{A(q^{-1})}u(t) \quad , \quad n(t) = \frac{C(q^{-1})}{D(q^{-1})}e(t) \tag{6.33}$$

$\frac{B(q^{-1})}{A(q^{-1})}$ represents the dynamics of the model and q^{-1} is the backward shift operator. The unmodelled part of the output, n, is considered as a coloured noise process. It can be defined as a white noise process e that goes through a filter $\frac{C(q^{-1})}{D(q^{-1})}$.

The disturbance model which is chosen in this study is

$$\frac{C(q^{-1})}{D(q^{-1})} = \frac{1}{1-q^{-1}} \tag{6.34}$$

For this choice of the disturbance model, the prediction of the values for n at future time instants are calculated as:

$$n(t+k|t) = n(t+k-1|t) + e(t+k|t) \tag{6.35}$$

Where k varies from $k = 1$ up to $k = N$. The value for $n(t)$, which is calculated from the estimated speed $\hat{\omega}$ and model output $x(t)$, is used over the complete prediction horizon. When the predictions for ω are made, they can be compared with the reference signal r in the interval $[t+1, t+N]$:

$$r(t+k|t) = \alpha r(t+k-1|t) + (1-\alpha)\omega^*(t+k|t) \tag{6.36}$$

The reference signal determines how fast the output should evolve to its set-point ω^*. The design parameter that controls this rate is α.

6.9 Advantages of the Self-Sensing MPC

In addition to the integration of the advantages of both techniques, implementation of a self-sensing MPC algorithm with a self-sensing technique provides extra advantages as well. In this section some of the advantages are studied.

6.9.1 Self-Sensing Start-Up

One of the drawbacks of the back-EMF based self-sensing commutation techniques for BLDC machines is that a closed-loop start-up from standstill is not possible. The back-EMF signal of the machine is zero at standstill so the rotor position information cannot be obtained from the back-EMF signal. Instead an open-loop pulsed voltage sequence is used in order to start rotating the machine (up to 5-10% of the nominal speed) and produce sufficiently detectable back-EMF amplitude. However, different problems have also been reported. In [Tsotoulidis2015] temporary reverse rotations and oscillations of the speed have been observed. In [Chun2014] temporary vibrations and large instantaneous peak currents have been reported during an open-loop start-up sequence.

The combination of the back-EMF based self-sensing and the MPC algorithm makes it possible to start the BLDC machine from standstill neither using an open-loop sequence nor motion sensors. The MPC algorithm determines the best duty ratio δ to accelerate the rotor and reach the speed set-point at start-up. The duty ratio should be applied to the inverter switches to produce an electromagnetic torque which results in a rotation in the desired direction. If sensors are used, the correct commutation state is determined by the sensors. However, in this self-sensing commutation method it starts from an arbitrary initial commutation state. The speed and current response of the machine to the first voltage pulse δV_{DC} is sampled and analysed by MPC. If the sampled current value and the estimated acceleration (based on the speed estimation $\hat{a}[k] = \hat{\omega}[k+1] - \hat{\omega}[k]$) are close to the predicted values the next δ value is calculated and applied to the same phases until the instant that commutation state is changed by the self-sensing algorithm. Then, the calculated duty ratios are applied to the other phases according to the new commutation state. If the current error is high and the estimated acceleration does not agree with the predicted one this means that the selected commutation state is not the correct one. Hence, the MPC overrules the self-sensing algorithm and triggers a commutation action. This changes the commutation state to another one until finding the correct sector. The duty ratio is updated once in each PWM period (100 μs) which is much faster than the mechanical time constant of the machine. This provides a quick determination of the correct commutation sequence. Fig. 6.23 shows the commutation sequence of the machine. The start-up procedure takes 25 ms to get to the correct sequence and then the machine accelerates towards the speed set-point.

6.9.2 Efficiency Improvement by the Self-Sensing Commutation

One of the advantages of using a self-sensing technique instead of low resolution Hall effect sensors is the improvement on the back-EMF and phase current synchronisation. In [JianchengFang2014] the authors studied the effects of the mis-

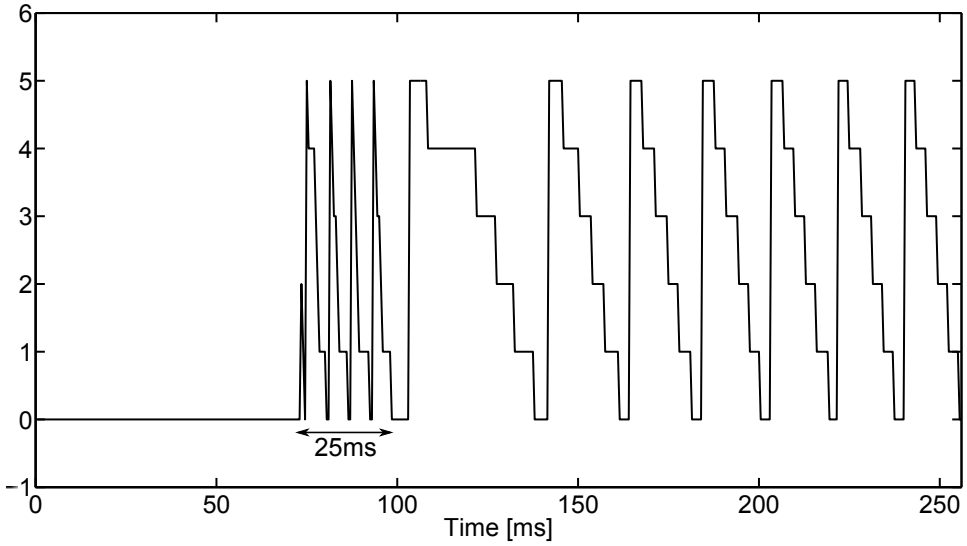

Figure 6.23. Experimental result, Commutation sequence signal

aligned sensors that result in wrong commutations and reduces the performance of the BLDC drive. The authors proposed a self-compensation technique based on the DC-bus current. By using an accurate self-sensing commutation detection technique the use of sensors and compensation of their errors is eliminated. A great improvement on the drive efficiency is achievable by a correct commutation. The generated mechanical power of a BLDC machine when it is commutated accurately is calculated by:

$$P_{\text{out}}(\omega t) = e_u(\omega t)i_u(\omega t) + e_v(\omega t)i_v(\omega t) + e_w(\omega t)i_w(\omega t) \tag{6.37}$$

The power at point A can be calculated as

$$\begin{aligned} P_{\text{out}}(A) &= (e_w(A) - e_v(A))i_w(A) \\ &= (e_w(A) - e_u(A))i_w(A) \end{aligned} \tag{6.38}$$

By considering a 3-phase symmetrical machine with ideal trapezoidal back-EMF waveform, at the instant $(A-\epsilon)$ the output power is given by $(e_w(A-\epsilon)-e_u(A-\epsilon))i_w$ where $e_w(A-\epsilon)$ and $e_u(A-\epsilon)$ attain their maximum value. The ideal commutation instant is the instant that the amplitude of e_u starts to decrease and at the same time the amplitude of e_v reaches its maximum value. Therefore, in order to have Maximum Torque Per Ampere (MTPA) and minimum commutation torque ripple the values of $e_u(A)$ and $e_v(A)$ must be equal at the commutation instant is shown by point A in Fig. 6.24(a). On the other hand, a misalignment

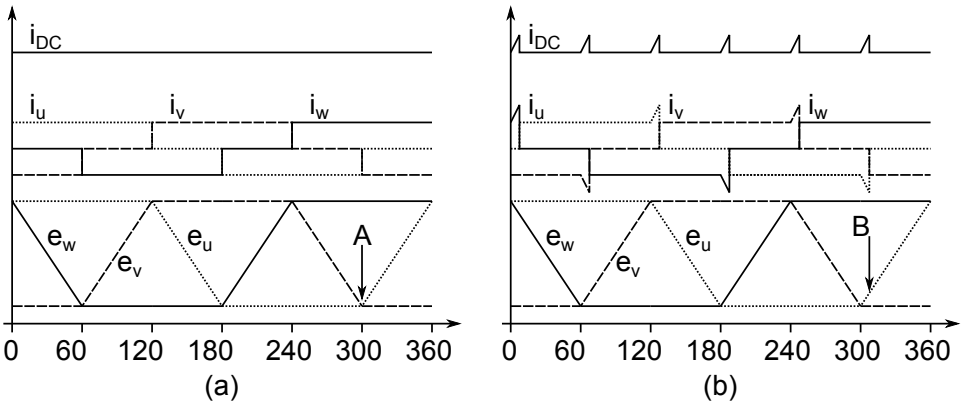

Figure 6.24. Important signals in a BLDC machine, (a): accurate commutation, (b): inaccurate commutation

in the mounting position of Hall sensors in unequal phase back-EMF values as it is shown by point B in Fig. 6.24(b). In this case due to a delayed commutation (where it should commutate at 300°) phase u carries the negative current while its back-EMF amplitude is lower than e_v so we may write that:

$$e_w(B) - e_v(B) > e_w(B) - e_u(B) \tag{6.39}$$

It follows that to drive a given load torque more current will be required when the commutation has a slight delay from its ideal instant. A similar scenario could be considered for early commutation instants as well.

6.9.3 Field Weakening

A constant power (field weakening) operation based on the phase advance technique is achievable using the features of the proposed self-sensing algorithm. The effort to realise the constant power operation is comparable to the constant torque (normal operation) operation. During constant torque operation a commutation is triggered when the function F reaches its threshold. Because the F function is a speed normalized back-EMF signal the value of F which gives the most accurate commutation is equal to one. Different flux weakening regions are achievable by simply reducing the threshold level to any value below one. This will result in an earlier commutation and the phase currents will lead the rotor flux. Each period of F function covers 60° electrical hence the value of the threshold amplitude (A_{Th}) for the required commutation advance angle (θ_{ca}) is calculated as

$$A_{\text{Th}} = 1 - \frac{3\theta_{\text{ca}}}{\pi} \tag{6.40}$$

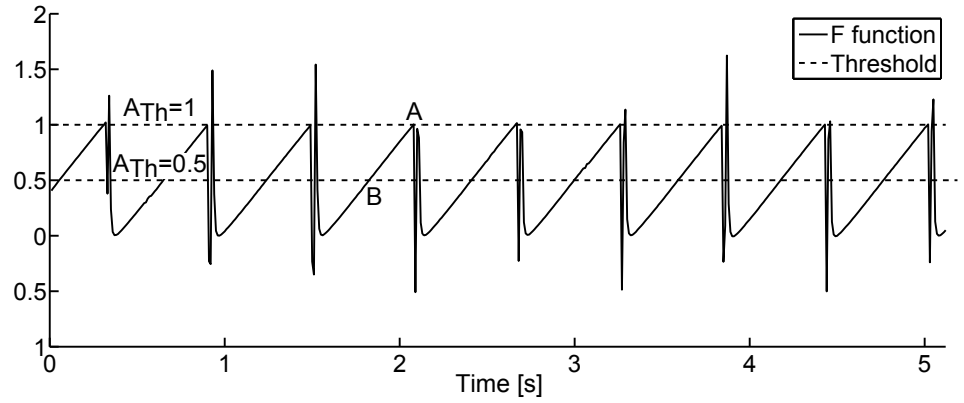

Figure 6.25. Experimental result, measured value for function F inside FPGA using Chipscope^{TM}

Fig. 6.25 shows the generated F function based on the measured back-EMF and speed values. For a constant torque operation $A_{\text{Th}} = 1$ is chosen. The commutation occurs when F reaches 1. In Fig. 6.25 this condition is shown by point A. For phase advance a lower value for A_{Th} is chosen for example 0.5 and the condition is shown by point B.

In literature field weakening operation has been realised by changing the cost function of the MPC [Preindl2013a]. It provides a good constant power operation but due to the change of the cost function the characteristics of the control performance change as well. Here, a constant power operation is introduced with a consistent dynamic control performance for both constant torque and constant power operation regions based on the self-sensing technique. By changing the parameter A_{Th} the phase advance can be changed continuously.

6.10 Experimental Results

In this section different advantages of the combination of self-sensing with MPC algorithms will be explained and experimental verifications will be provided. The drive system is implemented on an SPARTAN 3E 1600 FPGA evaluation board with a maximum clock frequency of 50MHz. To obtain more flexibility on the control of the drive and load torque, two identical test benches have been configured and set up in which one machine is used as motor and the other one as generator. An isolation circuit is used to deploy a galvanic isolation between the control and the power circuits using IL715 digital isolator ICs. Three terminal voltages of the

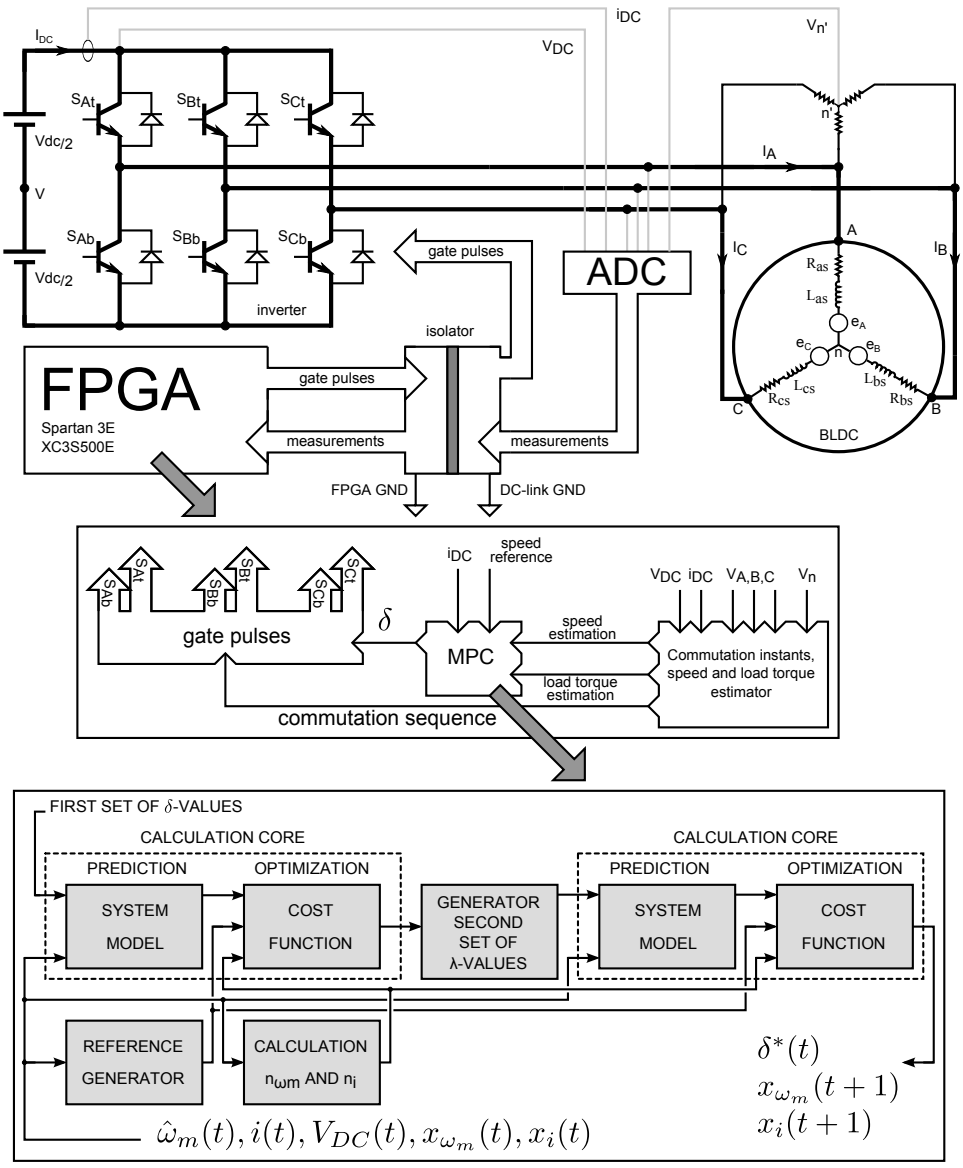

Figure 6.26. Schematic diagram of the test setup

machine, the virtual neutral point and DC-bus voltages are measured referred to the negative side of the DC-bus as well as the DC-bus current which is measured using a series resistor. All of the measured quantities are converted to digital data and fed to the FPGA board after passing through a digital isolation channel. The measured

data is processed inside the FPGA and the inverter gate control pulses are applied to the inverter after passing an isolation channel as mentioned in Fig. 6.26.

6.10.1 Self-Sensing Start-Up

Fig. 6.27 shows the start-up procedure of a BLDC machine driven for two cases. Firstly using Hall effect sensors 6.27-(a), secondly in self-sensing mode as shown in Figs. 6.27-(b) and (c). During the operation with sensors it takes about 15 ms to start the machine successfully where the startup command is applied at 20 ms after starting the measurement. Here, a successful start-up is defined by two features:

- The current reduces to a value below rated current of the machine so that the applied voltage is not modulated
- A symmetrical back-EMF signal is detectable from the unenergized phase of the machine

For the case of self-sensing start-up, based on the initial rotor position the synchronisation time can vary. Two different self-sensing start-up procedures from random rotor positions are shown in Figs. 6.27-(b) and (c) with 15ms and 22 ms to synchronise. Fig. 6.28 shows the start-up procedure while the machine is mechanically loaded. It can be seen that the proposed algorithm is capable of starting the machine in loaded conditions as well.

6.10.2 Efficiency Improvement by the Self-Sensing Commutation

To evaluate the effects of an accurate commutation the machine is driven using sensors and the proposed self-sensing technique and the input and output power are calculated for both cases. In Fig. 6.29(a) the terminal voltage of the machine (V_T) is compared during the operation with sensors and self-sensing operation. It can be seen that the detected back-EMF is not symmetric around the neutral point voltage (V_n) which is equal to 2 V here. This results from a delayed commutation due to the sensors inaccurate mounting compared to the ideal location. On the other hand, the back-EMF detected from the self-sensing method is symmetric around V_n due to the accurate commutation. The effect of this inaccuracy can be seen in the DC-bus current waveform of the machine (Fig. 6.29(b)) resulting in a higher average current with the use of sensors which reduces the efficiency. Based on the input/output power measurements during the no-load condition the self-sensing algorithm produces 4.3% more power for a similar input power compared to the operation with sensors.

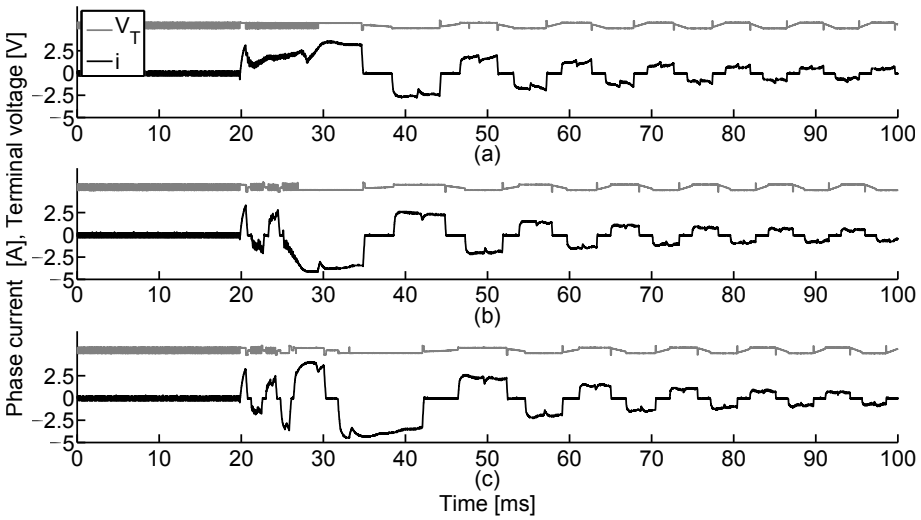

Figure 6.27. Experimental results, no-load start-up procedure, (a): with Hall effect sensors, (b): self-sensing - start-up duration 15 ms, (c): self-sensing - start-up duration 22 ms

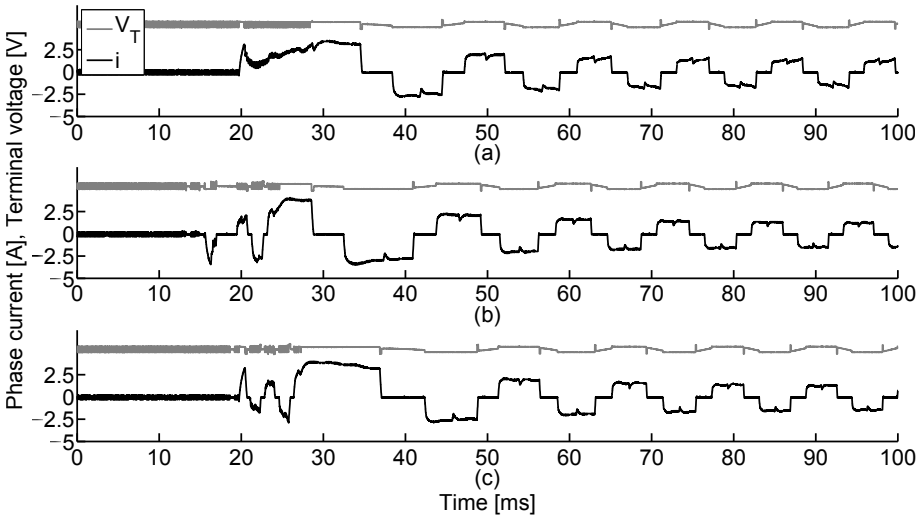

Figure 6.28. Experimental results, start-up procedure under load, (a): with Hall effect sensors, (b): self-sensing - start-up duration 12 ms, (c): self-sensing - start-up duration 18 ms

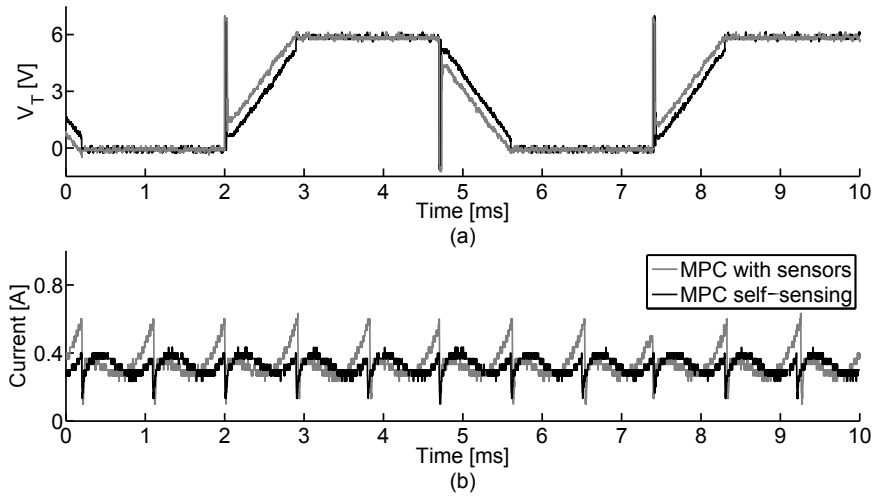

Figure 6.29. Experimental results, comparative measurement, (a): Terminal voltage of the machine, (b): DC-bus current, The measured speed while operation with sensors: 1380 rpm and in self-sensing 1386 rpm

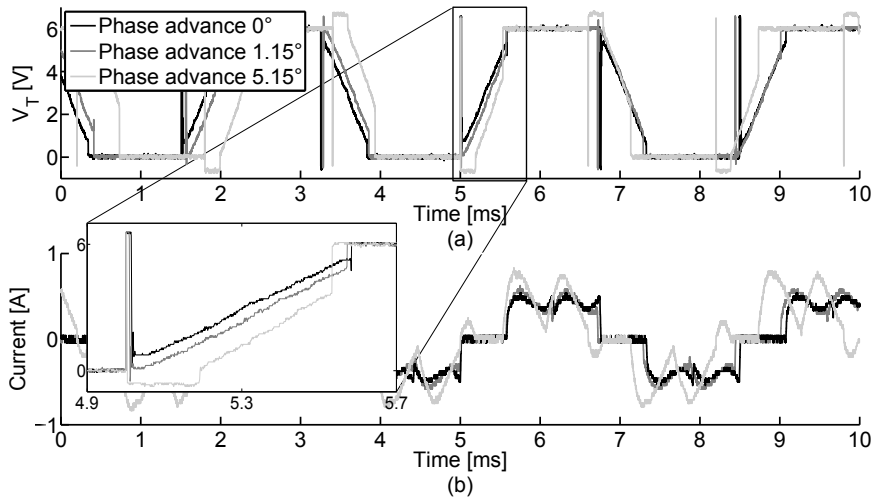

Figure 6.30. Experimental results, comparative phase advance measurement, (a): Terminal voltage of the machine, (b): Phase current

6.10.3 Field Weakening

Fig. 6.30 shows the terminal voltage and DC-bus current of the machine with different phase advances. The current ripple increases with the increase of the phase

advance and its average value as well. The measured speed and average DC-bus current are: for a phase advance of $0°$, 2145 rpm and 0.42 A, for a phase advance of $1.15°$, 2180 rpm and 0.43 A and for a phase advance of $5.15°$: 2344 rpm and 0.5 A.

6.10.4 Step Change of the Speed Set-Point

The dynamic behaviour of the proposed self-sensing MPC algorithm is evaluated in this section and Section 6.10.5. The response of the rotor speed to a step change in the speed set-point is measured and the results are shown in Fig. 6.31. To measure the rotor speed the time intervals between successive commutations are measured and these time intervals are translated to the rotor speed. This is a good measure of the actual rotor speed where no motion sensor is installed in the system. The information is updated every $60°$ electrical. In Fig. 6.31 each subfigure includes three different measurements: the light grey trace represents the measured rotor speed when the machine is driven by Hall effect sensors and MPC algorithm, the dark grey trace is related to the operation of the machine with the proposed self-sensing method and MPC algorithm and the black trace is the measured speed of the machine while working in self-sensing MPC phase advance mode. It should be mentioned that the phase advance for field weakening is only used when the speed is high. In these tests, the phase advance is used at a low speed operation in order to compare its performance with the other two conditions. The speed control performance is evaluated for different values of the parameter α which is introduced in (6.36). By changing the parameter α the dynamic response of the machine can be controlled: the lower the value of α the faster the speed response. In 6.5.2 a more detailed explanation can be found about the working mechanism of the parameter α. It can be seen from Fig. 6.31 that during the steady state and transient states all three methods have similar performance. By increasing the parameter α the speed control system becomes more agile. Some overshoot can be seen during hard braking ($\alpha = 0.04$, $\alpha = 0.12$) especially while phase advance is used. In Figs. 6.31-(f) and (h) a speed increase can also be seen immediately after the step down command. The reason is that by a sudden breaking action a large current is injected to the source. This increases the DC-bus voltage which results in a change in the transformer tap of the power supply to a higher level. Dissipating the excess power in the source and returning the transformer tap back again takes a short time. However, this time is sufficient for the machine to speed up (the tested machine has very low inertia, see specifications in Appendix A.1). After this transient, the MPC reduces the speed and the DC-bus voltage is regulated again so that the machine operates normally.

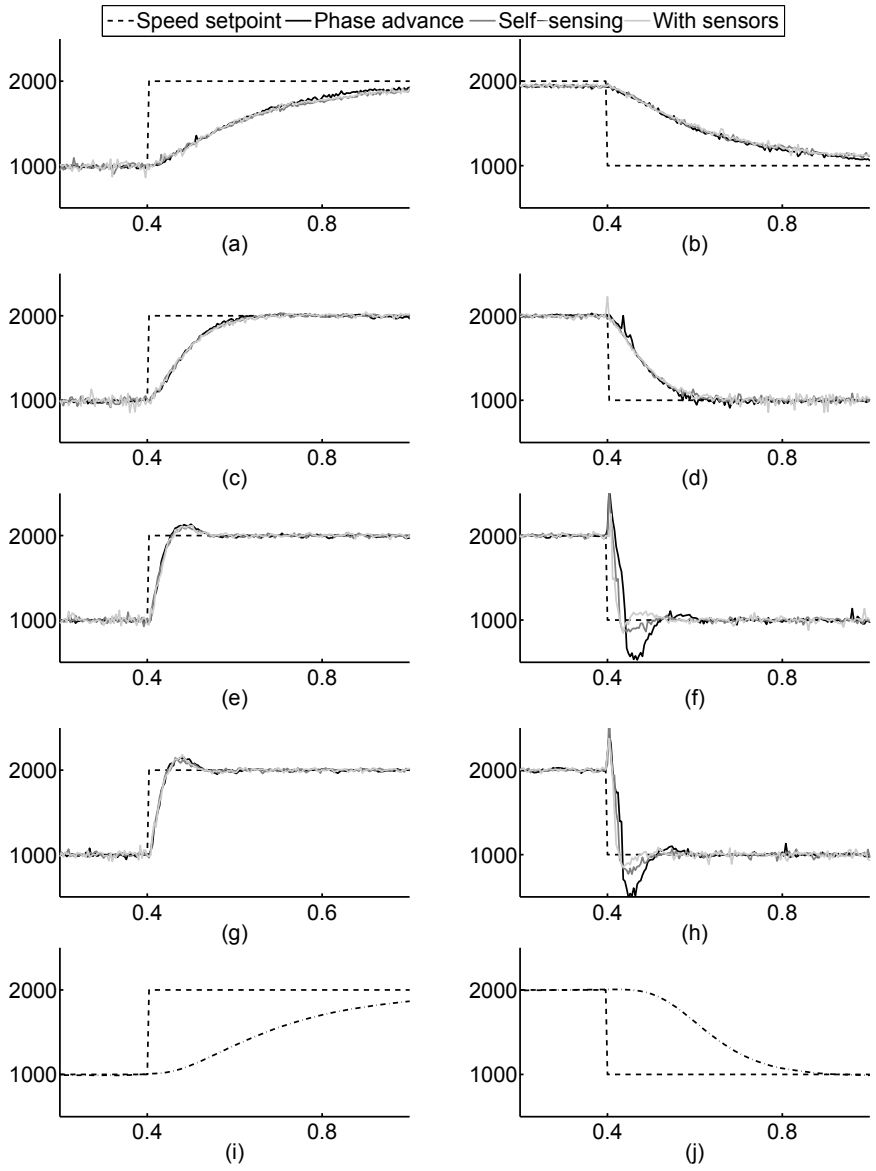

Figure 6.31. Experimental results, comparative measurement of the speed response to the step change in the set-point, x-axis: time [s], y-axis speed [rpm], (a),(b): step-up and step-down $\alpha = 0.64$, (c),(d): step-up and step-down $\alpha = 0.52$, (e),(f): step-up and step-down $\alpha = 0.12$, (g),(h): step-up and step-down $\alpha = 0.04$, (i),(j): step-up and step-down using cascaded PI controller

6.10.5 Loading and Unloading

The performance of the proposed algorithm is also evaluated while loading and unloading the machine. To run the experiments the value of the parameter α is set to 0.12 as done before to produce the results shown in Figs. 6.31-(e) and (f). Three sets of experiments are carried out for loading and unloading transients of the operation with Hall effect sensors Figs. 6.32-(a) and (b), self-sensing Figs. 6.32-(c) and (d) and phase advance mode Figs. 6.32-(e) and (f). For each test condition, a step load of $0.85T_n$ is applied and then removed (T_n is the nominal load torque of the machine). The machine terminal voltages and phase currents are captured using an oscilloscope. The measured average no-load current is 0.3 A. The average phase current for operation with sensors and self-sensing with no phase advance is 2.0 A and for self-sensing phase advance is 2.1 A. In these tests the speed is set to 2000 rpm in order to be able to compare the results of field weakening with the constant torque region. It can be seen that the current is increased in field weakening compared to the normal operation in order to produce the required torque while maintaining the speed set point. In each subfigure of Fig. 6.32 a zoomed view is provided for more details. It can be seen that both loading and unloading transients are reaching the steady state within 30 ms to 100 ms.

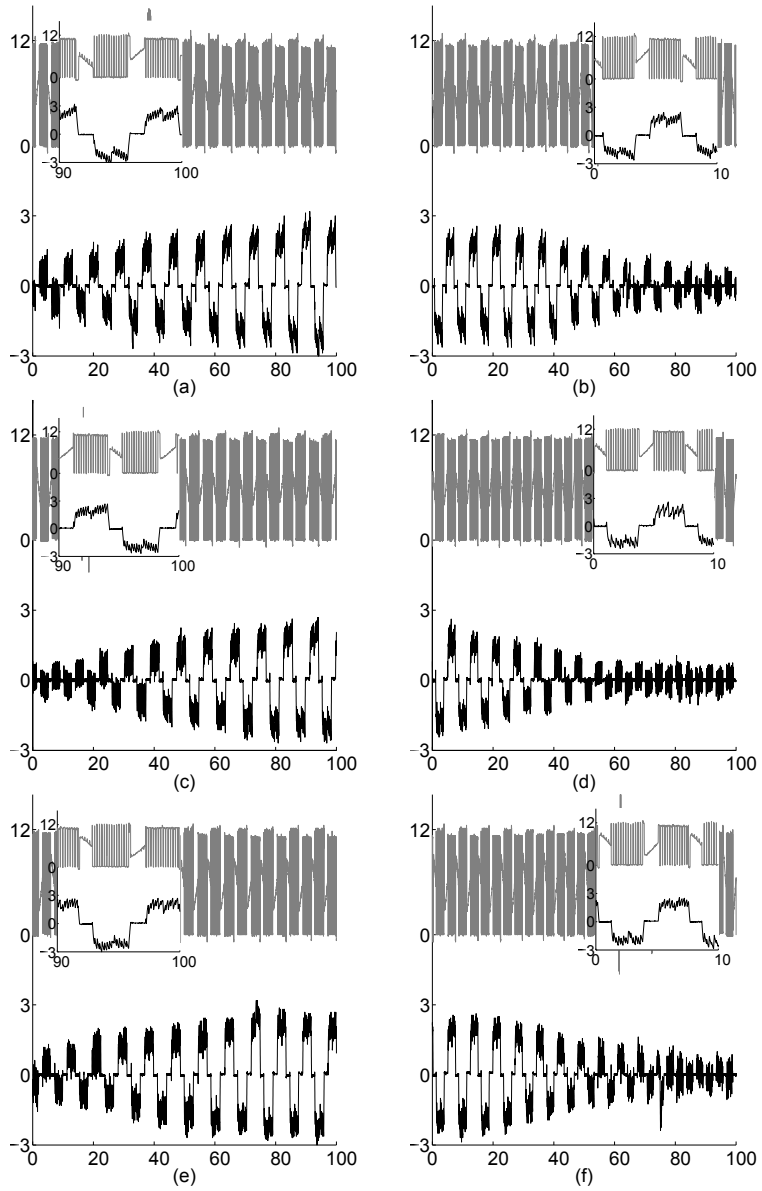

Figure 6.32. Experimental results, loading and unloading transients, x-axis: time [ms], y-axis: voltage [V], current [A], (a): loading while operation with sensors, (b): unloading while operation with sensors, (c): loading while self-sensing operation, (d): unloading while self-sensing operation, (e): loading while phase advancing, (f): unloading while phase advancing

6.11 Conclusions

In this chapter an MPC algorithm is discussed and applied to control the rotor speed and stator currents of a BLDC machine. It is demonstrated that it is possible to obtain a cost function that forces the rotor speed to stay close to its set-point, while keeping the current limited to its maximum value. The effect of the design parameters of the MPC algorithm on the BLDC drive is investigated by simulations and by experiments on a practical setup.

From the experiments, it can be concluded that the dynamic stiffness and disturbance rejection of the controlled drive can be improved by tuning the weight factors. The feedback of the internal state variables for current and speed has a significant effect on the disturbance rejection of the drive and helps to eliminate the effect of modelling errors.

While the MPC strategy is a computationally an intensive algorithm, the possibility of pipelining and parallelism on an FPGA allows to calculate the optimal input δ in real time here done by using a SPARTAN 3E FPGA.

In addition a self-sensing technique is combined with a model based predictive control algorithm to drive a BLDC machine. In addition to the individual advantages of each method some extra features can be achieved to improve the overall performance of the drive. The self-sensing algorithm provides an accurate commutation instants detection that improves the efficiency of the drive. By having an estimate about the position of the machine a phase advance technique can be implemented that makes the MPC algorithm able of working in the constant power region without notable changes in the performance of the control. The phase delay can vary continuously during operation of the machine. In the case of a cascaded speed control scheme, the machine is considered as two uncoupled first order systems when there is a large difference in times constants. However in the case of a very low inertia machine it must be considered as a second order system. The MPC algorithm provides an improved dynamic performance for the BLDC drive by controlling the speed and current of the machine simultaneously and deals with the machine as a second order system. Application of the MPC also provides a start-up ability for the back-EMF based self-sensing technique. Different experimental tests are carried out to demonstrate the individual advantages of each algorithm and the advantages of the combination of the self-sensing and MPC algorithm to improve the capabilities of a BLDC drive.

Chapter 7

Concluding Remarks and Further Research

Conventional self-sensing commutation methods based on the back-EMF signals are widely used in different industrial and low-power applications with their own drawbacks. Two enhanced self-sensing commutation methods based on the back-EMF measurement are proposed in this these and the theoretical background and experimental results are given. The results show that a satisfactory performance can be achieved with the proposed self-sensing commutation methods. The advantages of the proposed methods are: better performance during transients, a more accurate commutation at higher speed owing to the use of the low slope part of the back-EMF. Using back-EMF samples also results in an increased control performance with the speed where a higher the back-EMF value is used. This work can be extended to adapt the parameter Δt with the speed in order to have improved transient performance.

The rotor speed of BLDC drives for back-EMF based self-sensing methods is studied when operating the drive in an open speed control loop. The effect of estimation errors in the current commutation instants on the rotor speed is analysed and verified with simulations. With the analysis given in this book, the dynamical behaviour of a back-EMF based self-sensing method can be studied and improved before the design and tuning of the speed control loop. Analytical expressions are derived that consider average speed values over periods between succeeding zero-crossing occurrences in the back-EMF waveforms. When operating the drive in open-loop speed control, a drift in the rotor speed can be expected. However, from the analytical expressions, it follows a speed drift at zero acceleration occurs when the difference in the average speed between succeeding periods crosses a threshold. Such speed variations should be avoided as these demand a higher steering force

of the speed control loop. The aforementioned threshold can be computed and increases with the drive inertia as well as rotor speed and decreases with the electromagnetic torque. Hence, achieving low speed operation with back-EMF based self-sensing methods is more difficult not only due to the low signal-to-noise ratio of the speed-induced back-EMF, but also due to a less robust dynamical behaviour of the self-sensing method at lower speed. However, for a given speed, torque and inertia, a better dynamical behaviour can be obtained by using a back-EMF symmetrical tracking method instead of a zero-crossing back-EMF self-sensing method.

A load torque estimation is used in order to improve the disturbance rejection properties of the control loop in a self-sensing BLDC drive. The positive effect of load torque feedforward on the dynamic stiffness was proven theoretically, by means of the frequency response of the transfer function that describes the relation between the rotor speed and the load torque. The algorithm is then tested on the experimental setup using an FPGA.

In the final chapter an MPC algorithm is discussed and applied to control the rotor speed and stator currents of a BLDC machine. It is demonstrated that it is possible to obtain a cost function that forces the rotor speed to stay close to its set-point, while keeping the current limited to its maximum value. The effect of the design parameters of the MPC algorithm on the BLDC drive is investigated by simulations and by experiments on a practical setup.

From the experiments, it can be concluded that the dynamic stiffness and disturbance rejection of the controlled drive can be improved by tuning the weight factors. The feedback of the internal state variables for current and speed has a significant effect on the disturbance rejection of the drive and helps to eliminate the effect of modelling errors.

While the MPC strategy is a computationally an intensive algorithm, the possibility of pipelining and parallelism on an FPGA allows to calculate the optimal input δ in real time here done by using a SPARTAN 3E FPGA.

In addition a self-sensing technique is combined with a model based predictive control algorithm to drive a BLDC machine. In addition to the individual advantages of each method some extra features can be achieved to improve the overall performance of the drive. The self-sensing algorithm provides accurate detection of commutation instants, improving the efficiency of the drive. By having an estimate about the position of the machine a phase advance technique can be implemented that makes the MPC algorithm able of working in the constant power region without notable changes in the performance of the control. The phase delay can vary continuously during operation of the machine. In the case of a cascaded speed control scheme, the machine is considered as two uncoupled first order systems when there is a large difference in times constants. However in the case of

in the case of a very low inertia machine it must be considered as a second order system. The MPC algorithm provides an improved dynamic performance for the BLDC drive by controlling the speed and current of the machine simultaneously and deals with the machine as a second order system. Application of the MPC also provides a start-up ability for the back-EMF based self-sensing technique. Different experimental tests are carried out to demonstrate the individual advantages of each algorithm and the advantages of the combination of the self-sensing and MPC algorithm to improve the capabilities of a BLDC drive.

As a stable back-EMF sampling algorithm is developed and the results are verified experimentally there is a good opportunity to use the information that is extracted from back-EMF signal such as rotor position to further improve the dynamic performance of the BLDC machines. It can include the torque ripple reduction in motor operation or maximum torque per ampere tracking during the breaking and generator mode.

Appendix A

Parameters of the Machines

A.1 Maxon Machine

The datasheet of the Maxon EC 45 flat 42.8 mm, brushless, 50 Watt machine is available online at:

http://www.maxonmotor.com/medias/sys_master/root/8816806854686/15-262-EN.pdf

Some of the selected parameters are as follows:

Table A.1. Parameters of the Maxon machine

Parameter	Value
Stator Resistance	1.03Ω
Stator Inductance	0.572 mH
Rotor Inertia	1.35×10^{-5}kgm^2
Number of Pole Pairs	8
Nominal Voltage	24 V
Nominal Current	2.33 A
Nominal Load	83.4 mNm
Torque Constant	33.5 Nm/A
Voltage Constant	3.51 V/krpm

Figure A.1. Maxon EC 45 flat 42.8 mm, brushless, 50 Watt machine

A.2 T-motor Machine

The datasheet of the MT4008-18 T-Motor machine is available online at:

http://www.flashrc.com/t_motor/10918-mt4008_18_t_motor_kv380_108gr.html

Some of the selected parameters are as follows:

Table A.2. Parameters of the T-Motor machine

Parameter	Value
Stator Resistance	154mΩ
Stator Inductance	0.161 mH
Number of Pole Pairs	12
Nominal Voltage	20 V
Nominal Current	18 A
Nominal power	360 W
Voltage Constant	2.63 V/krpm

Figure A.2. MT4008-18 T-Motor machine

A.3 TONGHUI Machine

The datasheet of the TONGHUI machine is available online at:

http://www.ectrade.info/sampleroom/onesample/278494899/DC_brushless_motor.html

Some of the selected parameters are as follows:

Table A.3. Parameters of the TONGHUI machine

Parameter	Value
Stator Resistance	0.16Ω
Stator Inductance	0.3 mH
Rotor Inertia	0.024kgm^2
Number of Pole Pairs	8
Nominal Voltage	48 V
Nominal Current	18 A
Nominal power	660 W
Torque Constant	0.11 Nm/A
Voltage Constant	11.5 V/krpm

Figure A.3. TONGHUI machine

A.4 Additional Test Machine

Some of the selected parameters of a machine prototype are as follows:

Table A.4. Parameters of the prototype machine

Parameter	Value
Stator Resistance	0.075Ω
Rotor Inertia	190μkgm^2
Number of Pole Pairs	2
Nominal Voltage	36 V
Nominal Current	25 A
Nominal power	400 W

A.5 Simulated Machine

The parameters of the machine model used in the continuous time simulations by PLECS are as follows:

Table A.5. Parameters of the simulated machine

Parameter	Value
Stator Resistance	0.388Ω
Stator Inductance Constant	$2.84e^{-3}$ H
Rotor Inertia	$2e^{-3}$kgm^2
Number of Pole Pairs	1
Nominal Voltage	300 V
Nominal Current	5 A
Nominal Load	3 Nm

Appendix B

Essential Components of the Experimental Test Setup

B.1 Power stage

The used power stage (voltage source inverter) is the *ATMEL MC300* motor control driver board. This power stage is developed for DC, BLDC and stepper motors. The board can supports supply voltage up to 40 V and motor currents up to 30 A. The power stage disposes of four half-bridges, of which three is used in the set-up.

The datasheet of the ATMEL MC300 motor control driver board is available online at:

http://www.atmel.com/images/doc8124.pdf

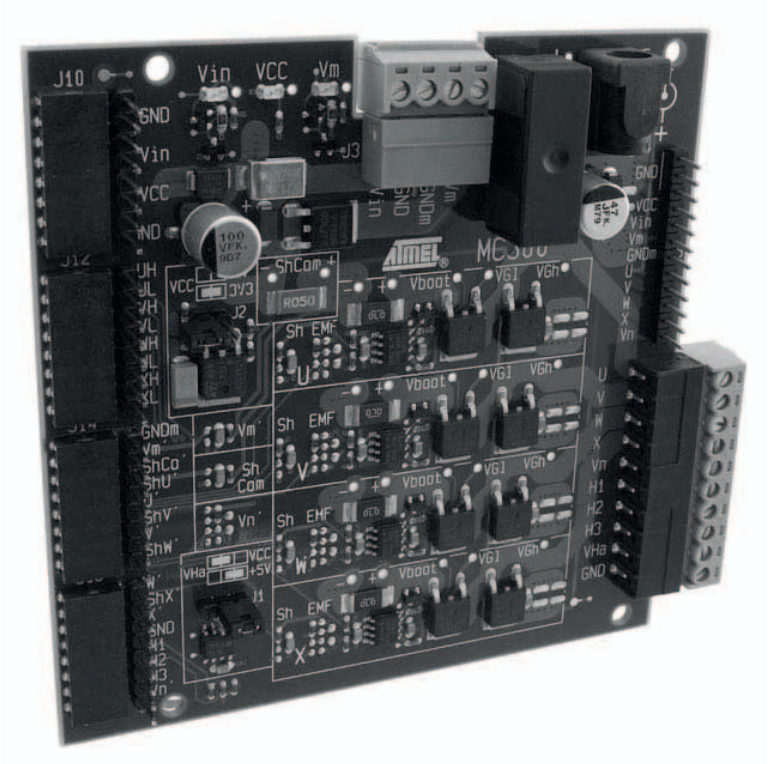

Figure B.1. ATMEL MC300 motor control driver board

B.2 FPGA

The FPGA boards used to control the motor and generator of the set-up are Xilinx® Spartan-3E Evaluation boards with a XC3S1600E and a XC3S500E FPGA chips.

The XC3S1600E FPGA has 14752 slices, 648 Kbits of RAM memory and 36 dedicated multipliers. The XC3S500E FPGA has 4656 slices, 360 Kbits of RAM memory and 20 dedicated multipliers The datasheet of the Spartan-3E FPGA family is available online at:

http://www.xilinx.com/support/documentation/data_sheets/ds312.pdf

To program the FPGA's, the Xilinx System Generator and ISE is used. The Xilinx ChipScope software is used in order to capture the internal signals of the FPGA.

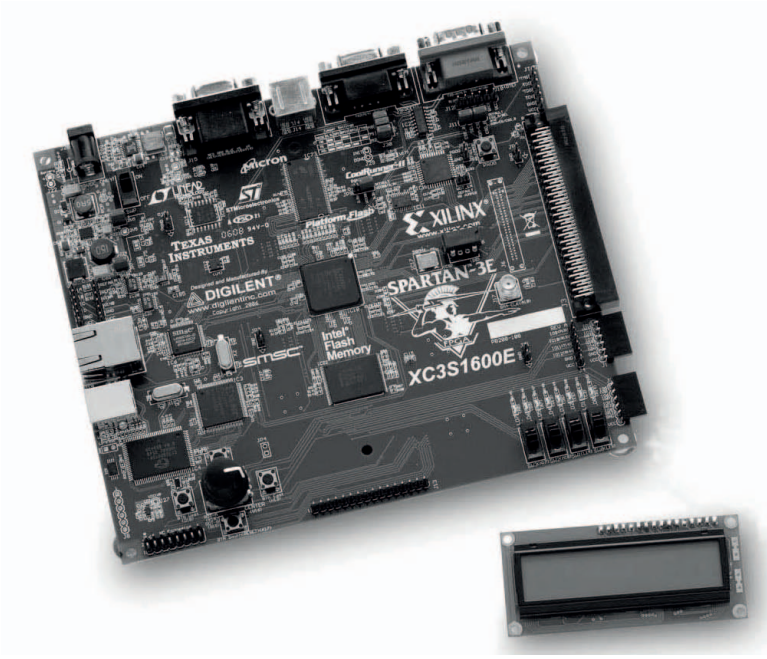

Figure B.2. XC3S1600E evaluation board

B.3 ADC modules

The phase voltages of the BLDC machine can be measured relative to the ground of the power stage. The power stage is equipped with a shunt resistor, which makes it possible to measure the DC link current. These analog signals are converted to digital ones using the Digilent PmodAD1^{TM} ADC modules. Each module has two built-in AD7476A ADC's, produced by Analog Devices. Each module allows for two signals to be read by the FPGA. A total of four ADC modules are used in the set-up. The ADC's have a 12-bit resolution. They achieve a maximum sampling rate of one million samples per second. Because the maximum voltage allowed by the modules is limited to 5 V and the maximum occurring voltage in the set-up is 18 V (the DC supply voltage), a voltage divider is used.

The datasheet of the Digilent PmodAD1^{TM} ADC modules is available online at: http://www.digilentinc.com/Data/Products/PMOD-AD1/Pmod%20AD1_rm.pdf

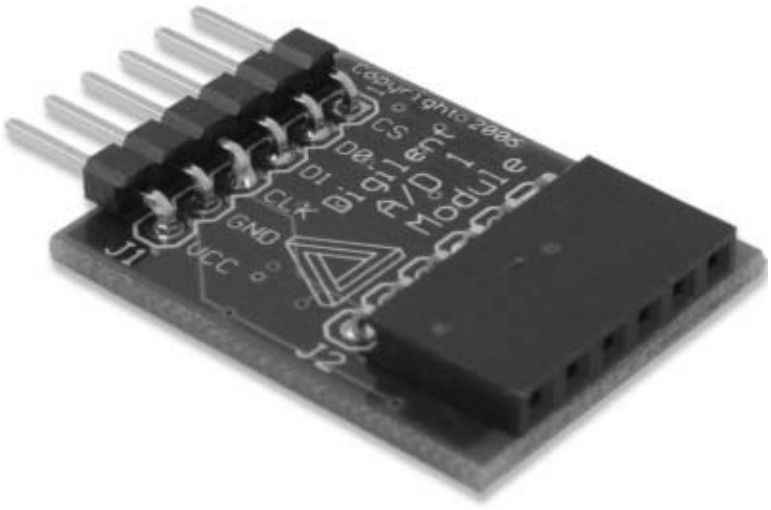

Figure B.3. PmodAD1^{TM} ADC module

B.4 Digital isolators

To get a galvanic isolation between the power stage and the FPGA board, IL715 digital isolators produced by NVE Corporation are used. These isolators implement the Isoloop® technology, which transfers the measured signals using a magnetic field and FM modulation. The isolators have to following properties:

- Data transfer rates of 110Mbps
- A quiescent current of 1.2mA for each channel
- A propagation delay of 10ns
- 2500V_{RMS} isolation voltage
- A barrier life of 44000 year.

The datasheet of the IL715 digital isolators is available online at: http://www.nve.com/Downloads/il71x.pdf

B.5 Encoder

As a validation of the commutation timing in transient conditions, the setup was equipped with a Wachendorff WDG 58H optical encoder.

- The encoder is suited for high operating speeds, the maximum operating speed is fixed to a rotor speed of 6000rpm.
- The pulses result from two waves in quadrature. The accuracy of the 90° phase shift between the two waveforms is determined as 7.5% of the pulse width.
- The encoder generates 5000 pulses per revolution.

.

The datasheet of the IL715 digital isolators is available online at: http://www.wachendorff-automation.com/thru-bore-encoder-incremtatal-quadrature-optical-wdgi58h.html?tx_pimproducts_pi1[tech_paper]=1

Figure B.4. Wachendorff WDG 58H optical encoder

Curriculum Araz Darba[1]

Publications in peer reviewed journals

1. **Darba Araz**, D'haese Pieter, De Belie Frederik, Melkebeek Jan, "Improving the Dynamic-stiffness in a Self-Sensing BLDC Machine Drive Using Estimated Load Torque Feedforward", *IEEE Transactions on Industry Applications*, vol.51, no.4, pp.3101-3114

2. **Darba Araz**, De Belie Frederik, Melkebeek Jan, "A Back-EMF Threshold Self-sensing Method to Detect the Commutation Instants in BLDC Drives", *IEEE Transactions on Industrial Electronics*, vol.62, no.10, pp.1,1

3. **Darba Araz**, De Belie Frederik, D'haese Pieter, Melkebeek Jan, "Improved Dynamic Behaviour in BLDC Drives Using Model Predictive Speed and Current Control", *IEEE Transactions on Industrial Electronics*, vol.PP, no.99, pp.1,1

4. S. Gorji Ghalamestani, **Darba Araz**, L. Vandevelde, Melkebeek Jan, "A Predictive Model of the Magnrtostrictive Behaviour of Electrical Steel in the Presence of High-Order Harmonics in the Magnetization", *IEEE Transactions on Magnetics*, [Submitted]

5. **Darba Araz**, De Belie Frederik, Melkebeek Jan, "A Self-sensing Model Predictive Speed and Current Control Algorithm for Brushless DC Machines", *IEEE Transactions on Industrial Electronics*, [Submitted]

[1] until 8th September 2015

Publications in proceedings

1. F. De Belie, **A. Darba**, Jan Melkebeek, "Open-Loop Behaviour of Back-EMF Based Self-Sensing BLDC Drives", *41st Annual Conference of the IEEE Industrial Electronics Society, IECON 2015, Yokohama, Japan*, vol., no., pp., 9-12 Nov. 2015.

2. F. De Belie, **A. Darba**, Jan Melkebeek, "Digitally current controlled three-phase machines: Enhancements in dynamic analysis and antiwind-up scheme", *2014 International Symposium on Power Electronics, Electrical Drives, Automation and Motion (SPEEDAM)*, vol., no., pp.854-859, 18-20 June 2014.

3. F. De Belie, **A. Darba**, Jan Melkebeek, "A bachelor-student project: Buck-boost operation of an integrated H-bridge for variable-speed energy storage systems using measurement coils in the stator of a DC-machine", *2014 International Power Electronics Conference (IPEC-Hiroshima 2014 - ECCE-ASIA)*, vol., no., pp.718-723, 18-21 May 2014.

4. **Darba, Araz**, D'haese, Pieter, De Belie, Frederik, Melkebeek, Jan, "Rotor speed, position and load torque estimation using back-emf sampling for self-sensing brushless DC machine drives", *2014 IEEE 5th International Symposium on Sensorless Control for Electrical Drives (SLED), Hiroshima, Japan*, vol., no., pp.1-7, 17-18 May 2014.

5. **A. Darba**, F. De Belie, J. Melkebeek, "Sensorless Control of Permanent Magnet Machines", *14th PhD Symposium Ghent University Faculty of Engineering and Architecture (FEA), Ghent, Belgium*, vol., no., pp., 06 Dec. 2013.

6. A. Salem, F. De Belie, **A. Darba**, M. Eissa, S.M. Wasfy, J. Melkebeek, "Evaluation of a Dual-T-type Converter Supplying an Open-End Winding Induction Machine", *39th Annual Conference of the IEEE Industrial Electronics Society, IECON 2013, Vienna, Austria*, vol., no., pp. 747-752, 10-13 Nov. 2013.

7. **A. Darba**, F. De Belie, A. Salem, J. Melkebeek, "FPGA-Based Implementation of the Back-EMF Symmetric-Threshold-Tracking Sensorless Commutation Method for Brushless DC-Machines", *2013 IEEE International Symposium on Sensorless Control for Electrical Drives and Predictive Control of Electrical Drives and Power Electronics (SLED/PRECEDE)*, Munich, Germany, vol., no., pp. 1-6, 17-19 Oct. 2013.

8. **A. Darba**, F. De Belie, J. Melkebeek, "Mechanical Sensorless Commutation and Speed Control of Brushless DC Motor Drives Based on the Back-EMF Symmetric Threshold Tracking", *2013 IEEE International Electric*

Machines & Drives Conference (IEMDC), Chicago, USA, vol., no., pp. 519-524, 12-15 May 2013.

9. Frederik De Belie, Jeroen De Backer, **Araz Darba**, Jan Melkebeek, "Low-speed salient-pole BLDC-machine control by using a single sensor", *2012 15th International Conference on Electrical Machines and Systems (ICEMS)*, vol., no., pp. 1-6, 21-24 Oct. 2012.

10. **A. Darba**, F. De Belie, J. Melkebeek, "FPGA Based Real-Time Simulation of Sensorless Control of PMSM Drive at Standstill Condition", *2012 International Symposium on Power Electronics, Electrical Drives, Automation and Motion (SPEEDAM), Sorrento, Italy*, vol., no., pp. 1063-1068, 20-22 June 2012.

11. **A. Darba**, F. De Belie, J. Melkebeek, "Improving Sensorless Control of Induction Machines by Modeling Saturation in Main and Leakage Flux Paths", *2012 IEEE Benelux Sixth Young Researchers Symposium (YRS)*, Delft, Netherlands, vol., no., pp. 1-6, 16-17 April 2012.

12. Odomari Shogo, **Darba Araz**, Uchida Kosuke, Senjyu Tomonobu, Yona Atsushi, "Robust position control of ultrasonic motor using VSS observer", *2010 International Conference on Electrical Machines and Systems (ICEMS)*, vol., no., pp. 787-791, 10-13 Oct. 2010.

13. Odomari Shogo, **Darba Araz**, Uchida Kosuke, Senjyu Tomonobu, Yona Atsushi, "Robust position control of ultrasonic motor considering deadzone", *2010 International Conference on Electrical Machines and Systems (ICEMS)*, vol., no., pp. 684-688, 10-13 Oct. 2010.

14. **Darba A.**, Salahshoor K., "EKF and UKF-based estimation of a sensorless axial flux PM machine under an internal-model control scheme using a SVPWM inverter", *2010 29th Chinese Control Conference (CCC)*, vol., no., pp. 5676-5681, 29-31 July 2010.

15. **Darba A.**, Esmalifalak M., Barazandeh E.S., "Implementing SVPWM technique to axial flux permanent magnet synchronous motor drive with internal model current controller", *2010 4th International Power Engineering and Optimization Conference (PEOCO)*, vol., no., pp. 126-131, 23-24 June 2010.

Attended conferences with its own presentation

- 5^{th} International Symposium on Sensorless Control for Electrical Drives (SLED), Hiroshima, Japan, 17-18 May 2014.
- 14^{th} PhD Symposium Ghent University Faculty of Engineering and Architecture
(FEA), Ghent, Belgium, 06 December 2013.
- 4^{th} International Symposium on Sensorless Control for Electrical Drives and Predictive Control of Electrical Drives and Power Electronics
(SLED/PRECEDE), Munich, Germany, 17-19 October 2013.
- 9^{th} International Electric Machines & Drives Conference
(IEMDC), Chicago, USA, 12-15 May 2013.
- 21^{st} International Symposium on Power Electronics, Electrical Drives, Automation and Motion
(SPEEDAM), Sorrento, Italy, 20-22 June 2012.
- 6^{th} Young Researchers Symposium
(YRS), Delft, The Netherlands, 16-17 April 2012.
- 29^{th} Chinese Control Conference
(CCC), Beijing, China, 29-31 July 2010.
- 4^{th} International Power Engineering and Optimization Conference,
(PEOCO), Shah Alam, Malaysia, 23-24 June 2010.

Bibliography

[Acarnley2006] P. Acarnley, J. Watson, "Review of Position-Sensorless Operation of Brushless Permanent-Magnet Machines," *IEEE Transactions on Industrial Electronics*, vol.53(2), pp.352-362, April 2006.

[Alkorta2014] P. Alkorta, O. Barambones, J.A. Cortajarena, A. Zubizarrreta, "Efficient Multivariable Generalized Predictive Control for Sensorless Induction Motor Drives," *IEEE Transactions on Industrial Electronics*, vol.61, no.9, pp.5126-5134, Sept. 2014.

[Barrero2009a] F. Barrero, M.R. Arahal, R. Gregor, S. Toral, M.J. Duran, "A Proof of Concept Study of Predictive Current Control for VSI-Driven Asymmetrical Dual Three-Phase AC Machines," *IEEE Transactions on Industrial Electronics*, vol.56, no.6, pp.1937-1954, June 2009.

[Barrero2009b] F. Barrero, M.R. Arahal, R. Gregor, S. Toral, M.J. Duran, "One-Step Modulation Predictive Current Control Method for the Asymmetrical Dual Three-Phase Induction Machine," *IEEE Transactions on Industrial Electronics*, vol.56, no.6, pp.1974-1983, June 2009.

[Barrero2011] F. Barrero, J. Prieto, E. Levi, R. Gregor, S. Toral, M.J. Duran, M. Jones, "An Enhanced Predictive Current Control Method for Asymmetrical Six-Phase Motor Drives," *IEEE Transactions on Industrial Electronics*, vol.58, no.8, pp.3242-3252, Aug. 2011

[Becerra1991] R.C. Becerra, T.M. Jahns, M. Ehsani, "Four-quadrant sensorless brushless ECM drive," *Sixth Annual Conference Proceedings Applied Power Electronics Conference and Exposition, 1991. APEC '91*, vol., no., pp.202-209, 10-15 Mar. 1991.

[Bianchi2007a] N. Bianchi, S. Bolognani, "Influence of Rotor Geometry of an IPM Motor on Sensorless Control Feasibility," *IEEE Transactions on Industry Applications*, vol.43, no.1, pp.87-96, Jan.-feb. 2007.

[Bianchi2007b] N. Bianchi, S. Bolognani, Ji-Hoon Jang, Seung-Ki Sul, "Comparison of PM Motor Structures and Sensorless Control Techniques for Zero-Speed

Rotor Position Detection," *IEEE Transactions on Power Electronics*, vol.22, no.6, pp.2466-2475, Nov. 2007.

[Bianchi2008] N. Bianchi, S. Bolognani, Ji-Hoon Jang, Seung-Ki Sul, "Advantages of Inset PM Machines for Zero-Speed Sensorless Position Detection," *IEEE Transactions on Industry Applications*, vol.44, no.4, pp.1190-1198, July-aug. 2008.

[Bianchi2009] N. Bianchi, S. Bolognani, "Sensorless-Oriented Design of PM Motors," *IEEE Transactions on Industry Applications*, vol.45, no.4, pp.1249-1257, July-aug. 2009.

[Bolognani2009] S. Bolognani, S. Bolognani, L. Peretti, M. Zigliotto, "Design and Implementation of Model Predictive Control for Electrical Motor Drives," *IEEE Transactions on Industrial Electronics*, vol.56, no.6, pp.1925-1936, June 2009.

[Buja1995] G.S. Buja, R. Menis, M.I. Valla, "Disturbance torque estimation in a sensorless DC drive," *IEEE Transactions on Industrial Electronics*, vol.42, no.4, pp.351-357, Aug 1995.

[Champa2009] P. Champa, P. Somsiri, P. Wipasuramonton, P. Nakmahachalasint, "Initial Rotor Position Estimation for Sensorless Brushless DC Drives," *IEEE Transactions on Industry Applications*, vol.45, no.4, pp.1318-1324, July-aug. 2009

[Cheng-HuChen2007] Cheng-Hu Chen, Ming-Yang Cheng, "A New Cost Effective Sensorless Commutation Method for Brushless DC Motors Without Phase Shift Circuit and Neutral Voltage," *IEEE Transactions on Power Electronics*, vol.22, no.2, pp.644-653, March 2007.

[ChangliangXia2013] Changliang Xia, Yingfa Wang, Tingna Shi, "Implementation of Finite-State Model Predictive Control for Commutation Torque Ripple Minimization of Permanent-Magnet Brushless DC Motor," *IEEE Transaction on Industrial Electronics*, vol.60, no.3, pp.896-905, March 2013.

[Carpaneto2012] M. Carpaneto, P. Fazio, M. Marchesoni, G. Parodi, "Dynamic Performance Evaluation of Sensorless Permanent-Magnet Synchronous Motor Drives With Reduced Current Sensors," *IEEE Transactions on Industrial Electronnics*, vol.59, no.12, pp.4579-4589, Dec. 2012.

[Chen-YenYu2013] Chen-Yen Yu, J. Tamura, D.D. Reigosa, R.D. Lorenz, "Position Self-Sensing Evaluation of a FI-IPMSM Based on High-Frequency Signal Injection Methods," *IEEE Transactions on Industry Applications*, vol.49, no.2, pp.880-888, March-April 2013,

[Chun2014] Tae-Won Chun, Quang-Vinh Tran, Hong-Hee Lee, Heung-Geun Kim, "Sensorless Control of BLDC Motor Drive for an Automotive Fuel Pump Using a Hysteresis Comparator," *IEEE Transactions on Power Electronics*, vol.29, no.3, pp.1382-1391, March 2014.

[Consoli2001] A. Consoli, G. Scarcella, A. Testa, "Industry application of zero-speed sensorless control techniques for PM synchronous motors," *IEEE Transactions on Industry Applications*, vol.37, no.2, pp.513-521, Mar/Apr 2001.

[Dadashnialehi2014] A. Dadashnialehi, A. Bab-Hadiashar, Z. Cao, A. Kapoor, "Intelligent Sensorless ABS for In-Wheel Electric Vehicles," *IEEE Transactions on Industrial Electronics*, vol.61, no.4, pp.1957-1969, April 2014.

[Dadashnialehi2015] A. Dadashnialehi, A. Bab-Hadiashar, Z. Cao, A. Kapoor, "Intelligent Sensorless Antilock Braking System for Brushless In-Wheel Electric Vehicles," *IEEE Transactions on Industrial Electronics*, vol.62, no.3, pp.1629-1638, March 2015.

[Damodharan2010] P. Damodharan, K. Vasudevan, "Sensorless Brushless DC Motor Drive Based on the Zero-Crossing Detection of Back Electromotive Force (EMF) From the Line Voltage Difference," *IEEE Transactions on Energy Conversion*, vol.25, no.3, pp.661-668, Sept. 2010.

[Darba2012] A. Darba, F. De Belie, T. Vyncke, J. Melkebeek, "FPGA-based real-time simulation of sensorless control of PMSM drive at standstill," *IEEE International Symposium on Power Electronics, Electrical Drives, Automation and Motion (SPEEDAM)*, vol., no., pp.1063-1068, 20-22 June 2012.

[Darba2013a] A. Darba, F. De Belie, J. Melkebeek, "Sensorless commutation and speed control of Brushless DC-machine drives based on the back-EMF symmetric threshold-tracking," *2013 IEEE International Electric Machines & Drives Conference (IEMDC)*, vol., no., pp.492-497, 12-15 May 2013.

[Darba2013b] A. Darba, A. Salem, F. De Belie, J. Melkebeek, "FPGA-based implementation of the back-EMF symmetric-threshold-tracking sensorless commutation method for Brushless DC-machines," *2013 IEEE International Symposium on Sensorless Control for Electrical Drives and Predictive Control of Electrical Drives and Power Electronics (SLED/PRECEDE)*, vol., no., pp.1-6, 17-19 Oct. 2013.

[Darba2014] A. Darba, P. D'haese, F. De Belie, J. Melkebeek, "Rotor speed, position and load torque estimation using back-emf sampling for self-sensing brushless DC machine drives," *2014 IEEE 5th International Symposium on Sensorless Control for Electrical Drives (SLED)*, vol., no., pp.1-7, 17-18 May 2014.

[Darba2015a] A. Darba, P. D'haese, F. De Belie, J. Melkebeek, "Improving the Dynamic-stiffness in a Self-Sensing BLDC Machine Drive by Using Estimated Load Torque Feedforward," *IEEE Transactions on Industry Application*,

[Darba2015b] A. Darba, F. De Belie, J. Melkebeek, "A Back-EMF Threshold Self-sensing Method to Detect the Commutation Instants in BLDC Drives," *IEEE IEEE Transactions on Industrial Electronics*,

[Davari2012] S. Alireza Davari, D.A. Khaburi, Fengxiang Wang, R. Kennel, "Using Full Order and Reduced Order Observers for Robust Sensorless Predictive Torque Control of Induction Motors," *IEEE Transactions on Power Electronics*, vol.27, no.7, pp.3424-3433, July 2012.

[DeAngelo2005] C. De Angelo, G. Bossio, Jorge Solsona, G.O. Garcia, M.I Valla, "A rotor position and speed observer for permanent-magnet motors with nonsinusoidal EMF waveform," *IEEE Transactions on Industrial Electronics*, vol.52, no.3, pp.807-813, June 2005.

[DeBelie2010] F.M.L. De Belie, P. Sergeant, J.A. Melkebeek, "A Sensorless Drive by Applying Test Pulses Without Affecting the Average-Current Samples," *IEEE Transactions on Power Electronics*, vol.25, no.4, pp.875-888, April 2010.

[DeBelie2012] F. De Belie, J. De Backer, A. Darba, J.A. Melkebeek, "Low-Speed Salient-Pole BLDC-Machine Control by Using a Single Sensor," *15th IEEE International Conference on Electrical Machines and Systems (ICEMS)*, vol., no., pp.1-6, 21-24 Oct. 2012.

[DeBelie2015] F. De Belie, A. Darba, J.A. Melkebeek, "Open-Loop Behaviour of Back-EMF Based Self-Sensing BLDC Drives," *IEEE 41th Annual Conference of IEEE Industrial Electronics IECON '15*

[DeCooman2012] G. De Cooman, "Lineaire systemen," *Universiteit Gent, Faculteit Ingenieurswetenschappen en Architectuur*, 2012.

[Druant2015] J. Druant, T. Vyncke, F. De Belie, P. Sergeant, J. Melkebeek, "Adding Inverter Fault Detection to Model-Based Predictive Control for Flying-Capacitor Inverters," *IEEE Transactions on Industrial Electronics*, vol.62, no.4, pp.2054-2063, April 2015.

[Duran2011] M.J. Duran, J. Prieto, F. Barrero, S. Toral, "Predictive Current Control of Dual Three-Phase Drives Using Restrained Search Techniques," *IEEE Transactions on Industrial Electronics*, vol.58, no.8, pp.3253-3263, Aug. 2011.

[FengxiangWang2014a] Fengxiang Wang, Zhenbin Zhang, P. Stolze, J.-F. Stumper, J. Rodriguez, R. Kennel, "Encoderless Finite-State Predictive Torque Control for Induction Machine With a Compensated MRAS," *IEEE Transactions on Industrial Informatics*, vol.10, no.2, pp.1097-1106, May 2014.

[FengxiangWang2014b] Fengxiang Wang, Zhe Chen, S. Alireza Davari, R. Fotouhi, D. Arab Khaburi, J. Rodriguez, R. Kennel, "An Encoderless Predictive Torque Control for an Induction Machine With a Revised Prediction Model and EFOSMO," *IEEE Transactions on Industrial Electronics*, vol.61, no.12, pp.6635-6644, Dec. 2014.

[Fuentes2014] E. Fuentes, D. Kalise, J. Rodriguez, R.M. Kennel, "Cascade-Free Predictive Speed Control for Electrical Drives," *IEEE Transaction on Industrial Electronics*, vol.61, no.5, pp.2176-2184, May 2014.

[Gabriel2013] F. Gabriel, F. De Belie, X. Neyt, P. Lataire, "High-Frequency Issues Using Rotating Voltage Injections Intended For Position Self-Sensing," *IEEE Transactions on Industrial Electronics*, vol.60, no.12, pp.5447-5457, Dec. 2013.

[Gao2010] Jin Gao, Yuwen Hu, "Direct Self-Control for BLDC Motor Drives Based on Three-Dimensional Coordinate System," *IEEE Transactions on Industrial Electronics*, vol.57, no.8, pp.2836-2844, Aug. 2010.

[Genduso2010] F. Genduso, R. Miceli, C. Rando, G.R. Galluzzo, "Back EMF Sensorless-Control Algorithm for High-Dynamic Performance PMSM," *IEEE Transactions on Industrial Electronics*, vol.57, no.6, pp.2092-2100, June 2010.

[Geyer2009a] T. Geyer, G. Papafotiou, M. Morari, "Model Predictive Direct Torque Control-Part I: Concept, Algorithm, and Analysis," *IEEE Transaction on Industrial Electronics*, vol.56, no.6, pp.1894-1905, June 2009.

[Geyer2009b] T. Geyer, G. Papafotiou, "Model Predictive Direct Torque Control of a variable speed drive with a five-level inverter," *IEEE 35th Annual Conference of IEEE Industrial Electronics IECON '09*, vol., no., pp.1203-1208, 3-5 Nov. 2009.

[Geyer2012] T. Geyer, S. Mastellone, "Model Predictive Direct Torque Control of a Five-Level ANPC Converter Drive System," *IEEE Transactions on Industry Applications*, vol.48, no.5, pp.1565-1575, Sept.-Oct. 2012.

[Geyer2013] T. Geyer, "Model Predictive Direct Torque Control: Derivation and Analysis of the State-Feedback Control Law," *IEEE Transaction on Industry Applications*, vol.49, no.5, pp.2146-2157, Sept.-Oct. 2013.

[Grignion2014] D. Grignion, Xiang Chen, N. Kar, Huijie Qian, "Estimation of Load Disturbance Torque for DC Motor Drive Systems Under Robustness and Sensitivity Consideration," *IEEE Transactions on Industrial Electronics*, vol.61, no.2, pp.930-942, Feb. 2014.

[Guzinski2009] J. Guzinski, M. Diguet, Z. Krzeminski, A. Lewicki, H. Abu-Rub, "Application of Speed and Load Torque Observers in High-Speed Train Drive for Diagnostic Purposes," *IEEE Transactions on Industrial Electronics*, vol.56, no.1, pp.248-256, Jan. 2009.

[Guzinski2010] J. Guzinski, H. Abu-Rub, M. Diguet, Z. Krzeminski, A. Lewicki, "Speed and Load Torque Observer Application in High-Speed Train Electric Drive," *IEEE Transactions on Industrial Electronics*, vol.57, no.2, pp.565-574, Feb. 2010.

[Guzinski2013] J. Guzinski, H. Abu-Rub, "Speed Sensorless Induction Motor Drive With Predictive Current Controller," *IEEE Transactions on Industrial Electronics*, vol.60, no.2, pp.699-709, Feb. 2013.

[Guzman2014] H. Guzman, M.J. Duran, F. Barrero, B. Bogado, S. Toral, "Speed Control of Five-Phase Induction Motors With Integrated Open-Phase Fault Operation Using Model-Based Predictive Current Control Techniques," *IEEE Transactions on Industrial Electronics*, vol.61, no.9, pp.4474-4484, Sept. 2014.

[Guzman2015] H. Guzman, F. Barrero, M. Duran, "IGBT-Gating Failure Effect on a Fault-Tolerant Predictive Current Controlled 5-Phase Induction Motor Drive," *IEEE Transactions on Industrial Electronics*, vol.62, no.1, pp.15-20, Jan. 2015.

[Hamida2013] M.A. Hamida, J. De Leon, A. Glumineau, R. Boisliveau, "An Adaptive Interconnected Observer for Sensorless Control of PM Synchronous Motors With Online Parameter Identification," *IEEE Transactions on Industrial Electronics*, vol.60, no.2, pp.739-748, Feb. 2013.

[Harke2006] L.A.. de S.Ribeiro, M.C. Harke, R.D. Lorenz, "Dynamic Properties of Back-emf Based Sensorless Drives," *IEEE 41st IAS Annual Meeting Industry Applications Conference*, vol.4, no., pp.2026-2033, 8-12 Oct. 2006.

[Harke2007] M.C. Harke, L.A.. de S.Ribeiro, R.D. Lorenz, "Disturbance rejection limitations of back-EMF based sensorless PM drives," *2007 European Conference on Power Electronics and Applications*, vol., no., pp.1-10, 2-5 Sept. 2007.

[Harke2008] M.C. Harke, G. De Donato, F. Giulii Capponi, T.R. Tesch, R.D. Lorenz, "Implementation Issues and Performance Evaluation of Sinusoidal, Surface-Mounted PM Machine Drives With Hall-Effect Position Sensors and a Vector-Tracking Observer," *IEEE Transactions on Industry Applications*, vol.44, no.1, pp.161-173, Jan.-feb. 2008.

[Hongryel2011] Hongryel Kim, Jubum Son, JangMyung Lee, "A High-Speed Sliding-Mode Observer for the Sensorless Speed Control of a PMSM," *IEEE Transactions on Industrial Electronics*, vol.58, no.9, pp.4069-4077, Sept. 2011.

[Iizuka1985] Iizuka Kenichi, Uzuhashi Hideo, Kano Minoru, Endo Tsunehiro, Mohri Katsuo, "Microcomputer Control for Sensorless Brushless Motor," *IEEE Transactions on Industry Applications*, vol.IA-21, no.3, pp.595-601, May 1985.

[Iepure2012] L.I. Iepure, I. Boldea, F. Blaabjerg, "Hybrid I-f Starting and Observer-Based Sensorless Control of Single-Phase BLDC-PM Motor Drives,"

IEEE Transactions on Industrial Electronics, vol.59, no.9, pp.3436-3444, Sept. 2012.

[Jang2005] Gunhee Jang, M.G. Kim, "A bipolar-starting and unipolar-running method to drive a hard disk drive spindle motor at high speed with large starting torque," IEEE Transactions on Magnetics, vol.41, no.2, pp.750-755, Feb. 2005.

[Jansen1995] P.L. Jansen, R.D. Lorenz, "Transducerless position and velocity estimation in induction and salient AC machines," *IEEE Transactions on Industry Applications*, vol.31, no.2, pp.240-247, Mar/Apr 1995.

[JianchengFang2014] Jiancheng Fang, Wenzhuo Li, Haitao Li, "Self-Compensation of the Commutation Angle Based on DC-Link Current for High-Speed Brushless DC Motors With Low Inductance," *IEEE Transactions on Power Electronics*, vol.29, no.1, pp.428-439, Jan. 2014.

[Ji-HoonJang2003] Ji-Hoon Jang, Seung-Ki Sul, Jung-Ik Ha, K. Ide, M. Sawamura, "Sensorless drive of surface-mounted permanent-magnet motor by high-frequency signal injection based on magnetic saliency," *IEEE Transactions on Industry Applications*, vol.39, no.4, pp.1031-1039, July-Aug. 2003.

[Jung-IkHa1999] Jung-Ik Ha, Seung-Ki Sul, "Sensorless field-orientation control of an induction machine by high-frequency signal injection," *IEEE Transactions on Industry Applications*, vol.35, no.1, pp.45-51, Jan/Feb 1999.

[Kenjo1985] Takashi Kenjo, Shigenobu Nagamori, "Permanent-magnet and brushless DC motors," Clarendon Press, 1985.

[Kyeong-Hwa2002] Kyeong-Hwa Kim, Myung-Joong Youn, "A nonlinear speed control for a PM synchronous motor using a simple disturbance estimation technique," IEEE Transactions on Industrial Electronics, vol.49, no.3, pp.524-535, Jun 2002.

[Kim2011] Taeyeon Kim, Chungil Kim, Joon Lyou, "A new sensorless drive scheme for a BLDC motor based on the terminal voltage difference," *37^{th} Annual Conference on IEEE Industrial Electronics Society IECON 2011*, vol., no., pp.1710-1715, 7-10 Nov. 2011.

[Kwon2008] Kwang-Woon Lee, Dae-kyong Kim, Byung-taek Kim, Byung-Il Kwon, "A Novel Starting Method of the Surface Permanent-Magnet BLDC Motors Without Position Sensor for Reciprocating Compressor," *IEEE Transactions on Industry Applications*, vol.44, no.1, pp.85-92, Jan.-feb. 2008.

[Lai2008] Yen-Shin Lai, Yong-Kai Lin, "Novel Back-EMF Detection Technique of Brushless DC Motor Drives for Wide Range Control Without Using Current and Position Sensors," *IEEE Transactions on Power Electronics*, vol.23, no.2, pp.934-940, March 2008.

[Lai2011] Yen-Shin Lai, Yong-Kai Lin, "A Unified Approach to Zero-Crossing Point Detection of Back EMF for Brushless DC Motor Drives without Current and Hall Sensors," *IEEE Transactions on Power Electronics*, vol.26, no.6, pp.1704-1713, June 2011.

[Lee2006] Wook-Jin Lee, Seung-Ki Sul, "A New Starting Method of BLDC Motors Without Position Sensor," *IEEE Transactions on Industry Applications*, vol.42, no.6, pp.1532-1538, Nov.-dec. 2006.

[Leidhold2011] R. Leidhold, "Position Sensorless Control of PM Synchronous Motors Based on Zero-Sequence Carrier Injection," IEEE Transactions on Industrial Electronics, vol.58, no.12, pp.5371-5379, Dec. 2011.

[Lim2013] Chee Shen Lim, N.A. Rahim, Wooi Ping Hew; E. Levi, "Model Predictive Control of a Two-Motor Drive With Five-Leg-Inverter Supply," *IEEE Transaction on Industrial Electronics*, vol.60, no.1, pp.54-65, Jan. 2013.

[Lim2014a] Chee Shen Lim; E. Levi, M. Jones, N.A. Rahim, W.P. Hew, "FCS-MPC-Based Current Control of a Five-Phase Induction Motor and its Comparison with PI-PWM Control," *IEEE Transactions on Industrial Electronics*, vol.61, no.1, pp.149-163, Jan. 2014.

[Lim2014a] C.S. Lim, E. Levi, M. Jones, N. Abd Rahim, W.P. Hew, "A Fault-Tolerant Two-Motor Drive with FCS-MP based Flux and Torque Control," *IEEE Transaction on Industrial Electronics*, vol.PP, no.99, pp.1-1 April 2014.

[Lim2014b] Chee Shen Lim, E. Levi, M. Jones, N.A. Rahim, Wooi-Ping Hew, "A Comparative Study of Synchronous Current Control Schemes Based on FCS-MPC and PI-PWM for a Two-Motor Three-Phase Drive," *IEEE Transaction on Industrial Electronics*, vol.61, no.8, pp.3867-3878, Aug. 2014.

[Lorenz1994] R.D. Lorenz, T.A. Lipo, D.W. Novotny, "Motion Control with Induction Motors," *Proceedings of the IEEE*, vol.82, no.8, pp.1215-1240, Aug. 1994.

[Miller1989] T.J.E. Miller, "Brushless Permanent-Magnet and Reluctance Motor Drives" *Oxford University Press*, New York, 1989.

[Moreira1996] J.C. Moreira, "Indirect sensing for rotor flux position of permanent magnet AC motors operating over a wide speed range," *IEEE Transactions on Industry Applications*, vol.32, no.6, pp.1394-1401, Nov./Dec. 1996.

[Nandi2004] S. Nandi, "Modeling of induction machines including stator and rotor slot effects," *IEEE Transactions on Industry Applications*, vol.40, no.4, pp.1058-1065, July-Aug. 2004

[Ogasawara1991] S. Ogasawara, H. Akagi, "An approach to position sensorless drive for brushless DC motors," *IEEE Transactions on Industry Applications*, vol.27, no.5, pp.928-933, Sep./Oct. 1991.

[Papafotiou2009] G. Papafotiou, J. Kley, K.G. Papadopoulos, P. Bohren, M. Morari, "Model Predictive Direct Torque Control-Part II: Implementation and Experimental Evaluation," *IEEE Transaction on Industrial Electronics*, vol.56, no.6, pp.1906-1915, June 2009.

[Perriard2012] O. Scaglione, M. Markovic,Y. Perriard, "First-Pulse Technique for Brushless DC Motor Standstill Position Detection Based on Iron B-H Hysteresis," *IEEE Transactions on Industrial Electronics*, vol.59, no.5, pp.2319-2328, May 2012.

[Pillay1988] P. Pillay, R. Krishnan, "Modeling of permanent magnet motor drives," *IEEE Transactions on Industrial Electronics*, vol.35, no.4, pp.537-541, Nov. 1988.

[Preindl2011a] M. Preindl, E. Schaltz, P. Thogersen, "Switching Frequency Reduction Using Model Predictive Direct Current Control for High-Power Voltage Source Inverters," *IEEE Transactions on Industrial Electronics*, vol.58, no.7, pp.2826-2835, July 2011.

[Preindl2011b] M. Preindl, E. Schaltz, "Sensorless Model Predictive Direct Current Control Using Novel Second-Order PLL Observer for PMSM Drive Systems," *IEEE Transactions on Power Electronics*, vol.58, no.9, pp.4087-4095, Sept. 2011.

[Preindl2013a] M. Preindl, S. Bolognani, "Model Predictive Direct Speed Control with Finite Control Set of PMSM Drive Systems," *IEEE Transactions on Power Electronics*, vol.28, no.2, pp.1007-1015, Feb. 2013.

[Preindl2013b] M. Preindl, S. Bolognani, "Model Predictive Direct Torque Control With Finite Control Set for PMSM Drive Systems, Part 2: Field Weakening Operation," *IEEE Transactions on Industrial Informatics*, vol.9, no.2, pp.648-657, May 2013.

[Preindl2013c] M. Preindl, S. Bolognani, "Model Predictive Direct Torque Control With Finite Control Set for PMSM Drive Systems, Part 1: Maximum Torque Per Ampere Operation," *IEEE Transactions on Industrial Informatics*, vol.9, no.4, pp.1912-1921, Nov. 2013.

[QuanJiang2005] Quan Jiang, Chao Bi, R. Huang, "A new phase-delay-free method to detect back EMF zero-crossing points for sensorless control of spindle motors," *IEEE Transactions on Magnetics*, vol.41, no.7, pp.2287-2294, July 2005.

[Reigosa2010] D.D. Reigosa, K. Akatsu, N. Limsuwan, Y. Shibukawa, R.D. Lorenz, "Self-Sensing Comparison of Fractional Slot Pitch Winding Versus Distributed Winding for FW- and FI-IPMSMs Based on Carrier Signal Injection at Very Low Speed," *IEEE Transaction on Industry Applications*, vol.46, no.6, pp.2467-2474, Nov.-Dec. 2010.

[Riveros2013] J.A. Riveros, F. Barrero, E. Levi, M.J. Duran, S. Toral, M. Jones, "Variable-Speed Five-Phase Induction Motor Drive Based on Predictive Torque Control," *IEEE Transaction on Industrial Electronics*, vol.60, no.8, pp.2957-2968, Aug. 2013.

[Rodriguez2012] J. Rodriguez, R.M. Kennel, J.R. Espinoza, M. Trincado, C.A. Silva, C.A. Rojas, "High-Performance Control Strategies for Electrical Drives: An Experimental Assessment," *IEEE Transaction on Industrial Electronics*, vol.59, no.2, pp.812-820, Feb. 2012.

[Ruderman2013] M. Ruderman, A. Ruderman, T. Bertram, "Observer-Based Compensation of Additive Periodic Torque Disturbances in Permanent Magnet Motors," *IEEE Transactions on Industrial Informatics*, vol.9, no.2, pp.1130-1138, May 2013.

[Scaglione2012] O. Scaglione, M. Markovic, Y. Perriard, "First-Pulse Technique for Brushless DC Motor Standstill Position Detection Based on Iron B-H Hysteresis," *IEEE Transaction on Industrial Electronics*, vol.59, no.5, pp.2319-2328, May 2012.

[Schmidt1992] P.B. Schmidt, R.D. Lorenz, "Design Principles and Implementation of Acceleration Feedback to Improve Performance of DC Drives," *IEEE Transactions on Industry Applications*, vol.28, no.3, pp.594-599, May/Jun 1992.

[Sergeant2012] P. Sergeant, F. De Belie, J. Melkebeek, "Rotor Geometry Design of Interior PMSMs With and Without Flux Barriers for More Accurate Sensorless Control," *IEEE Transaction on Industrial Electronics*, vol.59, no.6, pp.2457-2465, June 2012.

[ShanChai2013] Shan Chai, Liuping Wang, E. Rogers, "A Cascade MPC Control Structure for a PMSM With Speed Ripple Minimization," *IEEE Transaction on Industrial Electronics*, vol.60, no.8, pp.2978-2987, Aug. 2013.

[ShanshanWu2009] Shanshan Wu, D.D. Reigosa, Y. Shibukawa, M.A. Leetmaa, R.D. Lorenz, Yongdong Li, "Interior Permanent-Magnet Synchronous Motor Design for Improving Self-Sensing Performance at Very Low Speed," *IEEE Transactions on Industry Applications*, vol.45, no.6, pp.1939-1946, Nov.-dec. 2009.

[Shao2003] Jianwen Shao, D. Nolan, M. Teissier, D. Swanson, "A novel microcontroller-based sensorless brushless DC (BLDC) motor drive for automotive fuel pumps," *IEEE Transactions on Industry Applications*, vol.39, no.6, pp.1734-1740, Nov./Dec. 2003.

[Shao2006] Jianwen Shao, "An Improved Microcontroller-Based Sensorless Brushless DC (BLDC) Motor Drive for Automotive Applications," *IEEE Transactions on Industry Applications*, vol.42, no.5, pp.1216-1221, Sept./Oct. 2006.

[Shen2006] J.X. Shen, S. Iwasaki, "Sensorless control of ultrahigh-speed PM brushless motor using PLL and third harmonic back EMF," *IEEE Transactions on Industrial Electronics*, vol.53, no.2, pp.421-428, April 2006.

[Stirban2012] A. Stirban, I. Boldea, G. Andreescu, "Motion-Sensorless Control of BLDC-PM Motor With Offline FEM-Information-Assisted Position and Speed Observer," *IEEE Transactions on Industry Applications*, vol.48, no.6, pp.1950-1958, Nov.-Dec. 2012.

[SungminKim2012] Sungmin Kim, Jung-Ik Ha, Seung-Ki Sul, "PWM Switching Frequency Signal Injection Sensorless Method in IPMSM," *IEEE Transactions on Industry Applications*, vol.48, no.5, pp.1576-1587, Sept.-Oct. 2012.

[Tae-Hyung2003] Kim Tae-Hyung, Lee Byung-Kuk, M. Ehsani, "Sensorless control of the BLDC motors from near zero to high speed," *Eighteenth Annual IEEE Applied Power Electronics Conference and Exposition, 2003. APEC '03*, vol.1, no., pp.306-312 vol.1, 9-13 Feb. 2003.

[Tae-Hyung2004] Kim Tae-Hyung, M. Ehsani, "Sensorless control of the BLDC motors from near-zero to high speeds," *IEEE Transactions on Power Electronics*, vol.19, no.6, pp.1635-1645, Nov. 2004.

[Tashakori2012] A. Tashakori and M. Ektesabi, "Stability Analysis of Sensorless BLDC Motor Drive Using Digital PWM Technique for Electric Vehicles " *38th Annual Conference on IEEE Industrial Electronics Society, IECON 2012*, 25-28 Oct. 2012, pp.4898-4903.

[Tsotoulidis2015] S. Tsotoulidis, A. Safacas, "Deployment of an Adaptable Sensorless Commutation Technique on BLDC Motor Drives exploiting Zero Sequence Voltage," *IEEE Transactions on Industrial Electronics*, vol.62, no.2, pp.877-886, Feb. 2015.

[Tuovinen2014] T. Tuovinen, M. Hinkkanen, "Adaptive Full-Order Observer With High-Frequency Signal Injection for Synchronous Reluctance Motor Drives," *IEEE Journal of Emerging and Selected Topics in Power Electronics*, vol.2, no.2, pp.181-189, June 2014.

[VanDeSype1999] David M. Van De Sype, K. De Gusseme, Alex P. Van den Bossche, J. A. A. Melkebeek, "A sampling algorithm for digitally controlled boost PFC converters," *IEEE Transactions on Industrial Electronics*, vol.46, no.4, pp.833-841, Aug 1999.

[Vyncke2013] T.J. Vyncke, S. Thielemans, J.A. Melkebeek, "Finite-Set Model-Based Predictive Control for Flying-Capacitor Converters: Cost Function Design and Efficient FPGA Implementation," *IEEE Transaction on Industrial Informatics*, vol.9, no.2, pp.1113-1121, May 2013.

[Wale2004] J.D. Wale, C. Pollock, "A low-cost sensorless technique for load torque estimation in a hybrid stepping motor," *IEEE Transactions on Power Electronics*, vol.19, no.3, pp.649-657, May 2004.

[Wook-JinLee2006] Wook-Jin Lee, Seung-Ki Sul, "A New Starting Method of BLDC Motors Without Position Sensor," *IEEE Transactions on Industry Applications*, vol.42, no.6, pp.1532-1538, Nov.-dec. 2006.

[Wu2014] Z. Wu,H. Lyu,Y. Shi and D. Shi, "On Stability of Open-Loop Operation without Rotor Information for Brushless DC Motors" *Mathematical Problems in Engineering*, vol. 2014, Article ID 740498, 7 pages.

[Zhu2011] Z.Q. Zhu, L.M. Gong, "Investigation of Effectiveness of Sensorless Operation in Carrier-Signal-Injection-Based Sensorless-Control Methods," *IEEE Transactions on Industrial Electronics*, vol.58, no.8, pp.3431-3439, Aug. 2011.